AEROSOL CHEMICAL SPECIES CONTRIBUTIONS TO THE EXTINCTION COEFFICIENT

Thesis by

James Richard Ouimette

In Partial Fulfillment of the Requirements

for the degree of

Doctor of Philosophy

California Institute of Technology

Pasadena, California

1981

(Submitted July 17, 1980)

ACKNOWLEDGEMENTS

It is a pleasure to acknowledge the guidance and support of my advisor Richard C. Flagan, who suggested many key experimental and analytical ideas used in this thesis. I would also like to acknowledge the important contributions of Sheldon K. Friedlander, who acted as my advisor while he was at Caltech, helped me formulate my thesis topic, and provided me critical opportunities to obtain field data for my thesis research.

I would like to extend my personal gratitude to Dr. Susanne Hering at UCLA and Dr. Ed Macias at Washington University for their invaluable assistance while we worked together in Project VISTTA.

I owe a special note of thanks to three good friends who have helped me in many ways while I was at Caltech--Paul Owens, Raymond Kelso, and my brother Steve Ouimette. My initial interest in desert visibility grew out of our shared experiences and pleasures in the Mohave Desert.

I would like to thank the following people for their assistance and suggestions: Dr. Will Richards of Meteorology Research, Inc.; Drs. Tom Cahill and Danny Shadoan of U. C. Davis; Scott Nimelstein of UCLA; Tom Dodson and Dr. Larry Mathews of the Naval Weapons Center, China Lake; Dr. Peter McMurry of the University of Minnesota; Dr. Alan Waggoner of the University of Washington; and Dr. George Colovos of Rockwell International's Environmental Monitoring Center.

I would like to say thanks to the following people at Caltech for their suggestions and assistance: Hiroshi Kosaka, Art Stelson, Dean

Taylor, Dr. Fred Shair, Dr. Glen Cass, Rayma Harrison, Gunilla Hastrup, Danny Reible, Daryl Roberts, Don Kuehne, Dr. Robert Koh, Bill Brownlie, and Dr. Norman Brooks. Elton Daly, Joe Fontana, and Rich Eastvedt are thanked for their outstanding work in designing and constructing much of the experimental apparatus used in my research.

I was fortunate to have had the two best office mates that Caltech had to offer in Lisa "Ella Mae" Anderson and Jim "J. R." Young. I will miss you and your warm feelings very much.

During my stay at Caltech Elaine Granger continually helped me by typing correspondence and papers, taking messages, and typing part of this thesis. Thank you, Elaine. I appreciate the efforts of Sharon Hage, who typed most of this thesis and Phil Dube, who prepared some of the figures.

My children Laurie and Galen endured many hardships living in Pasadena while I was attending Caltech. I will always be grateful for their good cheer and spontaneity, and for helping me see life in its proper perspective and balance.

In my wife Patti I have been blessed with a loving companion with whom I have shared almost half my life. Her strength, friendship, and good humor add so much joy to my life and have made the completion of my research possible.

ABSTRACT

A model was developed for determining the contributions of aerosol chemical species to the extinction coefficient. The model assumes that the suspended particles are spherical and that particle volume is conserved with condensation and coagulation.

In general, the diameter, refractive index, and chemical composition of each particle must be known to rigorously calculate each species contribution. It is shown that species mass distributions with respect to particle diameter are sufficient to determine the species contributions exactly for some simple aerosols. Requirements were derived for each of the simple aerosols in which linear regression analysis could be legitimately applied to historical species mass concentrations data in order to estimate species contributions to light extinction.

The model was field tested at two remote arid locations in the southwestern United States where aerosol water content was ofsumed to be negligible. A low pressure impactor (LPI) was used in this research to size segregate aerosol from 0.05 to 4 μm aerodynamic diameter for elemental analysis. Two new techniques were developed for analysis of aerosol deposits collected with the LPI. Nanogram sensitivities were achieved for soot and many elements.

A three-week experiment was conducted in remote northeastern Arizona to calculate the contributions of fine aerosol species to the extinction coefficient. Theoretical mass extinction efficiencies were calculated and numerically integrated with measured mass distributions

to determine the contribution of each species to the extinction coefficient. The measured chemical species could account for 94 $\pm$ 19% of the fine aerosol mass concentration and 85 $\pm$ 34% of the measured particle extinction coefficient. All important species balances were met, both in total and with respect to size. The satisfactory agreement between the calculated and measured extinction coefficient indicates that the model and experimental technique are useful for determining the contributions to various aerosol species to visibility degradation at an arid site.

A one-year experiment was conducted at China Lake, California. Multiple regression analysis was applied to the measured particle scattering coefficient and fine aerosol species mass concentrations from 61 filter samples collected during 1979. Contributions of various aerosol species to the particle scattering coefficient, b_{sp}, were estimated. The statistically estimated contributions were compared with those determined theoretically using measured aerosol mass distributions. It was found that the statistically inferred species contributions to b_{sp} agreed qualitatively with those calculated theoretically using measured aerosol distributions. Regression analysis overestimated the contribution of sulfate relative to that calculated theoretically. Using measured 1979 values, a light extinction budget was calculated for China Lake. Measured mass extinction coefficients were used to predict the reduction in visibility at China Lake which would occur by increasing the concentrations of various aerosol species.

TABLE OF CONTENTS

	Page
ACKNOWLEDGEMENTS	ii
ABSTRACT	iv
LIST OF FIGURES	ix
LIST OF TABLES	xiv
LIST OF SYMBOLS	xvi
CHAPTER 1: INTRODUCTION	1
1.1 Visibility and the Extinction Coefficient	1
1.2 Aerosols and Light Extinction: A Comparison of Theoretical and Experimental Results	3
1.3 Chemical Species Contributions to Visibility Reduction	7
1.4 Organization of Thesis and Summary of Results	11
CHAPTER 2: THEORY	15
2.1 Introduction	15
2.2 Visibility and the Extinction Coefficient	15
2.3 Light Extinction Due to Single Component Spherical Aerosols	19
2.4 Chemical Species Contributions to the Extinction Coefficient	22
2.4.1 External Mixture	25
2.4.2 General Theory for Multicomponent Aerosol	26
2.4.3 Application of General Theory to Limiting Cases	32
2.4.4 Aerosol Species Mass Concentration-Extinction Coefficient Relationships	40
2.5 Aerosol Mass and Extinction Coefficient Balances	44
2.6 Summary	45

CHAPTER 3: APPLICATION OF THEORY TO A REMOTE ARID SITE IN ARIZONA 49

3.1 Introduction 49

3.2 Experimental Technique 51

3.3 Experimental Results 65

3.4 Chemical Species Extinction Coefficient Balance 104

3.5 Summary and Conclusions 121

CHAPTER 4: CHEMICAL SPECIES CONTRIBUTIONS TO LIGHT SCATTERING BY AEROSOLS AT A REMOTE ARID SITE: COMPARISON OF STATISTICAL AND THEORETICAL RESULTS 124

4.1 Introduction 124

4.2 Experimental Technique 126

4.3 Experimental Results 134

4.4 Particle Extinction Coefficient Budget 152

4.5 Summary and Conclusions 167

CHAPTER 5: SUMMARY 171

5.1 Summary of Results 171

5.2 Some Comments on Aerosols and Visibility Degradation in Pristine Arid Regions 175

REFERENCES 178

APPENDIX A: AEROSOL ELEMENTAL MASS DISTRIBUTIONS USING THE LOW PRESSURE IMPACTOR AND ANALYSIS BY PARTICLE INDUCED X-RAY EMISSIONS 185

A.1 Introduction 185

A.2 Experimental 186

A.3 Results 198

A.4 Summary and Conclusions 208

APPENDIX B: AEROSOL ABSORPTION COEFFICIENT AND SOOT MASS DISTRIBUTIONS USING THE LOW PRESSURE IMPACTOR AND THE INTEGRATING PLATE TECHNIQUE 210

B.1 Introduction 210

B.2 Experimental 213

B.3 Results 221

B.4 Summary and Conclusions 230

APPENDIX C: DETERMINATION OF AEROSOL MASS DISTRIBUTIONS USING THE LOW PRESSURE IMPACTOR AND THE TWOMEY NONLINEAR INVERSION ALGORITHM 231

C.1 Introduction 231

C.2 Background 232

C.3 Cases Where Unique Solutions Exist 237

C.4 Twomey Algorithm 242

C.5 Characteristics of the Solutions Obtained by the Twomey Algorithm 245

C.6 Test of the Twomey Algorithm 247

C.7 Summary and Conclusions 258

APPENDIX D: EXPERIMENTAL DATA 265

LIST OF FIGURES

Figure		Page
1.1	Ambient aerosol sulfur mass distributions obtained at Trona, California, May 13, 1978.	9
1.2	Normalized aerosol sulfur mass distributions, Trona and Pasadena, California.	10
2.1	Mass scattering efficiencies for homogeneous spheres.	23
2.2	Mass absorption efficiencies for homogeneous spheres.	24
3.1	Location of Zilnez Mesa sampling site in northeastern Arizona.	52
3.2	Sampling arrangement for fine aerosol chemical analysis, Zilnez Mesa, Arizona.	55
3.3	Normalized aerosol volume distributions, Zilnez Mesa, Arizona.	68
3.4	Particle extinction coefficient size distributions, Zilnez Mesa, Arizona, June 27-July 13, 1979.	72
3.5	Elemental mass distributions, Zilnez Mesa, Arizona, June 27-July 13, 1979, average.	86
3.6	Elemental lead and zinc mass distributions, Zilnez Mesa, Arizona, June 27-July 13, 1979, average.	88
3.7a	Normalized aluminum mass distribution, Zilnez Mesa, Arizona, June 27-July 13, 1979, average.	89
3.7b	Normalized silicon mass distribution, Zilnez Mesa, Arizona, June 27-July 13, 1979, average.	90
3.7c	Normalized sulfur mass distribution, Zilnez Mesa, Arizona, June 27-July 13, 1979, average.	91
3.7d	Normalized potassium mass distribution, Zilnez Mesa, Arizona, June 27-July 13, 1979, average.	92
3.7e	Normalized calcium mass distribution, Zilnez Mesa, Arizona, June 27-July 13, 1979, average.	93
3.7f	Normalized iron mass distribution, Zilnez Mesa, Arizona, June 27-July 13, 1979, average.	94

3.7g	Normalized sulfur mass distribution, Zilnez Mesa, Arizona, June 27-July 13, 1979, average.	96
3.8	Soot mass distribution, Zilnez Mesa, Arizona, June 27-July 13, 1979 average.	98
3.9	Aerosol mass distribution balance, Zilnez Mesa, Arizona, June 27-July 13, 1979 average.	103
3.10a	Normalized aluminum oxide mass and scattering coefficient distributions, Zilnez Mesa, Arizona, June 27-July 13, 1979 average.	109
3.10b	Normalized silicon dioxide mass and scattering coefficient distributions, Zilnez Mesa, Arizona, June 27-July 13, 1979 average.	110
3.10c	Normalized ammonium sulfate mass and scattering coefficient distributions, Zilnez Mesa, Arizona, June 27-July 13, 1979 average. Sulfur analysis by PIXE.	111
3.10d	Normalized potassium mass and scattering coefficient distributions, Zilnez Mesa, Arizona, June 27-July 13, 1979 average.	112
3.10e	Normalized calcium oxide mass and scattering coefficient distributions, Zilnez Mesa, Arizona, June 27-July 13, 1979 average.	113
3.10f	Normalized iron oxide mass and scattering coefficient distributions, Zilnez Mesa, Arizona, June 27-July 13, 1979 average.	114
3.10g	Normalized ammonium sulfate mass and scattering coefficient distributions, Zilnez Mesa, Arizona, June 27-July 13, 1979 average.	115
3.10h	Organic aerosol scattering coefficient distribution, Zilnez Mesa, Arizona, June 27-July 13, 1979 average.	116
3.10i	Soot scattering coefficient distribution, Zilnez Mesa, Arizona, June 27-July 13, 1979 average.	117
3.11a	Chemical species contributions to the fine aerosol mass concentration, Zilnez Mesa, Arizona. 13 sample average, June 26-July 13, 1979.	119

3.11b	Chemical species contributions to the fine particle extinction coefficient, Zilnez Mesa, Arizona. 12 sample average, June 27-July 13, 1979.	120
4.1	Location of sampling site within the Naval Weapons Center (NWC), China Lake, California.	128
4.2	Normalized aerosol volume distribution, China Lake, California, 1979 average.	136
4.3	Particle scattering coefficient, China Lake, California, 1979 average.	138
4.4	Normalized fine aerosol volume distribution, China Lake, California, 1979 average.	141
4.5a	Normalized sulfur mass distribution, China Lake, California, July 2-4, 1978.	149
4.5b	Normalized sulfur mass distribution, China Lake, California, Oct. 20-22, 1978.	150
4.5c	Normalized sulfur mass distribution, China Lake, California, Sept. 5-7, 1979.	151
4.6a	Normalized silicon mass distribution, China Lake, California, 0823-1430 PST, Sept. 7, 1979.	153
4.6b	Normalized calcium mass distribution, China Lake, California, 0823-1430 PST, Sept. 7, 1979.	154
4.6c	Normalized iron mass distribution, China Lake, California, 0823-1430 PST, Sept. 7, 1979.	155
A.1	Mylar collection surface for elemental and light absorption analysis.	189
A.2	Aerosol sulfur mass distributions as function of 50% cutoff aerodynamic diameter. Average of 11 ground level samples obtained at Zilnez Mesa, Arizona and 4 airborne samples obtained in Southwest region during June and July, 1979.	201
A.3	Aerosol sulfur mass distributions as function of 50% cutoff aerodynamic diameter. Average of 7 samples obtained on roof of Keck Laboratory, Caltech, during February, 1979.	203

A.4	Mass distributions of major elemental species as function of 50% cutoff aerodynamic diameter. Sample obtained on roof of Guggenheim Laboratory, Caltech, 1127-1437 PST, February 6, 1980.	205
A.5	Mass distributions of minor elemental species as function of 50% cutoff aerodynamic diameter. Sample obtained on roof of Guggenheim Laboratory, Caltech, 1127-1437, PST, February 6, 1980.	206
B.1	Apparatus for measuring light absorption by small area aerosol deposits.	215
B.2	Voltage-intensity calibration curve for Fairchild FPT 120 phototransistor.	217
B.3	Cumulative spatial light intensity distribution from laser at opal glass surface, 0.75 mm from end of optical fiber.	218
B.4	Particle absorption coefficient distributions. Solid histogram is for sample obtained in downtown Los Angeles, 0800-0815 PST, February 5, 1980. Dashed histogram is for sample obtained on roof of Guggenheim Laboratory, Caltech, 1430-1515 PST, February 6, 1980.	222
B.5	Comparison of ambient soot mass distribution with that obtained from a laboratory diesel engine.	224
B.6	Comparison of ambient soot and sulfur mass distributions. LPI samples collected on roof of Guggenheim Laboratory, Caltech, 1430-1515 PST, February 6, 1980.	226
C.1	Fractional collection efficiency for each stage of the low pressure impactor (LPI) when operating downstream of the AIHL cyclone preseparator.	235
C.2a	Test of Twomey inversion algorithm. Input parameters: 0.20 μm geometric mean diameter; 1.3 geometric standard deviation.	250
C.2b	Test of Twomey inversion algorithm. 0.30 μm geometric mean diameter; 3.0 geometric standard deviation.	251
C.2c	Test of Twomey inversion algorithm. Input parameters: 0.75 μm and 2.0 μm geometric mean diameters; 1.3 and 1.5 geometric standard deviations, respectively.	252

C.2d	Test of Twomey inversion algorithm. Input parameters: 0.1 and 0.4 μm geometric mean diameters; 1.1 and 2.0 geometric standard deviations, respectively.	253
C.2e	Test of Twomey inversion algorithm. Input parameters: 0.2 and 0.7 μm geometric mean diameters; 1.3 and 1.3 geometric standard deviations, respectively.	254
C.2f	Test of Twomey inversion algorithm. Input parameters: 0.05 μm geometric mean diameter; 1.3 geometric standard deviation.	255
C.3a	Sensitivity of inverted mass distribution to uncertainty in LPI calibration data. Standard deviations in δ_1 and δ_2 were 0.01 and 0.01, respectively.	259
C.3b	Sensitivity of inverted mass distribution to uncertainty in LPI calibration data. Standard deviations in δ_1 and δ_2 were 0.05 and 0.05, respectively.	260
C.3c	Sensitivity of inverted mass distribution to uncertainty in LPI calibration data. Standard deviations in δ_1 and δ_2 were 0.05 and 0.001, respectively.	261
C.3d	Sensitivity of inverted mass distribution to uncertainty in LPI calibration data. Standard deviations in δ_1 and δ_2 were 0.001 and 0.10, respectively.	262
C.3e	Sensitivity of inverted mass distribution to uncertainty in LPI calibration data. Standard deviations in δ_1 and δ_2 were 0.10 and 0.10, respectively.	263

LIST OF TABLES

Table		Page
2.1	Refractive Indices and Bulk Densities for Selected Aerosol Chemical Species	22
2.2	Chemical Species Contributions to the Extinction Coefficient: Balances on Measured Parameters	46
3.1	Time Averaged Normalized Aerosol Volume Distributions, Zilnez Mesa, 1979	67
3.2	Summary of Selected Time-Averaged Measurements, Zilnez Mesa, 1979	70
3.3	Values of the Aerosol Volume Scattering Efficiency, $\overline{G}_s$, Used to Calculate the Particle Scattering Coefficient Distribution	71
3.4	Normalized Aerosol Absorption Coefficient Distributions, Zilnez Mesa, 1979	75
3.5	Mass Balance on Chemical Species, Fine Aerosol, Zilnez Mesa, 1979	77
3.6	Comparison of Different Techniques for Determination of Total Aerosol Sulfate, Zilnez Mesa, 1979	79
3.7	Ratios of Determined Sulfate Concentrations (from Table 3.6)	80
3.8	Total Fine Aerosol Elemental Concentrations by PIXE Analysis: Comparison of Low Pressure Impactor and Filter Results, Zilnez Mesa, 1979	81
3.9	Comparison of Different Techniques for Determination of Soot Concentration, Zilnez Mesa, 1979	83
3.10	Elemental Mass Distributions, Zilnez Mesa, June 27-July 13, 1979, Average	100
3.11	Chemical Species Densities and Refractive Indices	105
3.12	Aerosol Chemical Species Contributions to the Extinction Coefficient, Zilnez Mesa, 1979	108
4.1	Meteorology, China Lake, 1946-1973 Average	129

4.2	Hourly Average Measured Particle Scattering Coefficient, b_{sp}, by Month for China Lake, 1979	135
4.3	Summary of Particle Scattering Coefficient Linear Regression Relationships, China Lake, 1979	139
4.4	Fine Aerosol Species Concentrations, 1979 Average, China Lake	142
4.5	Aerosol Elemental Enrichment Factors, 1979, China Lake	145
4.6	Fine Aerosol Species Mass Balance	146
4.7	Aerosol Mass Concentrations and b_{sp}: Results of Univariate Regressions for China Lake, 1979	157
4.8	Sulfate Average Mass Extinction Efficiency, α_i: Comparison of Statistically Inferred Values	160
4.9	Aerosol Species Contributions to the Particle Scattering Coefficient: Comparison of Statistical and Theoretical Results for China Lake	163
4.10	1979 China Lake Light Extinction Coefficient Budget	166
4.11	Estimated Reduction in Median Visual Range at China Lake due to a 2 $\mu g/m^3$ Increase in Aerosol Species Mass Concentration	168
A.1	Detection Limits and Average Blank Values for CNL PIXE Focused Beam	195
A.2	Estimate of CNL Focused Beam Precision from Repeated Measurements of Field Samples	197
A.3	Elemental Mass Concentrations Determined by LPI-PIXE, Pasadena, 1127-1437 PST, February 6, 1980	207
B.1	Particle Absorption Coefficient Lower Detection Limit vs. LPI Sample Time	219
B.2	Particle Absorption Coefficient, b_{ap} and Soot Concentrations: Comparison of Low Pressure Impactor Results with Filter Measurements	228

LIST OF SYMBOLS

Symbol	Definition	Units	Thesis Section Where First Used
A	aerosol deposit area	cm^2	3.2.3.6
b_{ag}	gas absorption coefficient	m^{-1}	1.1
b_{ap}	particle absorption coefficient	m^{-1}	1.1
$\overline{b}_{ap}$	time average measured particle absorption coefficient	m^{-1}	3.3.1.2
$\Delta b_{ap}/\Delta x$	particle absorption coefficient distribution with respect to dimensionless particle diameter	m^{-1}	B.1
b_e	extinction coefficient	m^{-1}	1.1
b_{ep}	particle extinction coefficient	m^{-1}	2.2
b_{epi}	contribution of species i to the particle extinction coefficient	m^{-1}	2.3.1
b_{sg}	gas (Rayleigh) scattering coefficient	m^{-1}	1.1
b_{sp}	particle scattering coefficient	m^{-1}	1.1
$\overline{b}_{sp}$ (calc.)	time average calculated particle scattering coefficient	m^{-1}	3.3.1.1
$\overline{b}_{spi}$ (calc.)	time average calculated fine particle scattering coefficient	m^{-1}	3.3.1.1
$\overline{b}_{sp}$ (meas.)	time average measured particle scattering coefficient	m^{-1}	3.3.1.1
$\Delta b_{sp}/\Delta x$	particle scattering coefficient distribution with respect to dimensionless particle diameter	m^{-1}	3.3.1.1
b_{spi}	contribution of species i to the particle scattering coefficient	m^{-1}	4.1

$\Delta b_{spi}/\Delta x$	contribution of species i to the particle scattering coefficient distribution	m^{-1}	3.4
C	optical contrast	none	2.1
C^*	optical contrast threshold	none	2.1
C(D)	Cunningham slip factor	none	3.3.3.1
C_T	total aerosol carbon concentration	$\mu g/m^3$	4.5.1
D	particle diameter	μm	1.2
D_a	aerodynamic particle diameter	μm	3.3.3.1
D_S	Stokes particle diameter	μm	3.3.3.1
D_{50i}	50% efficiency cutoff diameter of stage i of low pressure impactor	μm	3.3.3.1
D_o	reference particle diameter, equal to 0.01 μm for this study	μm	2.2
$E_a(x)$	particle mass absorption efficiency as function of particle size x	m^2/g	2.2
$E_e(x)$	particle mass extinction efficiency as function of particle size x	m^2/g	2.2
$E_i(x)$	particle collection efficiency of LPI stage i as function of particle size x	none	C.2
$E_S(x)$	particle mass scattering efficiency as function of particle size x	m^2/g	C.2
f(x)	aerosol mass distribution, equal to dM/dx	$\mu g/m^3$	2.2
$f_i(x)$	aerosol mass distribution of species i, equal to dM_i/dx	$\mu g/m^3$	2.3.1
$\overline{f}_i(x)$	normalized mass distribution of species i	none	2.3.4.1
$f_s(x)$	soot mass distribution	$\mu g/m^3$	B.1

$F_i(x)$	fraction of particles of size x penetrating the previous i LPI stages	none	C.2
g	size-composition probability density function	μm^{-3}	2.3.2
G_a	particle volume absorption efficiency function	m^{-1}	2.2
G_e	particle volume extinction efficiency function	m^{-1}	2.2
G_s	particle volume scattering efficiency function	m^{-1}	2.2
$\overline{G}_{sj}$	particle volume scattering efficiency averaged over particle size interval $[D_j, D_{j+1}]$	m^{-1}	3.3.1.1
h	size-composition-refractive index probability density function	μm^3	2.3.2
I	radiation intensity	W/cm^2	2.1
I_o	reference radiation intensity	W/cm^2	3.2.3.6
K_a	single particle absorption efficiency	none	2.2
K_e	single particle extinction efficiency	none	1.2
K_e^a	average single particle extinction efficiency	none	2.3.2
$K_{ei}^{a'}$	average single particle extinction efficiency without species i	none	2.3.2
$K_i(x)$	fractional particle collection efficiency of LPI stage i; also called kernel	none	C.2
$\overline{K}_{ij}$	average of $K_i(x)$ over the particle size interval $[x_j, x_{j+1}]$	none	C.2.1
K_s	single particle scattering efficiency	none	2.2
ℓ	mean free path	μm	3.3.3.1

m	refractive index	none	1.2
m^*	particle refractive index for internal mixture	none	2.3.3.2
m_a	species volume average particle refractive index	none	2.3.3.3
m_i	particle refractive index of species i	none	2.3.1
M_i	aerosol mass concentration of species i	$\mu g/m^3$	2.1
	aerosol mass collected on stage i of LPI (Appendix C only)	$\mu g/m^3$	C.2
M_T	total aerosol mass concentration	$\mu g/m^3$	2.3.4.2
M_u	aerosol mass concentration of chemically unaccounted species	$\mu g/m^3$	4.5.1
dM/dx	aerosol mass distribution with respect to dimensionless particle size	$\mu g/m^3$	2.2
$\Delta M_i/\Delta \log D_{50i}$	mass distribution with respect to 50% efficiency cut point of stage i of LPI	$\mu g/m^3$	3.3.3.1
$n(D)$	particle size distribution function with respect to particle diameter	$cm^{-3}\mu m^{-1}$	2.2
$n_i(D)$	particle size distribution function of species i	$cm^{-3}\mu m^{-1}$	2.3.1
$n(v)$	particle size distribution function with respect to particle volume	$cm^{-3}\mu m^{-3}$	2.3.2
N_T	total particle number concentration	cm^{-3}	2.3.2
p	dimensionless optical size parameter, equal to $\pi D/\lambda$	none	1.2
P	atmospheric pressure	mm Hg	3.3.1
r	correlation coefficient	none	4.4
S	total volume of air sampled	m^3	3.2.3.6
v	particle volume	μm^3	2.3.2

V_i	aerosol volume concentration of species i	$\mu m^3/cm^3$	2.3.4.2
V_R	local visual range	km	1.1
V_{RO}	initial local visual range	km	4.5.4
V_T	total aerosol volume concentration	$\mu m^3/cm^3$	2.3.3.1
V_{T1}	total aerosol volume concentration of particles less than 1.78 μm diameter	$\mu m^3/cm^3$	3.3.1
VT.5	total aerosol volume concentration of particles less than 0.50 μm diameter	$\mu m^3/cm^3$	4.4
VT2	total aerosol volume concentration of particles less than 2.0 μm diameter	$\mu m^3/cm^3$	4.4
VT10	total aerosol volume concentration of particles less than 10 μm diameter	$\mu m^3/cm^3$	4.4
dV/dlogD	aerosol volume distribution	$\mu m^3/cm^3$	2.2
$dV_i/dlogD$	aerosol volume distribution of species i	$\mu m^3/cm^3$	2.3.2
$d\bar{V}/dlogD$	normalized aerosol volume distribution	none	2.3.4.2
W_i	molecular weight of species i	g/mole	2.3.2
x	dimensionless particle diameter, equal to log (D/D_o)	none	2.2
y_i	moles of species i	mole	2.3.2
z	path length	m	2.1
α_i	average mass extinction efficiency of species i	m^2/g	2.1
$\delta(x)$	Dirac delta function	none	2.3.3.1
δ_{ij}	Kronecker delta	none	C.2.2

λ	wavelength of electromagnetic radiation	μm	1.2
μm	micrometer, equal to 10^{-6} m		
$\bar{v}_i$	partial molar volume of species i	cm^3/mole	2.3.2
ρ	particle density	g/cm^3	2.2
ρ_i	particle density of species i	g/cm^3	2.3.2
σ	geometric standard deviation	none	C.5.1
τ	optical thickness	none	2.1
ϕ_{ij}	kernel vector product	none	C.2.2
EAA	Electrical Aerosol Analyzer		
FVFPD	Flash Volatilization and Flame Photometric Detection		
LPI	Low Pressure Impactor		
OPC	Optical Particle Counter		
PIXE	Particle Induced X-ray Emission		
WAA	Whitby Aerosol Analyzer		

CHAPTER 1

INTRODUCTION

1.1 VISIBILITY AND THE EXTINCTION COEFFICIENT

Visibility reduction in both urban and rural areas of the world is often associated with particulate matter suspended in the atmosphere, defined as aerosols. The recognition of this problem in the United States has led Congress to amend the Clean Air Act in 1977, requiring that states implement plans to preserve areas of near-pristine air quality. Within the continental United States most near-pristine air quality exists in the generally arid West. The outstanding scenic resources in the West require excellent visibility for their appreciation. Future energy development and production, if not properly controlled, may have a detrimental regional impact on visibility due to the production of NO_2 and aerosols.

A proper control strategy for visibility protection at a given location requires information about the relationship between each source and its contribution to a quantity called the extinction coefficient, b_e. It will be shown in Chapter 2 that the visual range, V_R, and b_e are related through the Koschmieder equation (Middleton, 1952)

$$V_R = \frac{3.9}{b_e}$$

The extinction coefficient can be expressed as the sum of terms which account for light scattering and absorption by gases and suspended particles (Charlson et al., 1978):

$$b_e = b_{sg} + b_{ag} + b_{sp} + b_{ap} \qquad (1.1)$$

where a, s, g, and p denote absorption, scattering, gases, and particles, respectively. The Rayleigh scattering coefficient, b_{sg}, has a value integrated over the solar spectrum of $15 \times 10^{-6} m^{-1}$ at sea level and 25 °C and varies linearly with air density. It provides an upper bound on visual range of about 260 km. It is not unusual in many remote locations in the western United States for the visibility to be limited by Rayleigh scattering due to air molecules (Trijonis and Yuan, 1978a). However, in many rural and urban locations, b_e is dominated by light scattering due to particles, b_{sp}. Atmospheric sulfates, nitrates, and organics, due to their distribution with respect to particle size, often contribute substantially to b_{sp}. There is substantial evidence that the particle absorption coefficient, b_{ap}, is due almost exclusively to airborne soot (Rosen et al., 1977; Pierson, 1978; Roessler and Faxvog, 1979). The absorption coefficient due to gases, b_{ag}, is primarily determined by NO_2 concentrations. Light absorption by NO_2 may be relatively important in plumes from power plants which remove particles with high efficiency from the stacks.

To assess the contribution of a particular source to b_e at a given location, it is then necessary to determine its contribution to b_{sp}, b_{ap}, and b_{ag}. As a good approximation, the contribution of a

particular source to b_{ag} would be directly proportional to its contribution to the total NO_2 concentration. The contribution of the source to the scattering and absorption of light due to aerosols, b_{sp} and b_{ap}, is not as straightforward. One must first link the source to concentrations of each chemical species in the aerosol. Secondly, the contribution of each chemical species to the particle scattering and absorption coefficients must then be determined. This is the topic of this thesis.

1.2 AEROSOLS AND LIGHT EXTINCTION: A COMPARISON OF THEORETICAL AND EXPERIMENTAL RESULTS

If the aerosol is composed of homogeneous spheres of known diameter, D, refractive index, m, and concentration, it is possible to calculate the extinction coefficient resulting from the aerosol at a given wavelength of light, λ , using so-called Mie theory (Mie, 1908). Mie's theoretical solution to the problem of light scattering and absorption by a homogeneous sphere in an infinite medium is described by van de Hulst (1957) and Kerker (1969). Simple computer algorithms to calculate single particle extinction efficiencies, K_e, from homogeneous and concentric spheres are found in Wickramasinghe (1973). This is discussed in greater detail in Chapter 2.

A number of investigators have compared measured aerosol optical properties with those predicted from Mie theory. The results of some of the experiments are summarized by Sverdrup (1977). Pinnick et al. (1973) generated monodisperse spherical aerosols of 0.26 to 2 μm

diameter using a vibrating capillary. Particle diameters of nitrosin dye (m = 1.67-0.26i), Flowmaster ink (m = 1.65-0.069i), and polystyrene latex (m = 1.59-0.0i) were determined by an electron microscope. Integrated light scattered from 8° to 38° from the direction of forward scattering was measured with a photoelectric particle counter and compared with Mie theory calculations. Agreement between predicted and measured values was good.

Pinnick et al. (1976) generated monodisperse nonspherical NaCl and K_2SO_4 particles using a vibrating capillary. They found that when the size parameter, p, (defined as the ratio of the particle circumference to the wavelength) was greater than about 5 (effective particle diameter, D, greater than 0.8 μm), the measured forward scattering was greater than that predicted by Mie theory for spheres of the same cross-sectional area. For particles with $p < 5$ agreement was better. Gibbs (1978) studied the white light scattered at various angles from glass spheres, crushed quartz, and mica flakes of 2-5 μm and 10-20 μm diameter in suspension in water. He found that the forward scattering from the various shapes was similar to that of spheres, but the backscattering was substantially different. Holland and Draper (1967) found that the average mass scattering efficiency, defined as the ratio of the scattering coefficient to the mass concentration, of polydisperse samples of irregular randomly oriented talc particles of D = 0.92 μm and m = 1.50 agreed with the theoretical value for spherical particles. Holland and Gagne (1970) found that the average mass scattering efficiency of polydisperse samples of irregularly shaped

randomly oriented SiO_2 particles of D = 0.45 μm and m = 1.55 also agreed with the theoretical value for spherical particles. Wieser et al. (1977) produced polydisperse NaCl particles between 0.3 μm and 2 μm and found that their forward light scattering approximated that of spheres of the equivalent projected area diameter. Elder et al. (1974) generated polydisperse flyash, soot, and SiO_2 aerosols of number median diameters between 0.28 μm and 0.70 μm. The measured mass extinction efficiencies were up to a factor of 2 lower than that calculated using Mie theory and an assumed lognormal mass distribution.

A number of investigators have compared measured and calculated optical properties in the ambient aerosol. Ensor et al. (1972) performed Mie scattering calculations on 212 Pasadena aerosol size distributions measured in 1969 with an electrical aerosol analyzer (EAA) and an optical particle counter (OPC). They found the calculated particle scattering coefficient averaged about one-half the measured value. Linear regression analysis yielded a correlation coefficient of 0.89 between the measured and calculated values. Sverdrup (1977) had much better success using size distributions obtained in the California Aerosol Characterization Experiment (ACHEX). On the average, the calculated particle scattering coefficient was 2.96% higher than the measured value for 549 size distributions, assuming a refractive index of m = 1.50-0.02i. Patterson et al. (1976) compared calculated and observed visibilities during episodes of wind-blown dust in Texas. Particles between 0.62 μm and 250 μm were measured. Good agreement between calculated and measured visibility was obtained over three

orders of magnitude. De Luisi et al. (1976) used an impactor to obtain airborne aerosol size distributions from 0.8 to 24 μm diameter. The optical depth (extinction coefficient integrated over a path length) was measured with a ground-based multi-wavelength photometer. On the average the calculated optical depth was 20% less than the measured value, presumably due to particles less than 0.8 μm diameter which were not sampled.

Patterson and Wagman (1977) sampled aerosol near New York City using Andersen impactors with uncoated impaction plates and glass fiber after filters. Size-fractionated chemical species and total mass distributions were obtained for four different levels of the measured particle scattering coefficient. The particle scattering coefficient was calculated using the measured distribution of total mass with respect to particle size. Agreement was fair. The contributions of various species to the scattering coefficient were not calculated. Not all of the measured total mass could be accounted for the measured chemical species.

Macias et al. (1979) measured airborne aerosol distributions from 0.01 μm to 10 μm in the Southwest and found good agreement between the calculated and measured particle scattering coefficient. An airborne impactor size segregated aerosol for elemental analysis by particle induced X-ray emissions (PIXE) (Cahill, 1975). Particles less than 0.5 μm aerodynamic diameter were collected on an after filter. The contributions of measured aerosol species to the particle extinction coefficient were estimated using the aerosol volume and elemental mass

distributions and assuming a refractive index of m = 1.54-0.015i. An aerosol mass balance was not performed to account for all species. Ammonium sulfate and silicon dioxide were calculated to be the principal contributors to visibility degradation at that time.

1.3 CHEMICAL SPECIES CONTRIBUTIONS TO VISIBILITY REDUCTION

Until recently, adequate instrumentation has not been available to determine chemical species mass distributions resolved sufficiently for extinction coefficient calculations. The previous attempts to infer the contributions of sulfates, nitrate, organics, and relative humidity to visibility reduction used linear and non-linear regression analysis (White and Roberts, 1977; Trijonis and Yuan, 1978a,b; Cass, 1979). These efforts are reviewed by Cass (1979). Sulfate was found to be responsible for the bulk of the variation in light extinction by particles at all locations, but that sulfate in the arid Southwest was not as efficient per mass concentration in reducing visibility as sulfate in the more humid regions. The results of these studies, particularly for nitrate, may be subject to error due to artifact nitrate and sulfate produced on the high volume filters used for aerosol collection (Spicer and Schumacher, 1977).

The development and calibration of the low pressure cascade impactor (LPI) (Hering et al., 1978; Hering et al., 1979) and a technique for determination of nanogram quantities of sulfur aerosol (Roberts and Friedlander, 1976) has made the measurement of sulfur aerosol size distributions through the light scattering range possible.

The results of such measurements in the Los Angeles Basin and in a variety of desert locations provide verification of the earlier statistical work. The LPI was used to obtain sulfur mass distributions during SO_2 gas-to-particle conversion at Trona, California, an arid site in the Mohave Desert, shown in Figure 4.1. Aerosol mass growth was found to occur primarily in the 0.08 to 0.26 μm particle diameter interval, as shown in Figure 1.1. This is consistent with measured and predicted growth due to the homogeneous oxidation of SO_2 to H_2SO_4 and subsequent coagulation and condensation (Gelbard and Seinfeld, 1979b; McMurry and Friedlander, 1979). Measurements using the LPI in more humid Pasadena showed that aerosol sulfur mass often accumulates between 0.5 and 1.0 μm diameter, perhaps due to droplet phase conversion (Friedlander, 1978; Gelbard and Seinfeld, 1979a). A comparison between the arid and humid aerosol sulfur distributions is shown in Figure 1.2. Calculations of the mass extinction efficiencies (Chapter 2) based on these distributions show that sulfate in Pasadena is more efficient in scattering light than sulfate in arid Trona, consistent with statistical results.

In order to estimate the impact of future aerosol sources on visibility in the Southwest, size distributions of chemical species in addition to sulfur are required. Primary emissions from coal fired power plants include Si, Al, Fe, Ca, C as well as many trace species. Some of these elements, particularly Si, have been found in significant quantities as fine particles in the Southwest (Macias et al., 1979; Allee et al., 1978). Techniques for obtaining the submicron mass

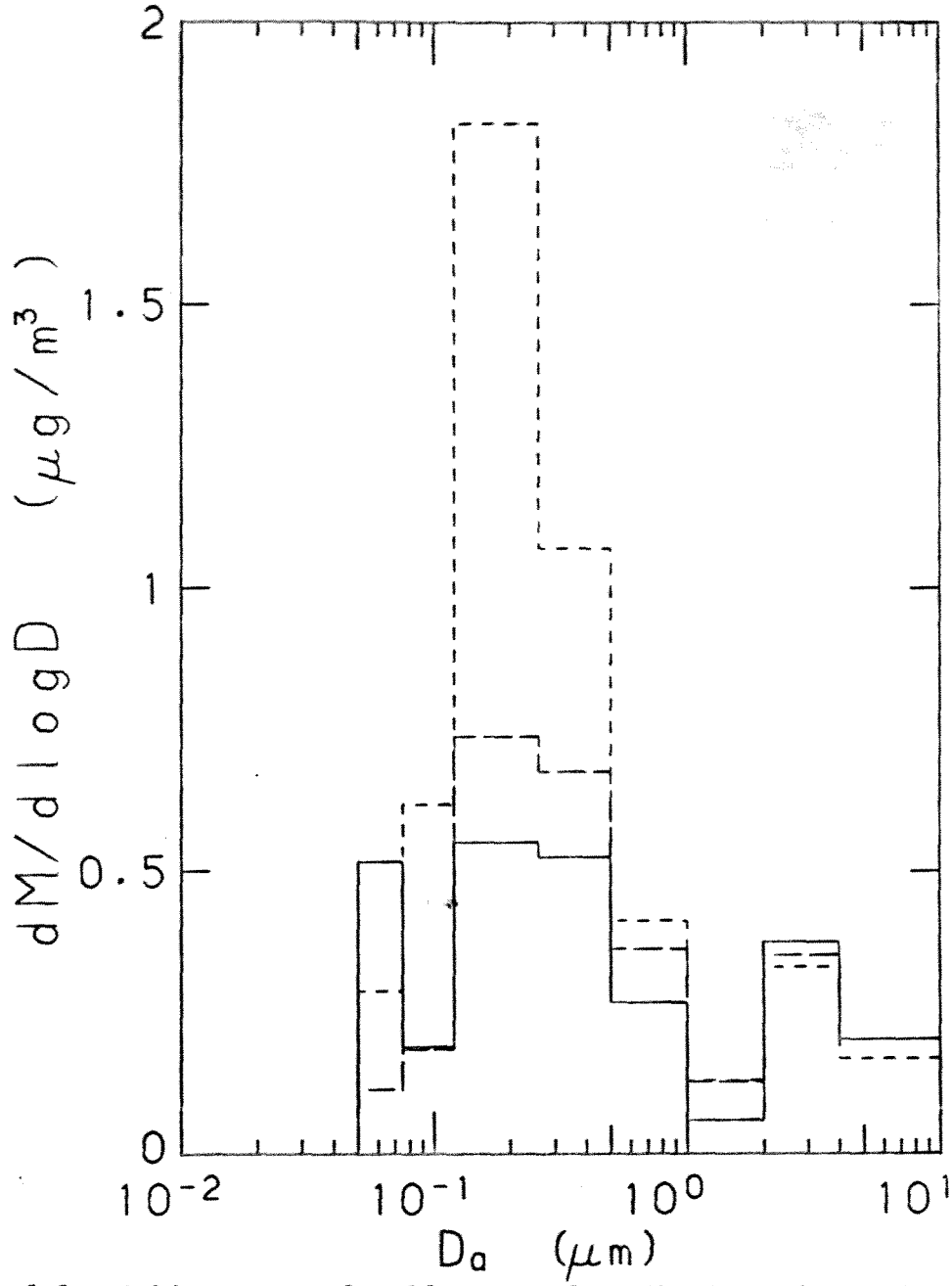

Figure 1.1. Ambient aerosol sulfur mass distributions obtained at Trona, California, May 13, 1978. Aerosol segregated by low pressure impactor (LPI) according to aerodynamic diameter, D_a, and analyzed by flash volatilization and flame photometric detection (FVFPD). The solid histogram is the average distribution measured between 0503-0629 PDT; total sulfur mass concentration, M, was 0.76 μg/m^3. The long dash histogram is the average measured between 0652-0840 PDT; M=0.83 μg/m^3. The short dash histogram is the average measured between 0946-1145 PDT; M=1.42 μg/m^3. Distributions show aerosol growth in arid location, probably due to gas phase oxidation of SO_2 to H_2SO_4 and subsequent condensation and coagulation.

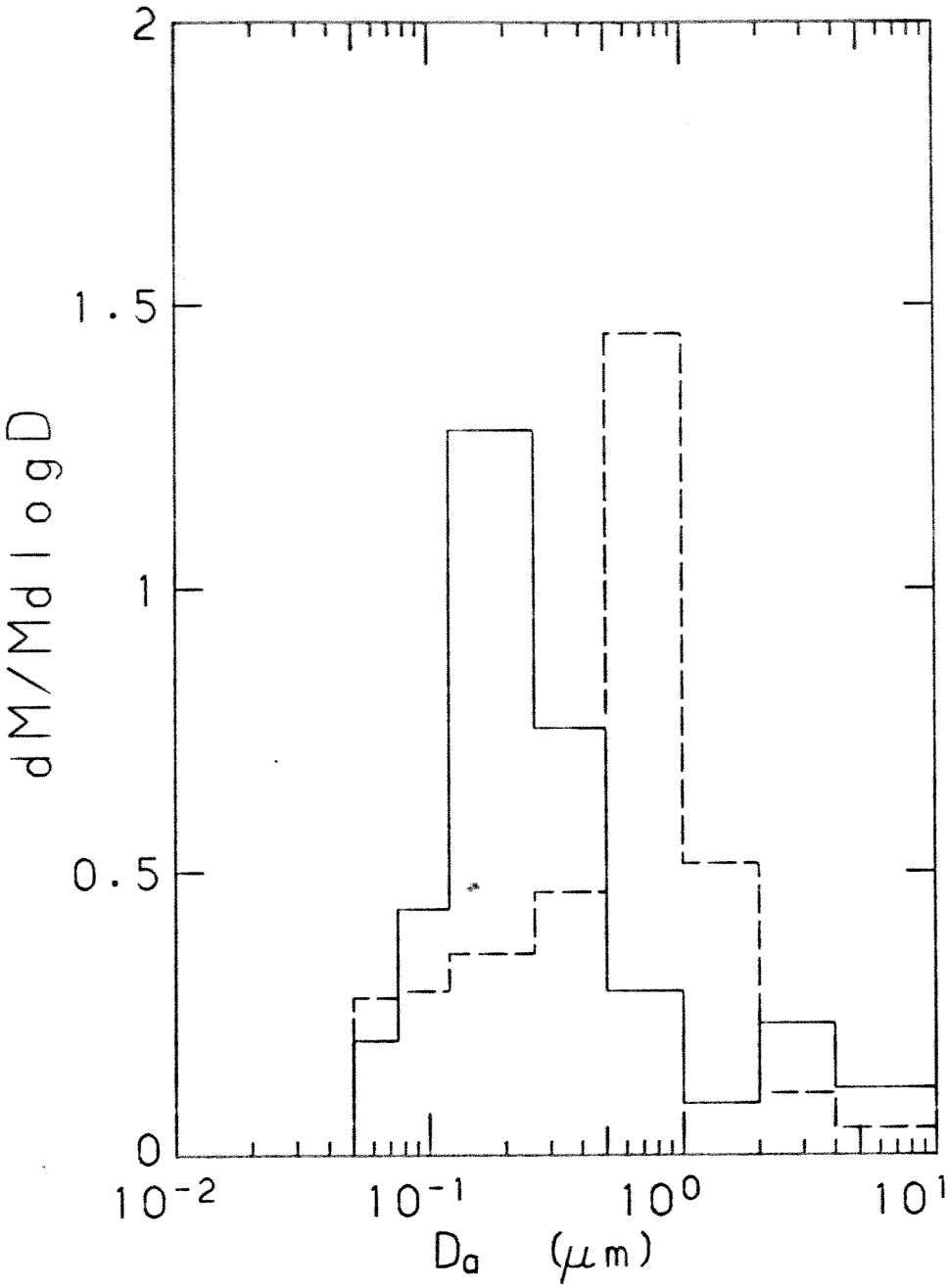

Figure 1.2. Normalized aerosol sulfur mass distributions, Trona and Pasadena, California. Aerosol size segregated by LPI and analyzed by FVFPD. The solid histogram is the average distribution measured at Trona on May 13, 1978 between 0946-1145$_3$PDT; total sulfur mass concentration, M, was 1.42 $\mu g/m^3$. The dashed histogram is the average distribution measured on the roof of Keck Laboratory, Caltech, from 1428-1600 PST, December 26, 1978; M = 10.6 $\mu g/m^3$. The difference in distributions may indicate different SO_2 gas-to-particle conversion mechanisms.

distributions of these species have been unavailable but are necessary for rigorously determining the contribution of each species to the extinction coefficient.

In addition to experimental techniques for determining species mass distributions, a more general and complete theory is needed for assessing chemical species contributions to the extinction coefficient. The theory needs to include aerosols in which individual particles may be composed of more than one chemical species and in which chemical composition may vary with particle size.

1.4 ORGANIZATION OF THESIS AND SUMMARY OF RESULTS

This thesis describes research conducted to determine the contributions of aerosol chemical species to the extinction coefficient.

A general theory is derived in Chapter 2 for predicting the contributions of chemical species to the extinction coefficient for a multicomponent aerosol composed of spheres. In general, the diameter, refractive index, and chemical composition of each particle must be known to rigorously calculate each species contribution. It is shown that species mass distributions of the kind obtained with a perfect impactor are sufficient to determine the species contributions exactly for three simple aerosols: an external mixture, an internal mixture, and a so-called specific mixture with an assumed volume average refractive index. A specific mixture is an aerosol in which the chemical composition may vary with particle size. Although each particle may be

composed of many species, it is assumed that all particles of the same size have the same composition. A specific mixture of spherical particles with a volume average refractive index is the most general aerosol for which the mass distributions can be used to determine the species contributions exactly. An additional requirement placed on the use of mass distributions to predict the species extinction coefficient contributions is that particle volume must be conserved with coagulation and condensation. The growth of hygroscopic particles by condensation of water would not be permitted if the partial molar volume of any species changes in the process. Requirements were derived for each of the three simple aerosols in which linear regression analysis could be legitimately applied to historical species mass concentrations data in order to estimate species contributions to light extinction.

Chapter 3 describes the results of a 3-week experiment in remote northeastern Arizona to calculate the contributions of fine aerosol species to the extinction coefficient. Theoretical mass extinction efficiencies were calculated and numerically integrated with measured mass distributions to determine the contribution of each species to the extinction coefficient. The measured chemical species could account for 94 $\pm$ 19% of the fine aerosol mass concentration and 85 $\pm$ 34% of the measured particle extinction coefficient. All important species balances were met, both in total and with respect to size. The satisfactory agreement between the calculated and measured extinction coefficient indicates that the technique is useful for determining the

contributions of various aerosol species to visibility degradation at an arid site.

Chapter 4 describes the results of a one-year experiment at China Lake, California. Multiple regression analysis was applied to the measured particle scattering coefficient and fine aerosol species mass concentrations from 61 filter samples collected during 1979. Contributions of various aerosol species to the particle scattering coefficient, b_{sp}, were estimated. The statistically estimated contributions were compared with those determined theoretically using measured aerosol mass distributions. It was found that the statistically inferred species contributions to b_{sp} agreed qualitatively with those calculated theoretically using measured aerosol distributions. Regression analysis overestimated the contribution of sulfate relative to that calculated theoretically. Using measured 1979 values, a light extinction budget was calculated for China Lake. Measured mass extinction coefficients were used to predict the reduction in visibility at China Lake which would occur by increasing the concentrations of various aerosol species.

Chapter 5 summarizes the thesis research and comments on the role of chemical composition and aerosol dynamics in visibility degradation in near-pristine arid regions.

The low pressure impactor (LPI) was used in this research to size segregate aerosol from 0.05 to 4 μm aerodynamic diameter for elemental analysis. Two new analytical techniques were developed for analysis of

aerosol deposits collected with the LPI. Appendix A describes the development and evaluation of the LPI-PIXE technique for mass determination of most elements between aluminum and lead. Aerosol is size segregated and impacted on coated mylar films which are then bombarded by a focused alpha-particle beam at the Crocker Nuclear Laboratory, University of California, Davis. Nanogram sensitivities are achieved.

Appendix B describes a technique in which a He-Ne laser is used with a 0.25 mm diameter optical fiber to measure the light absorbed by aerosol deposited on coated mylar film. The particle absorption coefficient distribution from 0.05 to 4 μm aerodynamic diameter can now be calculated by using this technique with LPI aerosol deposits. The soot mass distribution can be inferred from these measurements with nanogram sensitivity. This technique is only semiquantitative at the present.

Appendix C describes the evaluation of a non-linear inversion algorithm to obtain improved mass distributions using calibration data and masses measured on each stage of the LPI. A more accurate determination of the particle extinction coefficient distribution is now possible with the distribution obtained from the LPI and the inversion algorithm.

CHAPTER 2

THEORY

2.1 INTRODUCTION

In this chapter relationships between measured species mass distributions and their contributions to visibility reduction are derived. The parameter which links aerosol properties to visibility reduction is the extinction coefficient, b_e. A review of the relationship between b_e and visual range is presented.

The functional dependence of the particle extinction coefficient, b_{ep}, on the aerosol mass distribution is derived for a single component aerosol. This is then generalized for a multicomponent aerosol. It is shown that for some simple aerosols the chemical species contributions to b_{ep} may be calculated exactly from their mass distributions. Requirements are derived for each of the simple aerosols for which b_{ep} can be expressed as a linear combination of the mass concentrations of the chemical species.

2.2 VISIBILITY AND THE EXTINCTION COEFFICIENT

A theoretical treatment of visibility and light extinction can be found in the classic reference by Middleton (1952). The topic has also been summarized by Friedlander (1977) and Charlson et al. (1978). Because of scattering and absorption of light by gases and aerosols, a light beam is reduced in intensity between two points. The fraction of incident light intensity, I, scattered and absorbed per unit path

length, z, is defined as the extinction coefficient, b_e:

$$b_e = - \frac{dI}{Idz}$$

The extinction coefficient has units of inverse length, m^{-1}. Ignoring multiple scattering effects, the above equation can be integrated between two points along the path to determine the reduction in light intensity:

$$\frac{I(x)}{I_o} = e^{-\tau}$$

where the optical thickness, $\tau = \int_o^x b_e dz$.

Objects can be recognized due to their contrast with the surrounding background. The contrast, C, between a test object and the horizon sky is defined by:

$$C = (I_1/I_2) - 1$$

where I_1/I_2 is the ratio of the test object intensity to that of the background. The brightness of both light and dark objects asymptomatically approaches that of the horizon as the distance between observer and test object increases (Charlson et al., 1978). Thus the contrast will decrease with distance to a point where the object can no longer be discernible against its background. It can be shown that the ratio of the contrast, C(x), of a test object perceived from a distance x to

its initial contrast C_o is given by

$$\frac{C(x)}{C_o} = \exp(-b_e x)$$

If the test object is black, $I_1(0) = 0$ and $C_o = -1$. The visual range V_R is defined as the distance at which a black test object is barely discernible from the background. Denoting the necessary contrast threshold as C^*, then

$$V_R = \frac{\ell n(-C^*)}{b_e}$$

Based on human observation, typical observers can detect a black object with a 2% contrast against the horizon, so C^* is taken to be -0.02, resulting in

$$V_R = \frac{3.9}{b_e} \qquad (2.1)$$

This is the Koschmeider equation relating the extinction coefficient, b_e, to the visual range by means of the contrast threshold, which is a psychophysical constant. If the extinction coefficient is measured along a sight path, then V_R is the visual range. If b_e is measured at a point, then V_R is taken to be the local visual range. The two values are equal in a homogeneous atmosphere. From Equation 2.1 one may derive the relative change in visual range due to an infinitesimal

change in the mass concentration of a particular species, M_i:

$$\frac{\partial V_R}{V_R \partial M_i} = - \frac{V_R}{3.9} \frac{\partial b_e}{\partial M_i}$$

It is seen that the relative change is proportional to the preexisting visual range. Thus, consistent with intuition, pristine visual areas are inherently more sensitive to degradation. The manner in which the extinction coefficient can vary with change in pollutant mass concentration will be discussed later. In certain simple systems, the infinitesimal variation in b_e with M_i may be a constant, α_i, denoted as the average mass extinction efficiency of species i. In this case, one obtains a linear relationship between the relative change in visual range, preexisting visual range, and α_i:

$$\frac{\partial V_R}{V_R \partial M_i} = - \frac{\alpha_i V_R}{3.9}$$

For finite changes in mass concentration, ΔM_i, the relative change in visual range is

$$\frac{\Delta V_R}{V_{RO}} = - \frac{V_{RO} \sum_{i=1}^{N} \alpha_i \Delta M_i}{3.9 + V_{RO} \sum_{i=1}^{N} \alpha_i \Delta M_i} \qquad (2.2)$$

where V_{RO} is the initial visual range.

2.3 LIGHT EXTINCTION DUE TO SINGLE COMPONENT SPHERICAL AEROSOLS

If the aerosol is composed of particles which are homogeneous spheres, the single particle light extinction efficiency, K_e, can be derived theoretically by Mie's solution to Maxwell's equations with the appropriate boundary conditions. A complete discussion of the derivation can be found in van de Hulst (1957) and Kerker (1969), among others. The particle extinction coefficient, b_{ep}, due to the aerosol is then given by

$$b_{ep} = \int_0^\infty \frac{\pi}{4} D^2 K_e(m,p) n(D) dD \tag{2.3}$$

where m is the complex refractive index of each particle and $p = \pi D/\lambda$ is the dimensionless size parameter relating the diameter, D, of each particle to the wavelength λ of the incident light. n(D) is the particle number density function denoting the concentration of particles per unit particle size increment. The single particle extinction efficiency, $K_e(m,p)$, can be expressed as an infinite series of amplitude functions. Since the single particle extinction efficiency is the sum of the particle scattering and absorption contributions, the analogous relationships are obtained:

$$b_{sp} = \int_0^\infty \frac{\pi}{4} D^2 K_s(m,p) n(D) dD$$

$$b_{ap} = \int_0^\infty \frac{\pi}{4} D^2 K_a(m,p) n(D) dD$$

where $b_{ep} = b_{sp} + b_{ap}$, and K_s and K_a are the single particle scattering and absorption efficiencies, respectively.

The particle extinction coefficient can also be conveniently expressed in terms of the aerosol volume distribution, dV/dlogD:

$$b_{ep} = \int_{-\infty}^{\infty} G_e(m,D,\lambda) \frac{dV}{dlogD} dlogD \tag{2.5}$$

where the particle volume extinction efficiency (Friedlander, 1977), G_e, is given by

$$G_e(m,D,\lambda) = \frac{3}{2D} K_e(m,p)$$

The volume scattering and absorption efficiencies, G_s and G_a, respectively, can be used to determine analogous relationships for b_{ap} and b_{sp}.

Similarly, b_{ep} can be expressed as a convolution of the mass extinction efficiency, E_e, and the particle mass distribution, f(x):

$$b_{ep} = \int_{o}^{\infty} E_e(m,x,\lambda) f(x) dx \tag{2.4}$$

where

$$x \equiv \log(D/D_o) \tag{2.5}$$

$$f(x) \equiv dM/dx \tag{2.6}$$

$$E_e(m,x,\lambda) = \frac{3}{2D\rho} K_e(m,p) \tag{2.7}$$

and ρ is the particle density. The logarithmic transformation from particle size D to x is used to account for the wide variation in

particle size. The reference diameter, D_o, is chosen in this thesis to be the lower limit of integration. Since no information on particle sizes less than 0.01 μm was obtained in this research, D_o was chosen to be 0.01 μm. The upper limit on D was 10 μm, resulting in x varying from 0 to 3. The mass scattering and absorption efficiencies, E_s and E_a, respectively, are then defined as follows:

$$E_s(m,x,\lambda) = \frac{3}{2D\rho} K_s(m,p) \tag{2.8}$$

$$E_a(m,x,\lambda) = \frac{3}{2D\rho} K_a(m,p) \tag{2.9}$$

The mass scattering and absorption efficiencies are strongly dependent upon particle size and the chemical composition of the suspended particulate. Refractive indices and bulk densities for representative fine aerosol species are shown in Table 2.1. Pentanedioic acid is a constituent of the secondary organic aerosol found in the Los Angeles basin. The properties of the model aerosol have been estimated by a member of investigators and have been used to compare calculated and measured scattering coefficients, to be discussed later.

The mass scattering efficiencies of homogeneous spheres composed of water, ammonium sulfate, and soot are plotted as a function of particle size in Figure 2.1. A wavelength of $\lambda = 0.53$ μm is assumed. It can be seen that particles between 0.2 and 0.9 μm scatter light efficiently.

Table 2.1

Refractive Indices and Bulk Densities for Selected Aerosol Chemical Species

Chemical Species	Refractive Index at λ = 0.5 μm	Bulk Density, g/cm^3
Water	1.33 - 0i	1.00
Ammonium Sulfate	1.53 - 0i	1.76
Soot	1.95 - 0.66i	2.0
Silica	1.55 - 0i	2.66
Pentanedioic Acid	1.42 - 0i	1.42
Model Aerosol	1.54 - 0.015i	1.7

The single particle absorption efficiency, K_a, has nonzero values only for a nonzero imaginary part of the refractive index. The variation in E_a with particle size for pure carbon spheres at λ = 0.53 μm is shown in Figure 2.2. Similarly to the scattering efficiency, the soot absorption efficiency has a maximum at 0.2 μm. However, the absorption efficiency approaches a constant nonzero value for very small particles. Thus, very small particles may contribute substantially to light absorption but not scattering.

2.4 CHEMICAL SPECIES CONTRIBUTIONS TO THE EXTINCTION COEFFICIENT

This section will discuss how chemical species in a multicomponent aerosol contribute to the particle extinction coefficient. It

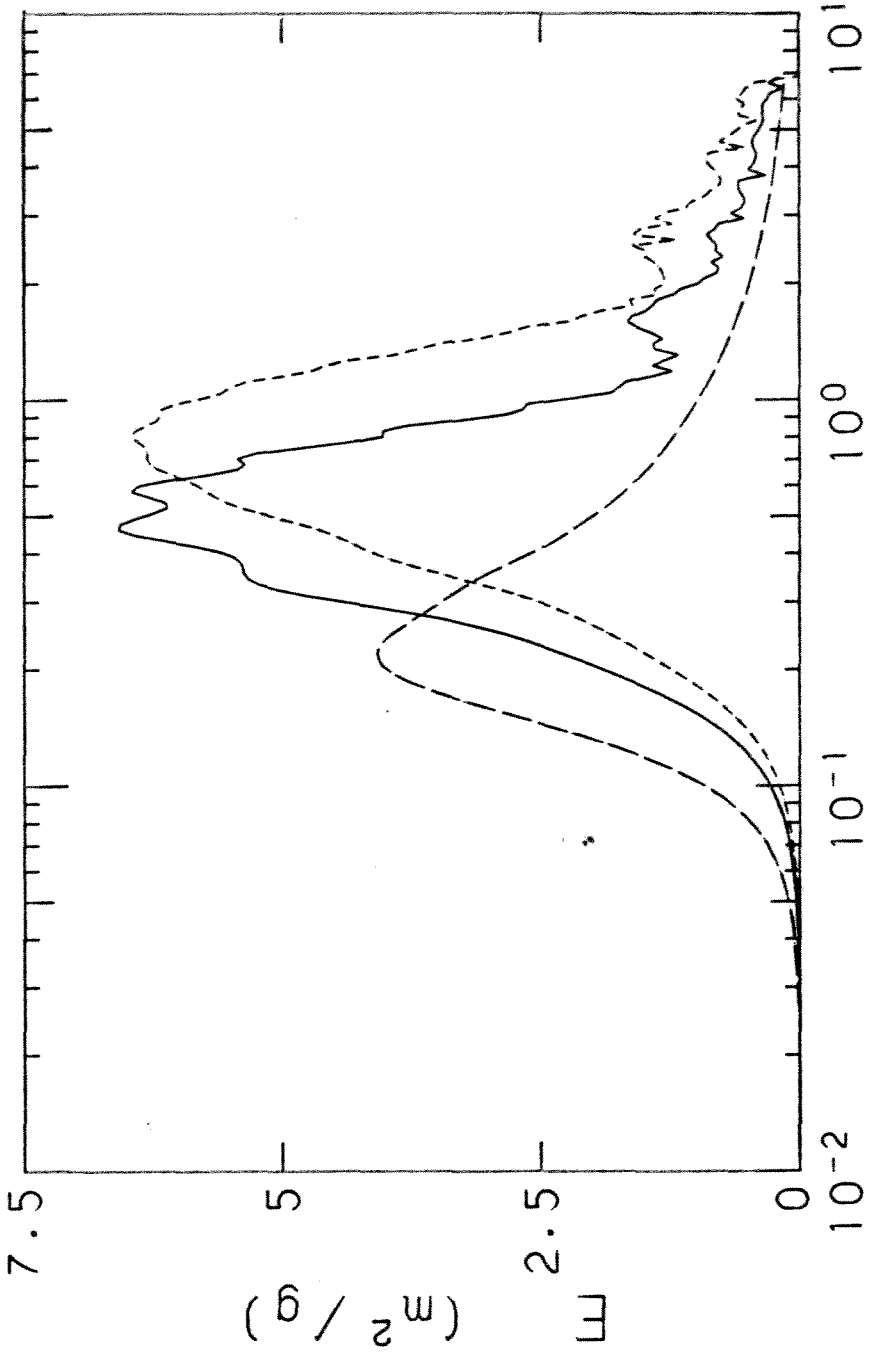

Figure 2.1. Mass scattering efficiencies for homogeneous spheres. Ammonium sulfate (ρ=1.7 g/cm^3, m=1.53) shown in solid curve; water (ρ=1.0 g/cm^3, m=1.33) in short dash curve; graphitic carbon (soot) (ρ=2.0 g/cm^3, m=1.96-0.66i) in long dash curve. Wavelength of radiation 0.53 μm.

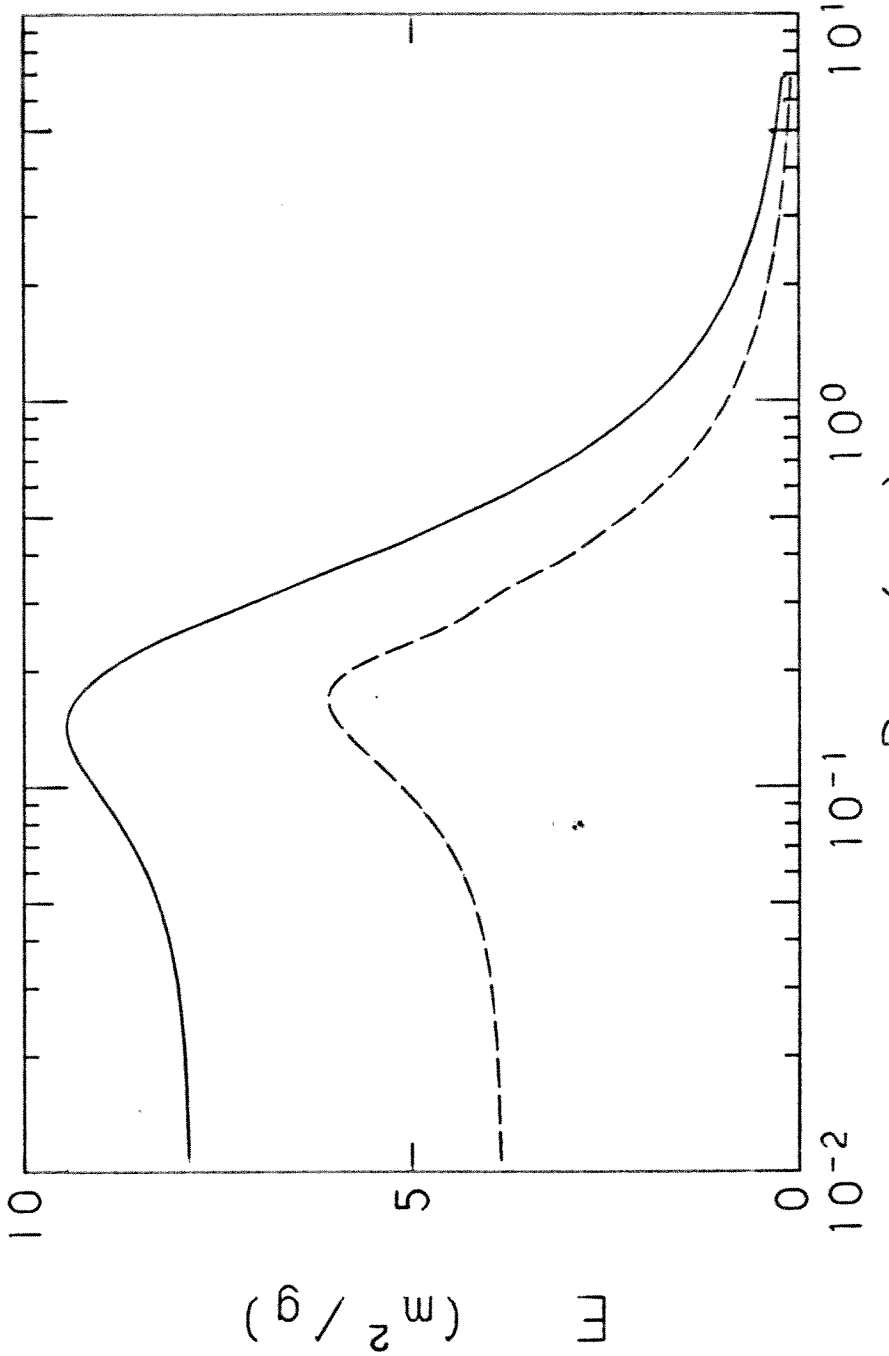

Figure 2.2. Mass absorption efficiencies for homogeneous spheres. Graphitic carbon (soot) (ρ=2.0 g/cm^3, m=1.96-0.66i) shown in dash curve. Solid curve is for ρ=1.0 g/cm^3 and m=1.56-0.47i, suggested values for loosely packed soot clusters which are still spherical (Roessler and Faxvog, 1979; Dalzell and Sarofim, 1969).

will be assumed that the particles are spherical. Theoretical mass extinction efficiencies can be computed to any desired accuracy for spheres. In addition, the transformation from particle diameter to volume is unique for spheres.

In the general case one must assume that chemical composition may vary over particle size and that individual particles are not chemically pure. It will be shown that in general the chemical composition, refractive index, and diameter of each particle must be known to rigorously calculate the contribution of a particular species. It will be shown that for certain simple aerosols chemical species contributions may be calculated exactly from their mass distributions.

2.4.1 External Mixture

The simplest multicomponent aerosol in which the species contributions to b_{ep} can be determined exactly from their mass distributions is the external mixture. An external mixture is an aerosol composed of N aerosol species which have been mixed without coagulation. Each individual particle is chemically pure and is characterized by a unique diameter, D, chemical species i, and refractive index m_i. The particle number distribution n(D) is then the sum of the number distribution of each species, $n_i(D)$:

$$n(D) = \sum_{i=1}^{N} n_i(D) \tag{2.10}$$

Each particle is characterized by a unique single particle extinction coefficient, $K_e(m_i,x)$. In this case the particle extinction coefficient is the sum of the contributions from each pure species, b_{epi}:

$$b_{ep} = \sum_{i=1}^{N} b_{epi} \tag{2.11}$$

where

$$b_{epi} = \int_0^\infty E_e(m_i,x,\lambda) f_i(x) dx \tag{2.12}$$

For an external mixture of homogeneous spheres the contribution of species i to the particle extinction coefficient is given exactly by Equation 2.12. Since the error in the mass extinction efficiency calculation can be made arbitrarily small, the accuracy in b_{epi} is determined by the error in the measurement of the species mass distribution.

2.4.2 General Theory for Multicomponent Aerosol

In the general case one must assume that chemical composition may vary over particle size and that individual particles are not chemically pure. It is assumed that the aerosol is composed of spherical particles so that the particle size may be characterized uniquely by either the particle diameter, D, or the particle volume $v = \pi/6\ D^3$. The multicomponent aerosol problem can be treated generally if it is assumed that the chemical composition is distributed continuously over the particle size interval v to v + dv. Following the convention of Friedlander (1970, 1971), let dN be the number of particles per unit volume of air containing molar quantities of each species i in the range between y_i and $y_i + dy_i$. Then the size-composition probability density

function, g, is defined by

$$dN = N_T g(v,y_2, \ldots ,y_N)dvdy_2 \ldots dy_N$$

N_T is the total particle number concentration. The particle volume v is a linear combination of the moles of each species:

$$v = \sum_{i=1}^{N} \bar{v}_i y_i \tag{2.13}$$

where the partial molar volume of species i is $\bar{v}_i = \left(\frac{\partial v}{\partial y_i}\right)_{y_{j,j\neq i}}$. By integration the following relationships are obtained:

$$\int_v \int_{y_N} \cdots \int_{y_2} g \, dy_2 \ldots dy_N dv = 1 \tag{2.14}$$

$$n(D)dD = n(v)dv = N_T \int_{y_N} \cdots \int_{y_2} g \, dy_2 \ldots dy_N dv \tag{2.15}$$

where n(v) is the particle size distribution function with respect to particle volume.

For the multicomponent aerosol the particle extinction coefficient is obtained from Equations 2.4 and 2.15:

$$b_{ep} = N_T \int_v \int_{y_N} \cdots \int_{y_2} \frac{\pi}{4} D^2 K_e(m,p) \, g \, dy_2 \ldots dy_N dv$$

g is obtained by measurements of the chemical composition of each particle in the aerosol, a formidable task. The problem is compounded,

however, by the fact that the refractive index of each particle is not uniquely determined by the chemical composition. Consider a concentric spherical particle of equal volumes of species A and species B. The theoretical single particle extinction efficiency K_e may differ slightly depending upon whether A has condensed on B or vice versa. In general, therefore, it is necessary to obtain measurements of not only chemical composition, but also the refractive index of each particle to adequately characterize the aerosol for extinction coefficient determination.

Extending on the convention of Friedlander (1970,1971), it is convenient to define the size-composition-refractive index probability density function, h, defined by

$$dN_m = N_T\, h\,(v,y_2, \ldots, y_N,m)dy_2 \ldots dy_N dm$$

The function, g, is obtained by integrating over all values of the refractive index for a given composition and size:

$$g(v,y_2, \ldots, y_N) = \int_m h(v,y_2, \ldots, y_N,m)dm \qquad (2.16)$$

The average single particle extinction efficiency, $K_e^a(v,\lambda)$, at a given particle size v can be defined by

$$K_e^a(v,\lambda) = \frac{N_T}{n(v)} \int_{y_N} \cdots \int_{y_2} \int_m K_e(m,p)h(v,y_2,\ldots,y_N,m)dmdy_2 \ldots dy_N \qquad (2.17)$$

Then the particle extinction coefficient is

$$b_{ep} = \int_0^\infty \frac{\pi}{4} D^2 K_e^a(v,\lambda) n(v) dv = \int_0^\infty \frac{\pi}{4} D^2 K_e^a(D,\lambda) n(D) dD \qquad (2.18)$$

which is functionally similar to the expressions for the simpler aerosols. Unlike the single species and external mixture aerosols, the single particle extinction efficiency, K_e^a, is now a nonlinear function of particle size and chemical composition. In general, K_e^a would not be an analytic function, but would be determined numerically from single particle measurements of chemical composition and refractive index.

A simpler expression for b_{ep} results if all particles of the same chemical composition have the same refractive index. Then h is separable:

$$h(v,y_2,\ldots,y_n,m) = g(v,y_2,\ldots,y_n)\, h^*(m,v)$$

$h^*(m,v)$ is the probability that a particle of size v has a refractive index of m. In this case single particle measurements of chemical composition are not necessary to calculate b_{ep}:

$$b_{ep} = \int_0^\infty \frac{\pi}{4} D^2 \left\{ \int_m K_e(m,p)\, h^*(m,D)\, dm \right\} n(D) dD$$

If it is also assumed that all particles of the same size have the same composition, then

$$h^*(m,D) = \delta(m-m(D))$$

where $\delta(x)$ is the Dirac delta function. In this case single particle

measurements of the refractive index are not necessary to calculate b_{ep}:

$$b_{ep} = \int_0^\infty \frac{\pi}{4} D^2 K_e(m(D),p)n(D)dD$$

The incremental mass concentration of species i in the interval v to v + dv is

$$\frac{dM_i}{dv} dv = N_T W_i \int_{y_N} \cdots \int_{y_2} g y_i dy_2 \cdots dy_N \qquad (2.19)$$

where W_i is the molecular weight of species i. One can then express b_{ep} in terms of the species mass distributions:

$$b_{ep} = \sum_{i=1}^{N} \int_0^\infty \frac{3}{2D} K_e^a \frac{\nu_i}{W_i} f_i(x)dx \qquad (2.20)$$

where K_e^a is given by Equation 2.17. Equation 2.20 is exact for spherical particles. For hygroscopic particles, water may be considered as one of the chemical species.

Strict application of Equation 2.20 to some aerosols may be difficult because $\bar{\nu}_i$ may vary with chemical composition. This is almost certainly the case of aqueous solutions formed in aerosols under humid conditions. When condensation and coagulation occur, aerosol mass is conserved but volume may not be conserved. However, it is the particle size, not its mass, that determines its optical effects.

If the aerosol is not an aqueous or solid solution, the partial molar volume $\bar{\nu}_i$ may be considered a constant:

$$\bar{\nu}_i = \frac{W_i}{\rho_i}$$

where ρ_i is the bulk density of pure species i. This is equivalent to requiring that particle volume be conserved. In this case,

$$b_{ep} = \sum_{i=1}^{N} \int_0^{\infty} \frac{3}{2D\rho_i} K_e^a f_i(x)dx \qquad (2.21)$$

where $f_i(x)$ is the mass distribution of species i.

One may then define the contribution of a particular species i to the particle extinction coefficient as the reduction in b_{ep} due to the removal of species i:

$$b_{epi} = \int_0^{\infty} \frac{3}{2D\rho_i} K_e^a f_i(x)dx + \sum_{\substack{j=1 \\ j\neq i}}^{N} \frac{3}{2D\rho_j} (K_e^a - K_{ei}^{a'}) f_j(x)dx \qquad (2.22)$$

where $K_{ei}^{a'}$ is the average single particle extinction efficiency evaluated without species i. It is seen that for a complex aerosol species i affects b_{ep} in two ways:

1) Most directly, through its mass distribution, $f_i(x)$

2) Secondly, by changing the average single particle extinction efficiency, K_e^a.

Equation 2.22 is exact for spherical particles whose partial molar volumes are constant. If the refractive index of species i is not appreciably different from that of the other species, then $K_e^a \simeq K_{ei}^{a'}$ and the contribution of species i is, to a good approximation, due directly to its mass distribution:

$$b_{epi} \simeq \int_0^\infty \frac{3}{2D\rho_i} K_e^a f_i(x)dx \tag{2.23}$$

2.4.3 Application of General Theory to Limiting Cases

2.4.3.1 Single Compound Aerosol -

For a simple aerosol composed of one species i of refractive index m_i, the aerosol volume of a particle of volume v is made up exclusively of species i

$$v = \bar{v}_i y_i \tag{2.24}$$

$$y_j = 0 \qquad \text{for } j = 1, \ldots, N, \quad j \neq i$$

The size composition probability density function is then a delta function

$$g = \frac{n(v)}{N_T} \delta\left(y_i - \frac{v}{\bar{v}_i}\right) \tag{2.25}$$

This can be checked by determining the number distribution, n(v), and the mass concentration, M_i:

$$n(v) = N_T \int_{y_N} \cdots \int_{y_2} g \, dy_2 \cdots dy_N$$

$$= n(v) \int_0^\infty \delta\left(y_i - \frac{v}{\bar{\nu}_i}\right) dy_i$$

$$= n(v).$$

Also,

$$M_i = W_i N_T \int_v \int_{y_N} \cdots \int_{y_2} g \, y_i dy_2 \cdots dy_N dv$$

$$= W_i N_T \int_v \int_{y_i} \frac{n(v)}{N_T} \delta\left(y_i - \frac{v}{\bar{\nu}_i}\right) y_i dy_i dv$$

$$= W_i \int_0^\infty n(v) \int_0^\infty y_i \, \delta\left(y_i - \frac{v}{\bar{\nu}_i}\right) dy_i dv$$

$$= W_i \int_0^\infty n(v) \frac{v}{\bar{\nu}_i} dv$$

$$= \frac{W_i}{\bar{\nu}_i} \int_0^\infty v n(v) dv$$

$$= \rho_i V_T$$

Here, V_T is the total aerosol volume concentration. Since the aerosol is composed of only one species, the mass-volume relationship is correct.

The refractive index of every particle is m_i, which leads to the

following simple expression for the size-composition refractive index probability density function, h:

$$h = g\,\delta(m - m_i)$$

$$= \frac{n(v)}{N_T}\,\delta\left(y_i - \frac{v}{\bar{\nu}_i}\right)\delta(m - m_i)$$

Evaluating the average single particle extinction efficiency, K_e^a, by Equation 2.17,

$$K_e^a(v,) = \frac{N_T}{n(v)} \int_{y_N}\cdots\int_{y_2}\int_m K_e(m,p)\frac{n(v)}{N_T}\,\delta\left(y_i - \frac{v}{\bar{\nu}_i}\right)\delta(m-m_i)\,dm\,dy_2\cdots dy_N$$

$$= \int_m K_e(m,p)\,\delta(m-m_i)\int_{y_i}\delta\left(y_i - \frac{v}{\bar{\nu}_i}\right)dy_i\,dm$$

$$= K_e(m_i,p)$$

Then, by Equation 2.22, the contribution of species i is

$$b_{epi} = \int_0^\infty \frac{3}{2D\rho_i}\,K^e(m_i,p)f_i(x)\,dx$$

$$= \int_0^\infty E_e(m_i,x,\lambda)f_i(x)\,dx$$

where E_e is the mass extinction efficiency of species i, given by

Equation 2.7. As expected, this reduces to the required relationship for a single species.

2.4.3.2 Internal Mixture

An internal mixture is defined as an aerosol where the chemical species are mixed within each particle in a fixed proportion which does not vary with particle size. The number of moles of species i in any particle of volume v is uniquely given by

$$y_i = \frac{C_i}{\bar{v}_i} v \tag{2.26}$$

Note that $\sum_{i=1}^{N} C_i = 1$. Since every particle has a fixed uniform composition, the refractive index of every particle is identical, say m^*, and not a function of composition or size.

For the internal mixture the size-composition-refractive index probability density function, h, becomes

$$h = \frac{n(v)}{N_T} \delta\left(y_2 - \frac{C_2}{\bar{v}_2} v\right) \ldots \delta\left(y_N - \frac{C_N}{\bar{v}_N} v\right) \delta(m - m^*) \tag{2.27}$$

In this case the mass concentration of species i is

$$M_i = W_i N_T \int_v \int_{y_N} \cdots \int_{y_2} y_i \frac{n(v)}{N_T} \delta\left(y_2 - \frac{C_2}{\bar{\nu}_2} v\right) \cdots \delta\left(y_N - \frac{C_N}{\bar{\nu}_N} v\right) dy_2 \cdots dy_N dv$$

$$= W_i \int_v n(v) \{1\} \cdots \left\{\frac{C_i}{\bar{\nu}_i} v\right\} \cdots \{1\} dv$$

$$= C_i \rho_i V_T$$

The average single particle extinction efficiency, K_e^a, becomes

$$K_e^a = K_e(m^*, p)$$

The contribution of species i is then

$$b_{epi} = \int_0^\infty \frac{3}{2D\rho_i} K_e(m^*, p) f_i(x) dx$$

$$+ \sum_{\substack{j=1 \\ j \neq i}}^{N} \int_0^\infty \frac{3}{2D\rho_i} [K_e(m^*, p) - K_e(m_i^{*'}, p)] f_j(x) dx \qquad (2.28)$$

If the resultant refractive index, $m_i^{*'}$, after the removal of species i is not appreciably different than m^*, then only the first term in Equation 2.28 is important:

$$b_{epi} \simeq \int_0^\infty \frac{3}{2D\rho_i} K(m^*, p) f_i(x) dx \qquad (2.29)$$

2.4.3.3 Specific Mixture with Volume Average Refractive Index

For the purposes of this thesis let a specific mixture be an aerosol having the property that all particles of size v have an identical chemical mix. The chemical mix is allowed to vary as a function of particle size, however, unlike the internal mixture. For a particle of volume v, the volume of species i is given by

$$\frac{v_i}{v} = C_i(v)$$

For any size v, $\sum_{i=1}^{N} C_i(v) = 1$. For the specific mixture, the number of moles of species i in any particle of volume v is uniquely given by

$$y_i = \frac{C_i(v)}{\bar{\nu}_i} v \tag{2.30}$$

The size-composition probability density function, g, is then

$$g = \frac{n(v)}{N_T} \delta\left(y_2 - \frac{C_2(v)}{\bar{\nu}_2} v\right) \ldots \delta\left(y_N - \frac{C_N(v)}{\bar{\nu}_N} v\right) \tag{2.31}$$

The mass concentration of species i becomes

$$M_i = \rho_i \int_0^\infty C_i(v) n(v) dv$$

It is not assumed that the species are internally mixed in a specific aerosol. Even though the species composition is identical for all particles of size v, species A could be condensed on species B, for

example, or vice versa for different particles of the same size. This results in generally different refractive indices for different particles of the same size, v. A simplification results if one assumes a volume average refractive index for each particle (Kerker, 1969):

$$m_a(v) = \frac{\sum_{i=1}^{N} v_i m_i}{v} = \frac{\sum_{i=1}^{N} y_i \bar{v}_i m_i}{v} \tag{2.32}$$

Since the chemical composition of all particles of size v is identical, the refractive index is identical for all particles of size v. The refractive index becomes a function of particle size alone and the following relationship results:

$$h(v,y_2,\ldots,y_N m) = g(v,y_2,\ldots,y_N)\delta(m-m_a(v)) \tag{2.33}$$

By substitution into Equation 2.17, the following simple expression is obtained for the average single particle extinction efficiency, K_e^a:

$$K_e^a = K_e(m_a(v),p)$$

The particle extinction coefficient is then

$$b_{ep} = \int_{-\infty}^{\infty} \frac{3}{2D} K_e(m_a(v),p) \frac{dV}{d\log D} d\log D \tag{2.34}$$

Assuming a constant $\bar{v}_i = W_i/\rho_i$, the contribution of species i to b_{ep} is

$$b_{epi} = \int_0^\infty \frac{3}{2D\rho_i} K_e(m_a(v),p) f_i(x)dx$$

$$- \sum_{\substack{j=1 \\ j\neq i}}^{N} \int_0^\infty \frac{3}{2D\rho_j} [K_e(m_a(v),p) - K_e(m_a'(v),p)] f_j(x)dx$$

As before, if the volume average refractive index does not change appreciably with the removal of species i, then the contribution of species in a specific mixture to the extinction coefficient is

$$b_{epi} \simeq \int_0^\infty E_e(m_a(v),p) f_i(x)dx \tag{2.35}$$

The volume average refractive index may be calculated from measured species mass distributions by use of Equation 2.19. Assuming constant partial molar volumes, the result is:

$$m_a(x) = \frac{\sum_{i=1}^{N} \frac{m_i}{\rho_i} f_i(x)}{\sum_{i=1}^{N} \frac{1}{\rho_i} f_i(x)} \tag{2.36}$$

The validity of the volume average refractive index was tested by Kerker (1969, p. 202) for coated spheres of varying diameters, coating thicknesses, and real refractive indices. The single particle

scattering efficiency, K_s, was calculated using the volume average refractive index and compared to the exact value. The K_s using the volume average refractive index was found to be within 23% of the exact value for $0.1 \leq x \leq 2.5$ ($0.017 \leq D \leq 0.42$ μm at $\lambda = 0.53$ μm), and $1.482 \leq m \leq 2.105$. The agreement is not necessarily as good with complex refractive indices.

2.4.4 Aerosol Species Mass Concentration-Extinction Coefficient Relationships

2.4.4.1 External Mixture -

Let $\bar{f}_i$ be the normalized mass distribution of species i:

$$\bar{f}_i(x,M_i) = f_i(x)/M_i$$

Then the contribution of species i to the extinction coefficient becomes

$$b_{epi} = \alpha_i(M_i)M_i$$

where

$$\alpha_i(M_i) = \int_0^\infty E_a(m_i,x,\lambda)\bar{f}_i(x,M_i)dx$$

α_i is the average mass extinction efficiency of species i. If the normalized mass distribution $\bar{f}_i$ does not vary with its total mass concentration, M_i, then α_i can be considered a constant and the following linear relationship results:

$$b_{ep} = \sum_{i=1}^{N} \alpha_i M_i$$

For an external mixture with constant α_i, the particle extinction coefficient is simply a linear combination of the species mass concentrations.

2.4.4.2 Internal Mixture -

In an internal mixture the chemical species are mixed within each particle in a fixed proportion which does not vary with particle size:

$$\frac{v_i}{v} = c_i$$

Then it follows that the volume distribution of species i follows the total volume distribution

$$\frac{dV_i}{d\log D} = c_i \frac{dV}{d\log D} \tag{2.37}$$

Integrating over all particle sizes, it is seen that c_i also represents the fractional total volume of species i:

$$V_i = c_i V_T$$

From Equation 2.5 it follows that

$$b_{epi} = c_i \int_{-\infty}^{\infty} G_e(m^*, D, \lambda) \frac{dV}{d\log D} d\log D$$

with the result that species i contributes to the extinction coefficient in the same proportion that it does to the total aerosol volume

concentration

$$b_{epi} = \frac{V_i}{V_T} b_{ep}$$

$$= \left(\frac{b_{ep}}{V_T}\right) \frac{1}{\rho_i} M_T$$

The ratio b_{ep}/V_T is determined by a convolution of the single particle scattering efficiency with the normalized total volume distribution, $d\bar{V}/d\log D$:

$$\frac{b_{ep}}{V_T} = \int_{-\infty}^{\infty} G_e(m^*, D, \lambda) \frac{d\bar{V}}{d\log D} d\log D$$

If the normalized volume distribution remains constant and is not a function of the total aerosol volume V_T, then b_{ep}/V_T is a constant and the following relationship is obtained for an internal mixture:

$$b_{epi} = \alpha_i M_i$$

where

$$\alpha_i = \frac{1}{\rho_i} \frac{b_{ep}}{V_T} \qquad (2.38)$$

Therefore, if the normalized aerosol volume distribution does not vary at a location and the aerosol is an internal mixture, the particle extinction coefficient is simply a linear combination of the mass

concentrations of each species

$$b_{ep} = \sum_{i=1}^{N} \alpha_i M_i$$

where α_i is given by Equation 2.38.

2.3.4.3 Specific Mixture -

For a specific mixture the following relationship exists between the aerosol volume distribution of species i and the total distribution:

$$\frac{dV_i}{d\log D} = c_i(D) \frac{dV}{d\log D}$$

and

$$V_i = \int_{-\infty}^{\infty} c_i(D) \frac{dV}{d\log D} d\log D$$

No simple relationship between the aerosol volume concentration of species i and the total volume concentration exists such as that found for an internal aerosol, Equation 2.37. Equation 2.35, which approximates the contribution of species i to the extinction coefficient in a specific mixture with constant α_i can be rewritten

$$b_{epi} = \alpha_i(M_i) M_i$$

where

$$\alpha_i(M_i) = \int_0^{\infty} E_a(m_a(x), x, \lambda) \overline{f}_i(x) dx \qquad (2.39)$$

α_i will be a constant if neither the volume average refractive index $m_a(x)$ nor the normalized species mass distribution $\bar{f}_i(x)$ varies with total mass concentration. By inspection of Equation 2.36, $m_a(x)$ will not vary with species mass concentrations if either the total normalized volume or mass distribution remains unchanged or if all of the refractive indices are equal. If these conditions are met, α_i will be a constant and the particle extinction coefficient can be expressed as a linear combination of species mass concentrations

$$b_{ep} = \sum_{i=1}^{N} \alpha_i M_i$$

2.5 AEROSOL MASS AND EXTINCTION COEFFICIENT BALANCES

This chapter has discussed the use of measured aerosol mass and volume distributions to determine the contributions of various chemical species to the particle extinction coefficient, b_{ep}. There are a number of parameters which can currently be measured directly to provide a check on the results. This is necessary experimentally because one does not directly measure the contribution of species i to b_{ep}; one calculates it using measured mass distributions, $f_i(x)$, and theoretical single particle extinction efficiencies, $K_e(m,p)$.

Currently the particle scattering coefficient, b_{sp}, can be continuously measured with an integrating nephelometer. The MRI Model 1561 was used in the research for this thesis. It has a very sharp wavelength response function centered at 0.53 um. All calculations of

K_e in this thesis assume $\lambda = 0.53$ μm. The aerosol volume distribution, dV/dlogD, can be measured with sample times of 2-3 minutes using principles of particle electrical mobility and light scattering. Filter samples can provide time average total, M_T, and species, M_i, mass concentrations as well as the particle absorption coefficient, b_{ap}. Impactors, such as the low pressure impactor, combined with chemical analysis can provide time average species mass distributions, $f_i(x)$. The analytical techniques are discussed in Chapter 3.

A listing of the balances used in this thesis is provided in Table 2.2. The measurement technique used in this thesis is given in parentheses. These will be discussed in detail in Chapter 3. LPI refers to the low pressure impactor, EAA refers to the electrical aerosol analyzer, and OPC refers to the optical particle counter.

The successful experimental meeting of these balances, particularly the mass and scattering coefficient balances, will provide strong evidence that the measured mass distribution of a species can be successfully used to calculate its contribution to the extinction coefficient.

2.6 SUMMARY

Theoretical expressions have been derived from which one may determine the contributions of various chemical species in an aerosol to the extinction coefficient. It is assumed that the aerosol is composed of spheres. In general, it is necessary to measure the chemical composition and refractive index of each particle to rigorously

Table 2.2

Chemical Species Contributions to the

Extinction Coefficient: Balances on Measured Parameters

1. MASS BALANCE

   i) $\int_0^\infty f_i(x)dx$ (LPI) = M_i (filter)

   ii) $\sum_{i=1}^{N} M_i$ (filter) = M_T (filter)

2. PARTICLE VOLUME BALANCE

   i) $\sum_{i=1}^{N} f_i(x)/\rho_i$ (LPI) = dV/dx (EAA,OPC)

   ii) M_T(filter) = $\bar{\rho}\ V_T = \bar{\rho} \int_0^\infty \frac{dV}{dx} dx$ (EAA,OPC)

3. SCATTERING COEFFICIENT BALANCE

   i) $\int_0^\infty G_s \frac{dV}{dx} dx$ (EAA,OPC) = b_{sp} (nephelometer)

   ii) $\sum_{i=1}^{N} b_{spi}$ (LPI) = b_{sp} (nephelometer)

4. ABSORPTION COEFFICIENT BALANCE

   i) $\int_0^\infty G_a \frac{dV}{dx} dx$ (EAA,OPC) = b_{sp} (filter)

   ii) $\sum_{i=1}^{N} b_{api}$ (LPI) = b_{sp} (filter)

Parameters defined in text

determine the contribution of a particular species. Since this is a formidable task, expressions were derived for different simple aerosols where the contribution of a species may be calculated exactly from its measured mass distribution function. Expressions were derived for an external and internal mixture and for a so-called specific mixture with an assumed volume average refractive index. The specific mixture is considered to be the most general case where one may use mass distributions rigorously, since particles are not assumed to be chemically pure and no assumptions are made regarding the form of the mass distributions of the species.

Requirements were established for each of the three simple aerosols for which the particle extinction coefficient, b_{ep}, can be expressed as a linear combination of the mass concentrations of the species, M_i:

$$b_{ep} = \sum_{i=1}^{N} \alpha_i M_i \qquad (2.40)$$

In general it is necessary for the normalized mass distribution of every species to remain unchanged; the shape of the distribution must be preserved. The partial molar volume, $\bar{v}_i$, of each species i must remain constant with the addition or removal of other species. This requirement is not obeyed by hygroscopic particles which form aqueous solutions, and thus Equation 2.40 would not be valid for such particles. In addition, the preservation of the normalized total aerosol volume distribution may be required. If the aerosol is not an external mixture, the refractive indices of each of the major species should not

differ significantly from each other. If these requirements are met, multiple regression analysis may be successfully applied to measured b_{ep} and M_i data to infer the average mass extinction efficiency, α_i, for each species.

One does not measure directly the contribution of each species to b_{ep}; it is calculated from its measured mass distribution. A table of mass and extinction balances is presented which provides the criteria for successful application of this theory and technique.

CHAPTER 3

APPLICATION OF THEORY TO A REMOTE ARID SITE IN ARIZONA

3.1 INTRODUCTION

Chapter 2 showed that the contributions of aerosol chemical species to the extinction coefficient can be estimated from knowledge of their mass distributions, densities, and refractive indices. The theory assumed that the particles can be represented as spheres. For an external mixture the contribution of species i to the extinction coefficient, b_{epi}, is given by Equation 2.12:

$$b_{epi} = \int_0^\infty E_e(m_i,x,\lambda)f_i(x)dx$$

where $f_i(x) = dM_i/dx$ and $x = \log(D/0.01\ \mu m)$. $f_i(x)$ is the mass distribution of species i as a function of the dimensionless particle diameter x. E_e is the mass extinction efficiency of species i, given by Equation 2.10. λ is the wavelength of light. For a specific mixture, the contribution of species i can be approximated by Equation 2.35:

$$b_{epi} = \int_0^\infty E_e(m_a(x),x,\lambda)f_i(x)dx$$

$m_a(x)$ is the volume average refractive index as a function of x, given by Equation 2.36. Equation 2.35 simplifies to Equation 2.12 if all the

species have equal refractive indices. This is approximately true for ambient aerosol if water is absent and soot makes up a small fraction of the fine mass loading. Strict application of Equation 2.35 requires information on all species, while Equation 2.12 does not.

In Eqns. 2.35 and 2.12 the species mass extinction efficiency, E_e, can be theoretically determined from Mie's classical solution to light extinction by a sphere in an infinite medium. Computer routines are available to calculate single particle extinction efficiencies, and, hence, E_e (Wickramasinghe, 1973). The mass distribution of each species is experimentally measured. One would then infer an optical property, b_{epi}, from measured mass distributions and theoretically predicted mass extinction efficiencies. It should be noted that one cannot currently directly measure the effect of a particular aerosol chemical species on the extinction coefficient. The experimental confirmation of the theory must come from the balances on mass and extinction coefficients as discussed in Chapter 2. Table 2.2 summarized the balances that must be met. The experimental adherence to these balances, while not providing a direct measurement of b_{epi}, does insure that all important species have been accounted for and that the sum of the contributions is correct. If the balances are met for a number of experiments with varying concentrations of aerosol species, this would provide strong evidence that the calculations for the individual species contributions would be correct.

This chapter discusses the application of the species extinction balance technique to an ambient aerosol in remote northeastern Arizona.

Measurements of aerosol and optical properties were made for a three week period in June and July of 1979. A total of 12 sets of samples were taken during the period. Fine aerosol species mass and extinction coefficient budgets were generated for each sample using measured chemical species mass distributions. The budgets were then compared to directly measured values of aerosol mass concentration and extinction coefficient to test the theory and technique.

3.2 EXPERIMENTAL TECHNIQUE

3.2.1 Location

Aerosol sampling was conducted during June and July of 1979 at Zilnez Mesa, Arizona. Shown in Figure 3.1, the Zilnez Mesa sampling site is located about 70 km ESE from the Navajo Generating Station near Page, Arizona. The measurements were made as part of Project VISTTA (Visibility Impairment due to Sulfur Transport and Transformation in the Atmosphere, sponsored by the Environmental Protection Agency (Macias et al., 1979). The objective of this phase of the VISTTA program is to quantify the contribution of coal-fired power plants to visibility impairment, especially in Western pristine areas.

The Navajo Generating Station is a modern coal-fired power plant similar to that which might be constructed in the future in the United States. It consists of three 775 MW (net) units, the first of which began operating in 1974. Particulate emissions are controlled with electrostatic precipitators with a design efficiency of 99.5 percent. Sulfur dioxide emissions are controlled by the use of low sulfur coal.

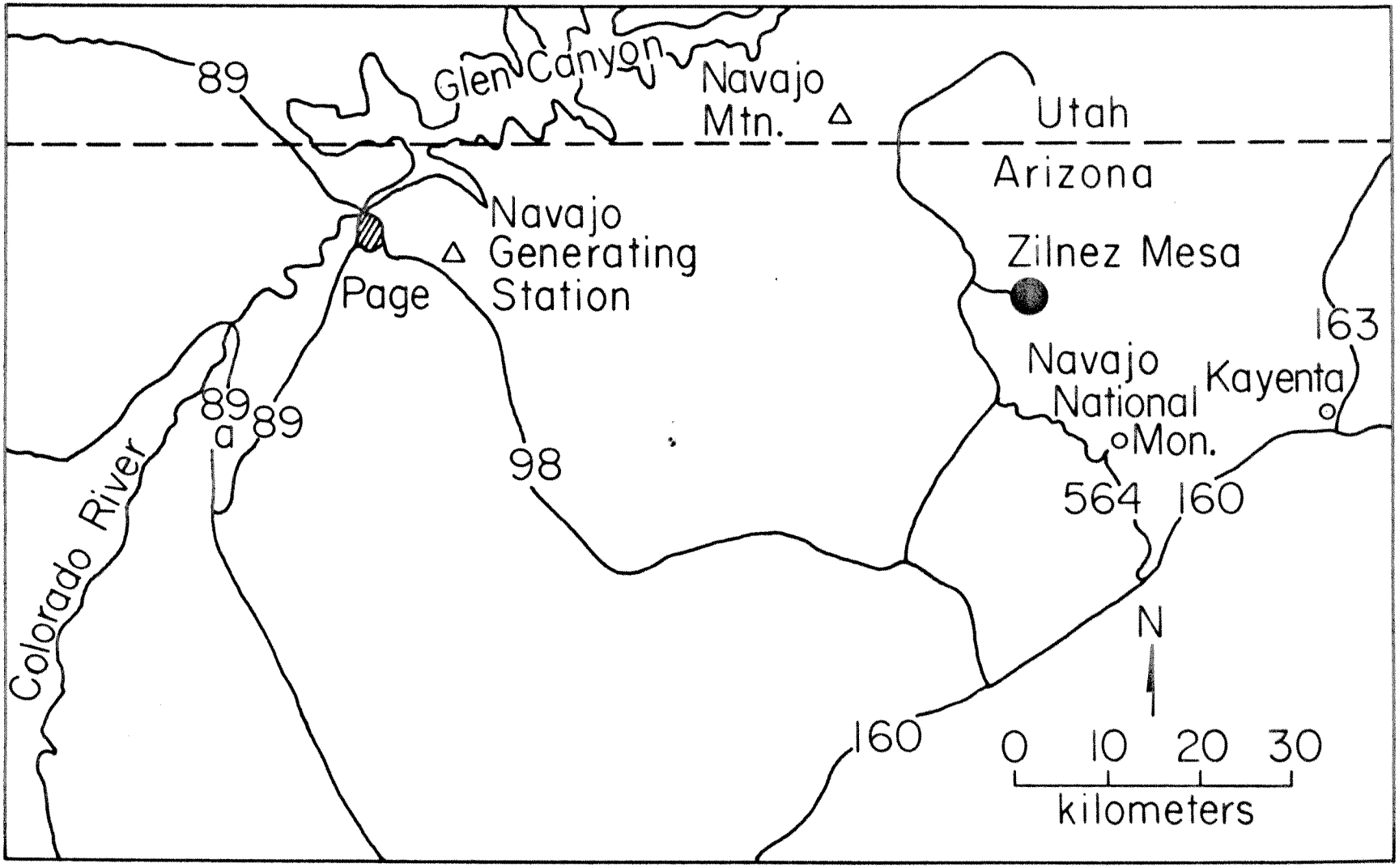

Figure 3.1. Location of Zilnez Mesa sampling site in northeastern Arizona. Site is located approximately 400 km northeast of Phoenix at an elevation of 2322m. Highway numbers designated on map.

The plant does not have scrubbers for removal of sulfur dioxide. The plant is isolated from other sulfur dioxide sources. It is in the vicinity of several Class 1 areas established by the 1977 Clean Air Act amendments for protection from visibility impairment (Blumenthal et al., 1980).

The Zilnez Mesa site was selected because of its remoteness from local sources of pollution, unusually good telephotometer views, view of the Navajo Generating Station, the good probability that the plume would be carried to the site, good access for instrumented vans, and the availability of electrical power. The site is at an elevation of 2322 meters (7620 ft.) above mean sea level. During sampling the atmospheric pressure averaged 589 mm Hg, about 0.78 atm.

Participants from the University of Minnesota Particle Technology Laboratory operated two mobile laboratories at Zilnez Mesa. These air-conditioned vans served as a base station and support facility for researchers from several other institutions. Measurements of optical, gaseous, aerosol, and meteorological parameters were routinely made by the University of Minnesota. Data were collected continuously from June 26 to July 13, 1979, with exceptions due to instrument failure, loss of power, and electrical storms. Aerosol size distributions were measured every 25 minutes. During the two-minute interval required to measure an aerosol size distribution, data from instruments with a continuous analog voltage output were recorded at the rate of once each 0.6 second. For the remaining 23 minutes of each interval, the sample rate was reduced to once each 30 seconds. During interesting episodes, such

as plume encounters, size distributions were measured more frequently (Blumenthal et al., 1980). For this thesis the University of Minnesota provided aerosol size distribution and particle scattering coefficient data which were averaged over the interval in which aerosol filter and impactor sampling were done, usually every 24 hours.

3.2.2 Aerosol Sample Collection

Aerosol for chemical analysis was sampled in one of the University of Minnesota's vans using the arrangement shown in Figure 3.2. The air inlet was 1.3 m above the roof of the van, a total of about 4 m above the ground. A screen and inverted cup assembly kept out rain and insects. The total length of 1.7 cm inner diameter (ID) aluminum tube was 3 m and the 1.3 cm ID tygon tube was 0.5 m. The Reynolds number for flow through the tubing was 2900. Loss of 0.1 micrometer (μm) diameter particles to the walls due to turbulent diffusion was calculated to be less than 1%, using the method of Friedlander (1977).

Cyclone separators were used to separate the coarse ($D > 2$ μm) aerosol from the airstream so that only the fine ($D < 2$ μm) aerosol would be collected by the filters and low pressure impactors. There are three reasons why this was done:

1. The mass concentration of dry, coarse particles in near-pristine arid regions is usually much greater than that of submicron aerosol. Bounceoff of the coarse particles to lower stages of the low pressure impactor during long sample times would lead to erroneous results.

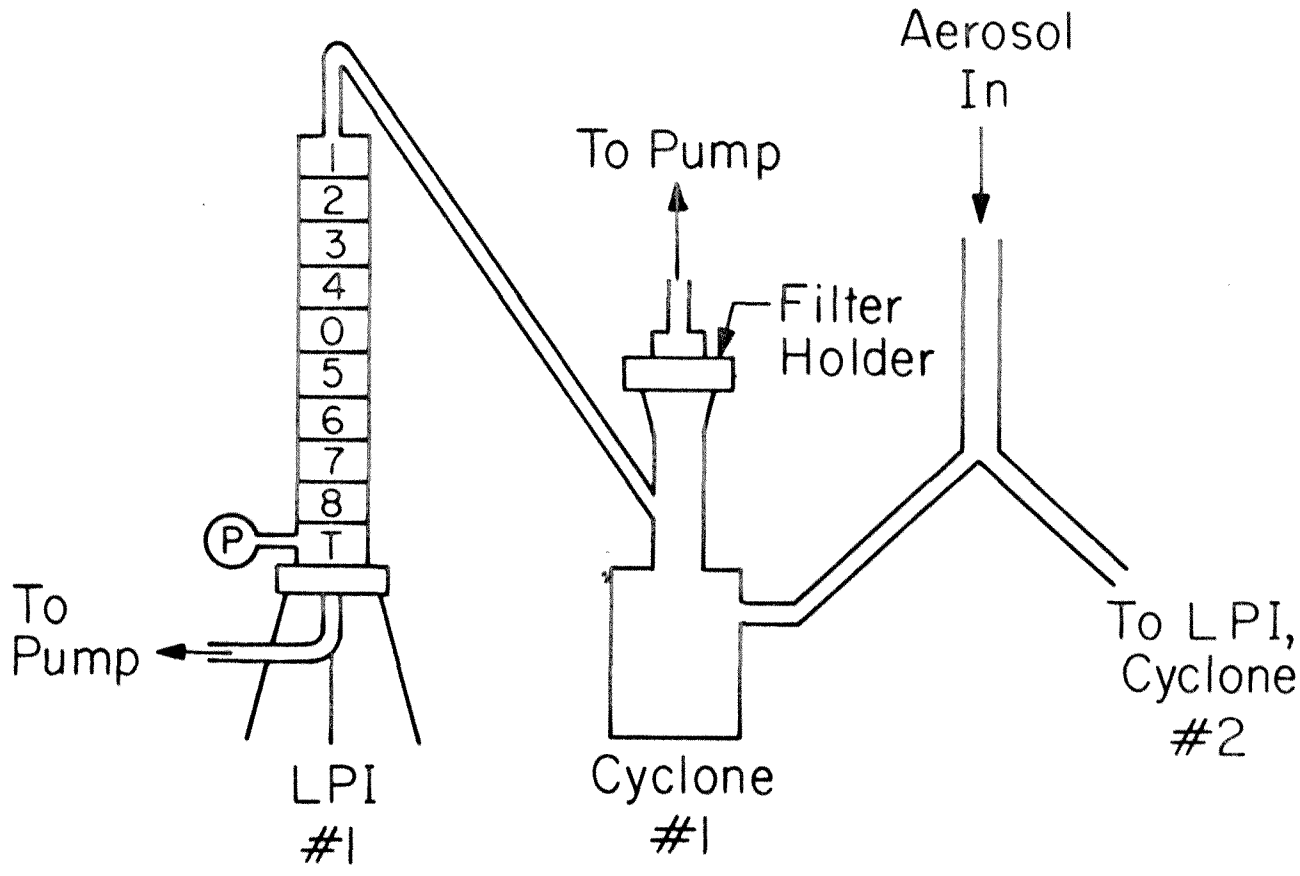

Figure 3.2. Sampling arrangement for fine aerosol chemical analysis, Zilnez Mesa, Arizona. Aerosol entered from 1.3 m above roof of van through 1.7 cm ID aluminum tubing to cyclone separators. Cyclones removed coarse (D > 2 μm) aerosol. Fine aerosol airstream flowed from cyclones to LPI's through 1.3 cm ID tygon tubing. Total lengths of aluminum and tygon tubing were 3.0 and 0.5 m, respectively. LPI stages designated by numbers. Critical orifice and pressure tap designated by "0" and "T", respectively.

2. Figure 2.1 shows that coarse particles are not theoretically efficient on a mass concentration basis in causing light extinction. This has been shown experimentally for locations in the arid Southwest using statistical regression techniques by Trijonis and Yuan (1978a).

3. The total particle scattering coefficient, b_{sp}, was measured with an integrating nephelometer. The sum of the calculated species contributions to the scattering coefficient was then compared to b_{sp}. The nephelometer, by virtue of the geometry of its viewing angle, is not efficient in "detecting" particles of greater than about 2 μm diameter (Sverdrup, 1977). Preseparation of aerosol with the cyclone provides a consistent basis of comparing calculated and measured particle scattering coefficient.

The cyclones in this study were constructed at Keck Laboratory using design specifications of John and Reischl (1978) of the California Air and Industrial Hygiene Laboratory (AIHL). They calibrated the cyclone using solid monodisperse methylene blue particles and liquid monodisperse dioctylpthalate (DOP) particles generated by a Bergland-Liu vibrating orifice aerosol generator. The cyclones were operated in this study at 20-25 liters per minute (lpm), resulting in 50% collection efficiencies from 2.2 to 2.7 μm aerodynamic diameter. A spherical particle of 2 g/cm^3 density and diameter of 1.8 μm would be collected with a 50% efficiency by the cyclone at 21 lpm.

The fine particle airstream from each cyclone was sampled by a total filter and a low pressure impactor (LPI) operating in parallel.

The calibrated LPI segregates aerosol into eight stages having 50% efficiency aerodynamic diameters of 4.0, 2.0, 1.0, 0.50, 0.26, 0.12, 0.075, 0.05 μm, respectively, when operated at 744 mm Hg ambient pressure (Hering et al., 1979; Hering et al., 1978). The LPI's were constructed at Keck Laboratory, Caltech. The volumetric flow rate of 1 LPI was controlled by a critical orifice.

The fine aerosol from cyclone #1 was collected by a 12.7 mm diameter Pallflex Tissuequartz No. 25000A0 quartz fiber filter which had been baked at 900 °C for one hour to drive off volatile contaminants. The Tissuequartz filters were chosen because of their suitability for carbon analysis (Macias et al., 1978). The fine aerosol from cyclone #2 was collected by a 0.4 μm pore size preweighed 47 mm diameter Nuclepore polycarbonate filter. The stainless steel backing plate was perforated, such that a 35 mm diameter aerosol deposit was created on the Nuclepore filter. Nuclepore filters were chosen because of stable mass, low artifact NO_3^- and $SO_4^=$ (Schumacher and Spicer, 1976), and suitability for light absorption measurements and elemental analysis.

In parallel with the Tissuequartz filter an LPI sampled aerosol for sulfur analysis. In parallel with the Nuclepore filter an LPI sampled aerosol for elemental analysis.

The airstream was drawn through the Nuclepore and Pallflex filters by Gast 60 lpm-displacement carbon vane pumps. The LPI's used Leybold-Haraeus S4A vacuum pumps. The volumetric flow rates through

the cyclones were measured with an American DTM-325 dry test meter. The volumetric flow rates through the LPI were measured with a Precision Scientific 10 lpm capacity wet test meter and a Matheson 603 rotameter. The stagnation pressure above each stage of the LPI was measured with a Wallace and Tiernan vacuum gauge.

Care was taken during field sampling to minimize contamination and sampling loss. All sample loading and unloading in the field was done in a glove box constructed at Keck Laboratory. Positive pressure was maintained inside the glove box by a small blower which drew air into the box through a triple thickness Fram filter. Each arm hole in the glove box had a sleeve with a garter to provide a snug fit. Disposable latex gloves were worn while working in the glove box. All work inside the glove box was done on a teflon sheet which was washed with methanol and decharged before each use.

Detailed written standard operating instructions were followed for measuring flow rates and pressures and in loading and unloading each of the samples. UCLA and University of Minnesota personnel changed most of the samples following the written procedures. This insured uniformity in sample handling and minimized contamination. Immediately after collection each sample was placed in a plastic container, sealed with Parafilm, enclosed in a ziplock bag, and placed in a refrigerator in the van. The samples were stored in an ice chest during the return trip back to Caltech.

3.2.3 Sample Analysis

3.2.3.1 Fine mass concentration -

The aerosol mass on each Nuclepore filter sample was determined by difference with its blank value using a Mettler M5 SA microbalance. A Nuclear Products Po 210 500 μc radioactive decharger and a tray of Dririte dessicant were kept in the microbalance to minimize static charge and water absorption on the aerosol and filter. Five field blanks were obtained at Zilnez Mesa by loading preweighed Nuclepore filters into the cyclone filter holder, drawing 50 l of filtered air through each, and then returning them to their containers. The average aerosol mass on the 5 field blanks was 2.2 μg, with a standard deviation of 7.6 μg. The error in mass measurement was then taken to be $\pm$ 8 ug, which was between 1.5 and 9.4% of the measured field sample masses. After the mass determination, each of the filters was cut into four pieces for additional analyses. All field blanks and field samples were handled identically for chemical analysis.

3.2.3.2 Elemental mass -

One-third of each Nuclepore filter was sent to Crocker Nuclear Laboratory, University of California, Davis, for elemental analysis by particle induced X-ray emissions (PIXE) (Cahill, 1975). Masses of many elements from Al to Pb can be analyzed quantitatively with this technique, including Si, S, K, Ca, Fe, and trace species such as V, Ni, and Zn. Detection limits range from about 20 to 200 ng/cm^2 area density on each filter, corresponding to about 0.2 to 2 μg/filter. Typical

uncertainties in the mass determination of a particular element were ± 15-20% or ± 2 μg/filter, whichever was larger. All elemental masses measured on the 5 Nuclepore filter blanks were below detectable limits except Al, with an average value of 2.98 ± 1.30 μg/filter.

3.2.3.3 Elemental mass distribution -

The aerosol sampled by the LPI for elemental analysis was impacted on coated mylar films affixed to 25 mm glass discs. The mylar was coated with Apiezon L vacuum grease which was applied as a 2% solution in Spectrograde toluene and allowed to evaporate. The details of the substrate preparation and sample handling procedures are in Appendix A.

After being returned to Caltech, each coated mylar sample collected by the LPI was peeled off the glass disc and mounted on a 35-mm slide with a 13-mm center hole.

The LPI samples were sent to Crocker Nuclear Laboratory for elemental analysis by PIXE using a focused alpha particle beam of 3 to 4 mm diameter. Nanogram sensitivities for most elements are achieved with the focused beam. A detailed description of the PIXE focused beam technique applied to LPI samples is found in Appendix A. Based upon repeated measurements of field samples, the estimated measurement error was about ± 15-20% or twice the minimum detectable limit, whichever was larger. Average field blank values, presented in Appendix A, ranged from 1 to 14 ng for common elements.

3.2.3.4 Sulfur mass distribution -

The aerosol sampled by the LPI for sulfur analysis was impacted on vaseline-coated stainless steel strips backed by 25-mm glass discs. Before coating with vaseline, each strip was wiped clean and baked at 900 °C for 45 minutes to drive off volatile contaminants. The sulfur mass deposited on each stage was determined by the technique of flash volatilization and flame photometric detection (FVFPD) (Roberts and Friedlander, 1976). Each stainless steel strip was placed between two tungsten posts and heated quickly by resistance using an electrical discharge of 11.3 V from a capacitance of 0.31 F. The volatilized aerosol was drawn into an airstream diluted with room air. The airstream was filtered with a 47 mm Teflon filter before sampling with a Meloy 285 Sulfur Analyzer. The output voltage from the sulfur analyzer was integrated over time using a Spectra-Physics integrator with automatic baseline correction. Calibration was accomplished with $(NH_4)_2SO_4$ standard solutions which were applied to vaseline-coated stainless steel strips and allowed to dry. A linear relation between integration counts and sulfur from 2 to 100 ng was obtained with correlation coefficients exceeding 0.995. Uncertainty in the measurement was $\pm$ 2 ng or $\pm$ 10%, whichever was larger. This analysis was performed at the Page, Arizona, Holiday Inn, in a room which had been temporarily converted to a field laboratory.

3.2.3.5 $SO_4^=$, NO_3^-, NH_4^+ mass -

One-half of each Nuclepore filter was stored in a plastic petri

dish, doubly wrapped, and sent in an insulated container with dry ice to Environmental Research and Technology, Inc. (ERT), Westlake Village, California. Their laboratory, under the direction of Dr. Kochy Fung, determined the masses of aerosol sulfate and nitrate on each filter by liquid ion chromatography and ammonium by colorimetry. The anions were analyzed in aqueous extracts of filters using an automated Dionex System 10 Ion Chromatograph. The ammonium from the same extract was analyzed colorimetrically with a Technicon Auto Analyzer II by reaction with phenol and alkaline sodium hypochlorite to produce indophenol. Based on duplicate analysis of samples and standards the uncertainty in the various determinations per filter were: $\pm$ 1.2 μg NO_3^-, $\pm$ 22.2 μg $SO_4^=$, and $\pm$ 0.3 μg NH_4^+. The 5 Nuclepore field blanks had the following values: 4.0 $\pm$ 1.2 μg $SO_4^=$, 13.2 $\pm$ 3.7 μg NO_3^-, and 0.37 $\pm$ 0.09 μg NH_4^+.

3.2.3.6 Particle absorption coefficient, b_{ap} -

The time average particle absorption coefficient was measured from one-sixth of each Nuclepore filter sample using the opal glass integrating plate technique (Lin et al., 1973).

An apparatus for this measurement was constructed at Keck Laboratory, and is described in Appendix B. The filter was held against a piece of opal glass and was illuminated by a narrow beam of coherent light at 0.6328 μm wavelength which had propagated through a 0.25 mm diameter optical fiber. The forward scattered light from the aerosol deposit was collected by the opal glass and reradiated. The light intensity from the opal glass was detected by a calibrated

phototransistor. The phototransistor collector current was applied across the resistance and is measured as a voltage with a digital voltmeter.

The opal glass is efficient in reradiating the scattered light, so that the light extinction through the sample is due to particle absorption. The following relation (Lin et al., 1973) was used to calculate the time average particle absorption coefficient, b_{ap}:

$$b_{ap} = A/S \ln(I_o/I) \qquad (3.1)$$

where A is the aerosol deposit area on the filter, 9.62 cm^2, and S is the total volume of air sampled through the filter in m^3. I_o is the light intensity measured through the filter blank, and I is the intensity measured through the filter sample. By varying the filter position with respect to the beam, it was determined that the aerosol was deposited uniformly on the filter.

3.2.3.7 Particle absorption coefficient distribution -

The LPI mylar samples were returned to Caltech after elemental analysis by Crocker Nuclear Laboratory. The time average particle absorption coefficient was measured from each of the LPI mylar deposits using the technique described in Appendix B. These measurements resulted in a measured distribution of b_{ap} as a function of particle size. This technique does not yet provide a strictly quantitative measure of particle absorption. For reasons to be discussed later, it is apparent that the filter measurement provided a more accurate

measure of the total particle absorption coefficient.

3.2.3.8 Carbon -

The aerosol collected on the Tissuequartz filters was analyzed for total carbon by the nondestructive technique of proton-induced gamma-ray emissions (Macias et al., 1978) and graphitic carbon (soot) by calibrated optical reflectance at Washington University, St. Louis, Missouri. The analyses were performed under the supervision of Dr. Edward Macias in the Department of Chemistry. The estimated error in measurement of total carbon per filter was $\pm$ 5 µg or $\pm$ 20%, whichever was greater. The estimated error for soot was $\pm$ 1 µg or $\pm$ 20%, whichever was greater. The resultant error per filter for the computed non-soot carbon was therefore $\pm$ 6 µg or $\pm$ 20% of the sum of the total and soot carbon measurements, whichever was greater.

3.2.3.9 Soot mass distribution -

The mass of soot on each LPI stage was inferred from the particle absorption coefficient measurement. The technique is described and evaluated in Appendix B. The technique assumes that the fine aerosol is due only to spherical soot particles. The theoretical mass absorption efficiency of carbon spheres of density 2 g/cm^3 and refractive index m=1.96 - 0.66i (Bergstrom, 1973; Hodkinson, 1964) was calculated as a function of particle size assuming a wavelength of 0.63 µm. The average mass absorption efficiency between the 50% efficiency cutoff diameters for each stage of the LPI was then calculated. The soot mass on each LPI stage was then equal to the ratio of the measured

absorption coefficient to the average mass absorption efficiency. The lower detection limit using this technique is about 3 ng soot. Because the technique has not been calibrated with aerosols of known size, it is difficult to estimate the error in measurement. Based on the variation in possible mass absorption efficiency (Roessler and Faxvog, 1979) and the error in the absorption measurement, it is estimated that the inferred soot mass measurement on any stage is correct to within a factor of 2.

3.3 EXPERIMENTAL RESULTS

3.3.1 Aerosol Volume and Extinction Distributions

A total of 13 samples were obtained from June 26 to July 13, 1979, of which 12 contained sufficient data for attempting an aerosol species extinction coefficient balance. Sample times varied from 17 to 52 hours, with an average of 26.2 hours. The long sample times were necessary due to the very low aerosol mass concentrations. Sampling times of one to three hours would have been sufficient for an average urban area. The Nuclepore and Pallflex filters sampled an average of about 34 m^3 per episode. The LPI sampled for PIXE analysis during the same interval as the filters, while the LPI sampled for sulfur by FVFPD an average of about ten hours. All values of sample volumes and concentrations in this chapter are with respect to P = 589 mm Hg, the pressure at Zilnez Mesa. Over a given interval, defined by the sample time of the filters, the nephelometer and aerosol distribution instrumentation generally sampled for a shorter time, due to calibration and

breakdown. On the average the EAA and OPC were on line for 80% of the time the filters were sampling; the nephelometer was on line 73% of the time.

During the three-week sampling period, wide variations in the particle scattering coefficient, b_{sp}, were measured. Zilnez Mesa was exposed to a regional haze episode of apparently urban origin from June 28 to June 30. Regional flights indicated that lightning-caused fires had a substantial effect on visibility reduction in the area during the first week of July. Very clean air with excellent visibility was sampled at Zilnez Mesa from July 9 to July 11. The average b_{sp} measured from June 27 to July 13 was 15.0×10^{-6} m^{-1}. The average fine aerosol mass concentration was 5.28 $\mu g/m^3$, while the average computed mass scattering efficiency was 2.80 m^2/g. These values are similar to those obtained in the 1977 VISTTA October regional flight (Macias et al., 1979). Elevated SO_2 concentrations were occasionally detected at Zilnez Mesa. It was assumed that they resulted from the Navajo Generating Station plume. However, the filter sampling intervals were much longer than the plume episodes, and this precluded direct assessment of the plume aerosol.

The time-averaged volume distribution of particles from 0.032 to 5.62 μm diameter for each episode is summarized in Table 3.1. They are normalized with respect to the total aerosol volume concentration, V_T. As expected, the distribution was bimodal with peaks in both the fine and coarse modes. It is seen in Figure 3.3 that the shape of the volume distribution was not always preserved, particularly during the

Table 3.1

Time Averaged Normalized Aerosol Volume Distributions

Zilnez Mesa, 1979

$$\frac{\Delta V}{V_T \Delta \log D}$$

	Start Date												
ΔD, μm	6/27	6/28	6/29	7/2	7/3	7/5	7/6	7/7	7/8	7/9	7/10	7/11	Average
.032-.056	.032	.022	.009	.012	.010	.136	.296	.152	.041	.053	.035	.039	0.070 ± .085
.056-.100	.072	.073	.035	.052	.020	.065	.063	.060	.046	.073	.064	.081	0.059 ± .018
.100-.178	.296	.423	.379	.393	.293	.264	.234	.287	.193	.274	.297	.312	0.304 ± .066
.178-.316	.583	.788	.460	.681	1.15	.600	.639	.687	.636	.584	.613	.566	0.666 ± .171
.316-.562	.548	.708	0.986	.241	1.33	.458	.291	.477	.524	.460	.450	.400	0.573 ± .307
.562-.750	.238	.217	.257	.213	.201	.203	.308	.243	.221	.148	.296	.507	0.254 ±0.090
.750-1.00	.196	.155	.188	.172	.108	.176	.177	.168	.203	.138	.288	.507	0.206 ± .107
1.00-1.78	.171	.143	.156	.196	.095	.191	.184	.177	.234	.176	.215	.277	0.184 ±0.046
1.78-3.16	.488	.428	.460	.556	.239	.512	.520	.511	.622	.555	.503	.543	0.495 ± .095
3.16-5.62	1.59	1.23	1.29	1.67	0.694	1.58	1.53	1.44	1.50	1.68	1.54	1.27	1.42 ± .27
V_T, $\mu m^3/cm^3$	3.67	4.00	7.28	6.75	10.8	4.43	4.02	4.15	3.57	3.46	3.18	5.23	5.05

Measurements made by U. Minnesota Electrical Aerosol Analyzer (EAA) and Optical Particle Counter (OPC).

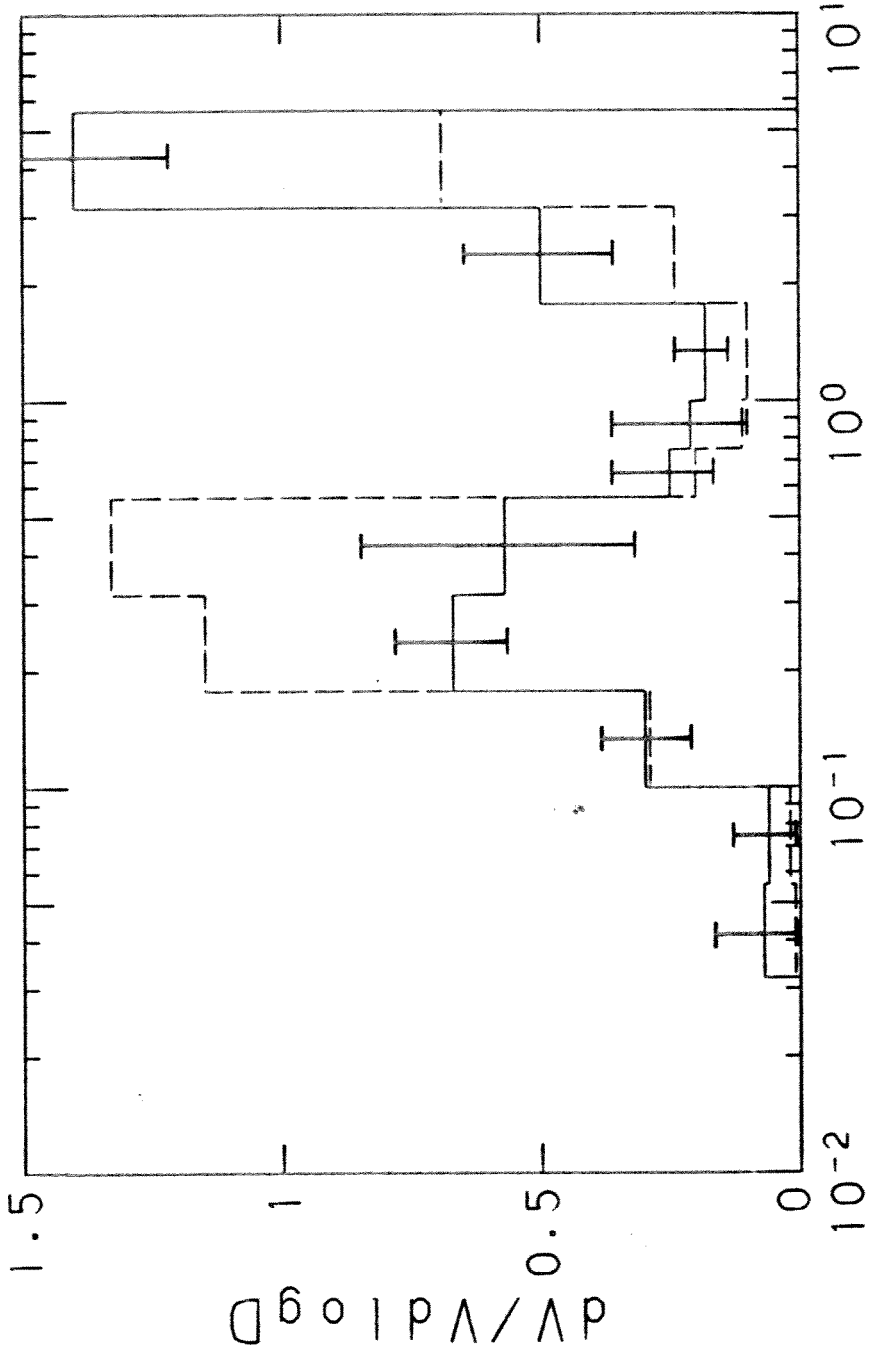

Figure 3.3. Normalized aerosol volume distributions, Zilnez Mesa, Arizona. Solid histogram is the June 27-July 13, 1979 average. Error bars are the standard deviations. The dashed histogram is the distribution for the July 3-5 forest fire episode.

July 3-5 forest fire episode. For each episode the aerosol volume concentration of particles of diameter less than 1.78 μm was calculated, V_{T1}. The average V_{T1} was 2.77 $\mu m^3/cm^3$, while the average fine aerosol particle density was computed to be 2.09 g/cm^3, in good agreement with bulk densities of chemical species in the aerosol. A summary of these data is found in Table 3.2.

3.3.1.1 Particle scattering coefficient distribution -

The b_{sp} distribution with respect to particle size was computed for each episode using the aerosol volume distribution and the theoretical volume scattering efficiency, $G_s(m,D,\lambda)$, defined in Equation 2.6. Values of m = 1.54 - 0.015i (Macias et al., 1979) and λ = 0.53 μm were assumed. The values of $\bar{G}_{sj}$, the volume scattering efficiency averaged over each particle size interval measured with the instrumentation, are given in Table 3.3. The incremental particle scattering coefficient for a size interval $[D_j, D_j + \Delta D_j]$ can be approximated over each interval by

$$(\Delta b_{sp}/\Delta x)_j \quad (\Delta V/\Delta x)_j \, \bar{G}_{sj}$$

The b_{sp} distribution averaged over the 12 episodes is plotted on Figure 3.4. It is seen that particles between about 0.2 μm and 0.7 μm diameter were responsible for the bulk of the particle light scattering. This is because the aerosol volume distribution and its scattering efficiency achieve maximum values in this particle size interval.

Table 3.2

Summary of Selected Time-Averaged Measurements,

Zilnez Mesa, 1979

	Start Date												
	6/27	6/28	6/29	7/2	7/3	7/5	7/6	7/7	7/8	7/9	7/10	7/11	Ave.
V_T, $\mu m^3/cm^3$	3.67	4.00	7.28	6.75	10.8	4.43	4.02	4.15	3.57	3.46	3.18	5.23	5.05
V_{T1}, $\mu m^3/cm^3$	1.76	2.34	4.09	2.98	8.26	2.10	1.96	2.12	1.69	1.53	1.56	2.85	2.77
M_T, $\mu g/m^3$	4.96	5.83	7.2-11.8	7.11	8.12	4.34	4.93	5.03	3.73	2.22	2.84	4.73	5.28
$\rho = M_T/V_{T1}$, g/cm^3	2.8	2.49	2.32	2.39	0.98	2.07	2.52	2.37	2.21	1.45	1.82	1.66	2.09
$\bar{b}_{sp}$(calc.)	11.6	14.9	29.3	15.1	59	12.8	10.6	12.8	11.2	9.8	9.7	16.6	17.8
$\bar{b}_{sp1}$(calc.)	9.9	13.5	26.5	14.1	57	10.8	8.8	11.0	9.7	8.1	8.3	14.5	16.0
$\bar{b}_{sp}$(meas.)	9.8	13	19.2	22.4	34.8	12.5	21.5	16.2	8.7	7.1	5.8	9.0	15.0
$\bar{b}_{ap}$(filter)	1.6	2.6	2.0	3.3	3.9	2.0	2.2	1.9	1.4	0.4	0.8	0.9	1.9
$\bar{b}_{ap}$(LPI)	0.68	-	0.85	0.95	1.30	-	-	0.87	-	0.39	0.48	0.39	0.74
Δt_1, hrs	21.93	11.48	21.18	14.95	38.08	17.05	15.38	20.63	19.82	15.35	18.55	35.92	20.9
Δt_2, hrs	18.32	9.07	18.92	17.32	38.13	16.33	16.05	19.63	8.62	13.92	20.45	34.03	19.2
Δt_3, hrs	24.58	16.17	25.12	22.48	45.49	19.51	23.45	23.08	22.97	25.03	25.17	41.75	26.2

V_T = total aerosol volume concentration, $D \leq 5.6$ μm

V_{T1} = total aerosol volume concentration, $D \leq 1.78$ μm

M_T = total aerosol mass concentration, $D \leq 2$ μm

ρ = calculated overall aerosol density, $D \lesssim 2$μm

Δt_1 = total sample time for EAA, OPC

Δt_2 = total sample time for nephelometer

Δt_3 = total sample time for Nuclepore, Tissuequartz filters and LPI

$\bar{b}_{sp}$, $\bar{b}_{ap}$ in units of 10^{-6} m^{-1}

Table 3.3

Values of the Aerosol Volume Scattering Efficiency, $\overline{G}_s$, Used to Calculate the Particle Scattering Coefficient Distribution

Particle Size Interval, ΔD μm	$\overline{G}_s$ $10^{-6}m^{-1}/(\mu m^3/cm^3)$
0.056-0.100	0.38
0.100-0.178	1.65
0.178-0.316	5.52
0.316-0.562	9.86
0.562-0.750	8.08
0.750-1.00	3.45
1.00-1.78	2.07
1.78-3.16	1.07
3.16-5.62	0.80

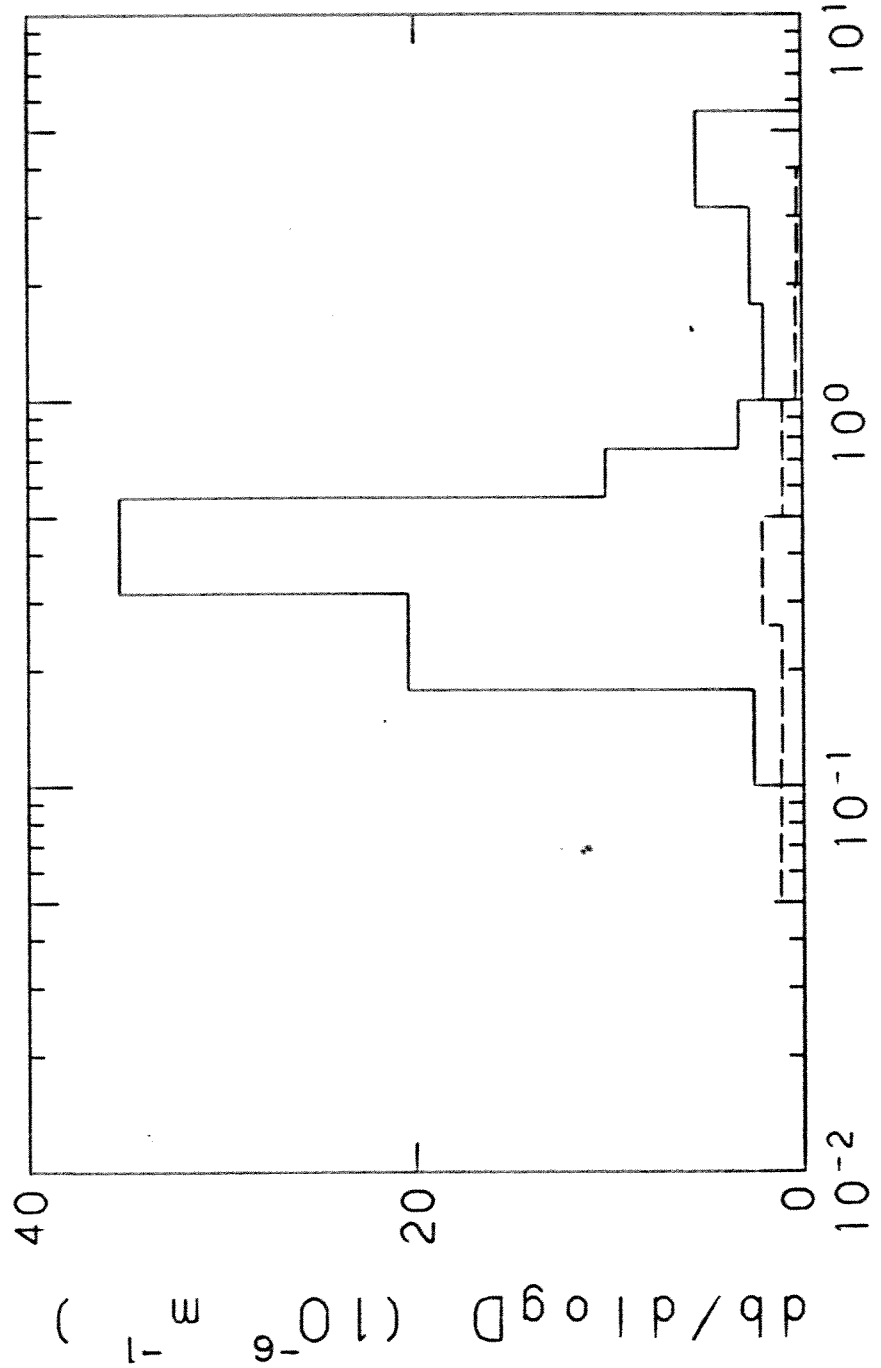

Figure 3.4. Particle extinction coefficient size distributions, Zilnez Mesa, Arizona, June 27 - July 13, 1979 average. The solid histogram is the particle scattering distribution calculated from measured particle size distributions assuming m=1.54-0.0151. The dashed histogram is the particle absorption coefficient distribution measured from light absorption by aerosol deposits collected with the low pressure impactor.

This result has been found previously in both urban and remote locations in the Southwest (Macias et al., 1979; Ensor et al., 1972).

Summing the contributions from particle diameters between 0.032 and 5.62 μm diameter results in the total calculated particle scattering coefficient, b_{sp} (calc.). Summing only the contributions from particles less than 1.78 μm provides the total fine particle scattering coefficient, b_{sp1} (calc.). These computed values were compared with the time average measured particle scattering coefficient, b_{sp} (meas.), in Table 3.2. On the average, the agreement was good between b_{sp1} (calc.) and b_{sp} (meas.). The average ratio of the calculated to measured scattering coefficient and the standard deviations are as follows:

$$\left[\frac{b_{sp}\ (\text{calc.})}{b_{sp}\ (\text{meas.})}\right]_{ave} = 1.23 \pm 0.43$$

$$\left[\frac{b_{sp1}(\text{calc.})}{b_{sp}\ (\text{meas.})}\right]_{ave} = 1.08 \pm 0.39$$

The calculated fine particle scattering coefficient agrees better with the measured value because the nephelometer does not view coarse particles effectively. This is due to the viewing geometry of the nephelometer and the large forward scattering component of the coarse particles (Sverdrup, 1977). By suppressing the effects of the coarse particles, the nephelometer underestimates the total particle scattering coefficient. In an urban area this error may not be large, but in a pristine, arid region where the coarse aerosol mass concentration may

be two to ten times that of the fine mode, the discrepancy may be substantial. Calculations using measured distributions up to 18 um at Zilnez Mesa indicate that from 20-40% of aerosol light scattering may be due to coarse particles during near-pristine conditions.

3.3.1.2 Particle absorption coefficient distribution -

The particle absorption coefficient distribution was measured from eight episodes using optical absorption through LPI deposits on coated mylar. The results are shown in Table 3.4. Although the total absorption coefficient, b_{ap}, varied from sample to sample, the normalized distribution remained rather constant. Absorption at Zilnez Mesa was dominated by submicron aerosol, assumed to be soot. The distribution was broad with a peak due to particles of 0.26 to 0.50 μm aerodynamic diameter. This contrasted with measured urban distributions in Pasadena and Los Angeles, shown in Appendix B, where fresh combustion soot having aerodynamic diameters of less than 0.12 μm dominated absorption.

As indicated earlier, the LPI-integrating plate technique does not provide a strictly quantitative measure of particle absorption. As seen in Table 3.2, b_{ap} determined by summing the contributions from each LPI stage averaged 39% of the total measured by the Nuclepore filter.

Figure 3.4 shows the average particle scattering and absorption coefficient distributions obtained at Zilnez Mesa. The absorption coefficient distribution was obtained by multiplying the normalized

Table 3.4

Normalized Aerosol Absorption Coefficient Distributions

Zilnez Mesa, 1979

$$\frac{\Delta \bar{b}_{ap}}{\bar{b}_{ap}\ \Delta \log D_a}$$

Aerodynamic diameter ΔD_a, μm	Start Date 6/27	6/29	7/2	7/3	7/7	7/9	7/10	7/11	Average
.05-.075	.57	.71	.85	.25	.35	.93	.80	.68	.64
.075-.12	.84	.55	.63	.37	.34	.97	.69	.48	.61
.12-.26	.72	.53	.69	.48	.42	.55	.57	.65	.58
.26-.50	.96	1.08	1.03	1.72	1.39	.62	1.03	.96	1.10
.50-1.0	.38	.50	.46	.48	.88	.63	.47	.63	.55
1.0-2.0	.18	.19	.12	.15	.11	.18	.22	.24	.18
2.0-4.0	.16	.25	.07	.15	.11	.10	.08	.14	.13
$\bar{b}_{ap}$, $10^{-6}m^{-1}$	0.68	0.85	0.95	1.30	0.87	0.39	0.48	0.39	0.74

Measurements by LPI and optical absorption

distribution obtained by the LPI by the measured total b_{ap} from the Nuclepore filter. It is obvious that light extinction and visibility degradation at Zilnez Mesa were due primarily to submicron aerosol.

3.3.2 Aerosol Composition

3.3.2.1 Chemical species mass balance -

The time average mass concentrations of the fine aerosol chemical species were computed from analysis of the Pallflex and Nuclepore filters. The results for each episode are shown in Table 3.5. The organic carbon concentration is taken to be 1.2 times the difference between the total and graphitic carbon concentrations. This was done to account for additional hydrogen and oxygen in the organic aerosol (Grosjean and Friedlander, 1975). It was assumed that the Al, Si, Ca, and Fe were present in their oxidized forms (Macias et al., 1979). Table 3.5 shows that organics and sulfate dominated the fine aerosol mass at Zilnez Mesa.

The NO_3^- masses determined from the field samples were all within one standard deviation of the average field blank value. The average molar ratio of $[NH_4^+]$ to $[SO_4^=]$ was 2.11. The average molar ratio of $([NH_4^+]-[NO_3^-])$ to $[SO_4^=]$ was 1.91. It was therefore assumed that the aerosol sulfate was usually in the form of ammonium sulfate, $(NH_4)_2SO_4$.

Using the assumed chemical compounds, the species which were chemically analyzed accounted for almost all of the fine aerosol mass. The average ratio of average species mass to gravimetrically measured

Table 3.5

Mass Balance on Chemical Species, Fine Aerosol,

Zilnez Mesa, 1979

Start Day	Time average concentration, $\mu g/m^3$									
	Organics	Soot	$SO_4^=$	NO_3^-	NH_4^+	SiO_2	K	Al_2O_3 +CaO Fe_2O_3	Total by species	Total gravimetric
6/26	0.24	0.1	0.65	0.11	0.15	1.04	0.06	0.37	2.7	3.71
6/27	0.24	0.2	1.11	0.28	0.39	0.31	0.05	0.25	2.8	4.96
6/28	2.3	0.2	2.29	0.23	0.71	0.49	0.08	0.21	6.5	5.83
6/29	2.3	0.2	2.85	0.00	0.93	0.47	0.09	0.26	7.1	9.5 ± 2.3
7/2	2.8	0.2	1.77	0.58	0.49	0.46	0.10	0.40	6.8	7.1
7/3	3.7	0.3	0.92	0.00	0.37	0.74	0.19	0.23	6.5	8.12
7/5	2.6	0.2	0.90	0.15	0.29	0.33	0.05	0.23	4.8	4.34
7/6	3.7	0.2	0.37	0.05	0.16	0.29	0.09	0.41	5.3	4.93
7/7	2.9	0.2	0.45	0.00	0.16	0.30	0.08	0.25	4.3	5.03
7/8	2.8	0.1	0.79	0.21	0.24	0.20	0.06	0.22	4.6	3.73
7/9	0.60	0.1	0.70	0.19	0.19	0.22	0.02	0.30	2.3	2.33
7/10	0.84	0.1	0.45	0.00	0.54	0.17	0.02	0.14	2.3	2.84
7/11	3.6	0.3	0.60	0.00	0.22	0.30	0.02	0.23	5.3	4.73
Average	2.2	0.18	1.07	0.14	0.37	0.41	0.07	0.29	4.7	5.17

Values from chemical analysis of filter samples

mass was 0.94 ± 0.19. Contrary to earlier results obtained at a different location in the Southwest (Macias et al., 1979), SiO_2 did not contribute substantially to the fine aerosol mass concentration.

3.3.2.2 Elemental mass balances: comparison of LPI and filter data -

3.3.2.2.1 Sulfur -

Total fine aerosol sulfur concentrations were determined by three techniques in addition to the ion-chromatographic determination of sulfate. The Nuclepore filters were analyzed by PIXE for sulfur and by liquid ion chromatography for sulfate. Each of the LPI's provided size resolved sulfur distributions; the total concentrations were found by summing the contributions from each stage. It was assumed that all the fine aerosol sulfur was sulfate. The results of the comparison are shown in Table 3.6. Table 3.7 provides the average ratios and standard deviations of the different determinations of sulfate concentration. Agreement among all methods was good, although the LPI-PIXE sulfate total averaged 2-9% lower than the other techniques and the LPI-FVFPD sulfate was 4-8% high. The LPI-PIXE discrepancy was probably due to error in the determination of the alpha beam area. Sample times for the LPI operated for FVFPD were, in general, not equal to the other techniques. Thus its comparison with the other techniques is subject to some error.

Table 3.6

Comparison of Different Techniques for Determination of Total Aerosol Sulfate, Zilnez Mesa, 1979

Start Date	Average Concentration, μg $SO_4^=/m^3$			
	Filter, Ion Chromatography	Filter, PIXE	LPI, PIXE	LPI, FVFPD
6/26	0.65	0.69	—	—
6/27	1.11	0.98	0.59	—
6/28	2.29	2.17	1.40	—
6/29	2.94	3.22	2.32	3.32
7/2	1.77	1.41	1.07	2.14
7/3	0.92	0.79	0.83	1.36
7/5	0.90	0.90	0.60	0.85
7/6	0.37	0.45	0.47	0.45
7/7	0.45	0.46	0.59	0.42
7/8	0.79	0.77	0.74	0.64
7/9	0.70	0.60	0.65	0.47
7/10	0.45	0.46	0.56	0.43
7/11	0.60	0.57	0.68	—

Table 3.7

Ratios of Determined Sulfate Concentrations (from Table 3.6)

Average Ratio, Technique A/Technique B

	Technique B		
Technique A	LPI(FVFPD)	Filter(PIXE)	Filter (Ion Chrom.)
LPI (PIXE)	0.98 ± .35	0.93 ± .25	0.91 ± .28
LPI (FVFPD)	—	1.08 ± .32	1.04 ± .25
Filter (PIXE)	—	—	0.96 ± .12

3.3.2.2.2 Elements by LPI-PIXE analysis -

In a manner similar to that used for sulfur, the total concentrations of other elements may be found by adding the contributions determined by PIXE analysis of each LPI stage. The total was compared with the concentrations of those species determined by PIXE analysis of the Nuclepore filters. The results for each episode are summarized in Table 3.8. The LPI samples consistently contained small quantities of Al, Zn, and Pb which were below detectable limits by PIXE analysis of Nuclepore filters. With the exception of sulfur, which was found almost exclusively in particles of less than 2 μm aerodynamic diameter, higher elemental mass concentrations were determined by LPI-PIXE than by PIXE analysis of the Nuclepore filters. This is probably due to loss of larger particles from the uncoated Nuclepore filter. The cyclone is operated such that the fine particle airstream flows vertically. Particles are collected on the underside of the Nuclepore filter. Gravitational forces may exceed van der Waals and

Table 3.8

Total Fine Aerosol Elemental Concentrations by PIXE Analysis:

Comparison of Low Pressure Impactor and Filter Results

Zilnez Mesa, 1979

Average concentration, ng/m^3

Start Date	Al		Si		S		K		Ca		Fe		Pb		Zn	
	LPI	Fil.	LPI	Fil	LPI	Fil.	LPI	Fil.	LPI	Fil.	LPI	Fil.	LPI	Fil.	LPI	Fil.
6/27	113	< 85	190	143	198	370	79	48	58	45	70	16	15	<35	4.0	< 9.4
6/28	73	<127	317	229	467	723	48	76	77	52	30	<13	11	<49	2	<13
6/29	37	<150	330	232	774	1070	89	94	70	62	70	57	19	<90	6.5	<16
7/2	72	44	321	214	356	470	98	105	77	67	61	27	5	<35	9.7	< 9.3
7/3	98	<45	346	344	277	265	185	191	123	86	75	30	8	<18	6.8	< 4.9
7/5	65	<106	375	154	200	300	42	54	59	29	24	<14	24	<53	1	<14
7/6	52	93	208	136	156	150	86	87	88	45	28	<13	0	<57	6	<14
7/7	73	<93	271	139	197	153	124	86	87	66	28	16	18	<32	13	< 9.7
7/8	54	<93	396	93	246	257	58	56	53	43	22	16	0	<37	7	<10
7/9	73	<89	194	103	217	200	32	17	86	35	36	11	13	<32	4.3	< 8.6
7/10	85	<85	143	78	188	153	40	<20	48	25	30	11	26	<34	3.0	<10
7/11	127	<53	259	142	226	190	40	22	83	38	54	19	17	<20	4.2	< 5.5
Ave. ratio, LPI/Filter	———		1.86±0.84		0.93±0.25		1.19±0.43		1.63±0.45		2.48±0.99		———		———	

electrostatic forces for the coarse particles, resulting in their loss by sedimentation. Handling of the filter may also result in loss of larger particles from the filter.

It was found from the LPI-PIXE results that Si, Ca, and Fe were found almost exclusively in particles greater than 1 μm aerodynamic diameter, whereas a substantial fraction of K was often found in the submicron mode, particularly during forest fire episodes. When only particles less than 2 μm aerodynamic diameter were considered in the LPI-PIXE results, the agreement with the filter measurement is acceptable. Thus, it appeared that by virtue of the coated surfaces the LPI was more efficient than the Nuclepore filter in collecting the fraction of coarse material which passed through the cyclone.

3.3.2.2.3 Soot -

The mass of soot on each LPI stage was inferred from the particle absorption coefficient measurement, described earlier. The total soot concentration obtained from the LPI was compared with that determined by Washington University from the Pallflex filter. The results, shown in Table 3.9, indicate that the agreement between the two measurements of total soot mass concentration is good. The average ratio of the LPI to the filter determined soot mass concentration was 1.23 ± 0.39.

Table 3.9

Comparison of Different Techniques for Determination of Soot Concentration, Zilnez Mesa, 1979

	Soot Mass Concentration, $\mu g/m^3$							
	Start Date							
Technique	6/27	6/29	7/2	7/3	7/7	7/9	7/10	7/11
Low Pressure Impactor	0.21	0.26	0.29	0.41	0.32	0.12	0.15	0.11
Pallflex filter	0.2	0.2	0.2	0.3	0.2	0.1	0.1	0.3

Since the soot distribution was inferred from the absorption coefficient, why was there a good balance on soot but not on the total absorption coefficient? The discrepancy was probably due to the fact that the mass absorption efficiencies used to infer the carbon mass from the LPI absorption measurement were calculated for spheres of m = 1.96-0.66i and ρ = 2 g/cm^3. This resulted in mass absorption efficiencies which averaged about 4 m^2/g for submicron soot. This is about a factor of 2 lower than those measured for laboratory and ambient soot (Roessler and Faxvog, 1979; Pierson, 1978). The discrepancy is probably due to the presence of loosely packed soot agglomerates, which introduce density and shape effects. Roessler and Faxvog (1979) suggest using the values proposed by Dalzell and Sarofim (1969) of m = 1.56 - 0.47i and ρ = 1 g/cm^3 to account for these effects. For the 12

Zilnez Mesa episodes the average ratio of the particle absorption coefficient measured from Nuclepore filters to the soot mass concentration was 9.5 m^2/g, consistent with Dalzell and Sarofim's proposed values. When these values are used the soot concentration determined from the LPI samples averages about one-half the value obtained from the Tissue-quartz filters.

3.3.3 Aerosol Species Mass Distributions

3.3.3.1 Determination of mass distribution -

The LPI size segregates aerosol according to aerodynamic diameter at the pressure in each stage (Hering et al., 1979). For display purposes it is convenient to graph the distribution as $\Delta M_i / \Delta \log D_{50i}$, where ΔM_i is the mass concentration of aerosol collected on stage i and $\Delta \log D_{50i}$ is the logarithmic particle size interval between the 50% efficiency aerodynamic cutoff diameter for stage i and the one upstream of it. The histogram that results only approximates the actual aerodynamic distribution due to crosstalk between stages of the LPI. An inversion algorithm by Twomey (1975) was used to obtain size distributions from measured values on each stage and impactor calibration data. A detailed description and evaluation of the algorithm can be found in Appendix C. The inversion program provides a histogram distribution of 16 equal logarithmic intervals per decade from 0.01 to 6.0 μm. Values of the inverted distribution outside the range of 0.05 to 4.0 μm may be subject to substantial error. A more accurate determination of the particle extinction coefficient is possible with the inverted

distribution from the LPI and the Twomey algorithm. The computations were performed with a PDP-11/60 computer. To calculate the mass distribution as a function of actual diameter, the following relationship was used to transform from aerodynamic diameter, D_a, to Stokes diameter, D_S:

$$D_S = \left(\frac{C_a}{\rho C_s}\right)^{1/2} D_a$$

where ρ is particle density and C_a and C_s are the slip corrections to the Stokes drag for particles of diameter D_a and D_S, respectively (Hering et al., 1979). The slip factor is given by:

$$C = 1 + \frac{2\ell}{D} [1.257 + 0.40 \exp(-0.55\ D/\ell)]$$

where D is particle diameter and ℓ is the mean free path. The transformation from D_a to D_S was made iteratively.

3.3.3.2 Elemental distributions using LPI-PIXE -

Elemental distributions were obtained with the LPI-PIXE technique for each of the 12 samples. In general, S, K, Zn, and Pb were found in submicron aerosol, while Al, Si, K, Ca, Fe, and Zn were found in the coarse aerosol that penetrated the cyclone. Figure 3.5 shows the composite mass distribution of the major elements as a function of 50% cutoff aerodynamic diameter. For the species measured by PIXE, sulfur dominated the submicron aerosol distribution, while silicon was the major coarse particle species. The presence of small amounts of Ca and Si in the 0.05-0.075 μm interval may be due to particle bounceoff. It

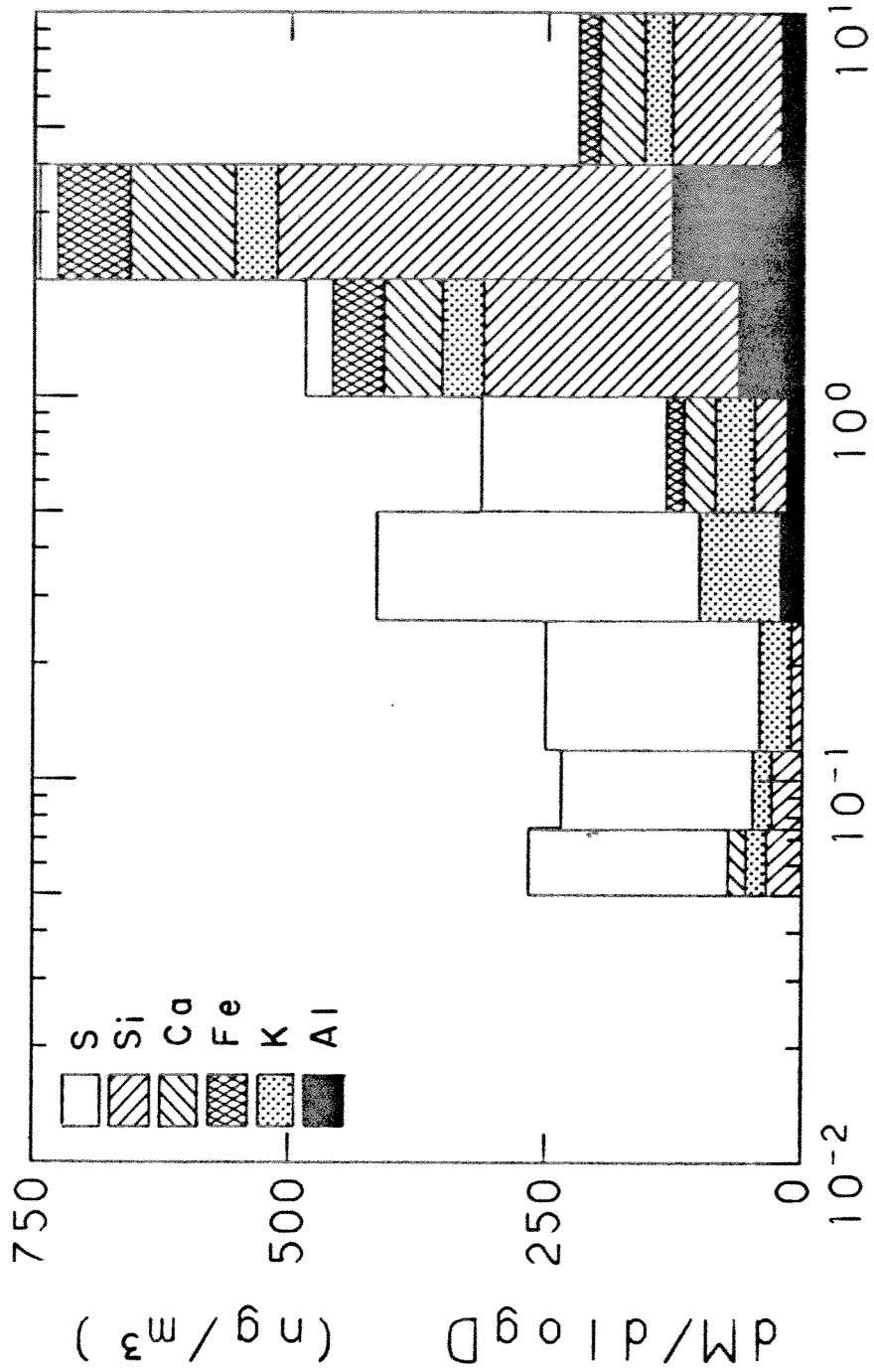

Figure 3.5. Elemental mass distributions, Zilnez Mesa, Arizona, June 27 - July 13, 1979, average. Aerosol size segregated by low pressure impactor (LPI) and analyzed by PIXE. Cyclone preseparator operated upstream of LPI.

is clear from the small amounts of these species that significant bounceoff of the coarse particles did not occur in the LPI samples collected at Zilnez Mesa. This is undoubtedly due to the cyclone separator upstream of the LPI.

The distributions of the trace species Pb and Zn obtained by the LPI-PIXE technique are shown in Figure 3.6. Although they are averages of the 12 episodes, the error in the measurement is estimated to be ±50%, and therefore the results are only semiquantitative. This is because the measured values for any episode were always within 7 ng of the detection limit. It is clear from Figure 3.6 that Pb accumulated strongly in the submicron range. It is somewhat disconcerting to note that even in the remote Zilnez Mesa location, the average submicron Pb mass concentration exceeded that of both Fe and Ca, common crustal species.

Inverted normalized mass distributions were obtained by applying the Twomey inversion algorithm to the average elemental masses measured in each stage of the LPI. The results for Al, Si, S, K, Ca, and Fe are plotted in Figures 3.7a-f. The solid histogram is the distribution of mass with respect to 50% efficiency cutoff aerodynamic diameter when operating at 744 mm Hg ambient pressure. An arbitrary upper diameter of 10 μm was assumed. Since the LPI was operated at 589 mm Hg ambient pressure, the actual results may differ somewhat from these. The dashed histogram is the inverted distribution as a function of aerodynamic diameter. Because the useful range of the inversion routine is from 0.05 to 4 μm diameter, results outside of this range are not

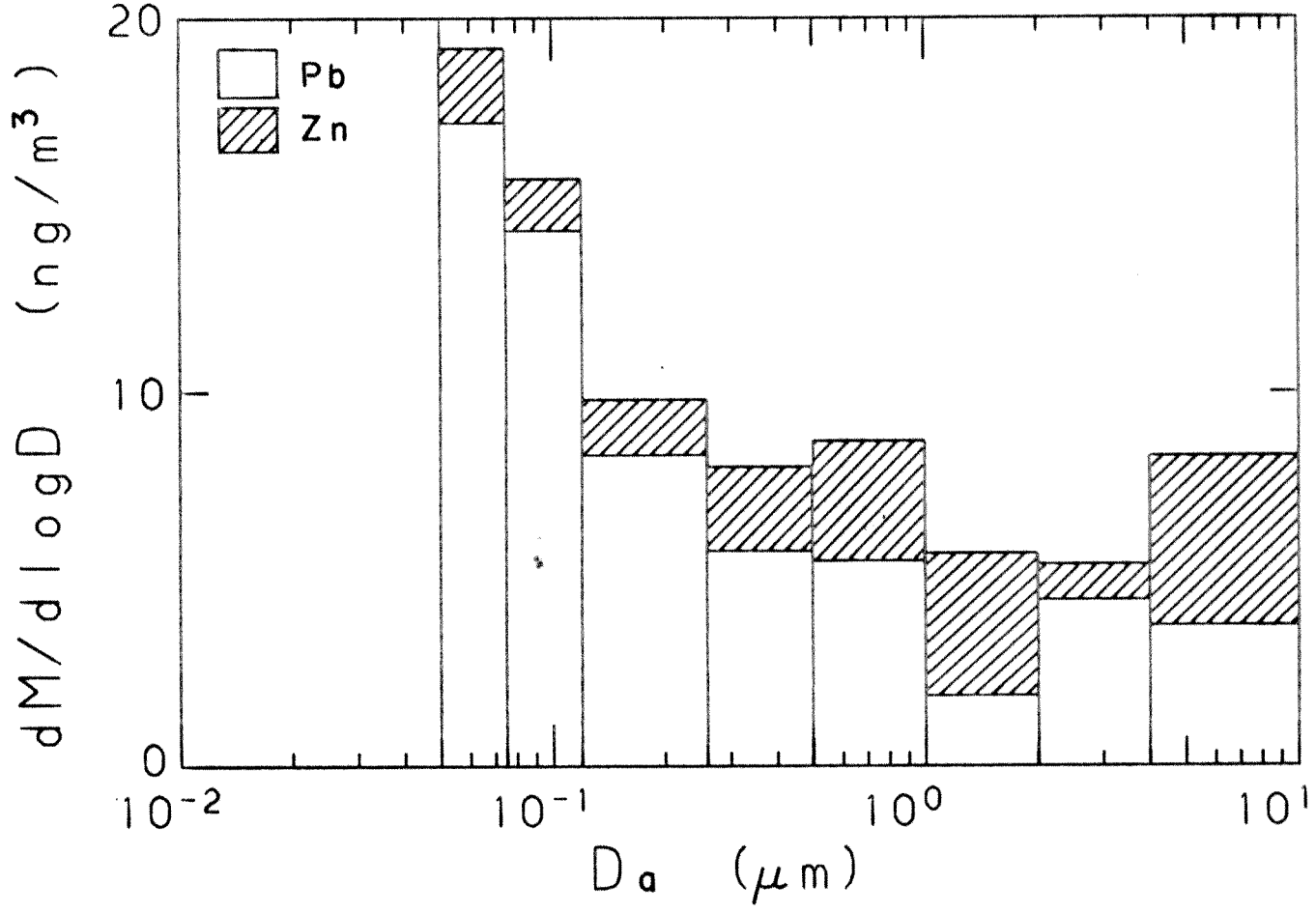

Figure 3.6. Elemental lead and zinc mass distributions, Zilnez Mesa, Arizona, June 27 - July 13, 1979 average. Aerosol size segregated by low pressure impactor (LPI) and analyzed by PIXE. Cyclone preseparator operated upstream of LPI.

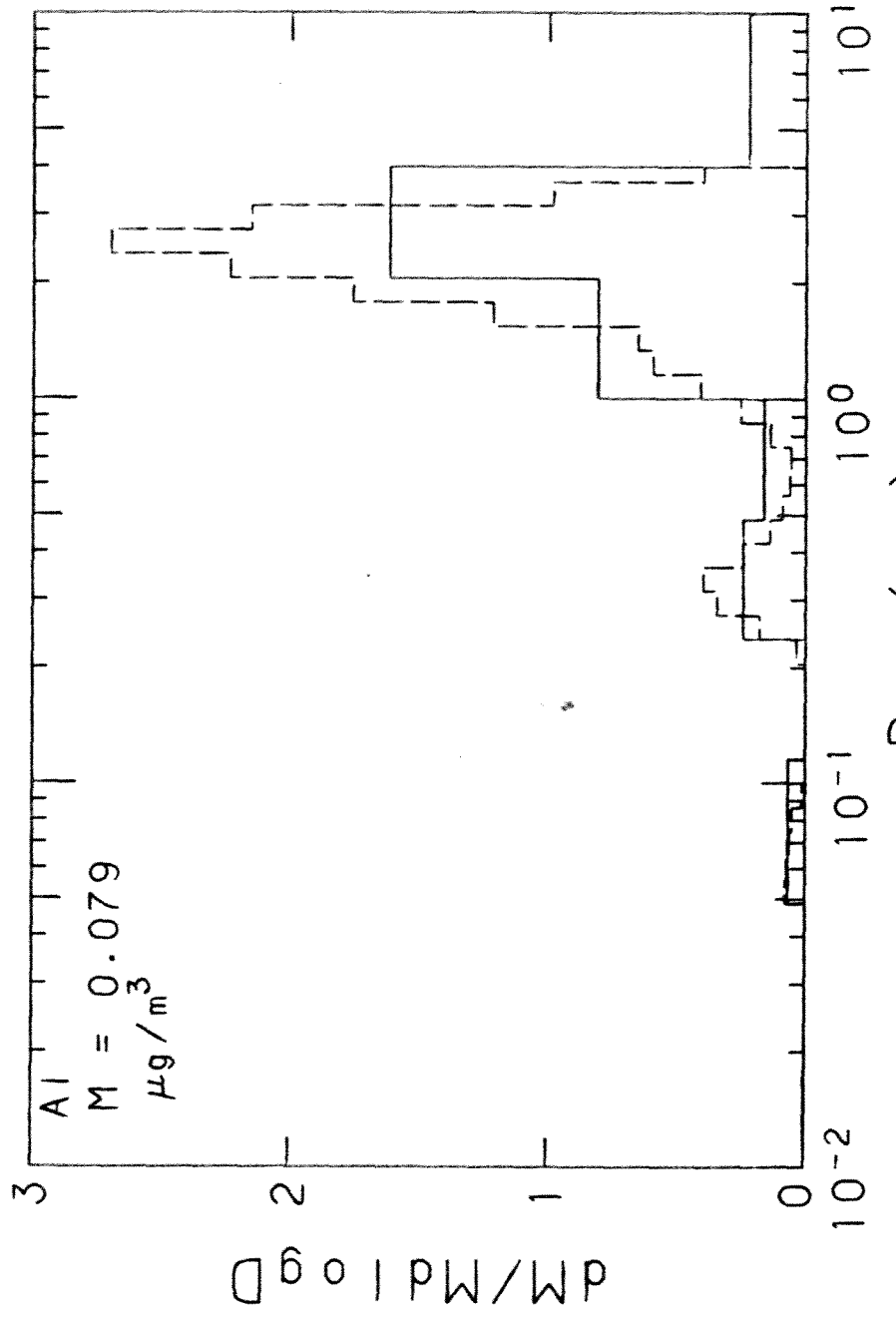

Figure 3.7a. Normalized aluminum mass distribution, Zilnez Mesa, Arizona, June 27 - July 13, 1979 average. Aerosol segregated by low pressure impactor (LPI) and analyzed by PIXE. The solid histogram is the mass distribution with respect to 50% aerodynamic cutoff diameter. The dashed histogram is the inverted distribution obtained from LPI calibration data and Twomey (1975) inversion algorithm.

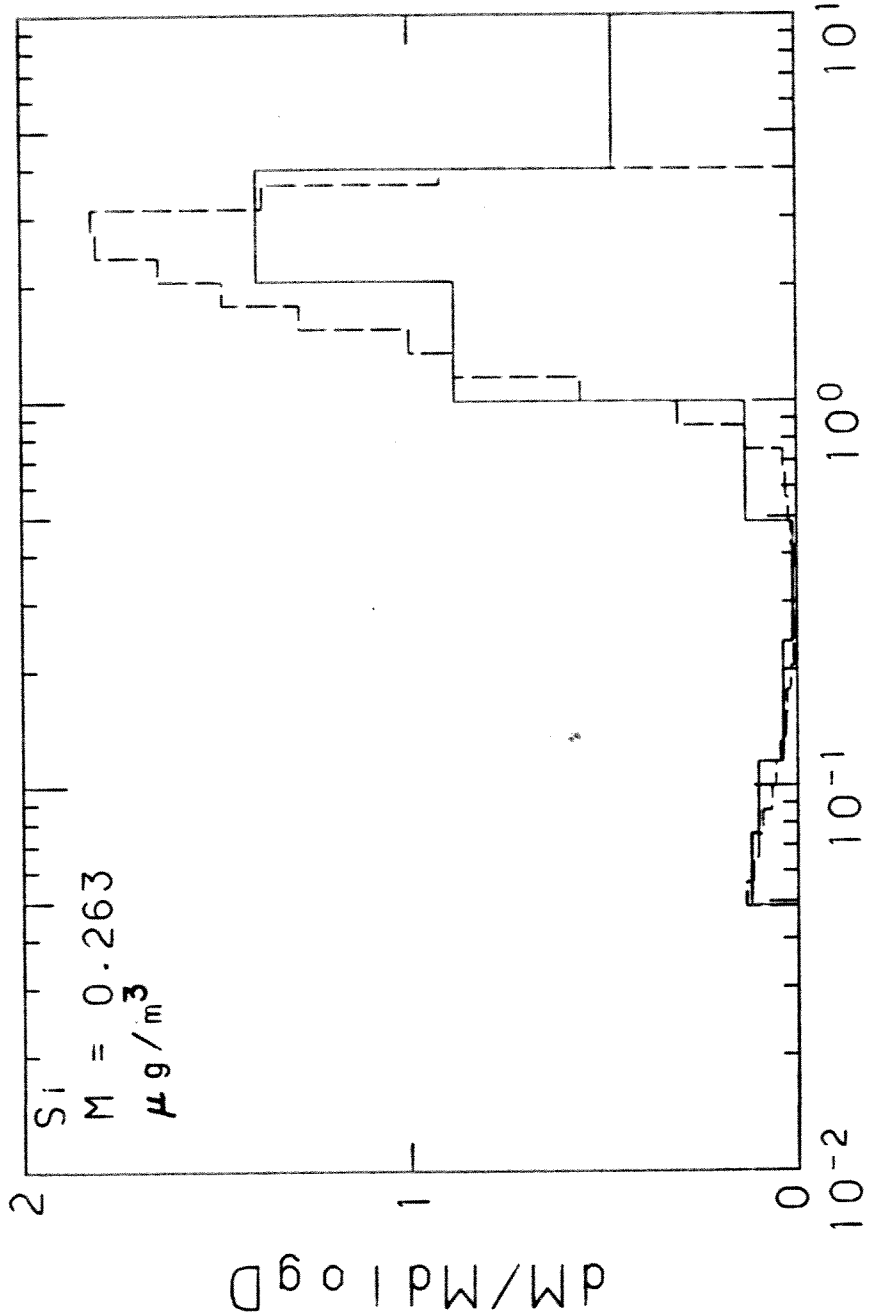

Figure 3.7b. Normalized silicon mass distribution, Zilnez Mesa, Arizona, June 27 - July 13, 1979 average. Aerosol segregated by low pressure impactor (LPI) and analyzed by PIXE. The solid histogram is the mass distribution with respect to 50% aerodynamic cutoff diameter. The dashed histogram is the inverted distribution obtained from LPI calibration data and Twomey (1975) inversion algorithm.

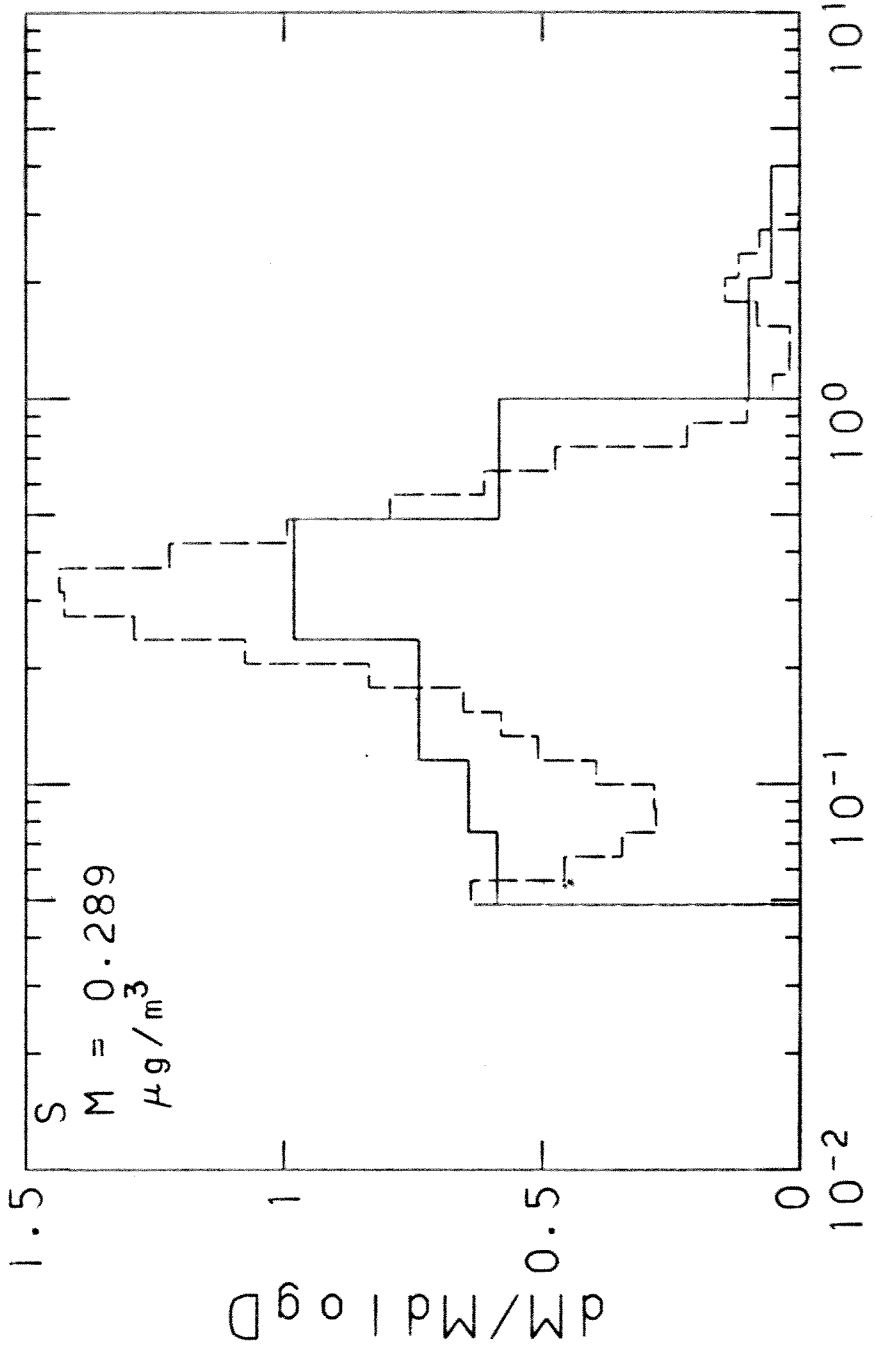

Figure 3.7c. Normalized sulfur mass distribution, Zilnez Mesa, Arizona, June 27 - July 13, 1979 average. Aerosol segregated by low pressure impactor (LPI) and analyzed by PIXE. The solid histogram is the mass distribution with respect to 50% aerodynamic cutoff diameter. The dashed histogram is the inverted distribution obtained from LPI calibration data and Twomey (1975) inversion algorithm.

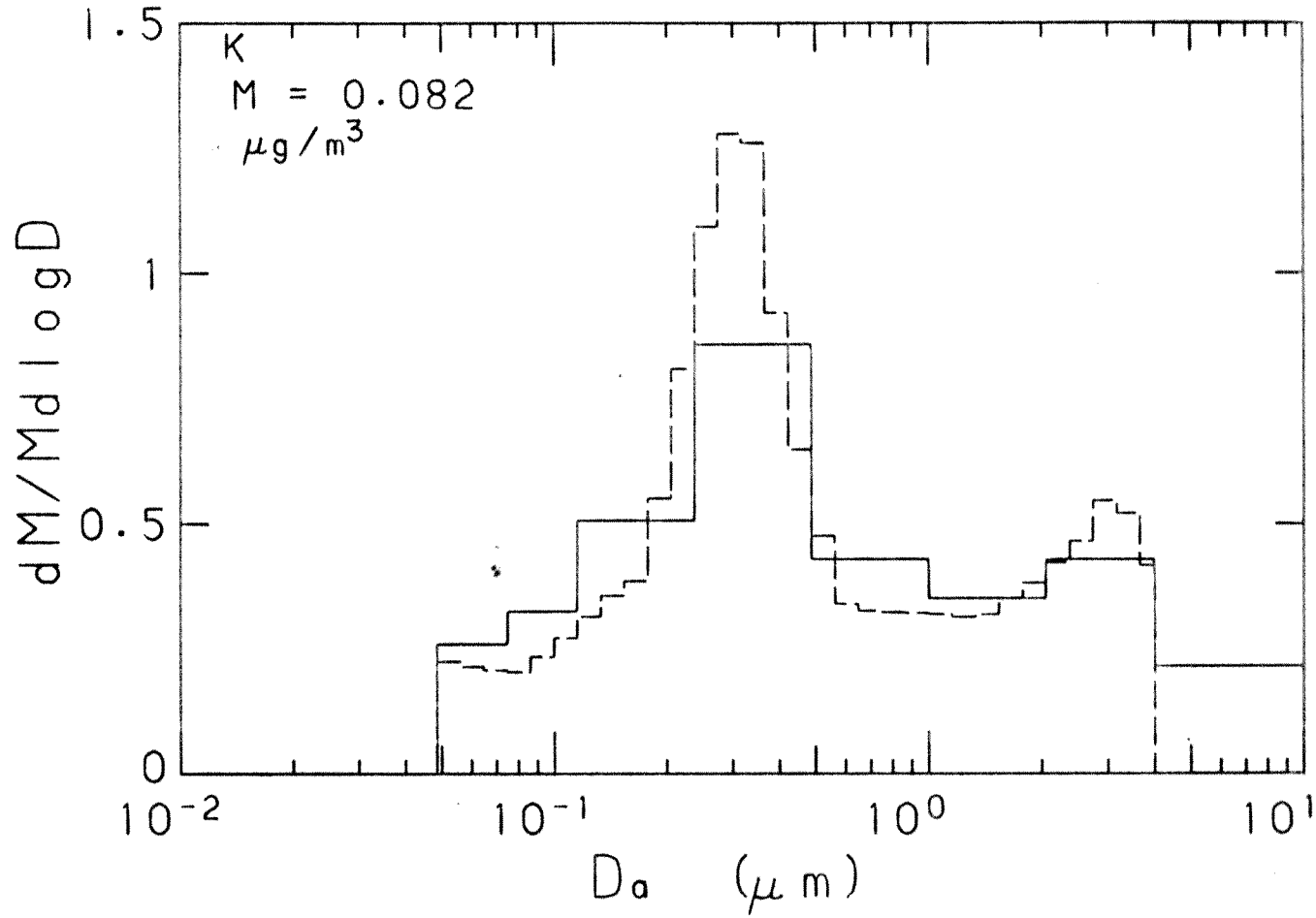

Figure 3.7d. Normalized potassium mass distribution, Zilnez Mesa, Arizona, June 27 - July 13, 1979 average. Aerosol segregated by low pressure impactor (LPI) and analyzed by PIXE. The solid histogram is the mass distribution with respect to 50% aerodynamic cutoff diameter. The dashed histogram is the inverted distribution obtained from LPI calibration data and Twomey (1975) inversion algorithm.

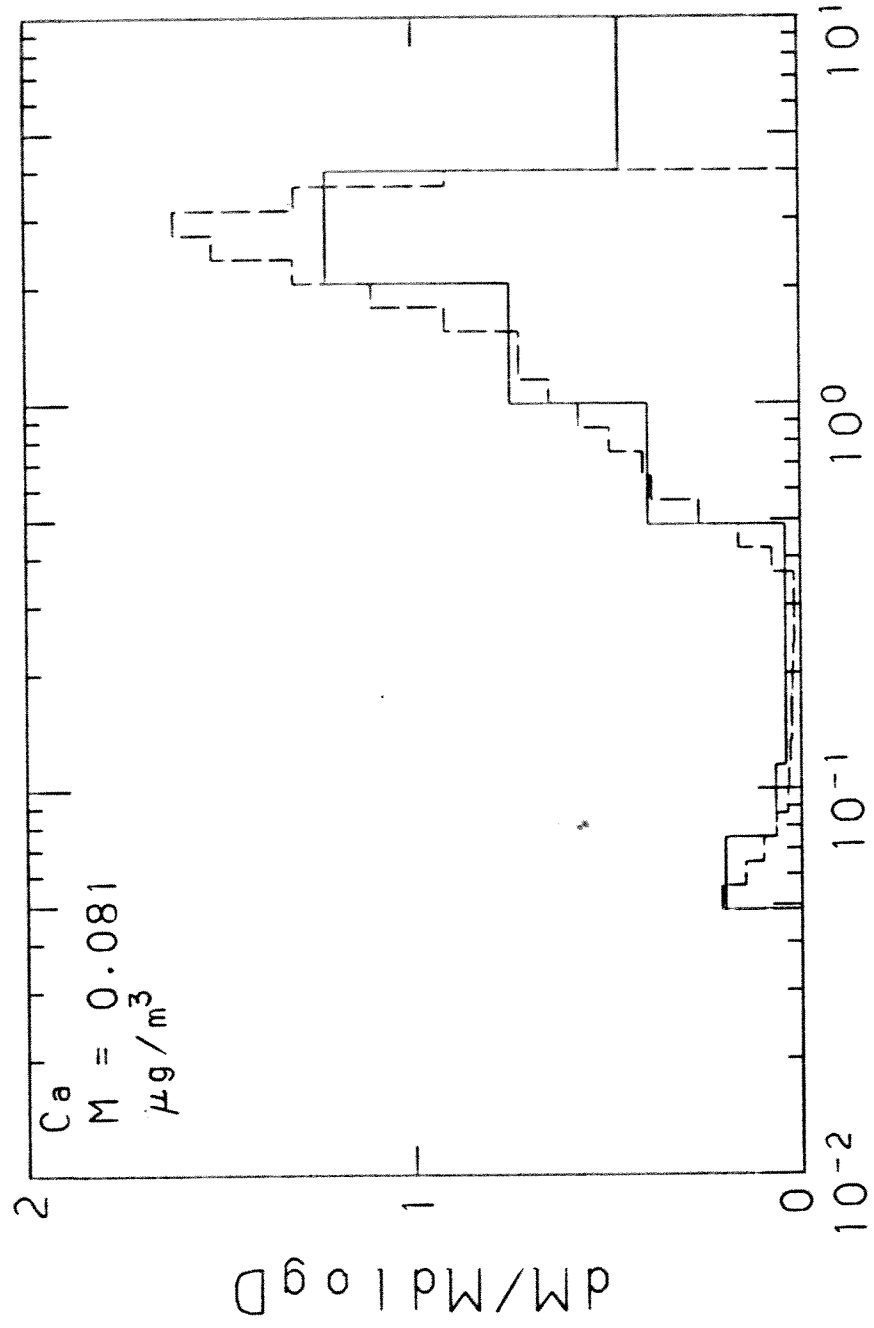

Figure 3.7e. Normalized calcium mass distribution, Zilnez Mesa, Arizona, June 27 - July 13, 1979 average. Aerosol segregated by low pressure impactor (LPI) and analyzed by PIXE. The solid histogram is the mass distribution with respect to 50% aerodynamic cutoff diameter. The dashed histogram is the inverted distribution obtained from LPI data and Twomey (1975) algorithm.

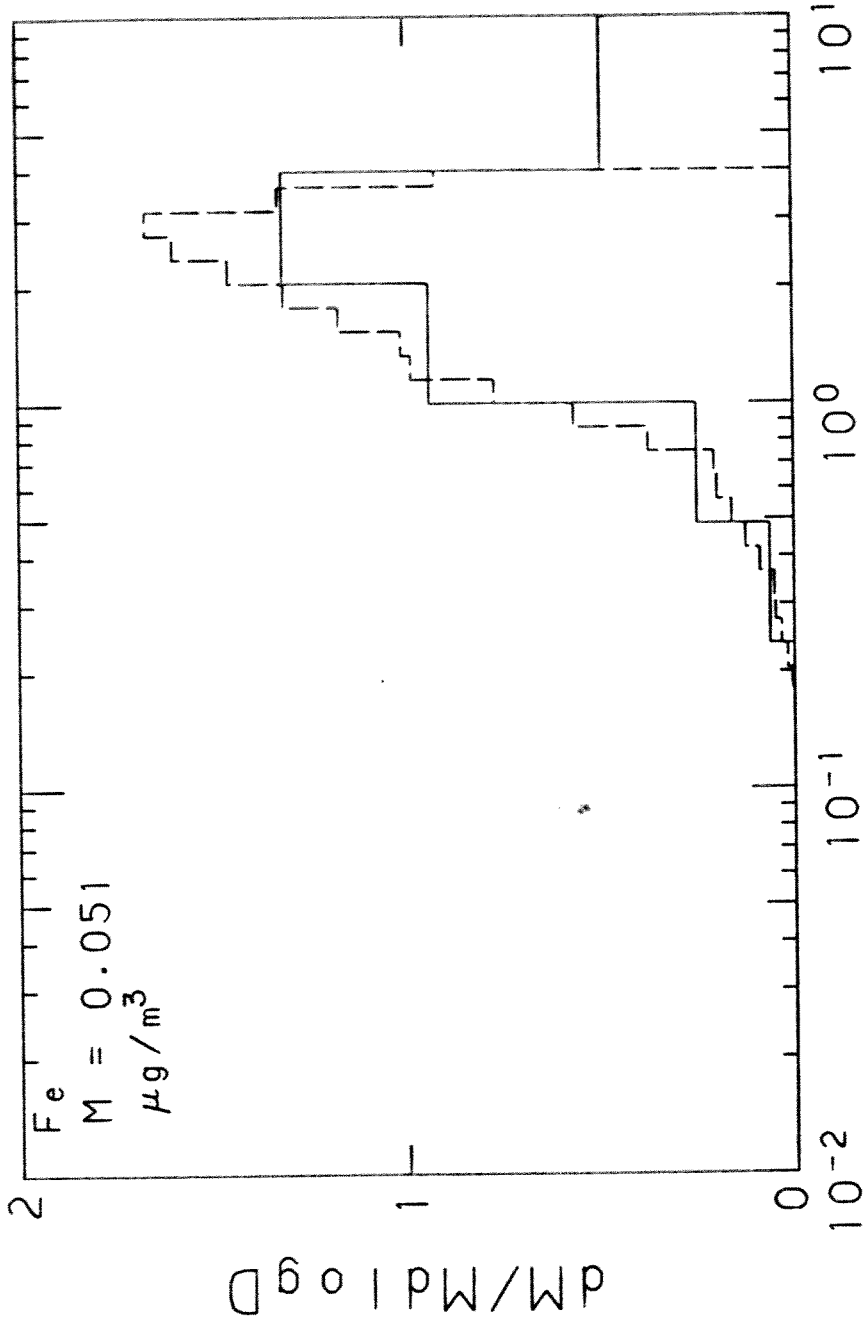

Figure 3.7f. Normalized iron mass distribution, Zilnez Mesa, Arizona, June 27 - July 13, 1979 average. Aerosol segregated by low pressure impactor (LPI) and analyzed by PIXE. The solid histogram is the mass distribution with respect to 50% aerodynamic cutoff diameter. The dashed histogram is the inverted distribution obtained from LPI calibration data and Twomey (1975) inversion algorithm.

shown. Although the cyclone separator was operated upstream of the LPI, its cutoff effect was not included in the inversion algorithm. The inverted mass distribution for particles greater than 2 μm is therefore less than what would have been measured without the cyclone upstream of the LPI. The number of iterations necessary to produce the inverted distribution to within the assumed measurement error, ± 2 ng per stage, ranged from 1 to 24. The value of M on each graph refers to the total average mass concentration of the element measured from the LPI samples. The distribution of each species is normalized with respect to the total mass concentration, M.

3.3.3.3 Sulfur measured by FVFPD -

The Twomey inversion algorithm was applied to the average sulfur mass measured by FVFPD on each stage of the LPI. The resultant distribution is plotted on Figure 3.7g. The solid histogram is the distribution with respect to 50% cutoff aerodynamic diameter, while the dashed histogram is the inverted distribution. The shape of the sulfur distribution obtained by FVFPD is quite similar to that obtained by PIXE except for particles less than 0.1 μm diameter. The discrepancy is probably due to bounceoff of particles from stages 5 and 6 of the LPI to stages 7 and 8 in the PIXE samples. The Apiezon L coating of 45-69 $\mu g/cm^2$ was not sufficient to eliminate bounceoff of the dry desert aerosol at the high jet velocities of the low pressure stages. This problem is discussed in detail in Appendix A.

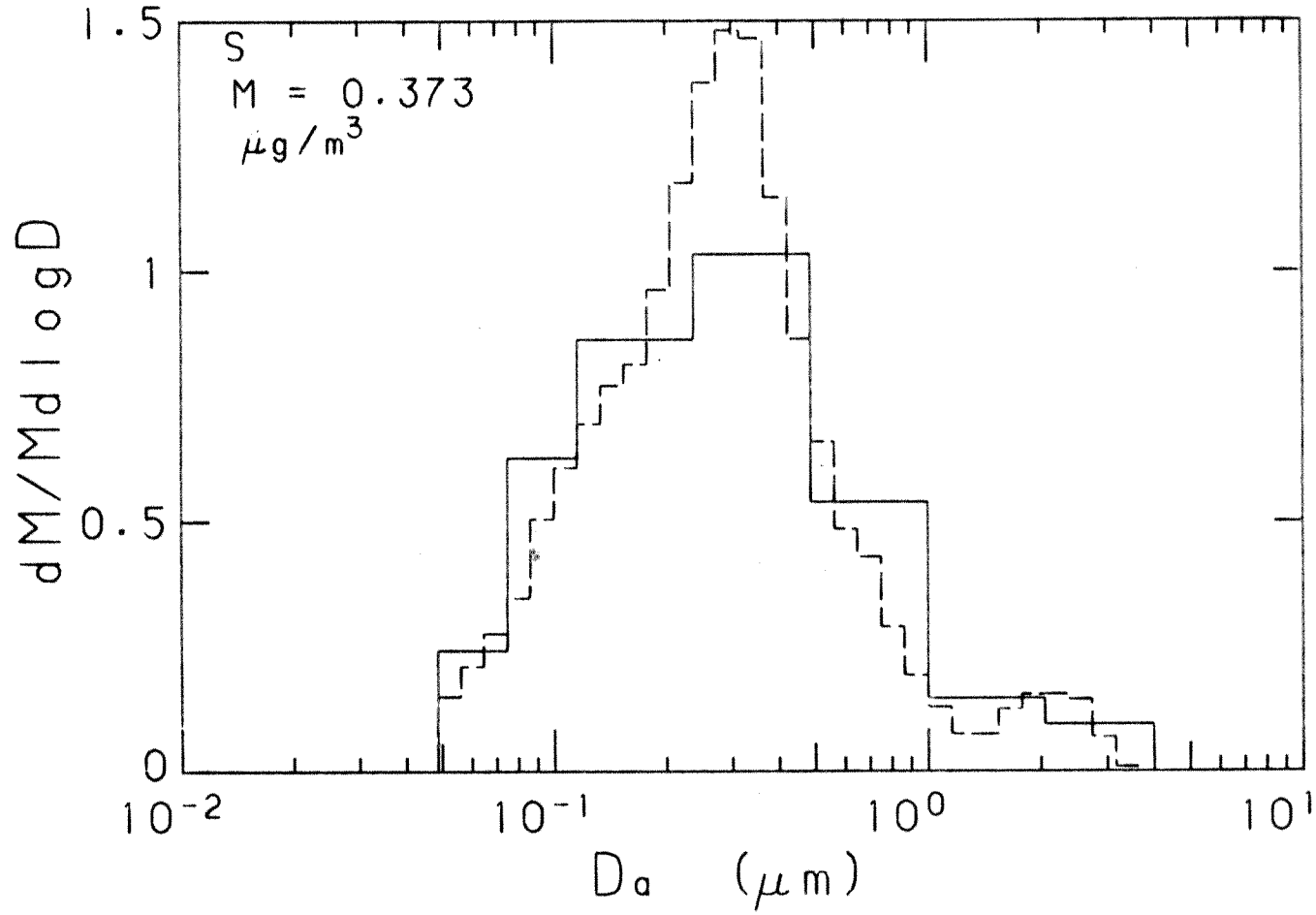

Figure 3.7g. Normalized sulfur mass distribution, Zilnez Mesa, Arizona, June 27 - July 13, 1979 average. Aerosol segregated by low pressure impactor (LPI) and analyzed by flash volatilization and flame photometric detection (FVFPD). The solid histogram is the mass distribution with respect to 50% aerodynamic cutoff diameter. The dashed histogram is the inverted distribution obtained from LPI calibration data and Twomey (1975) inversion algorithm.

The FVFPD technique is more sensitive than PIXE and is specific to sulfur. The vaseline coating produces a smaller blank, 1-2 ng S, than the Apiezon L coating. Because of the better sensitivity, lack of bounceoff, and better agreement with total sulfate concentration by ion chromatography, the FVFPD technique currently provides a more accurate sulfur distribution than that obtained by PIXE analysis.

On the basis of the sulfur distribution comparison between FVFPD and PIXE, vaseline was evaluated as a coating for the mylar substrate. The results are shown in Appendix A. The recommended coating for LPI-PIXE analysis is now 1.0 µl of 2% by weight vaseline in Spectrograde toluene, applied 0.5 µl at a time to the center of the impaction surface. This coating will prevent particle bounceoff and will produce low elemental blank values.

3.3.3.4 Soot distribution -

The soot mass distribution was inferred from the measured particle absorption coefficient distribution, described previously. The soot distribution as a function of diameter was averaged over eight episodes at Zilnez Mesa and is plotted in Figure 3.8. Comparing with Figure 3.4, it is seen that the b_{ap} peak occurs at 0.26-0.50 µm, while the inferred soot mass peak occurs at 0.50-1.0 µm. This is because the theoretical mass absorption efficiency of carbon spheres between 0.5 and 1.0 µm diameter is low, whereas an appreciable amount of absorption was still measured in this size range. This resulted in a higher inferred soot concentration at this size.

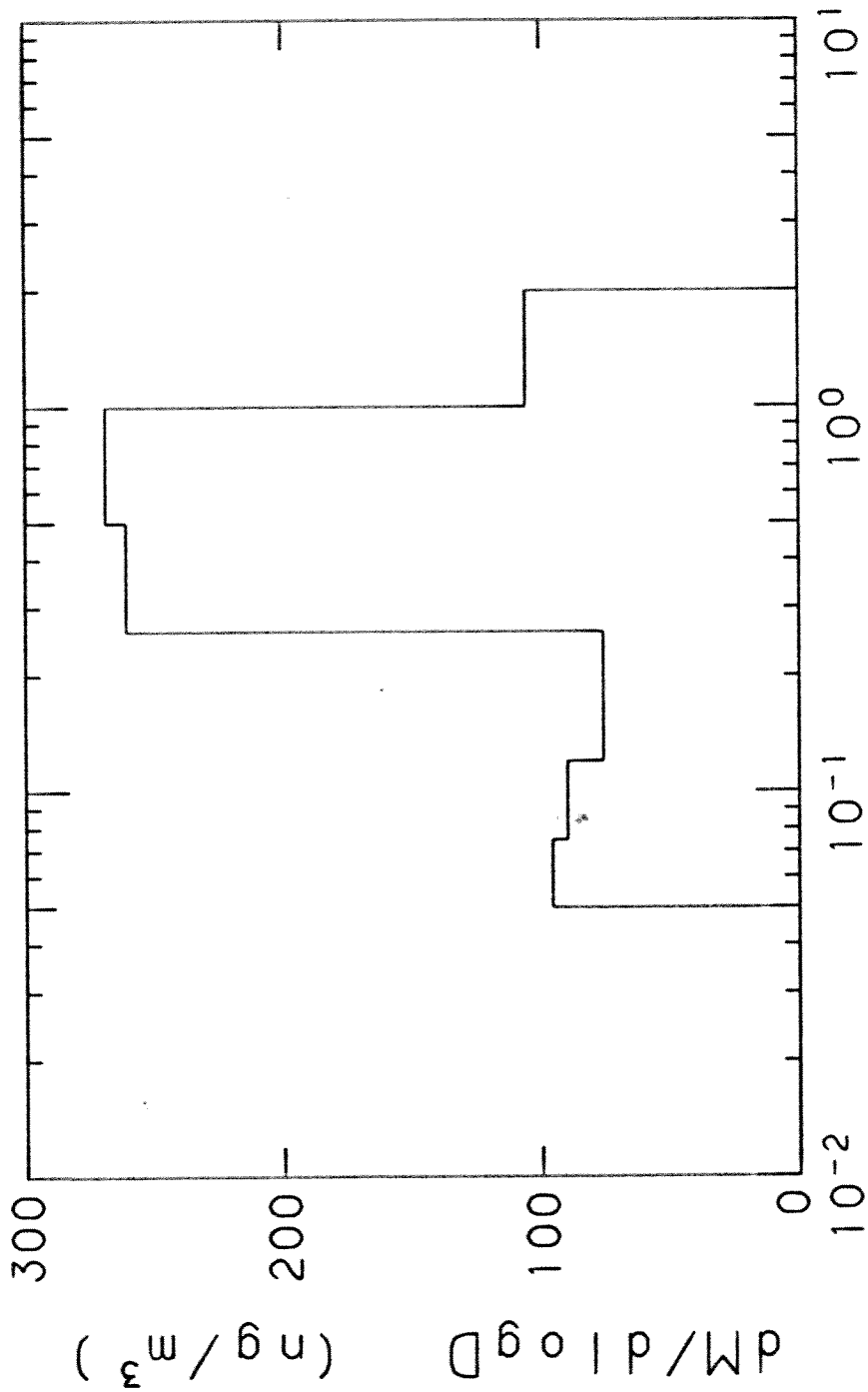

Figure 3.8. Soot mass distribution, Zilnez Mesa, Arizona, June 27 - July 13, 1979 average. Mass distribution inferred from measured particle absorption coefficient distribution assuming m = 1.96-0.66i, ρ=2.0 g/cm^3, and λ=0.63 μm.

The inferred soot distribution obtained at Zilnez Mesa was substantially different than that for Los Angeles, shown in Appendix B. Soot accumulated in particles of less than 0.2 μm diameter in Los Angeles, consistent with measured diesel soot distributions obtained by Kittleson and Dolan (1979) at the University of Minnesota. The different soot distribution at Zilnez Mesa may result from coagulation or from a different source, such as forest fires.

A summary of the elemental masses measured in each stage of the LPI is shown on Table 3.10. The error in each of the average values is about $\pm$ 2 ng, except for soot, which is estimated to be $\pm$ 10 ng.

3.3.3.5 Organic carbon -

Although organic aerosol was found to be the most important constituent of the fine aerosol on a mass basis, its distribution with respect to particle size could not be measured with the low pressure impactor. Both vaseline and Apiezon L are hydrocarbon greases. When applied as a coating to prevent particle bounceoff in the LPI stages, they produce a carbon blank of about 10 μg per stage. This is about 10 to 1000 times higher than the mass of organic aerosol which would be expected to impact on any stage. Until a non-hydrocarbon coating is found, organic aerosol mass distributions will not be feasible with the LPI.

In the absence of other data it was assumed that the organic aerosol followed the total distribution measured with the EAA and OPC. That is, the normalized distributions of each were assumed equal. This

Table 3.10

Elemental Mass Distributions, Zilnez Mesa,

June 27 - July 13, 1979, Average

	Mass per LPI stage, ng/m^3								
	Aerodynamic size interval, μm								
Element	.05-.075	.075-.12	.12-.26	.26-.50	.50-1.0	1.0-2.0	2.0-4.0	4.0$^+$	Total
Al	1.1	1.1	0.2	5.7	4.2	20	40	7.1	79
Si	5.5	5.0	2.9	0.5	11	73	115	50	263
S,PIXE	32	35	67	89	53	9.1	5	0	289
S,FVFPD	17	44	101	121	63	17	11	0	373
K	3.8	5.4	13	22	11	9.0	11	6.9	82
Ca	2.6	1.4	1.2	0.9	9.5	19	31	15	81
Fe	0	0.3	0.2	1.3	3.7	15	21	9.5	51
Zn	0.4	0.3	0.4	0.6	0.8	1.1	0.3	1.8	5.7
Pb	3.0	2.9	2.8	1.7	1.8	0.6	1.3	1.5	16
Soot	17	18	25	74	81	31	0	0	246

Distributions obtained with low pressure impactor.

was probably a fair assumption since organics were the most important constituent of the fine aerosol on a mass concentration basis. The organic aerosol mass distribution was then obtained by multiplying the normalized total distribution by the total non-soot mass concentration measured from Tissuequartz filter samples.

3.3.3.6 Nitrate aerosol -

Aerosol nitrate distributions were not measured. Aerosol nitrate distributions had been previously attempted using the LPI in 1978 at two other arid locations--China Lake, California, and near Farmington, New Mexico. In all cases the total nitrate concentrations measured with the LPI were a factor of 2-10 higher than those measured by ion chromatographic analysis of Teflon and polycarbonate filters sampling the same airstream. This may have been due to artifact nitrate being produced by condensation of nitric acid vapor in the cooler, low pressure stages of the LPI. Difficulties with standards and analysis may also have been responsible for the discrepancy.

It is apparent from simultaneous nitric acid and aerosol nitrate measurements in non-urban arid locations such as China Lake, Farmington, and Zilnez Mesa that virtually all airborne nitrate is usually in the form of gaseous nitric acid. Since aerosol nitrate quantities were small to nonexistent on the Nuclepore filter samples, the absence of size distribution information is not considered to be important for this study.

3.3.3.7 Balance of aerosol mass as a function of size -

The aerosol was characterized using instruments which operate on a number of physical principles. The EAA and OPC measured total aerosol size distributions based on principles of aerosol mobility in an electric field and aerosol light scattering. The LPI provided elemental aerosol mass distributions based on size segregation by inertial impaction. An aerosol species mass balance as a function of particle diameter was attempted using the measured quantities. It was assumed that the average particle density was 1.7 g/cm^3 for the submicron aerosol, primarily sulfates and organics, and 2.3 g/cm^3 for the coarse aerosol, primarily crustal species. The measured total aerosol volume distributions were transformed into mass distributions using these values. The elemental distributions as a function of 50% cutoff aerodynamic diameter were converted to species distributions as a function of Stokes diameter by assuming the elements were present in their oxidized forms and using the assumed particle densities. The LPI-determined distributions were than apportioned to the EAA and OPC size intervals on the basis of the 50% efficiency diameters of each instrument. Only the LPI size cuts were transformed by the density correction, since the particle density does not affect the particle mobility and optical measurements.

The results of the aerosol species size distribution balance applied to the average of the 12 samples are shown in Figure 3.9. The ammonium sulfate distribution obtained by LPI-FVFPD was used in this figure. The agreement is quite acceptable for submicron aerosol,

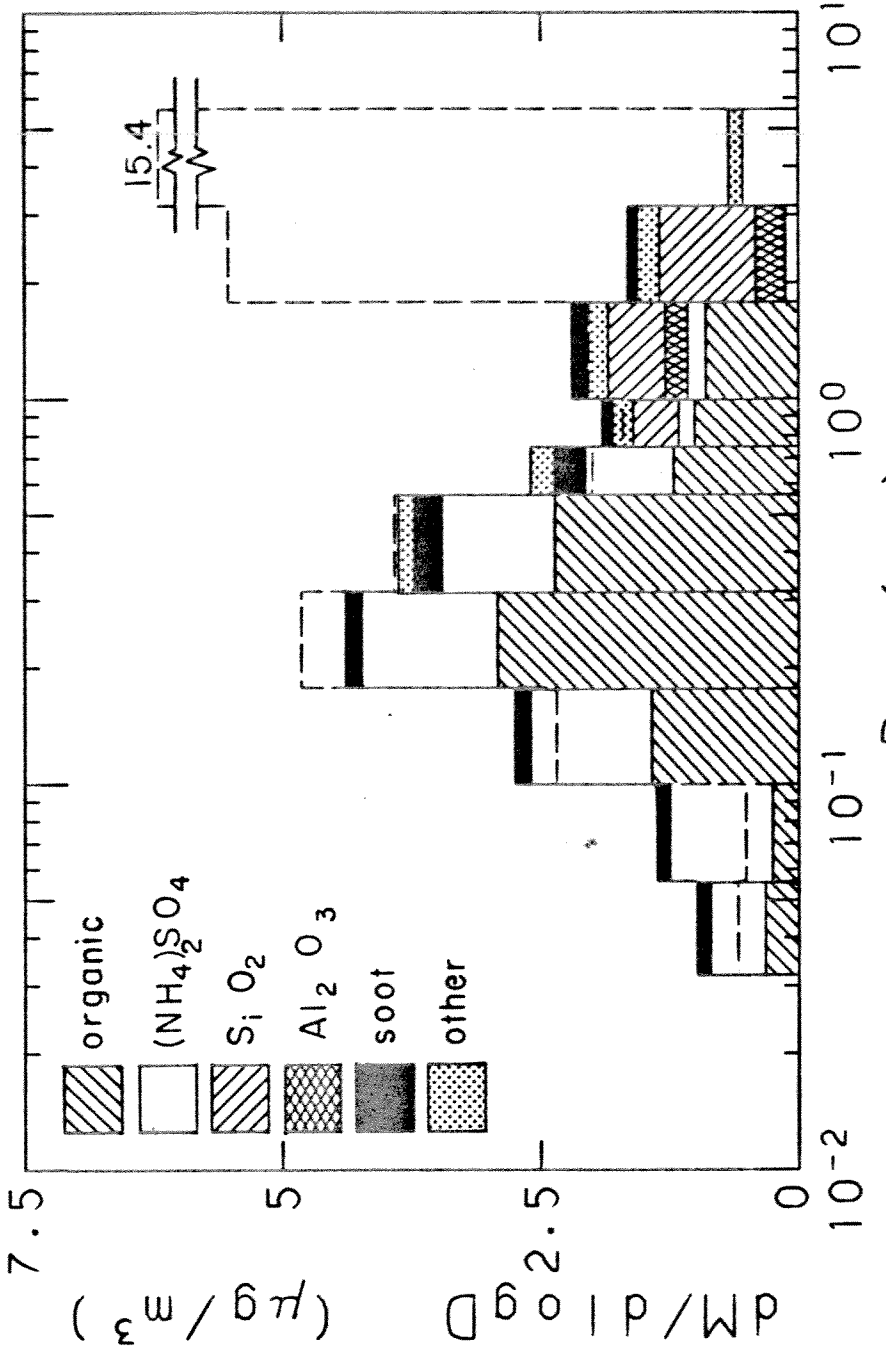

Figure 3.9. Aerosol mass distribution balance, Zilnez Mesa, Arizona, June 27 - July 13, 1979 average. The dashed histogram is the total mass distribution computed from measured aerosol volume distribution. A particle density of 1.7 g/cm^3 was assumed for particles less than 1.0 μm diameter; a density of 2.3 g/cm^3 was assumed for particles greater than 1.0 μm diameter.

particularly for the 0.1 to 1.0 μm "optically active" range. The huge discrepancy in the coarse aerosol distribution between the LPI and OPC measurements indicates that the cyclone successfully removed the coarse particles from the airstream before entering the LPI.

In summary, the mass balances indicate that the chemical analyses accounted for virtually all of the light scattering aerosol. The size resolved mass balance indicate that the species distributions obtained from the LPI were satisfactorily resolved for extinction coefficient calculations.

3.4 CHEMICAL SPECIES EXTINCTION BALANCE

The mass distribution of each chemical species was used to compute its scattering coefficient distribution and its contribution to the particle scattering coefficient, b_{spi}. The assumed refractive index and density for each species that were used in the calculations are listed in Table 3.11. The values for Al, K, Ca, and Fe are typical for aerosol of crustal origin (Sverdrup, 1977). Most other values were obtained from the Handbook of Physics and Chemistry, 45th Edition. The values for soot by Dalzell and Sarofim (1969) assume the soot to be in the form of a loose agglomerate and provide good agreement between measured soot mass concentrations and particle absorption coefficient. The refractive index for organic carbon was estimated based on values for common urban aerosol organics such as pentanedioic acid (Grosjean, 1977). The model aerosol refractive index was used to calculate the b_{sp} distribution, Figure 3.4, from the aerosol volume distribution

Table 3.11

Chemical Species Densities and Refractive Indices

Element	Assumed Chemical Species	Assumed Density, g/cm^3	Assumed Refractive index at λ=0.53 μm
Aℓ	$Aℓ_2O_3$	2.3	1.62
Si	SiO_2	2.3	1.55
S	$(NH_4)_2SO_4$	1.7	1.53
K	K	2.3	1.62
Ca	CaO	2.3	1.62
Fe	Fe_2O_3	2.3	1.62
C(soot)	C	1.0	1.56 - 0.47i
C(organic)	CH_xO_y	1.7	1.54
NO_3^-	NH_4NO_3	1.7	1.53
Model aerosol		1.7 (D< 1 μm)	1.54 - 0.015i
		2.3 (D> 1 μm)	

measured with the EAA and OPC. It is a volume averaged refractive index which accounts for the species found. The general theory allows for the volume averaged refractive index m_a to vary with particle size. Soot, by virtue of its imaginary refractive index, would have the greatest effect on the volume average. Since the inferred soot distribution at Zilnez Mesa was broad, the volume average refractive index of the submicron aerosol was assumed to not vary with particle size.

The contribution of a species to the scattering coefficient, b_{spi}, was calculated using the external mixture model, described earlier. b_{spi} was calculated from Equation 2.12 using the inverted mass distributions as a function of Stokes diameter. The single particle efficiency, K_s, and, hence, the mass scattering efficiency, were calculated numerically for each particle size using an iterative algorithm by Wickramasinghe (1973). Defining f_{ij} as the inverted mass distribution histogram of species i as a function of Stokes diameter, then the contribution of species i to the scattering coefficient is given by

$$b_{spi} = \sum_{j=1}^{N} \overline{E}_{sj}(m_i,\lambda)\ f_{ij}\ \Delta x_j$$

$\overline{E}_{sj}$ is the mass scattering efficiency averaged over particle size interval $[x_j,\ x_j + \Delta x_j]$. The scattering coefficient distribution due to species i is

$$\left(\frac{\Delta b_{spi}}{\Delta x}\right)_j = \overline{E}_{sj}\ f_{ij}$$

The calculated contribution of each aerosol chemical species to the scattering coefficient for each sampling episode at Zilnez Mesa is provided in Table 3.12. Carbonaceous and sulfate aerosols dominated light scattering by particles during the sampling period. Even in this remote location natural crustal species did not contribute substantially to visibility degradation. Agreement between the total calculated and measured b_{sp} is satisfactory. The average ratio of the calculated to measured particle scattering coefficient was 0.85 ± 0.34 for the 12 samples. The sulfate contribution to the total was obtained from the distribution measured by FVFPD.

The calculated scattering coefficient distributions for the major species averaged over the 12 samples are shown in Figures 3.10a-i. It is seen that particles between 0.2 and 1 μm diameter provided the most light scattering for all species.

The average mass scattering efficiency of ammonium sulfate was calculated to be 2.6 m^2/g. This was comparable to the value of 2.80 m^2/g calculated for the fine aerosol as a whole. It is apparent that at the arid Zilnez Mesa site the sulfate was not more efficient in scattering light and causing visibility degradation that the other major submicron aerosol species. These calculations assumed that the aerosol contained no water, a reasonable assumption at the very low relative humidities measured, usually less than 30% (Ho et al., 1974). The absence of high relative humidities suppresses the relative contribution of sulfate to light scattering in two ways. Gas phase

Table 3.12

Aerosol Chemical Species Contributions to the Extinction Coefficient,

Zilnez Mesa, 1979

Start Day	Organics	Contributions to particle scattering coefficient, $b_{sp}, 10^{-6}m^{-1}$									Soot Particle Absorption Coefficient $b_{ap}, 10^{-6}m^{-1}$
		Soot	$(NH_4)_2SO_4$ PIXE	$(NH_4)_2SO_4$ FVFPD	NH_4NO_3 (est.)	SiO_2	Al_2O_3 +CaO +Fe_2O_3	K	Total species	Total measured	
6/27	0.7	0.3	1.8	-	0.8	0.3	0.8	0.1	4.8	9.8	1.6
6/28	6.9	0.6	5.3	-	0.7	0.4	0.4	0.1	14.4	13	2.6
6/29	7.7	0.6	9.7	11.2	0	0.9	0.4	0.2	21.0	19	2.0
7/2	6.1	0.6	3.7	7.5	1.7	1.0	0.5	0.2	17.6	22	3.3
7/3	14.2	1.1	2.9	5.4	0	0.5	0.4	0.1	22.4	35	3.9
7/5	6.8	0.6	2.0	2.3	0.5	0.5	0.4	0.1	11.2	13	2.0
7/6	8.5	0.6	1.4	2.1	0.2	0.4	0.7	0.1	12.6	22	2.2
7/7	7.7	0.6	2.3	1.1	0	0.6	0.8	0.2	11.0	16	1.9
7/8	7.7	0.3	2.2	2.3	0.6	0.5	0.5	0.1	12.0	8.7	1.4
7/9	1.6	0.3	1.5	0.7	0.6	0.4	0.3	0.1	4.0	7.1	0.4
7/10	2.3	0.3	1.6	1.4	0	0.5	0.4	0.1	5.0	5.8	0.8
7/11	9.3	0.9	1.6	-	0	1.1	0.6	0.1	13.6	9.0	0.9
Average	6.6	0.6	3.0	3.8	0.4	0.6	0.5	0.1	12.4	15.0	1.9

Values computed from measured species mass distributions

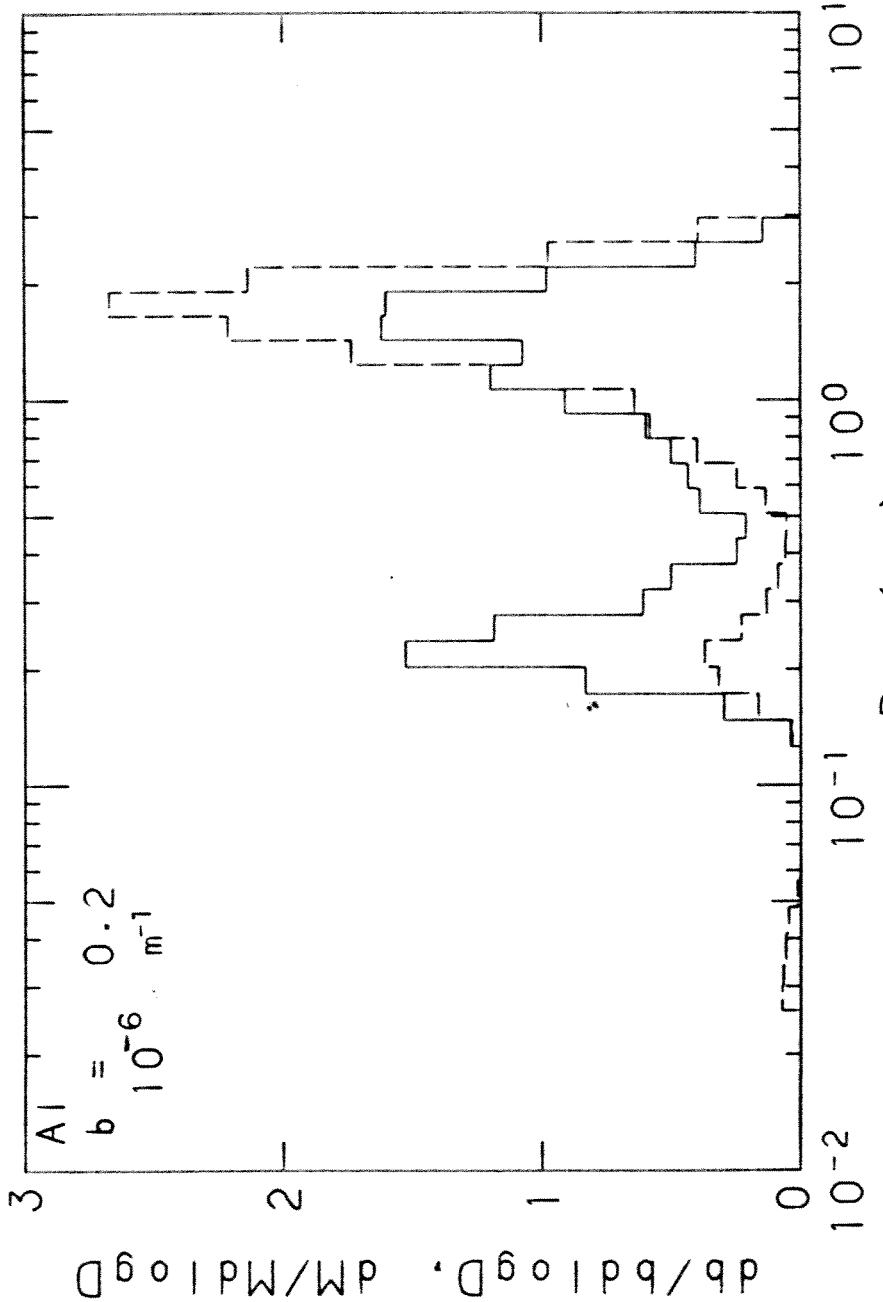

Figure 3.10a. Normalized aluminum oxide mass and scattering coefficient distributions, Zilnez Mesa, Arizona, June 27 - July 13, 1979 average. Dashed histogram is inverted distribution from Figure 3.7a with Stokes diameter correction assuming a density of 2.3 g/cm^3. Solid histogram is the scattering coefficient distribution calculated from the inverted distribution.

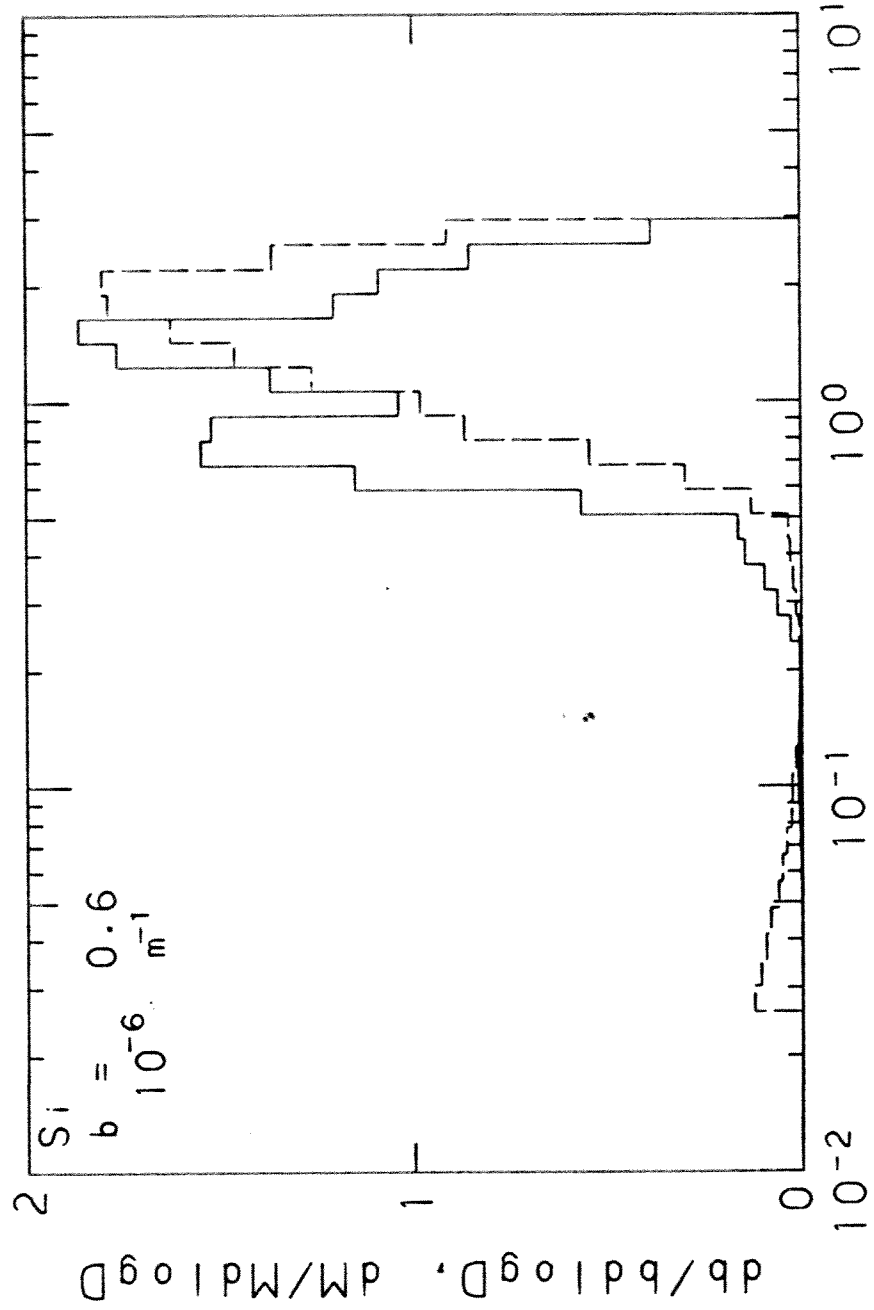

Figure 3.10b. Normalized silicon dioxide mass and scattering coefficient distributions, Zilnez Mesa, Arizona, June 27 - July 13, 1979 average. Dashed histogram is inverted distribution from Figure 3.7b with Stokes diameter correction assuming a density of 2.3 g/cm^3. Solid histogram is the scattering coefficient distribution calculated from the inverted distribution.

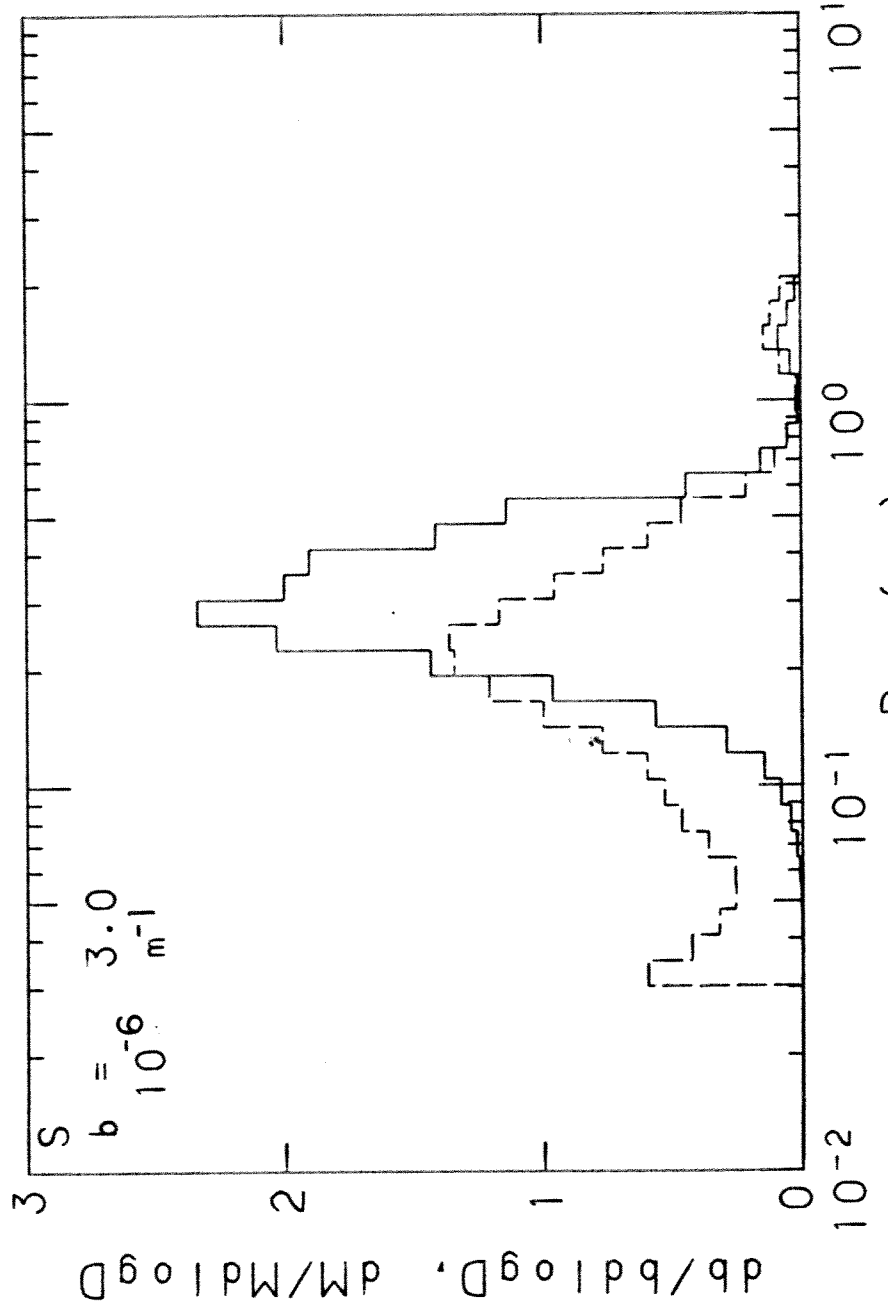

Figure 3.10c. Normalized ammonium sulfate mass and scattering coefficient distributions, Zilnez Mesa, Arizona, June 27 - July 13, 1979 average. Dashed histogram is inverted distribution from Figure 3.7c with Stokes diameter correction assuming a density of 1.7 g/cm^3. Solid histogram is the scattering coefficient distribution calculated from the inverted distribution. Sulfur analysis by PIXE.

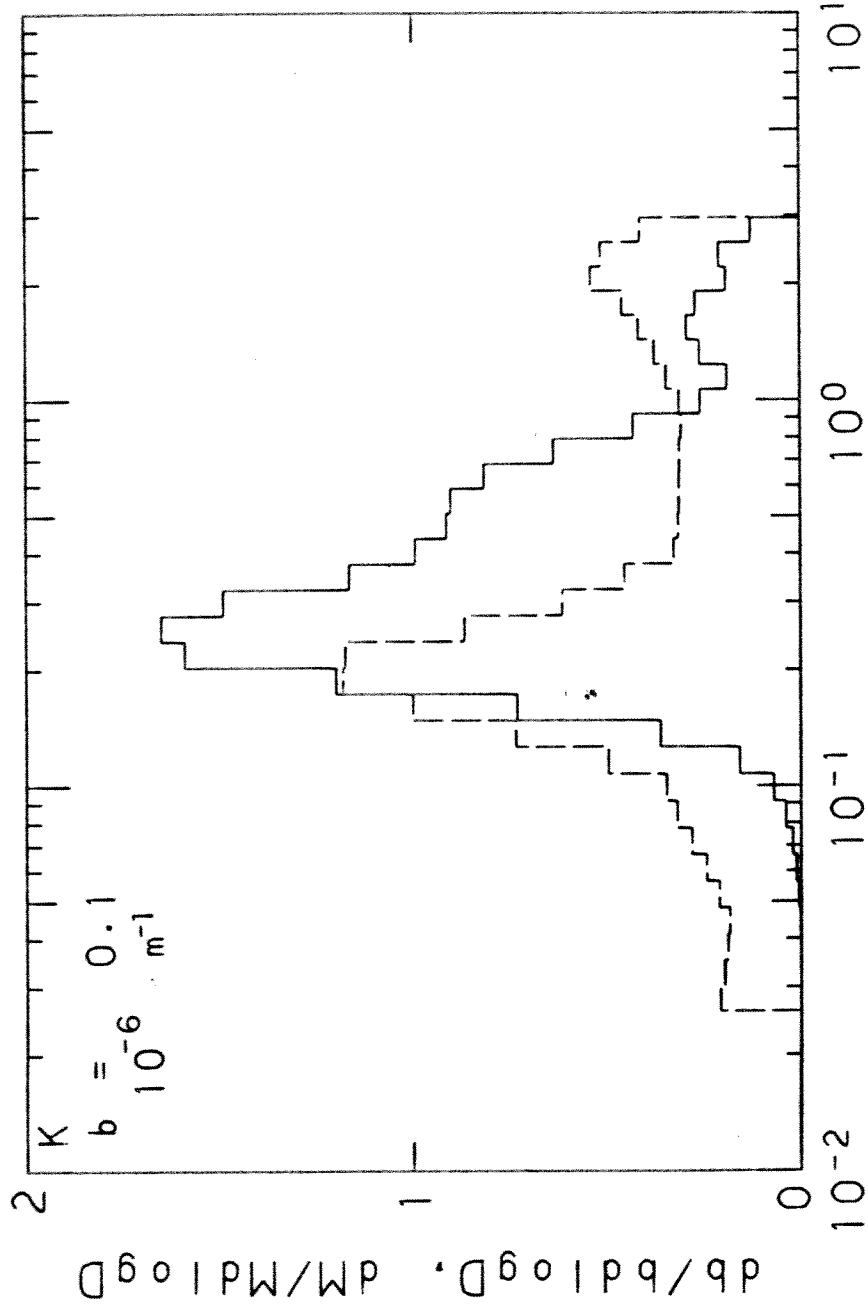

Figure 3.10d. Normalized potassium mass and scattering coefficient distributions, Zilnez Mesa, Arizona, June 27 - July 13, 1979 average. Dashed histogram is inverted distribution from Figure 3.7d with Stokes diameter correction assuming a density of 2.3 g/cm^3. Solid histogram is the scattering coefficient distribution calculated from the inverted distribution.

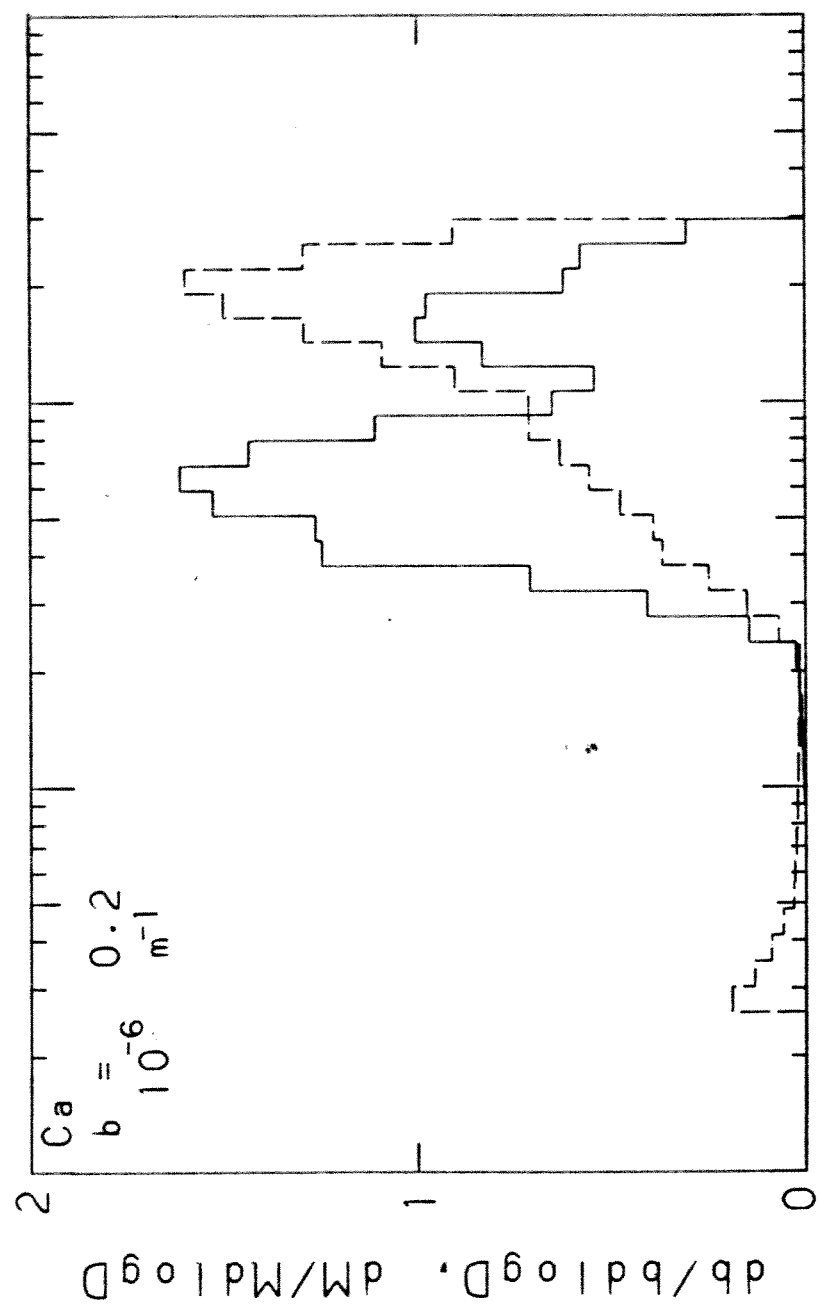

Figure 3.10e. Normalized calcium oxide mass and scattering coefficient distributions, Zilnez Mesa, Arizona, June 27 - July 13, 1979 average. Dashed histogram is inverted distribution from Figure 3.7e with Stokes diameter correction assuming a density of 2.3 g/cm^3. Solid histogram is the scattering coefficient distribution calculated from the inverted distribution.

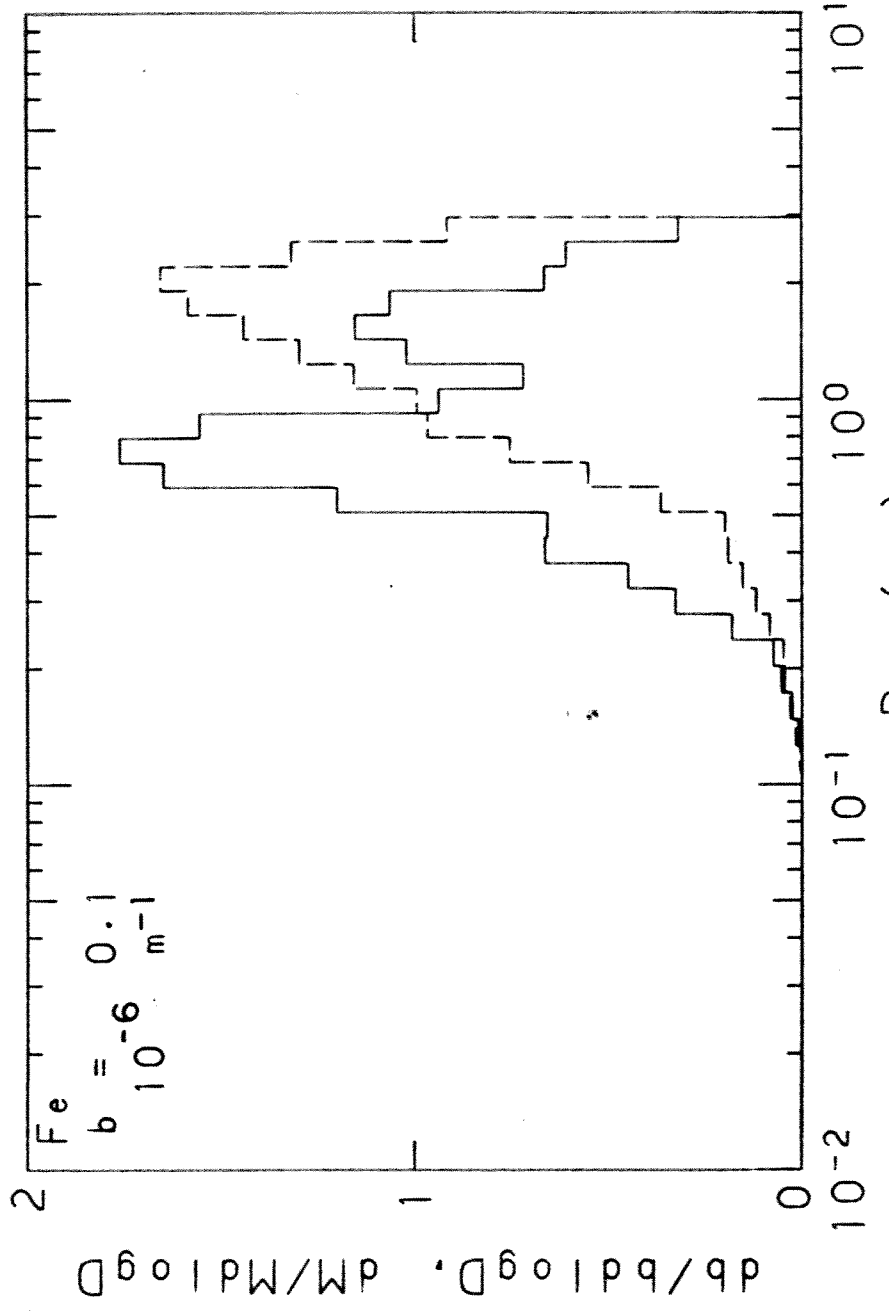

Figure 3.10f. Normalized iron oxide mass and scattering coefficient distributions, Zilnez Mesa, Arizona, June 27 - July 13, 1979 average. Dashed histogram is inverted distribution from Figure 3.7f with Stokes diameter correction assuming a density of 2.3 g/cm^3. Solid histogram is the scattering coefficient distribution calculated from the inverted distribution.

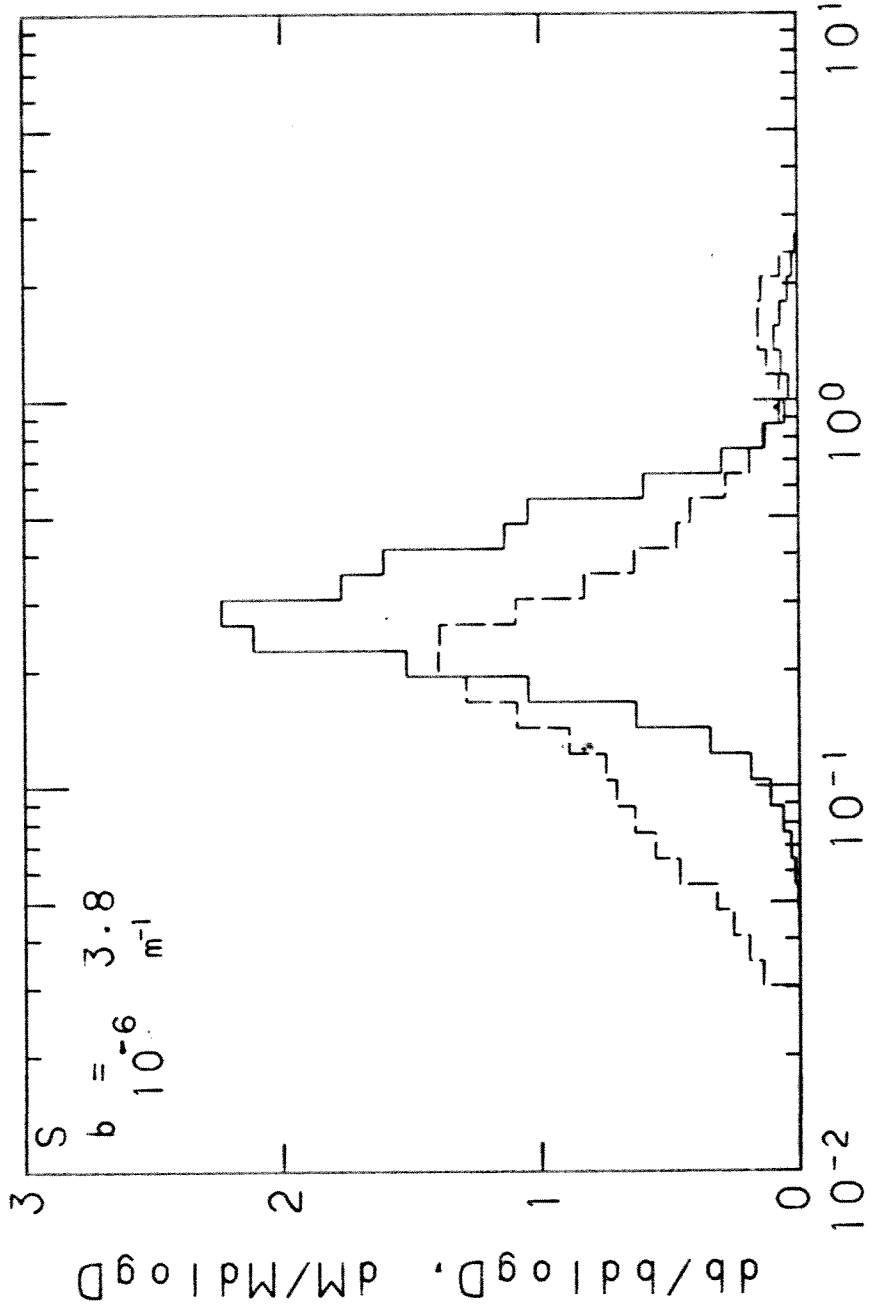

Figure 3.10g. Normalized ammonium sulfate mass and scattering coefficient distributions, Zilnez Mesa, Arizona, June 27 - July 13, 1979 average. Dashed histogram is inverted distribution from Figure 3.7g with Stokes diameter correction assuming a density of 1.7 g/cm^3. Solid histogram is the scattering coefficient distribution calculated from the inverted distribution.

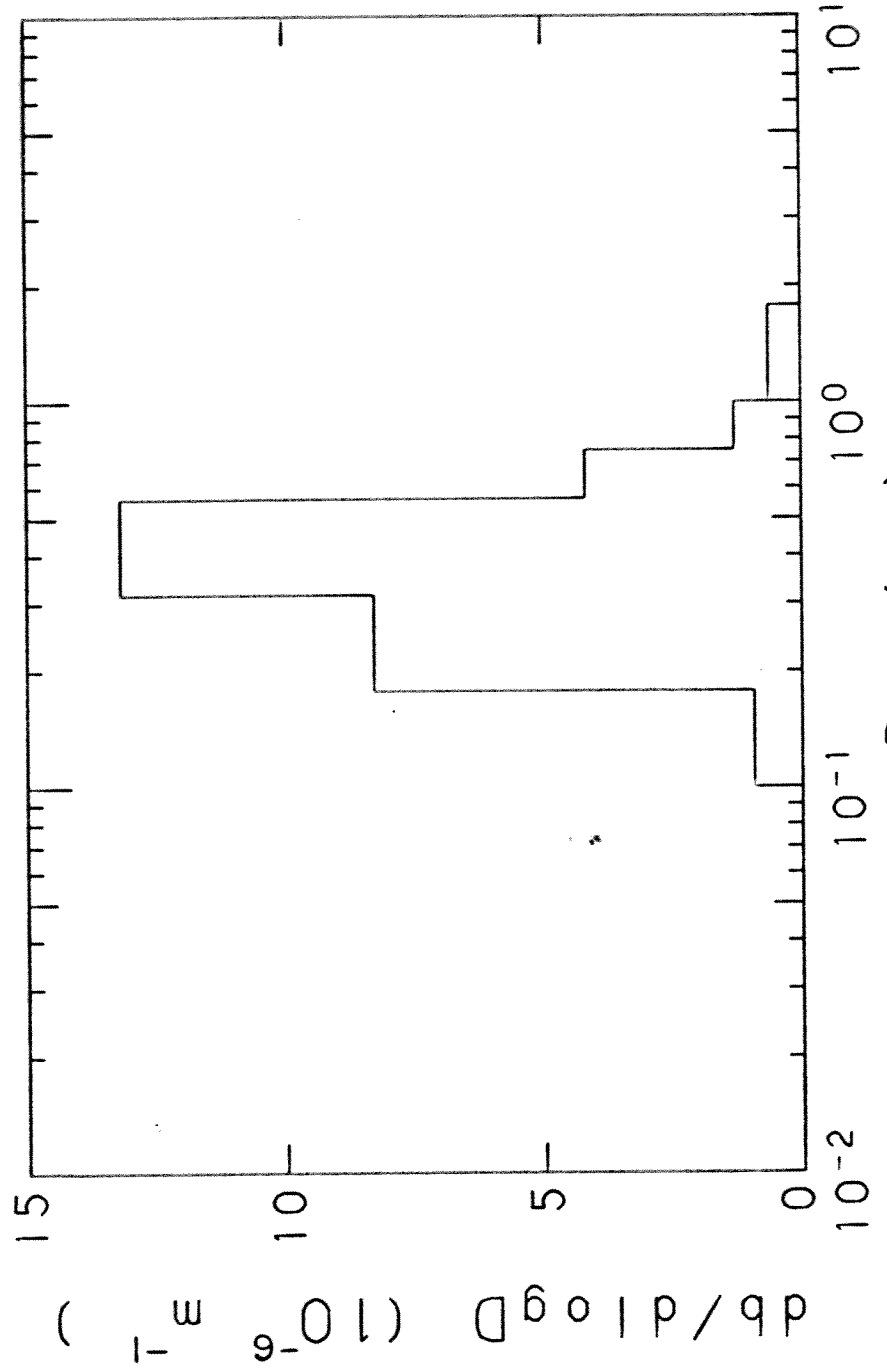

Figure 3.10h. Organic aerosol scattering coefficient distribution, Zilnez Mesa, Arizona, June 27-July 13, 1979 average. Distribution calculated from assumed mass distribution.

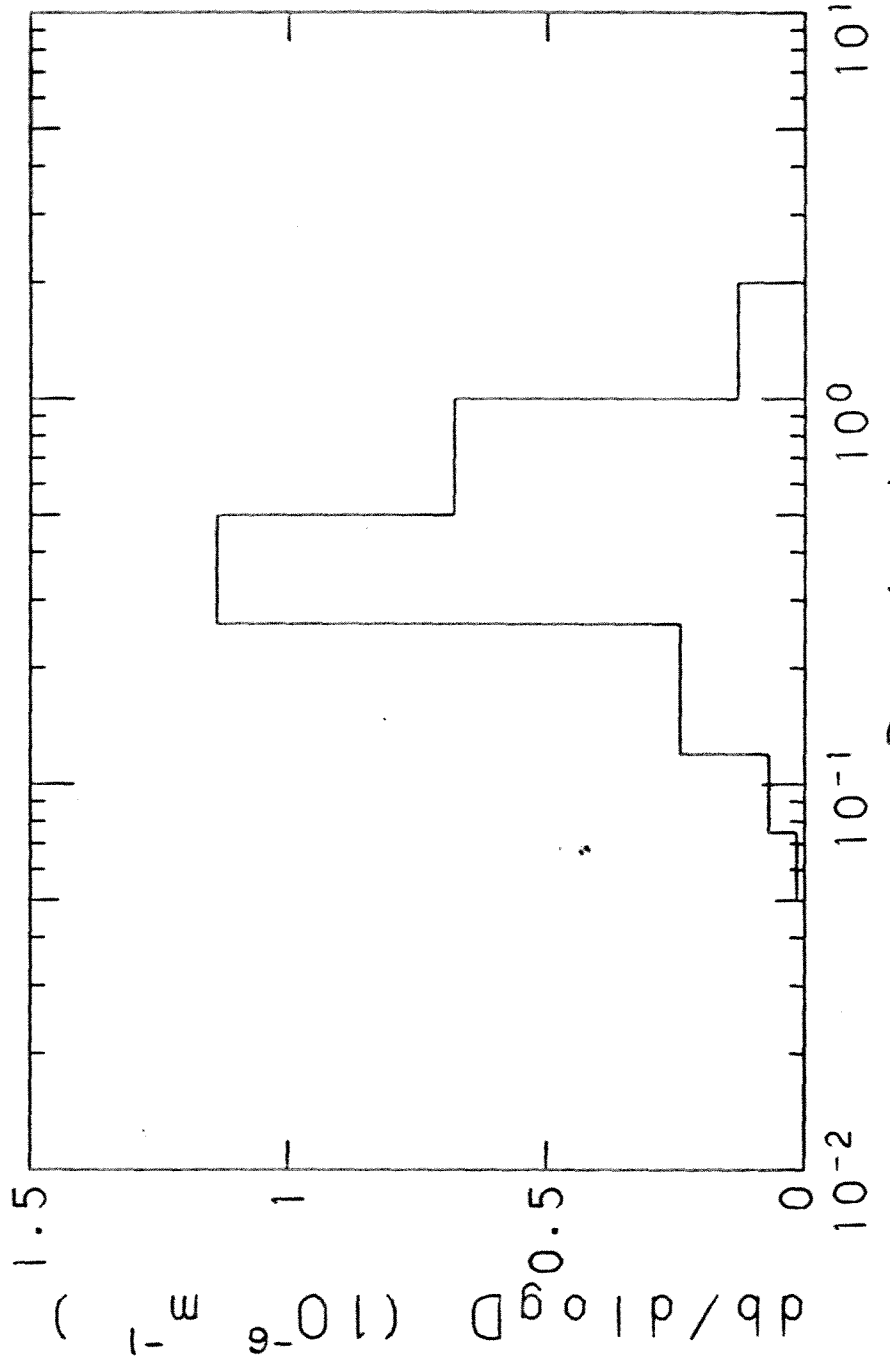

Figure 3.10i. Soot scattering coefficient distribution, Zilnez Mesa, Arizona, June 27-July 13, 1979 average. Distribution calculated from inferred soot mass distribution, Figure 3.8.

homogeneous oxidation of SO_2 is likely the major aerosol sulfate production mechanism, leading to the accumulation of mass in 0.1 to 0.3 μm diameter. These diameters are below the optimal size for light scattering, which, according to Figure 2.1, is 0.4 to 0.5 μm for a wavelength of 0.53 μm and refractive index of 1.54. Secondly, the absence of water prevents the hygroscopic sulfate from growing into a more efficient light scattering size.

A summary of the fine aerosol balances on mass and extinction coefficient averaged over the 12 samples is shown in Figures 3.11a-b. It is seen that the fine aerosol species contributed to the particle scattering coefficient in roughly the same proportion that they contributed to fine aerosol mass concentration. It should be remembered that the mass balance was obtained from filter measurements, while the extinction coefficient budget was generated from mass distribution measurements.

In examining Figures 3.11a-b, the optical effects of soot are the most striking. Soot contributed an average of only about 4% to the fine mass concentration and 1.5% to the average total aerosol mass concentration of 14 $\mu g/m^3$, measured by the University of California, Davis. However, soot contributed an average of 15% to light extinction. This is primarily due to soot's high mass absorption efficiency.

The average values shown in Figures 3.11a-b may not be representative of the Zilnez Mesa location due to the forest fire influence during the first week of July. Other sampling episodes were probably

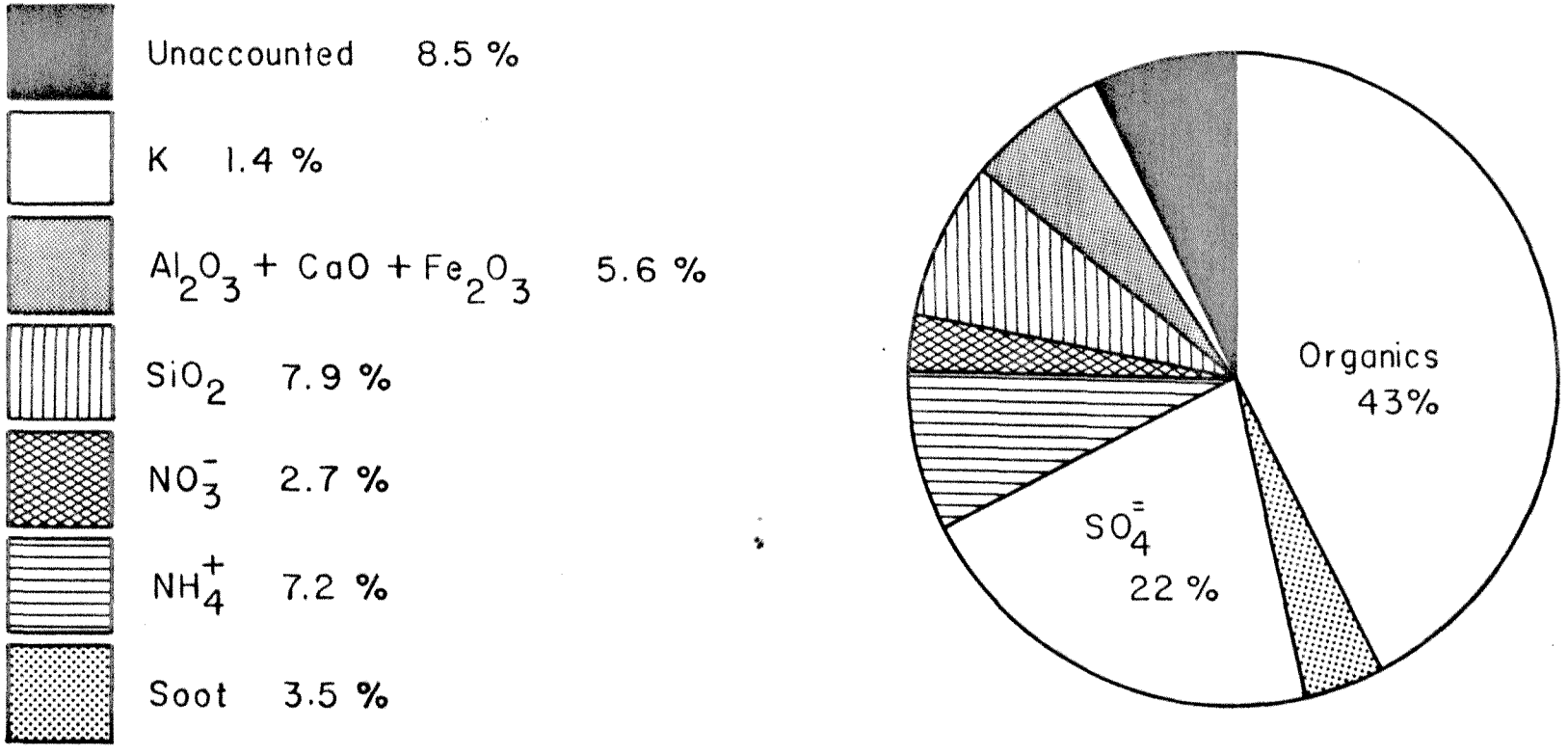

Figure 3.11a. Chemical species contributions to the fine aerosol mass concentration, Zilnez Mesa, Arizona. 13 sample average, June 26 - July 13, 1979. Values determined by chemical analysis of filter samples. Average total fine aerosol mass concentration, determined gravimetrically, was 5.2 $\mu g/m^3$.

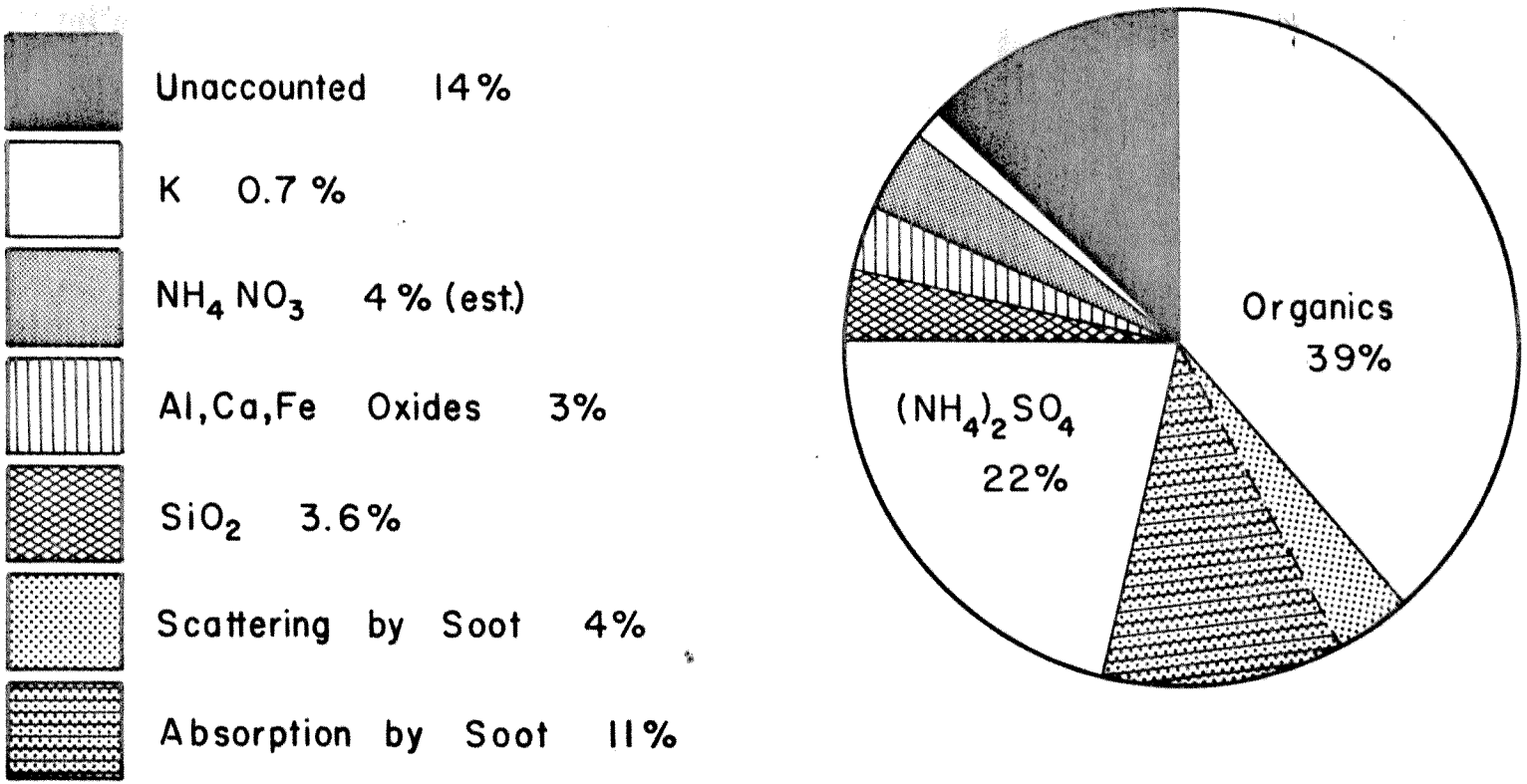

Figure 3.11b. Chemical species contributions to the fine particle extinction coefficient, Zilnez Mesa, Arizona. 12 sample average, June 27 - July 13, 1979. Contributions determined by numerically integrating theoretical mass extinction efficiencies with measured species mass distributions. Contributions to the fine particle scattering coefficient, b_{sp}, unless otherwise noted. Average b_{sp} measured by nephelometer was 15.0×10^{-6} m^{-1}. Average particle absorption coefficient, b_{ap}, measured from light absorption by Nuclepore filter sample was 1.9×10^{-6} m^{-1}. Average measured fine particle extinction coefficient was 16.9×10^{-6} m^{-1}.

more typical. It appears that the June 29 sample was more typical of a regional haze episode, while the July 10 sample was representative of clean background. The mass and extinction coefficient balances for these episodes are shown in Tables 3.5 and 3.12. It is clear that carbonaceous aerosol remained relatively important in causing visibility degradation at Zilnez Mesa during these episodes but that the contribution of sulfate was greater during the regional haze episode.

3.5 SUMMARY AND CONCLUSIONS

Aerosol mass distribution measurements with the calibrated low pressure impactor were used to estimate an aerosol species extinction budget for Zilnez Mesa, Arizona. Twelve episodes from June 27 to July 13, 1979, were sampled. Theoretical mass extinction efficiencies were calculated and numerically integrated with measured mass distributions to determine the contribution of each species to the extinction coefficient. Species mass and extinction balances were checked by other direct measurements.

It was found that the particle extinction coefficient at Zilnez Mesa was dominated by contributions from carbonaceous and sulfate aerosols. The fine aerosol species contributed to the particle scattering coefficient in approximately the same proportion they contributed to fine aerosol mass concentration. Silicon dioxide did not contribute significantly to light extinction, contrary to earlier findings by Macias et al. (1979).

The measured chemical species could account for 94 ± 19% of the fine aerosol mass concentration and 85 ± 34% of the measured particle extinction coefficient. All important species balances were met, both in total and with respect to size. The satisfactory agreement between the calculated and measured extinction coefficient indicates that the technique is useful for determining the contributions of various aerosol species to visibility degradation at a site.

The results of this work indicate that it may be possible to estimate species contributions to light scattering by particles in arid locations by measuring mass concentrations from filter samples. If only fine aerosol is sampled and if all the chemical species can be accounted for, the major fine aerosol species may contribute to light scattering in approximately the same proportion as to mass concentration. The contribution of soot to light extinction will be enhanced by its efficient absorption of light.

Important parameters which were not measured in this study include direct measurements of the organic aerosol size distribution and the particle scattering coefficient distribution. Organic aerosol mass distributions could not be determined using current LPI substrate anti-bounce coatings. Calculations using the measured mass and volume distributions indicate the importance of particles between 0.2 and 0.7 μm diameter in scattering light of wavelength 0.53 μm. The LPI could be used with a vacuum tight nephelometer to measure the scattering coefficient distribution directly in this range. This would provide another test of the technique that was used in this chapter.

It was assumed in this experiment that the aerosol contained no water. The application of the species extinction coefficient balance to humid locations would need to account for the presence of water in the aerosol.

CHAPTER 4

CHEMICAL SPECIES CONTRIBUTIONS TO LIGHT SCATTERING BY AEROSOLS AT A REMOTE ARID SITE: COMPARISON OF STATISTICAL AND THEORETICAL RESULTS

4.1 INTRODUCTION

It was shown in Chapter 2 that it is generally necessary to determine the diameter, refractive index, and chemical composition of each aerosol particle to rigorously calculate the contribution of each chemical species to the extinction coefficient. If the particles are spherical and if particle volume is conserved then the species mass distributions are sufficient to calculate each species contribution exactly if the aerosol is either an external, internal, or specific mixture. For the specific mixture a volume average refractive index is assumed. In Chapter 3 aerosol species mass distributions measured at Zilnez Mesa were successfully used to calculate the contribution of each species to the extinction coefficient. At most air monitoring stations, however, only the aerosol mass concentration of each species, M_i, is measured from filter samples. This raises three questions: Can statistical techniques be used to infer chemical species contributions to the extinction coefficient using data obtained from filter samples? Can we place any confidence limits on the quality of the statistical results? And, lastly, can an improved sampling technique be used to enhance the quality of the statistical results?

In Chapter 2 it was shown that if certain conditions are met, the particle light extinction coefficient, b_{ep}, at a given location can be represented as a linear combination of the total mass concentration, M_i, of each species i:

$$b_{ep} = \sum_{i=1}^{N} \alpha_i M_i \qquad (4.1)$$

For Equation 4.1 to be rigorously true for a external mixture (N pure species which mix without coagulation), the normalized distribution of each species must not vary with its total mass concentration. For an aerosol in which the chemical composition of the particles is distributed continuously in each particle size range, Equation 4.1 will apply to a specific mixture if the following conditions are met:

a) The normalized mass distribution of each species must be preserved

b) The normalized total aerosol volume distribution must be preserved.

c) Each of the species must have equal refractive indices.

d) The partial molar volume of each species must remain constant with the addition or removal of other species. That is, particle volume must be conserved with coagulation and condensation. Aqueous solutions would not be permitted.

Requirement (c) will not be met for soot due to its refractive index. In Chapter 3 and in Appendix B it was found that soot contributes to light extinction principally by absorption. Therefore, for a complex aerosol one might expect to find a satisfactory linear relationship only between the scattering due to particles, b_{sp}, and mass concentrations:

$$b_{sp} = \sum_{i=1}^{N} \alpha_{is} M_i$$

To test the applicability of statistical techniques to determine the species contributions to the extinction coefficient, a one-year study was conducted in 1979 at China Lake, California. Aerosol of aerodynamic diameter less than 2 μm was collected on filters and analyzed for total fine mass, all major chemical species, and the particle absorption coefficient, b_{ap}. At the same time and location, b_{sp} was measured with a sensitive nephelometer. A total of 61 samples were analyzed. Multiple regression analysis was applied to the average particle scattering coefficient and mass concentrations for each filter sample to estimate α_i and its average contribution to light scattering, b_{spi}. Supplementary measurements of the chemical-size distribution with the LPI were used to theoretically determine each b_{spi} and were used as a test of the effectiveness of the statistical approach.

4.2 EXPERIMENTAL TECHNIQUE

4.2.1 Location

For this study aerosol sampling was routinely conducted from February through December, 1979, at China Lake, California. Shown in Figure 4.1, the sampling site is located in the Mohave Desert within the U.S. Naval Weapons Center (NWC), a missile research and testing facility. The site is about 200 km northeast of Los Angeles in extreme northeastern Kern County. It is 100 feet from a paved access road which averages about 30 vehicles per day.

The sampling site is at an elevation of 670 m above mean sea level. Table 4.1 summarizes the meteorology at China Lake. It is characterized by abundant sunlight, low relative humdity, and hot daytime summer temperatures.

The site was chosen because it is an arid site with no significant local sources of air pollution (Ouimette, 1974) and because the particle scattering coefficient has been continuously measured since 1976. NWC helped support this study by providing manpower and funds for chemical analysis. Measurements of the particle size distribution have been made daily since 1978, providing the data base necessary to assess the preservation of the normalized aerosol volume distribution.

4.2.2 Aerosol Measurement and Sample Collection

Aerosol was sampled in an air conditioned monitoring trailer operated by NWC. The particle scattering coefficient, b_{sp}, was continuously measured with an MRI Model 1561 integrating nephelometer which had been modified by Dr. Alan Waggoner of the University of Washington. The nephelometer automatically zeroed daily and was calibrated

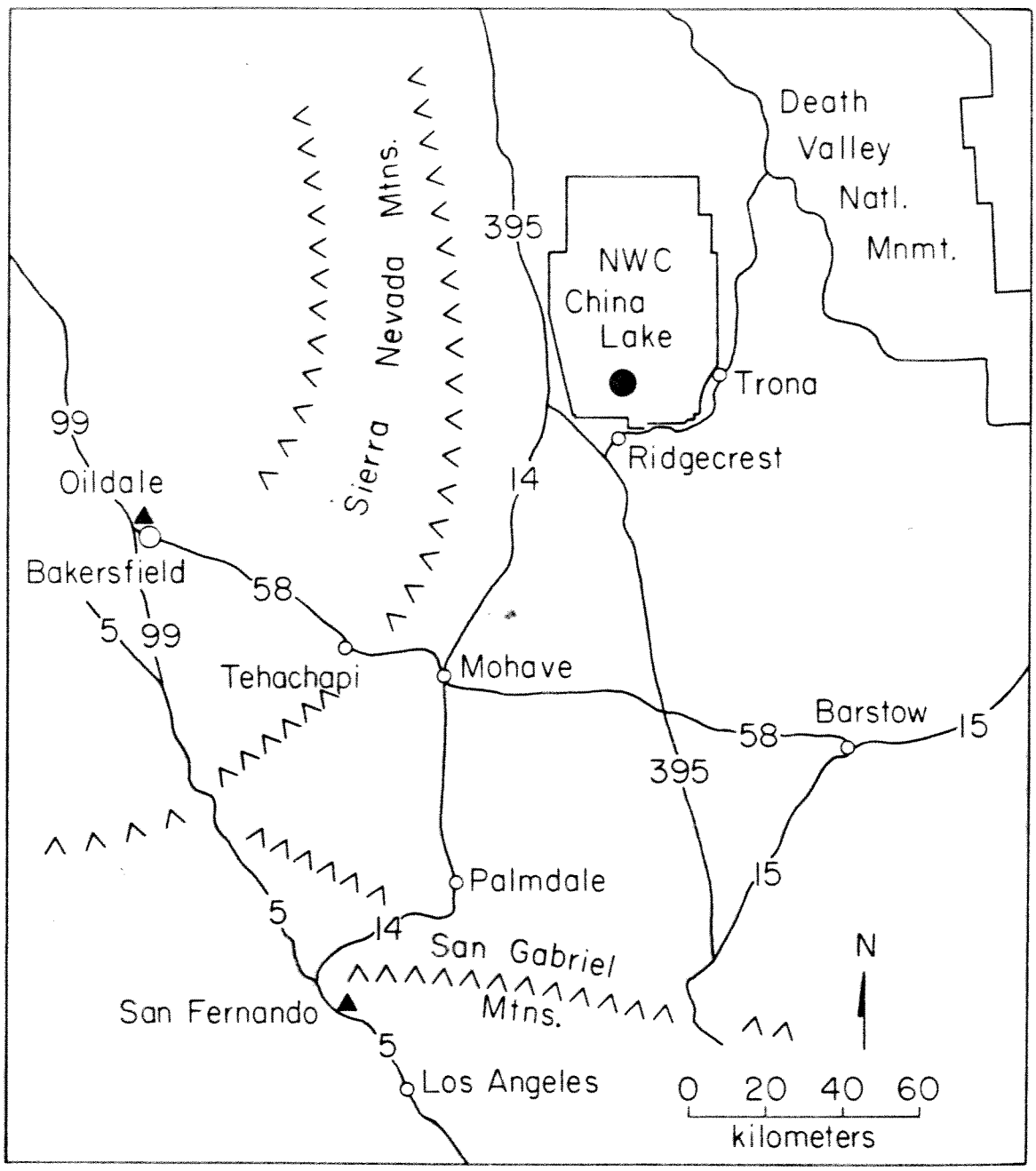

Figure 4.1. Location of sampling site within the Naval Weapons Center (NWC), China Lake, California. Site is located in Indian Wells Valley about 6 miles north of Ridgecrest, population (1979 estimate) 16,000. Highway numbers designated on map.

Table 4.1

Meteorology, China Lake, 1946-1973 Average

Month	Station Pressure, mm Hg	Mean max. Temp., °C	Mean min. Temp., °C	Mean Temp., °C	Mean Relative Humidity %	Average Precipitation cm	Prevailing Wind Direction	Average Hourly Speed, m/sec	Average Cloudiness %[a]
Jan	704.9	13.9	-1.7	6.1	52	1.12	SW	2.5	37
Feb	703.7	17.7	1.3	9.4	47	1.19	SW	3.1	34
Mar	701.7	20.6	4.3	12.4	39	0.53	SW	4.1	34
Apr	700.6	25.1	8.3	16.8	34	0.38	SW	4.4	31
May	699.4	29.9	12.9	21.4	29	0.08	SW	4.4	27
June	698.6	35.1	17.3	26.3	24	0.05	SW	4.1	15
Jul	699.8	29.0	21.1	30.1	23	0.30	SW	3.9	16
Aug	700.1	38.1	10.1	29.1	24	0.25	SSW	3.8	14
Sep	700.1	34.4	15.7	25.1	26	0.53	SSW	3.3	13
Oct	701.2	27.8	9.4	18.6	31	0.23	SW	3.1	21
Nov	704.2	19.9	2.9	11.3	42	1.27	SSW	2.5	26
Dec	704.9	14.7	-1.4	6.5	52	1.09	SW	2.4	34
Total	...	...	...	...	...	7.04	...	...	...
Avg.	...	26.3	9.2	17.8	35	...	SW	3.4	25

[a]Cloudiness 1946 through 1964

quarterly. The estimated error in measurement was $\pm$ 2.5 x 10^{-6} m^{-1} over the range 0-250 x 10^{-6} m^{-1}.

The number distribution of particles having diameters from 0.03-10 um was measured twice daily on most weekdays with a Thermo Systems Whitby Aerosol Analyzer (WAA) (Whitby et al., 1972) and a Royco Model 202 Optical Particle Counter (OPC). The WAA is an earlier version of the Electrical Aerosol Analyzer (EAA), and operates on the same principle of particle electrical mobility. These measurements were performed by Dr. Larry Mathews of the NWC Research Department at a site three miles southeast of the air monitoring trailer (Mathews and Cronin, 1980). The WAA time current product $n_i t$ had been adjusted by the manufacturer to be 10^7 ion-sec/cm^3. The constants of Whitby and Cantrell (1979) were used to convert current changes in the WAA to particle number concentrations. The aerosol distributions obtained with the WAA from 0.06 to 0.30 um compared favorably with those measured by a Thermo Systems Model 3030 Electrical Aerosol Analyzer on September 7, 1979. The OPC was used to measure particle size distributions from 0.3 to 10 μm. In the instrument overlap region between 0.3 and 0.6 μm the calculated particle number concentration was generally higher with the WAA than the OPC.

Aerosol for chemical analysis was sampled in the air monitoring trailer through a 1.3 cm ID stainless steel pipe. The air inlet was about 1 m above the roof of the trailer, a total of 4 m above the ground. Loss of 0.1 μm diameter particles to the walls due to turbulent diffusion was calculated to be less than 1% using the method of

Friedlander (1977). As in the Zilnez Mesa study, Chapter 3, a cyclone preseparator (John and Reischl, 1978) was used to separate the coarse ($D > 2$ μm) aerosol from the airstream so that only the fine ($D < 2$ μm) aerosol would be collected for analysis. The cyclone was operated at 26-30 liters per minute (lpm) and was cleaned every 8-10 weeks.

The fine particle airstream from the cyclone was sampled by two total filters in parallel. A Millipore Fluoropore 1 μm pore size 47 mm diameter Teflon filter was used for the first seven samples. Subsequent samples were obtained with a Nuclepore 0.4 μm pore size 47 mm diameter polycarbonate filter. Particle absorption measurements and elemental analysis by particle induced X-ray emission (PIXE) were easier and more accurate using the Nuclepore filters. In parallel with the Nuclepore filter a tape sampler collected aerosol using a Pallflex Tissuequartz tape. The tape sampler was a TWOMASS sampler loaned by Dr. Edward Macias of Washington University. The aerosol deposit area was 9.62 cm^2 on the Nuclepore and Millipore filters and 0.317 cm^2 on the Tissuequartz tape. The flow was 16-20 lpm through the Nuclepore and Millipore filters and 10 lpm through the Tissuequartz tape. The airstream was drawn through the each filter by a Gast 60 lpm displacement carbon vane pump. The volumetric flow rate through each filter was measured by a Dwyer 25 lpm rotameter which was calibrated at the site with an American DTM-325 dry test meter.

Similarly to the Zilnez Mesa study, detailed written operating instructions were followed for measuring flow rates and loading and unloading samples. NWC personnel changed most of the samples following

the written procedures. Flow rates, sample times, b_{sp}, temperature, relative humidity, and wind speed and direction values were routinely entered in the log book. Immediately after collection each Millipore or Nuclepore filter was placed in a labeled plastic container, sealed with Parafilm, enclosed in a ziplock bag, and placed in a refrigerator in the trailer. The tape in the TWOMASS sampler was advanced between samples. The tape sample was removed about once every 8-10 weeks and stored similarly to the Nuclepore filters. The TWOMASS was cleaned at that time. All samples were stored in an ice chest during the return trip to Caltech. Field blanks were handled identically to the samples.

Of approximately 100 filter samples collected in 1979, 61 were selected for analysis. The 61 were chosen to span the variation in b_{sp} and to obtain representative seasonal and diurnal samples. Sample times varied from 6 to 72 hours, with an average of 20.1 hours. All values of the sample volumes and concentrations in this chapter are with respect to 701 mm Hg atmospheric pressure, the average pressure at China Lake.

Aerosol was occasionally sampled with low pressure impactors (LPI's) to obtain sulfur and elemental mass distributions. The techniques were identical to those described in Chapter 3.

From September 5-7, 1979 gas phase nitric acid and ammonia were sampled using, in succession, a Teflon filter, a prewashed Ghia nylon filter, and two oxalic acid impregnated glass fiber filters. The Teflon filter collected the aerosol and allowed the gaseous species to

pass. It was assumed that the nylon and oxalic acid impregnated filters collected the HNO_3 and NH_3, respectively, with 100% efficiency and no interferences (Spicer, 1979; Richards, 1979). The species were then analyzed by liquid ion chromatography for nitrate and ammonium ions.

4.2.3 Sample Analysis

The filter and LPI samples were analyzed in the same manner as the Zilnez Mesa samples in Chapter 3. Total carbon and soot were determined from the Tissuequartz tape. The Nuclepore filter was measured for total mass; particle absorption coefficient; $SO_4^{=}$; NO_3^{-}; and NH_4^{+}; and elemental analysis by PIXE. The detection limits, errors, and field blank values are the same as for the Zilnez Mesa samples, except for the total carbon and soot. Because the deposit spot in the TWOMASS was about 1/4 the area of the 12.7 mm Pallflex filter used in the Zilnez Mesa study, the estimated error in measurement was smaller, about $\pm$ 2 μg for the China Lake samples.

PIXE analysis was performed on the first 30 samples by Dr. Alistair C. D. Leslie of Florida State University. PIXE analysis was performed on the last 53 samples by Crocker Nuclear Laboratory, University of California, Davis, resulting in 23 samples where analysis was performed by both laboratories.

4.3 EXPERIMENTAL RESULTS

The particle scattering coefficient, b_{sp}, was measured continuously throughout 1979. A summary of the monthly hourly average b_{sp} is shown in Table 4.2. It seen that both seasonal and diurnal variations in b_{sp} occurred at China Lake. Winter had the best visibility, with summer the worst. Nighttime b_{sp} values were higher than those in the afternoon; the average ratio of 3-4 AM b_{sp} to 3-4 PM b_{sp} was 1.77. It is likely that the diurnal variation in b_{sp} at China Lake is coupled to the diurnal cycle of afternoon winds and nighttime inversions. Polluted air from urban sources is evidently transported by winds in the early evening and trapped by a stable inversion through the night, causing elevated values of b_{sp}. The inversion lifts the next morning, reducing the b_{sp} by mixing with cleaner air aloft. A minimum in b_{sp} then occurs in the midafternoon before the cycle repeats in the evening.

A total of 254 particle size distributions were measured throughout 1979 with the WAA and OPC. The 1979 average normalized volume distribution is plotted in Figure 4.2. The error bars are standard deviations. It is seen that the distribution is bimodal, with the coarse mode dominating the aerosol volume concentrations. The average aerosol volume concentration in each particle size range was as follows:

Table 4.2

Hourly Average Measured Particle Scattering Coefficient, b_{sp}, by Month for China Lake, 1979

Hour, PST	Hourly Average b_{sp}, $10^{-6}m^{-1}$												Ave.
	J	F	M	A	M	J	J	A	S	O	N	D	1979
0	25	16	18	23	31	34	39	33	35	40	24	28	29
1	24	16	19	22	31	33	39	33	37	37	26	25	29
2	22	16	21	24	31	33	39	34	36	36	25	24	28
3	20	15	23	25	34	35	40	34	36	38	21	23	29
4	22	15	21	22	34	38	41	36	35	36	19	21	28
5	21	15	20	22	34	33	43	39	34	36	19	20	28
6	21	15	20	22	34	33	45	40	33	40	18	19	28
7	22	16	19	23	31	33	44	40	34	40	18	19	28
8	22	16	20	22	30	30	44	38	33	44	19	18	28
9	20	18	17	20	28	27	41	34	32	45	20	19	27
10	18	19	15	20	26	22	33	30	28	38	19	19	24
11	23	16	13	18	23	19	27	25	25	33	17	18	21
12	22	15	13	17	24	19	22	22	25	27	14	17	19
13	19	11	12	17	22	16	20	20	23	24	12	14	18
14	17	11	10	16	21	15	17	19	22	23	10	13	16
15	15	14	9	15	22	14	18	19	21	25	12	15	17
16	14	16	12	15	21	15	20	20	23	21	14	16	17
17	21	15	14	16	22	19	23	21	24	22	17	23	20
18	21	16	17	18	23	21	25	23	26	26	17	28	22
19	23	14	21	22	26	27	31	28	31	32	30	41	27
20	24	21	21	22	27	29	34	30	34	38	35	45	30
21	28	20	21	23	28	32	37	32	35	39	29	47	31
22	23	18	20	24	29	33	38	33	36	42	28	42	31
23	23	17	22	23	31	34	38	33	35	41	24	33	30
												1979 Average	25.2

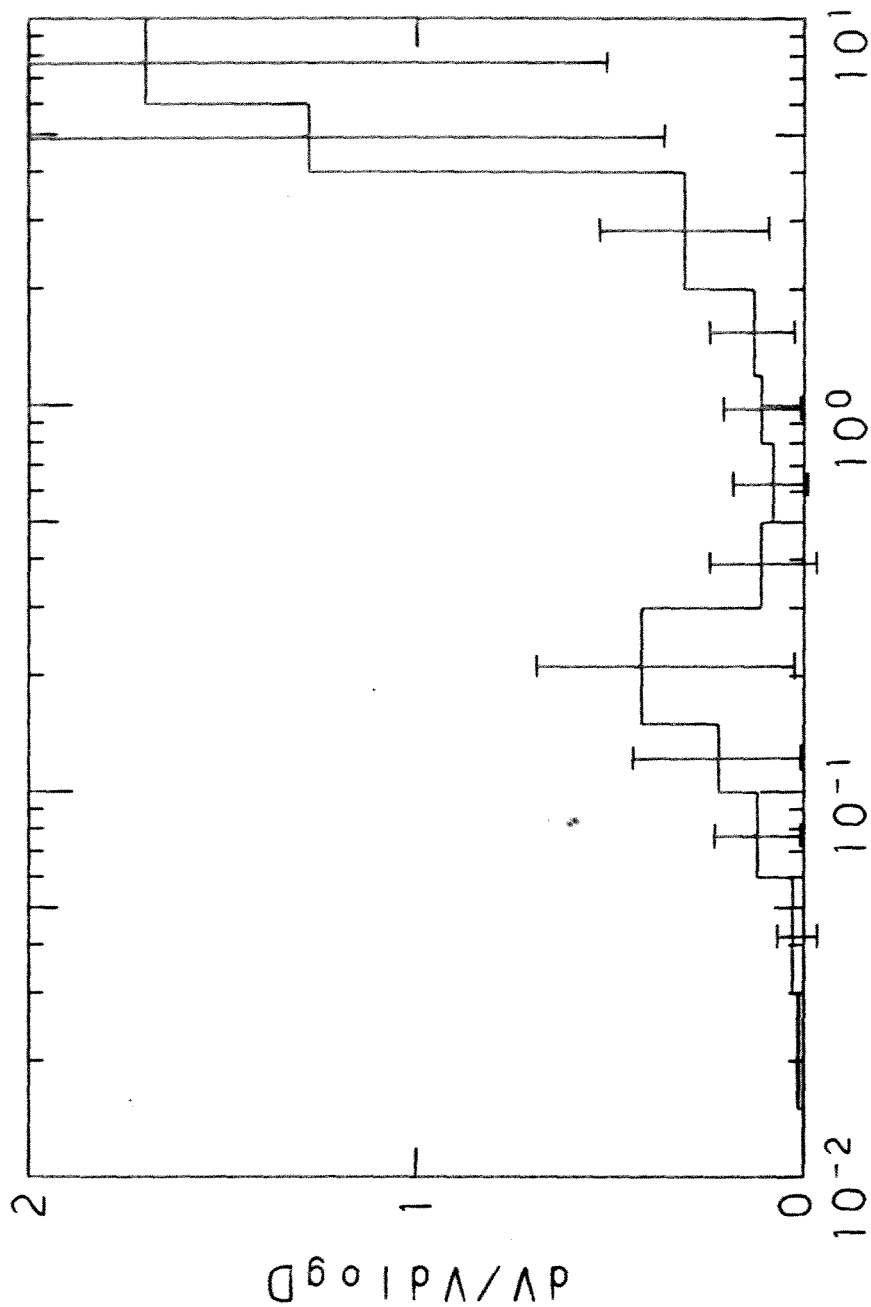

Figure 4.2. Normalized aerosol volume distribution, China Lake, California, 1979 average. Average of 254 measurements. The error bars are standard deviations. Distribution normalized with respect to total aerosol volume concentration of particles less than 10 μm diameter.

Particle Size Interval um	1979 Average Aerosol Volume Concentrations ± Standard Deviation $\mu m^3/cm^3$
0.01-0.50	VT.5 = 4.2 ± 3.2
0.01-2.0	VT2 = 5.6 ± 3.9
0.01-10.0	VT10 = 32.4± 44.3

From its large standard deviation, it is clear that the coarse particle concentration, VT10, exhibited considerable variation throughout the year. Records show that high coarse mode volume concentrations accompanied moderate to high winds. The coarse material was very likely wind-blown dust of crustal composition.

The aerosol scattering coefficient distribution was calculated from the aerosol volume distribution, using the method described in Chapters 2 and 3. The resultant distribution is plotted in Figure 4.3. The contribution of the fine aerosol to visibility degradation at China Lake is seen in this figure. Over half the computed particle scattering coefficient is due to particles less than 0.5 μm diameter, although the particles contributed an average of only 13% to VT10.

The computed scattering coefficient for each size distribution measurement was compared to the hourly average scattering coefficient measured during the same hour. The results are shown in Table 4.3. Similarly to the Zilnez Mesa data, the calculated b_{sp} overestimates the measured b_{sp} by an average of 52%. As discussed in Chapter 3, this is

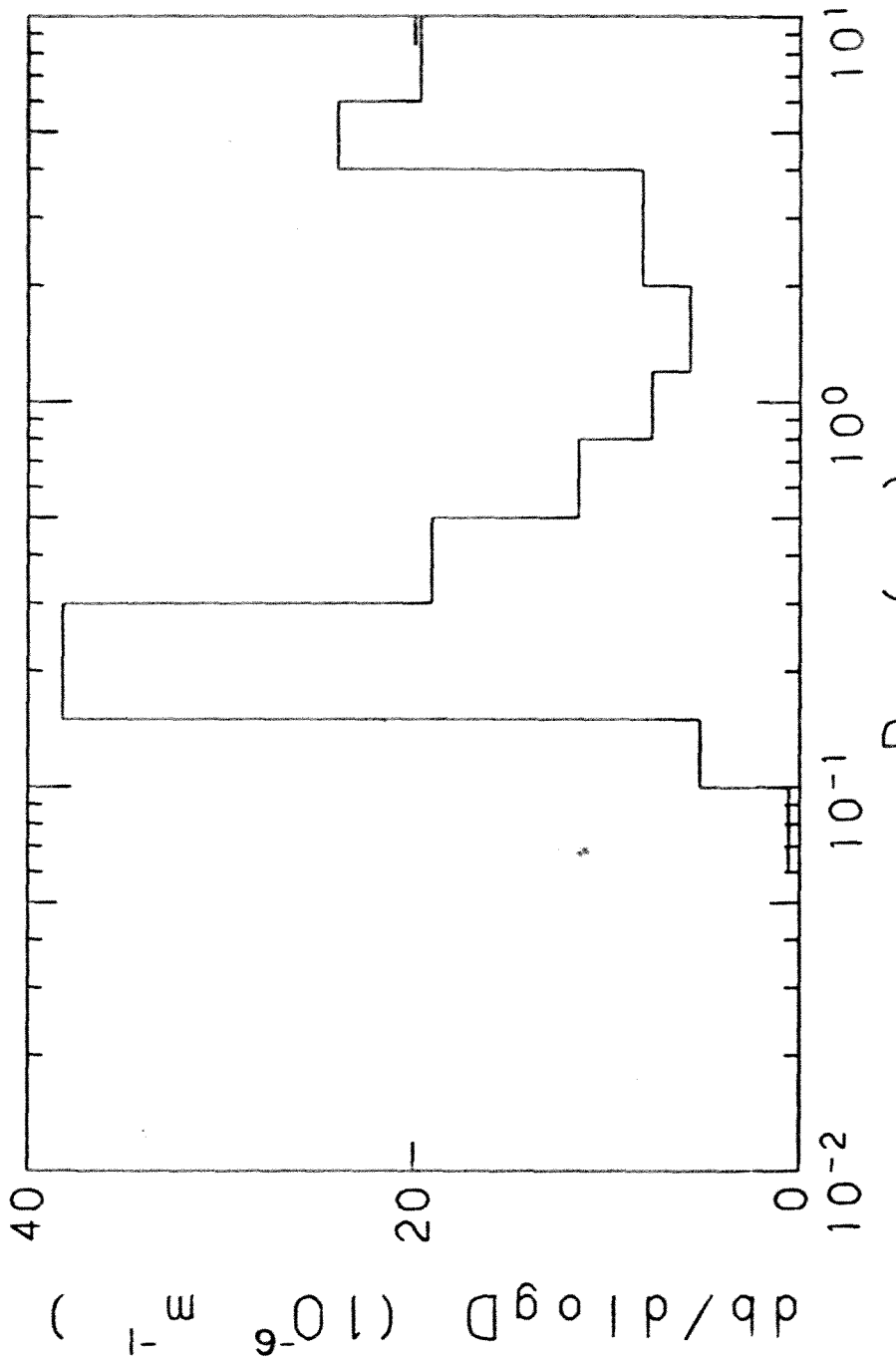

Figure 4.3. Particle scattering coefficient, China Lake, California, 1979 average. Distribution calculated from 254 measured aerosol volume distributions assuming m = 1.54-0.0151.

Table 4.3

Summary of Particle Scattering Coefficient Linear Regression Relationships, China Lake, 1979

y	x	y_o	m	r
b_{sp} (calc.)	b_{sp} (meas.)	2.48	1.37	0.78
b_{sp1} (calc.)	b_{sp} (meas.)	0.5	0.92	0.88
b_{sp} (meas.)	VT10	17.2	0.16	0.44
b_{sp} (meas.)	VT2	4.3	3.22	0.81
b_{sp} (meas.)	VT.5	7.6	3.50	0.71

Values above are least squares best fit of form:

$y = y_o + mx$ r = correlation coefficient

210 measurements used for analysis
Parameters defined in text

because the nephelometer does not effectively detect particles greater than 2 μm diameter. When only the fine aerosol is considered, the calculated scattering coefficient agrees very well with that which was measured. The measured scattering coefficient correlated poorly with VT10. Trijonis and Yuan (1978a) found similar results for Phoenix, where total mass concentration was found to be a poor indicator of visual range. However, a correlation of 0.81 was found between the measured scattering coefficient at China Lake and the fine volume concentration VT2.

Because the fine aerosol was found to be responsible for the bulk of light scattering at China Lake, this mode was examined to see of its normalized distribution remained constant throughout 1979. Figure 4.4 shows the 1979 average fine aerosol volume distribution at China Lake normalized with respect to VT2. The error bars represent standard deviations in the 254 measurements. The particle volume distribution in the fine mode is seen to preserve its shape rather well. Over half the fine particle volume is due to particles of less than 0.3 μm diameter.

4.3.1 Aerosol Composition

The time average particle extinction and mass concentrations of the fine aerosol chemical species for the 61 filter samples are compiled in Appendix D. Table 4.4 summarizes the 1979 annual average concentrations of the species. Similarly to Zilnez Mesa, organics and sulfates dominated the chemically determined fine aerosol mass at China

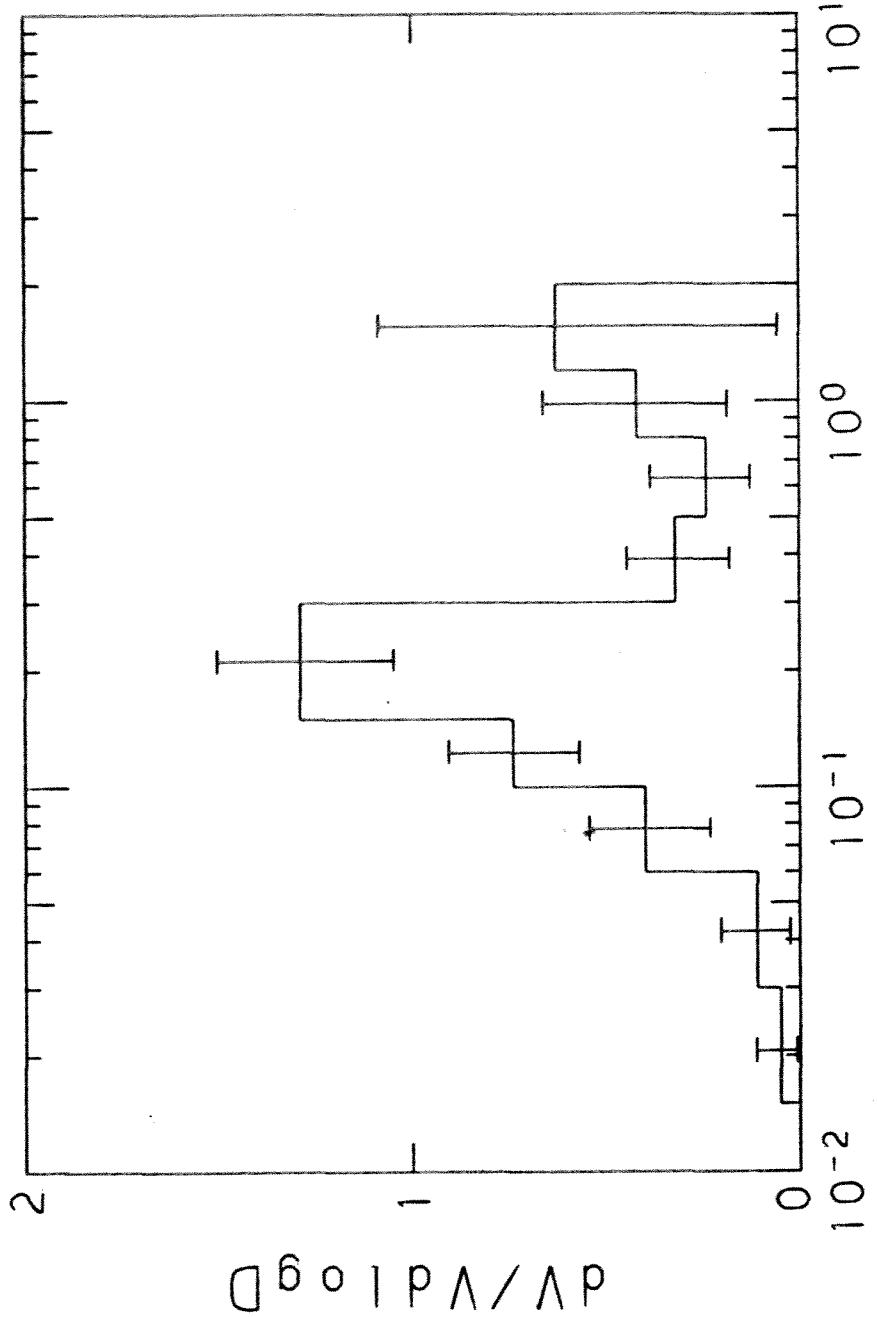

Figure 4.4. Normalized fine aerosol volume distribution, China Lake, California, 1979 average. Average of 254 measurements. The error bars are standard deviations. Distribution normalized with respect to total aerosol volume concentration of particles less than 2 μm diameter.

Table 4.4

Fine Aerosol Species Concentrations,

1979 Average, China Lake

Species	Average Concentration, ug/m^3
Total mass	10.7 ± 4.8
Total carbon	1.71 ± 1.26
Soot	0.39 ± 0.30
$SO_4^=$	1.91 ± 1.21
NO_3^-	0.19 ± 0.18
NH_4^+	0.64 ± 0.44
Al	0.048 ± 0.069
Si	0.46 ± 0.24
S	0.76 ± 0.48
K	0.15 ± 0.10
Ca	0.086 ± 0.061
Fe	0.090 ± 0.049
Pb	0.076 ± 0.075
b_{sp}, $10^{-6}m^{-1}$	25.4 ±13.2
b_{ap}, $10^{-6}m^{-1}$	5.1 ± 2.3

Average of 61 filter samples
Errors are standard deviations

Lake in 1979. A linear least squares fit between molar concentrations of NH_4^+ and $SO_4^=$ gave a zero intercept, a slope of 1.87 and a correlation coefficient of 0.98. It is therefore assumed that the fine sulfate aerosol was in the form of ammonium sulfate. Carbonaceous and sulfate aerosol mass concentrations were, on the average, comparable in magnitude.

The average and standard deviation of the particle scattering coefficient, b_{sp}, during filter sample collection was $25.4 \pm 13.2 \times 10^{-6}\ m^{-1}$. This compares favorably with the annual measured average of $25.2 \times 10^{-6}\ m^{-1}$. The average and standard deviation of the particle absorption coefficient, b_{ap}, by filter analysis was $5.1 \pm 2.3 \times 10^{-6}\ m^{-1}$. On the average, the ratio of the particle absorption to scattering coefficient was 0.22 ± 0.13, roughly twice the value measured at Zilnez Mesa.

To estimate the contribution of wind-blown dust of crustal origin to the fine aerosol concentration, elemental enrichment factors were calculated using the method of Macias et al. (1979). The enrichment factor, EF_i, for an element i was calculated as follows:

$$EF_i = \frac{([M_i]/[Fe])_{aerosol}}{([M_i]/[Fe])_{crust}}$$

Iron was chosen as the reference element because its major source is likely to be soil and it is measured with good accuracy and precision by PIXE. Crustal abundances were taken from Mason (1966, p. 45).

Enrichment factors greater than 1 indicate an enrichment of that element relative to crustal abundances; values less than 1 indicate a depletion. The results of this calculation are shown in Table 4.5. For this calculation it was assumed that ammonium and nitrate accounted for all aerosol nitrogen. It is seen that Si and Ca are near their crustal abundance, indicating a probable soil dust source. The low EF for Al is almost certainly due to a systematic error in the Al measurement rather than a true depletion. Potassium, although present in small concentrations, is slightly enriched relative to crust. The other fine aerosol species, C, N, S, and Pb are enriched by factors of thousands over their natural crustal abundance, indicating that they are not due to wind-blown dust.

A chemical species mass balance was calculated for China Lake using the 1979 average measured species concentrations. The balance is shown in Table 4.6. The organic carbon concentration is taken to be 1.2 times the difference between the total and graphitic carbon concentrations. This was done to account for additional hydrogen and oxygen in the organic aerosol (Grosjean and Friedlander, 1975). The NO_3^- masses determined from the field samples were usually within one standard deviation of the average blank value. The low nitrate concentrations are consistent with measured gas phase nitric acid and ammonia concentrations made from September 5-7, 1979. The concentrations of HNO_3 and NH_3 each averaged between 0.2 and 3 ppb at that time. At the temperatures measured, the data indicate no pure NH_4NO_3 should be in the aerosol phase (Stelson et al., 1979). The crustal aerosol

Table 4.5

Aerosol Elemental Enrichment Factors,

1979, China Lake

Element, X	$([X]/[Fe])_{aerosol}$	$([X]/[Fe])_{crust}$	Enrichment Factor, EF
C	19.1	4.0×10^{-3}	4.78×10^{3}
N	6.03	4.0×10^{-4}	1.51×10^{4}
Al	0.53	1.63	0.33
Si	5.12	5.54	0.92
S	8.51	5.2×10^{-3}	1.64×10^{3}
K	1.65	0.518	3.19
Ca	0.955	0.726	1.32
Fe	1.0	1.0	1.0
Pb	0.848	2.6×10^{-4}	3.26×10^{3}

Values computed using 1979 average species mass concentrations

Table 4.6

Fine Aerosol Species Mass Balance

Species	1979 Average Concentration $\mu g/m^3$
Organic	1.58
Soot	0.34
$SO_4^=$	1.91
NO_3^-	0.19
NH_4^+	0.64
Crustal	1.94
Other	0.3
Total Accounted	7.0
Total Measured	10.7

concentration was computed from the Si, Ca, and Fe concentrations assuming their crustal abundances (Mason, 1966). It includes the contribution of poorly measured species such as aluminum and oxygen, and is a reliable estimate of the contribution of wind-blown dust to the fine aerosol concentration.

It is seen that organics, sulfates, and crustal species contributed approximately equally to the measured fine mass concentration. However, the measured species accounted for an average of only 65% of the total measured mass concentration. The most likely unmeasured species are Na and H_2O. If it were Na, however, it could not be in the form of NaCl or Na_2SO_4 since measured Cl concentrations were less than 0.1 $\mu g/m^3$ and $SO_4^=$ was titrated with NH_4^+. The low average relative humidity, 35%, (Table 4.1) probably minimizes water condensation on the hygroscopic ammonium sulfate. Although water could condense on the filter during refrigeration, the filters were desiccated before and during weighing.

It is assumed that the particles less than 0.5 μm had an average density of 1.7 g/cm^3 and that the average density of particles between 0.5 and 2 μm was 2.3 g/cm^3. From the value of VT.5 one then estimates an average mass concentration of 7.1 $\mu g/m^3$ due to particles less than 0.5 μm diameter and 10.3 $\mu g/m^3$ due to particles having diameters less than 2 μm, which agrees well with the directly measured average fine mass concentration of 10.7 $\mu g/m^3$. If it is assumed that all the sulfates and organics accumulate in particles less than 0.5 μm diameter, this would still account for only 63% of the computed mass. Similarly

the crustal and remaining species account for 78% of the computed mass between 0.5 μm and 2 μm. Within the accuracy of these measurements it is apparent that the unaccounted mass is primarily due to particles less than 0.5 μm diameter.

4.3.2 Elemental Size Distributions

Aerosol sulfur mass distributions were measured by the LPI-FVFPD technique on three separate occasions for 3 days each during 1978 and 1979. A total of 25 distributions were obtained. It was determined that during each 3-day period the total sulfur concentration would vary diurnally with the scattering coefficient, but that the normalized sulfur mass distribution was preserved. However, the shape of the distribution was not preserved from period to period, as can be seen in Figures 4.5a-c. As in Chapter 3, the dashed histogram in the figures is the inverted distribution using the Twomey inversion algorithm (Appendix C). During the July 2-4, 1978 and September 5-7, 1979 periods, aerosol sulfur mass accumulated in particles between 0.05 and 0.5 μm aerodynamic diameter. The shapes of these distributions are quite similar to the total average volume distribution, Figure 4.4. The average b_{sp} during each of these periods was within one standard deviation of the annual average.

During the October 20-22, 1978 period, the sulfur accumulated in larger particle sizes and in greater concentrations. This sampling period was characterized by high relative humidity (45-100%) associated with the aftermath of a tropical storm. It is likely that the source

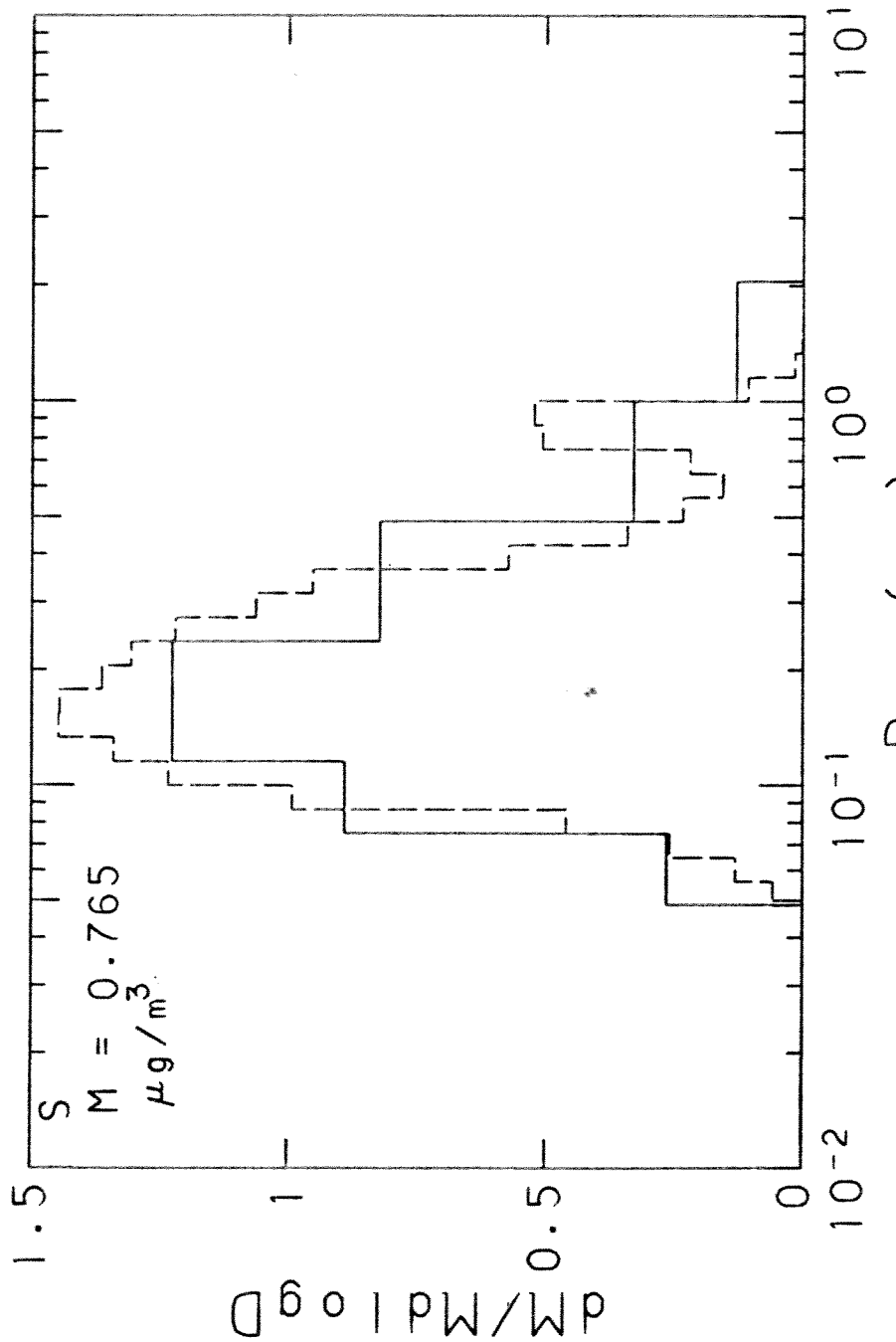

Figure 4.5a. Normalized sulfur mass distribution, China Lake, California, July 2-4, 1978. Average of 8 samples. Aerosol segregated by low pressure impactor (LPI) and analyzed by flash volatilization and flame photometric detection (FVFPD). The solid histogram is the mass distribution with respect to the 50% aerodynamic cutoff diameter. The dashed histogram is the inverted distribution obtained from LPI calibration data and Twomey (1975) inversion algorithm.

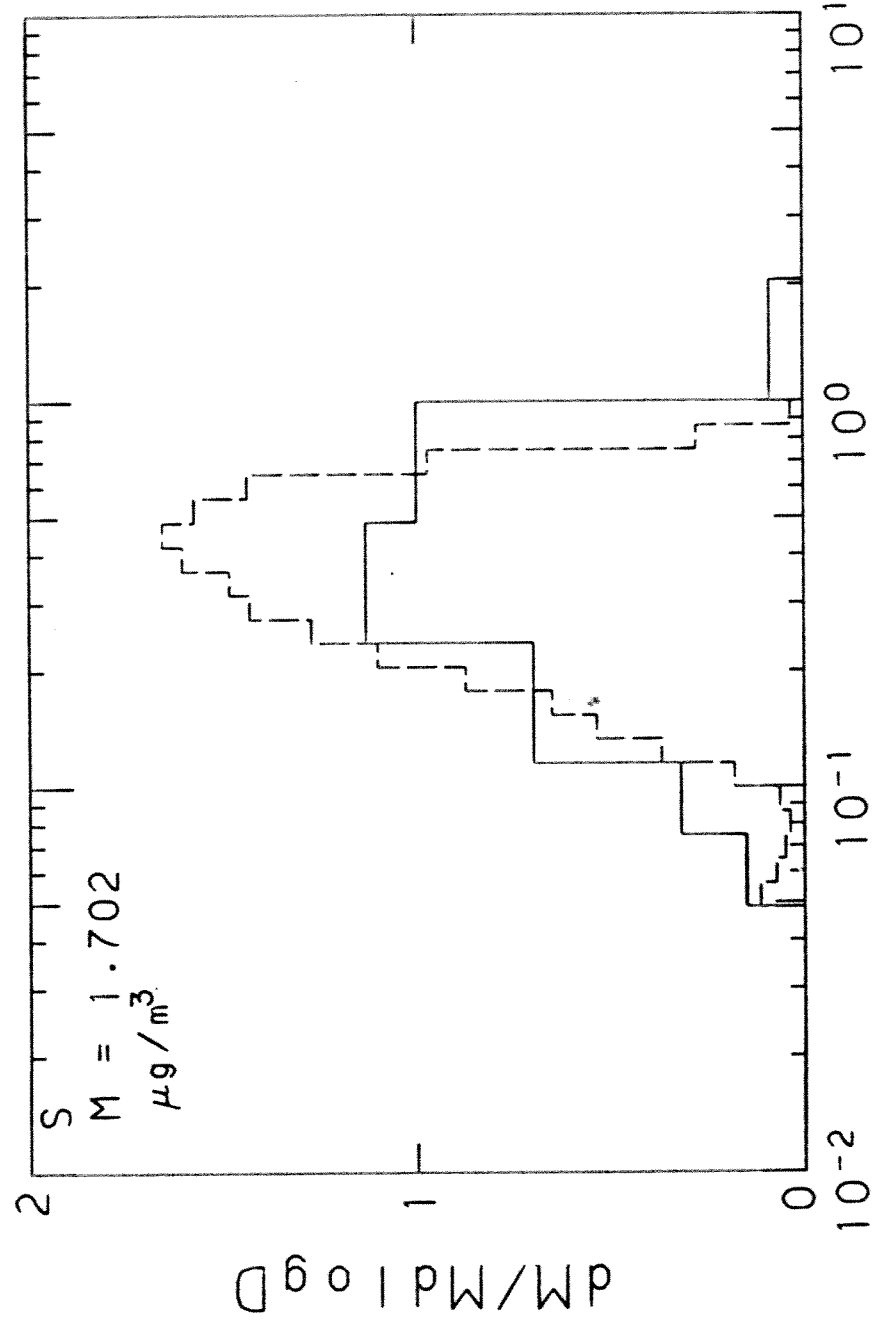

Figure 4.5b. Normalized sulfur mass distribution, China Lake, California, Oct. 20-22, 1978. Average of 11 samples. Aerosol segregated by low pressure impactor (LPI) and analyzed by flash volatilization and flame photometric detection (FVFPD). The solid histogram is the mass distribution with respect to the 50% aerodynamic cutoff diameter. The dashed histogram is the inverted distribution obtained from LPI calibration data and Twomey (1975) inversion algorithm.

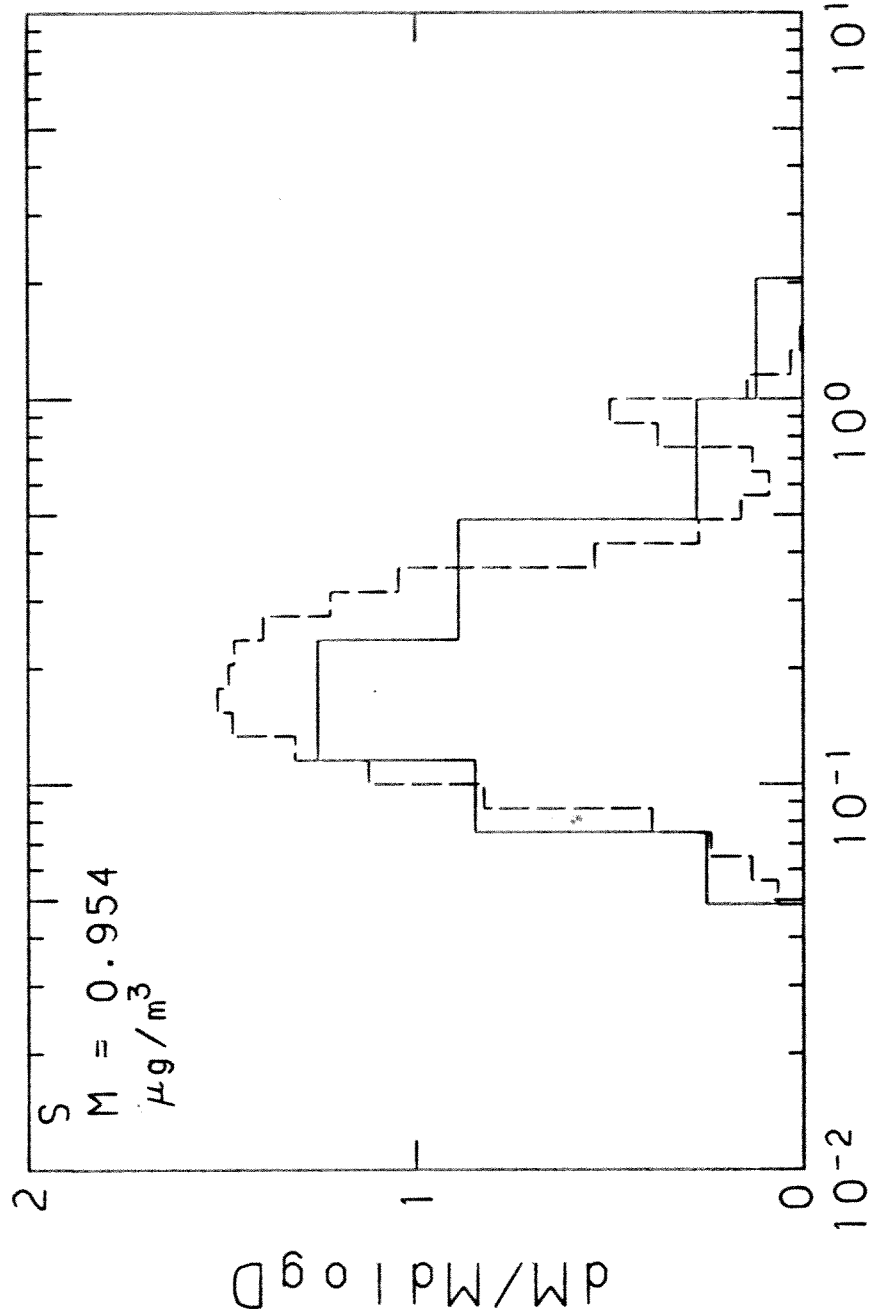

Figure 4.5c. Normalized sulfur mass distribution, China Lake, California, Sept. 5-7, 1979. Average of 6 samples. Aerosol segregated by low pressure impactor (LPI) and analyzed by flash volatilization and flame photometric detection (FVFPD). The solid histogram is the mass distribution with respect to the 50% aerodynamic cutoff diameter. The dashed histogram is the inverted distribution obtained from LPI calibration data and Twomey (1975) inversion algorithm.

of the aerosol was the Los Angeles Basin where sulfate usually accumulates in particles between 0.5 and 1.0 μm diameter, shown in Figure 1.2. The particle scattering coefficient during this episode was much higher than the average, often exceeding 100 x 10^{-6} m^{-1}, about 4 times the annual average. In examining the 1979 b_{sp}, temperature, and relative humidity data, it is clear that the July 1978 and September 1979 sample periods were more typical of the average than the October 1978 period. The filter samples from only the September 5-7, 1979, period were included in the statistical analysis.

Elemental mass distributions were measured using the LPI-PIXE technique on September 7, 1979. A cyclone preseparator upstream of the LPI removed coarse aerosol. The results are presented in Figures 4.6a-c. The concentration of coarse particles in these figures is reduced from the ambient value because of the cyclone preseparator. Similar to the Zilnez Mesa results, Si, Ca, and Fe accumulated in larger particle sizes, another indication of the crustal origin of these elements.

The distribution of organic aerosol with respect to particle size could not be measured with the LPI because of the hydrocarbon anti-bounce coatings used.

4.4 PARTICLE EXTINCTION COEFFICIENT BUDGET

4.4.1 Statistical Estimation of Species Mass Scattering Efficiencies

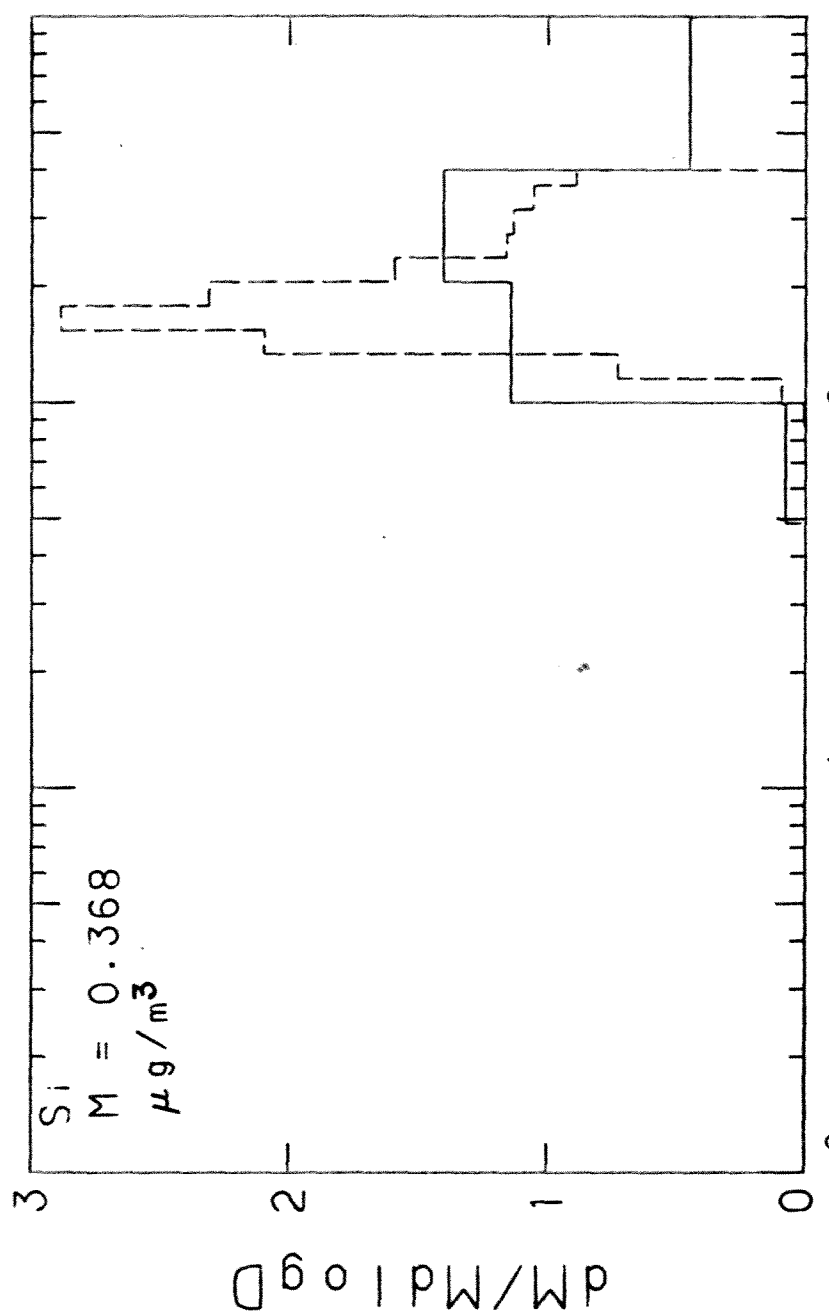

Figure 4.6a. Normalized silicon mass distribution, China Lake, California, 0823-1430 PST, Sept. 7,1979. Aerosol segregated by low pressure impactor (LPI) and analyzed by PIXE. The solid histogram is the mass distribution with respect to 50% aerodynamic cutoff diameters. The dashed histogram is the inverted distribution obtained from LPI calibration data and Twomey (1975) inversion algorithm.

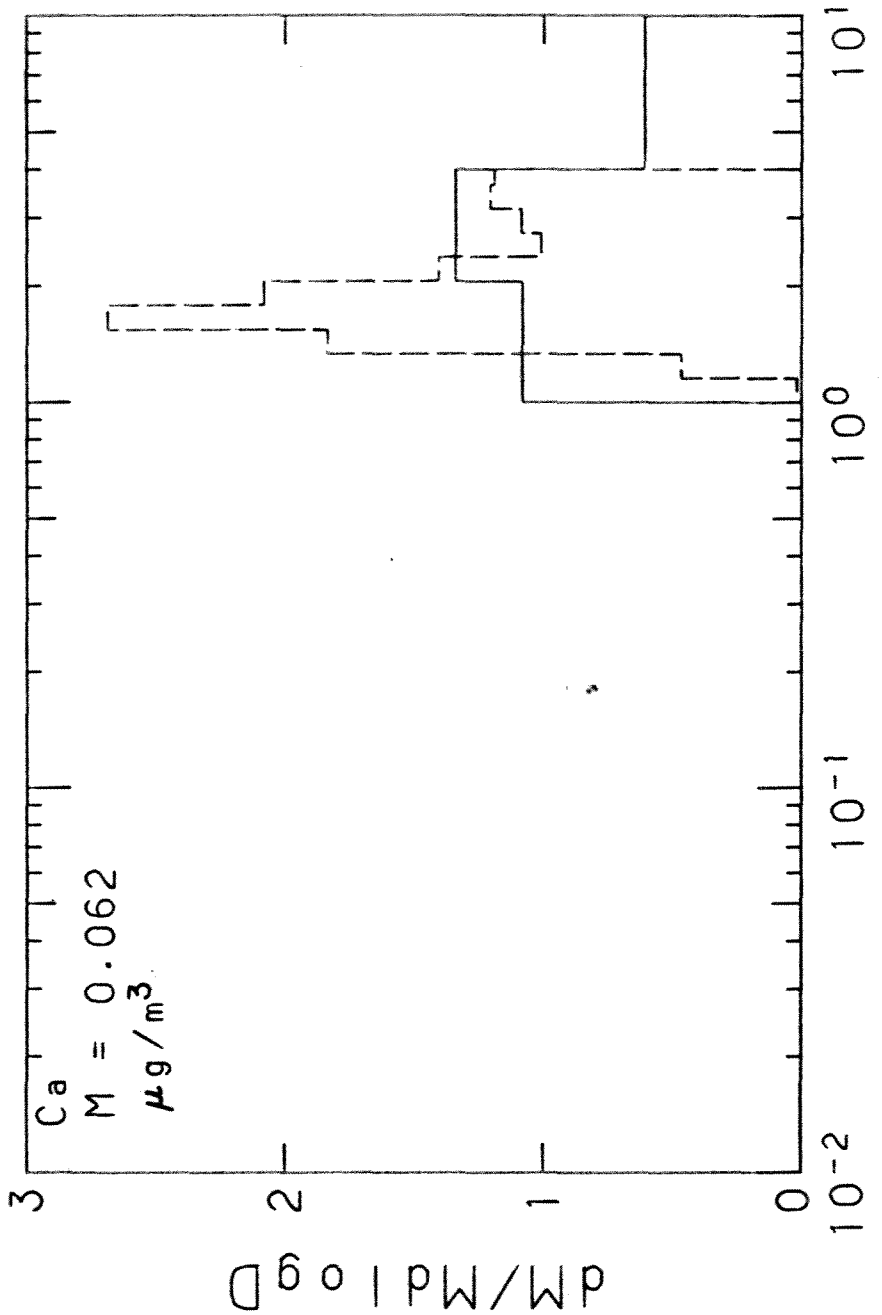

Figure 4.6b. Normalized calcium mass distribution, China Lake, California, 0823-1430 PST, Sept. 7, 1979. Aerosol segregated by low pressure impactor (LPI) and analyzed by PIXE. The solid histogram is the mass distribution with respect to 50% aerodynamic cutoff diameter. The dashed histogram is the inverted distribution obtained from LPI calibration data and Twomey (1975) inversion algorithm.

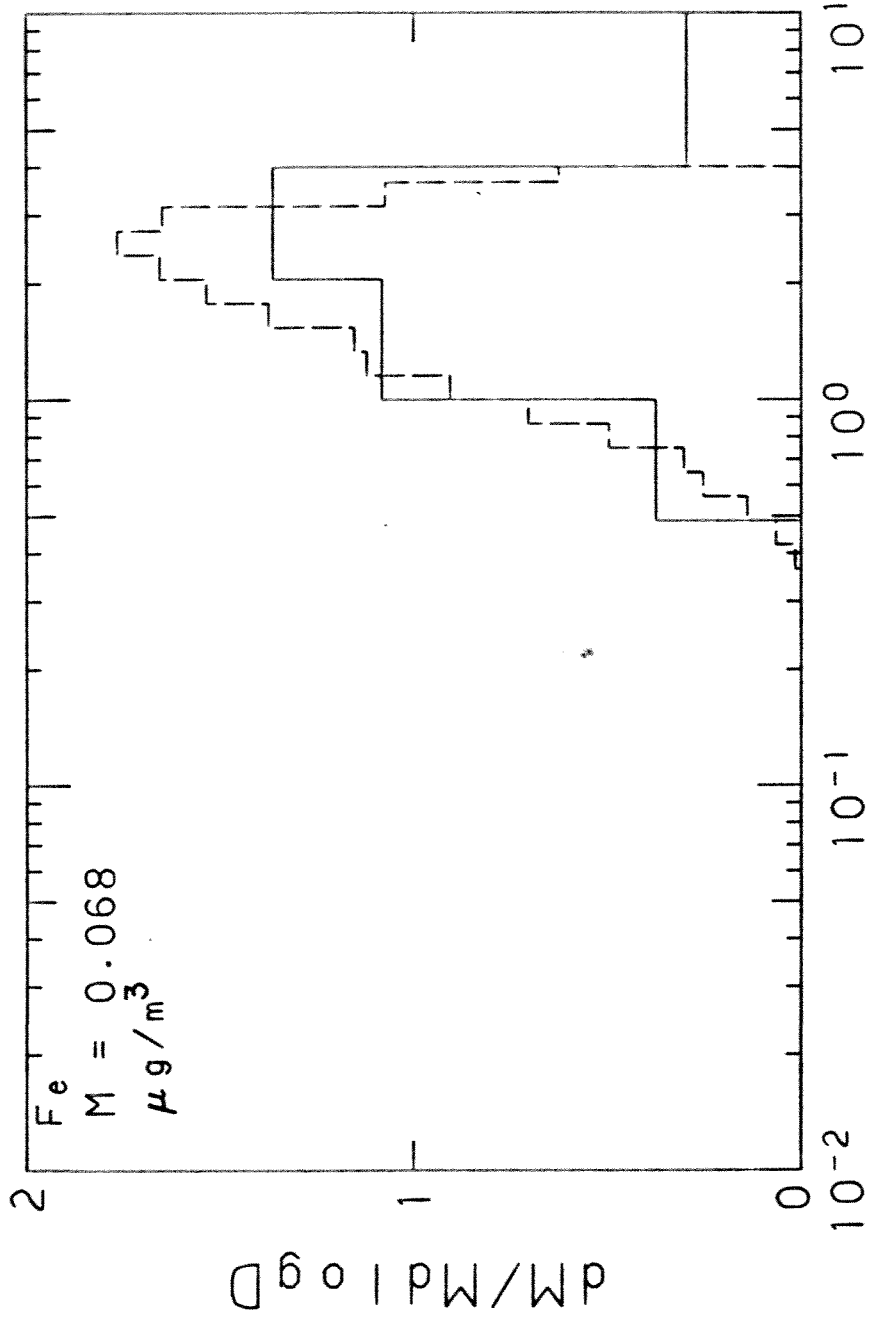

Figure 4.6c. Normalized iron mass distribution, China Lake, California, 0823-1430 PST, Sept. 7, 1979. Aerosol segregated by low pressure impactor (LPI) and analyzed by PIXE. The solid histogram is the mass distribution with respect to 50% aerodynamic cutoff diameter. The dashed histogram is the inverted distribution obtained from LPI calibration data and Twomey (1975) inversion algorithm.

The goal of the year-long study at China Lake was to test the applicability of statistical techniques to determine the aerosol species contributions to the scattering coefficient. On the average, the requirements for application of the statistical technique to filter data were met. Analysis of the 254 measured particle size distributions in 1979 indicates that the fine aerosol volume distribution preserved its shape. The measured sulfur mass distribution followed the total submicron volume distribution. By difference, it was assumed that the organics did the same. The low relative humidity at China Lake minimized water condensation on the particles and formation of aqueous solutions. Therefore, it is expected that the statistical technique can be used with some success with the China Lake filter data.

Initially, as a first cut, univariate regression was used to see relationships between pairs of measured variables. The results are summarized in Table 4.7. It is seen that the particle scattering coefficient is highly correlated with the total fine aerosol mass concentrations, sulfate, and ammonium. To a lesser degree it is correlated with the particle absorption coefficient, potassium, and the unaccounted mass concentration, M_u. The correlations between the particle scattering coefficient and the nitrate, total carbon (C_T) and crustal species are poor. The poor correlation, r=0.63, between b_{ap} and the soot concentration is probably an indication of the error in the soot measurement. Although the sulfate and the unaccounted mass are highly

Table 4.7

Aerosol Mass Concentrations and b_{sp}: Results of Univariate Regressions for China Lake, 1979

$b_{sp} = 0.30 + 2.35\ [M_T]$	r = 0.86
$b_{sp} = 7.5 + 9.36\ [SO_4^{=}]$	r = 0.86
$b_{sp} = 8.9 + 25.8\ [NH_4^{+}]$	r = 0.85
$b_{sp} = 4.2 + 4.13\ b_{ap}$	r = 0.72
$b_{sp} = 14.1 + 79.3\ [K]$	r = 0.58
$b_{sp} = 14.3 + 2.41\ [M_u]$	r = 0.57
$b_{sp} = 18.8 + 34.1\ [NO_3^{-}]$	r = 0.47
$b_{sp} = 17.4 + 4.80\ [C_T]$	r = 0.46
$b_{sp} = 15.6 + 114\ [Fe]$	r = 0.41
$b_{sp} = 19.9 + 71.3\ [Ca]$	r = 0.32
$b_{sp} = 18.2 + 17.1\ [Si]$	r = 0.31
$b_{ap} = 3.2 + 4.53\ [Soot]$	r = 0.63
$[M_T] = 4.83 + 1.27\ [M_u]$	r = 0.81
$[M_t] = 4.3 + 3.33\ [SO_4^{=}]$	r = 0.83
$[M_u] = 2.20 + 1.26\ [SO_4^{=}]$	r = 0.49

Values computed from 61 filter samples

correlated with the total mass, they are not well correlated with each other (r=0.49).

It was found that the crustal species Fe, Ca, and Si were well correlated with each other, as expected. On the basis of the regression analysis, the fine aerosol was grouped into four species: sulfates, organics, crustal species, and the unaccounted species. The concentrations of these four species were calculated in the following manner:

1. [sulfates] = $[SO_4^=]$ + $[NH_4^+]$
2. [organics] = 1.2 x $[C_T]$
3. [crustal] = 21.6 x [Fe]
4. [unaccounted] = $[M_T]$ - [sulfates] - [organics] - [crustal]

Multiple regression analysis was applied to the four species to seek a best statistical fit of the form:

$$\overline{b}_{sp} = \sum_{i=1}^{N} \alpha_i M_i$$

where M_i is the time average mass concentration of species i. α_i could then be interpreted as the average mass scattering efficiency of species i. The results of the technique applied to the 61 China Lake filter samples are as follows:

$$b_{sp} = (0.97 \pm 1.92) + (5.03 \pm 0.64)[\text{sulfates}] + (1.54 \pm 0.62)[\text{organics}] + (2.36 \pm 0.67)[\text{crustal}] + (1.00 \pm 0.31)[\text{unaccounted}]$$

$$r=0.905$$

where b_{sp} is in units of 10^{-6} m^{-1} and the species concentrations are in units of $\mu g/m^3$. The $\pm$ values in the above equation represent one standard error in the coefficient estimates. The contributions to the variance in b_{sp} were as follows: sulfates, 68.0%; organics, 6.8%; crustal, 13.9%; and unaccounted, 11.3%. The statistically inferred average mass scattering efficiency for sulfates at China Lake in 1979 is compared to values obtained by other investigators in Table 4.8. The China Lake value is intermediate between those found in other desert locations and in Los Angeles. The fine organic aerosol was not statistically important in explaining the variance in b_{sp}, and its inferred mass scattering efficiency was less than one-third of the sulfate value. Similar results were found by White and Roberts (1975) in Los Angeles and Trijonis and Yuan (1978a) in Phoenix. The crustal species in the fine aerosol are, surprisingly, more important than the organics in explaining the variance in the b_{sp}, but were less efficient per unit mass in scattering light.

In summary, the variance in the measured fine particle scattering coefficient, b_{sp} was dominated by sulfate concentrations. Organics and crustal species were much less important statistically. The inferred mass scattering efficiency for sulfates was intermediate between other desert values and Los Angeles. The statistical results for China Lake are quite similar to those by other investigators at other locations, even though only the fine aerosol was sampled at China Lake.

Table 4.8

Sulfate Average Mass Extinction Efficiency, α_i:

Comparison of Statistically Inferred Values

Source	Location	α_i, m^2/g
This study	China Lake	5.0
Trijonis & Yuan (1978a)	Phoenix	3.4
	Salt Lake City	4
White & Roberts (1975)	Los Angeles	7
Cass (1979)	Los Angeles	16
	Los Angeles	9 (nonlinear RH)
Waggoner et al. (1976)	Southern Sweden	5

4.4.2 Theoretical Estimation of Species Mass Scattering Efficiencies

Using the technique described in Chapters 2 and 3, the mass distribution of each chemical species was used to compute its scattering coefficient distribution and its contribution to the particle scattering coefficient, b_{sp}. The theoretical average species mass scattering efficiency, α_i, was then calculated from the ratio of the computed scattering coefficient to the measured mass concentration.

The sulfate mass scattering efficiency was computed using the 25 mass distributions measured in July 1978, October 1978, and September 1979. The average value for all measurements was 3.20 m^2/g, slightly greater than that of the fine aerosol as a whole, which was 2.35 m^2/g.

The crustal crustal mass scattering efficiency was assumed to be the average of the calculated values for Si, Ca, and Fe. Using the distributions measured in September 1979, the crustal average was 1.42 m^2/g. The fine crustal aerosol is substantially less efficient than the sulfate because it does not accumulate in particles which are optimum for light scattering--between 0.4-0.5 μm diameter for a wavelength of 0.53 μm.

The organic aerosol average mass scattering efficiency was calculated by assuming that the organic aerosol accumulated in particles less than 0.8 μm and followed the 1979 average measured volume distribution, Figure 4.4. Assuming a density of 1.7 g/cm^3, the computed mass scattering efficiency was 2.46 m^2/g, between the values for sulfate and the fine crustal material.

The average mass scattering efficiency of the unaccounted species was calculated by assuming that the species followed the overall distribution. This resulted in a mass scattering efficiency of 2.35 m^2/g.

The uncertainty in each of the theoretical mass scattering efficiencies is about 30%, resulting principally from the uncertainty in the measured species mass distributions.

4.4.3 Fine Aerosol Scattering Coefficient Balances: Comparison of Statistical and Theoretical Results

The average contribution of each major aerosol species to the 1979 average particle scattering coefficient, $\bar{b}_{spi}$ at China Lake, was calculated using the following relationship

$$\bar{b}_{spi} = \alpha_i \bar{M}_i$$

where $\bar{M}_i$ is the 1979 average mass concentration of species i and α_i is its average mass scattering efficiency. Both statistical and theoretical techniques were used to calculate α_i. The results are shown in Table 4.9. It is seen that there is excellent agreement between the average measured and calculated b_{sp} using both techniques. Both techniques show that sulfate is the most important identified light scattering species, but that the statistical technique overestimates the contribution of sulfate compared to the theoretical model. The contributions of organics and crustal species to b_{sp} are each 10-20% for both techniques. The unaccounted species contribute 39% to the theoretical scattering balance, approximately the same as its

Table 4.9

Aerosol Species Contributions to the Particle Scattering Coefficient:

Comparison of Statistical and Theoretical Results for China Lake

Aerosol Species, i	1979 Average Mass Concentration, M_i $\mu g/m^3$	Mass Scattering Efficiency, α_i m^2/g		Contribution to b_{sp}, $10^{-6} m^{-1}$		% Contribution to Total Measured b_{sp}	
		Stat. (S.E.)	Theor. (S.E.)	Stat.	Theor.	Stat.	Theor.
Sulfates	2.55	5.03 (0.64)	3.20 (0.96)	12.8	8.2	50.4	32.3
Organics	1.97	1.54 (0.62)	2.46 (0.75)	3.0	4.8	11.8	18.9
Crustal	1.94	2.36 (0.67)	1.42 (0.42)	4.6	2.8	18.1	11.0
Unaccounted	4.24	1.00 (0.31)	2.35 (0.71)	4.2	9.9	16.5	39.0
Computed Total				24.6	25.7	97	101
Measured Total				25.4	25.4	100	100

Stat. - Statistical
Theor. - Theoretical
(S.E.) - Standard error of estimate

contribution to the fine mass concentration.

When the uncertainties in the values are included, it is found that the statistically determined mass scattering efficiencies are not significantly different than those calculated theoretically. For example, representing the uncertainty as twice the standard error results in a statistically inferred sulfate mass scattering efficiency of 5.0 ± 1.2 as compared with a theoretical value of 3.2 ± 1.9.

From Table 4.9 it is seen that roughly half the theoretically unaccounted light scattering is statistically associated with sulfate. The earlier fine mass balance indicated that not all the aerosol in the 0.05-0.5 um diameter range could be accounted for by sulfates and organics. It is possible that the unaccounted species whose light scattering is statistically associated with sulfate may also be physically associated with sulfate in this size range. Water is the most obvious candidate, but is is not likely to condense on $(NH_4)_2SO_4$ at the low relative humidities found at China Lake.

In summary, both techniques present a qualitatively similar picture of the contributions of aerosol chemical species to b_{sp}. Ammonium sulfate is the most important measured species, while the contributions of organics and crustal species are smaller, but not negligible. The species which could not be identified by chemical analysis also contributed to b_{sp}, but roughly half of this contribution is statistically linked to sulfate.

4.4.4 A Light Extinction Budget for China Lake

As noted in the introductory chapter, the light extinction coefficient, b_e, is the sum of the contributions of particles and gases to scattering and absorption:

$$b_e = b_{sg} + b_{sp} + b_{ag} + b_{ap}$$

Both fine and coarse particles contribute to light extinction. The nephelometer efficiently measures only the fine particle contribution to b_{sp}. From Figure 4.3 it is calculated that, on the average, coarse (D > 2 um) particles contributed approximately 13 x $10^{-6}m^{-1}$ to b_{sp}. The median value will be somewhat less than this, since a small number of wind-blown dust episodes contributed the most to the average coarse particle contribution.

The calculated theoretical values were used to compute the 1979 China Lake light extinction budget shown in Table 4.10. As discussed earlier, the measured particle scattering coefficient varied diurnally, achieving maximum values at night and minimum values in early afternoon. For this reason Table 4.10 includes an estimated median 1 PM extinction budget. This may more closely reflect the people's perception of daytime visibility at China Lake. It is seen that, on the average, 51% of light extinction is due to Rayleigh scattering and wind-blown dust. Organics, soot, and sulfates contribute an average of 32% to extinction, while the remaining 17% is unaccounted. Interestingly, the carbonaceous aerosol contributes more than sulfates to light

Table 4.10

1979 China Lake Light Extinction Coefficient Budget

Type of Light Extinction	Contribution to b_e, $10^{-6}m^{-1}$		Contribution to b_e, %	
	Average	Median 1 PM (est.)	Average	Median 1 PM (est.)
Rayleigh Scattering, b_{sg}	14	14	24.6	34.1
Absorption by gases, b_{ag} (est.)	0	0	0	0
Absorption by fine particles	5.1	3.6	8.9	8.8
Soot	5.1	3.6	8.9	8.8
Absorption by coarse particles	0	0	0	0
Scattering by coarse particles	13	5	22.8	12.2
Crustal species	13	5	22.8	12.2
Scattering by fine particles	25	18	43.9	43.9
Sulfate	8.2	5.9	14.4	14.4
Organics	4.8	3.4	8.4	8.3
Crustal species	2.8	2.0	4.9	4.9
Unaccounted	9.9	7.1	17.4	17.3
Total,	57	41	100	100
Average local visual range, km	68	95		

extinction due to its ability to scatter and absorb light. This result was also found at Zilnez Mesa.

Using the calculated average mass extinction efficiencies, α_i, for each major chemical species, it is possible to estimate the percentage decrease in current visibility that would result from an increase in the mass concentration of each species. For a finite change in the mass concentration of a particular species, ΔM_i, the percentage decrease, $\Delta V_R/V_{RO}$ in current visual range, V_{RO}, is given by Equation 2.2:

$$\frac{\Delta V_R}{V_{RO}} = \frac{V_{RO}\ \alpha_i \Delta M_i}{3.9 + V_{RO}\ \alpha_i \Delta M_i}$$

The calculations were performed assuming the median 1 PM visual range of 95 km and that 2 $\mu g/m^3$ of the species were added. The results are provided in Table 4.11. The reduction in visual range resulting from the increase in soil dust would be insignificant. The visibility reduction resulting from a 2 $\mu g/m^3$ increase in each of the other species would be significant, 11-33%. Soot, due to its efficient light absorption efficiency, would reduce the median 1 PM visual range at China Lake by one-third.

4.5 SUMMARY AND CONCLUSIONS

Multiple regression analysis was applied to the measured particle scattering coefficient and fine aerosol species mass concentrations from 61 filter samples collected at China Lake, California in 1979.

Table 4.11

Estimated Reduction in Median 1 PM Visual Range at China Lake Due to 2 $\mu g/m^3$ Increase in Aerosol Species Mass Concentration

Aerosol Species	Average Mass Extinction Efficiency, m^2/g	% Decrease in Current Visual Range Due to Additional 2 $\mu g/m^3$ of Species
Soil dust (coarse and fine)	0.29	1.4
Ammonium Sulfate	3.2	13
Organics	2.5	11
Soot	10	33

Assumes current median 95 km visual range

Contributions of various aerosol species to the particle scattering coefficient were estimated. The statistically estimated contributions were compared with those determined theoretically using measured aerosol mass distributions.

It was found that the requirements described in Chapter 2 for application of the linear regression technique to species mass concentrations in a complex aerosol were satisfied. Based on 254 particle size distributions measured at China Lake in 1979 that the normalized fine aerosol volume distribution remained approximately constant. The agreement between the calculated and measured fine particle scattering coefficient was excellent. The measured aerosol sulfur mass distribution usually followed the total distribution for particles less than 1 μm. It was assumed that organic aerosol also followed the total submicron distribution.

The measured fine aerosol species were grouped into sulfates, organics, and crustal species, each having annual average mass concentrations of about 2-2.5 micrograms per cubic meter. An average of 35% of the measured fine mass concentration could not be accounted by chemical analysis.

The results of the statistically inferred species contributions to b_{sp} agreed qualitatively with those calculated theoretically using measured aerosol distributions. Within the errors in the measurements and analysis, the statistically and theoretically determined values were not significantly different. Ammonium sulfate was the most

important fine aerosol light scattering species, whereas the contributions of the organics and crustal species were smaller, but not negligible. Regression analysis overestimated the contribution of sulfate relative to that calculated theoretically. Species which were not identified chemically also contributed significantly to b_{sp}. The regression analysis indicated that roughly half of the b_{sp} contribution by the unaccounted species was statistically linked to sulfate. Water is suspected but is probably not a significant component of the aerosol at China Lake due to the low relative humidity.

Using measured 1979 values, a light extinction budget was calculated for China Lake. On the average, 51% of light extinction at 0.53 μm wavelength was due to Rayleigh scattering and wind-blown dust, in roughly equal proportions. Fine carbonaceous and ammonium sulfate aerosol contributed an average of 32% to extinction, while the remaining 17% was unaccounted.

The quality of statistically inferred species extinction balances can be enhanced with proper aerosol sampling. Due to its important role in light scattering, only the fine aerosol should be sampled. A mass balance should account for all major fine aerosol species. Ideally the particle scattering coefficient should be measured directly at the location where aerosol is sampled by the filters. The importance of soot and other carbonaceous aerosol to light extinction in arid regions should not be overlooked.

CHAPTER 5

SUMMARY

5.1 SUMMARY OF RESULTS

This thesis describes research conducted to determine the contributions of aerosol chemical species to the extinction coefficient.

A general theory was derived for predicting the contributions of chemical species to the extinction coefficient for a multicomponent aerosol composed of spheres. In general, the diameter, refractive index, and chemical composition of each particle must be known to rigorously calculate each species contribution. It is shown that species mass distributions of the kind obtained with a perfect impactor are sufficient to determine the species contributions exactly for three simple aerosols: an external mixture, an internal mixture, and a specific mixture with an assumed volume average refractive index. A specific mixture is an aerosol in which the chemical composition may vary with particle size. Although each particle may be composed of many species, it is assumed that all particles of the same size have the same composition. A specific mixture of spherical particles with a volume average refractive index is the most general aerosol for which the mass distributions can be used to determine the species contributions exactly.

An additional requirement placed on the use of mass distributions to predict the species extinction coefficient contributions is that

particle volume must be conserved with coagulation and condensation. The growth of hygroscopic particles by condensation of water would not be permitted if the partial molar volume of any species changes in the process. For each of the three simple aerosols requirements were derived in which linear regression analysis could be legitimately applied to historical species mass concentrations data in order to estimate species contributions to light extinction.

Experiments were conducted at two remote arid locations to determine the contributions of aerosol chemical species to visibility degradation. Desert visibility degradation resulting from future energy development is of current national importance and of personal interest to me. In addition, arid sites avoid the theoretical and experimental problems of accounting for water in the aerosol.

A 3-week experiment was conducted in remote northeastern Arizona to calculate the contributions of fine aerosol species to the extinction coefficient. Theoretical mass extinction efficiencies were calculated and numerically integrated with measured mass distributions to determine the contribution of each species to the extinction coefficient. The measured chemical species could account for 94 $\pm$ 19% of the fine aerosol mass concentration and 85 $\pm$ 34% of the measured particle extinction coefficient. Carbonaceous and sulfate aerosols were found to be the principal contributors to visibility degradation by fine ($D < 2$ μm) particles. All important species balances were met, both in total and with respect to size. The satisfactory agreement between the calculated and measured extinction coefficient indicates that the

technique is useful for determining the contributions of various aerosol species to visibility degradation at an arid site.

A one-year experiment was conducted at China Lake, California, to determine the accuracy in using statistical analysis of filter samples to estimate chemical species contributions to the particle scattering coefficient, b_{sp}. Multiple regression analysis was applied to the measured particle scattering coefficient and fine aerosol species mass concentrations from 61 filter samples collected during 1979. Contributions of various aerosol species to the particle scattering coefficient, b_{sp}, were estimated. The statistically estimated contributions were compared with those determined theoretically using measured aerosol mass distributions. It was found that the statistically inferred species contributions to b_{sp} agreed qualitatively with those calculated theoretically. Within the errors of the measurements and analysis, the statistically and theoretically determined values were not significantly different. Ammonium sulfate was the most important light scattering species, whereas the contributions of the organics and crustal species were smaller but not negligible. Regression analysis overestimated the contribution of sulfate relative to that calculated theoretically. Using measured 1979 values, an aerosol species light extinction budget was calculated for China Lake. Measured mass extinction coefficients were used to predict the reduction in visibility at China Lake which would occur by increasing the concentrations of various aerosol species.

The low pressure impactor (LPI) was used in this research to size segregate aerosol from 0.05 to 4 μm aerodynamic diameter for elemental analysis. Two new analytical techniques were developed for analysis of aerosol deposits collected with the LPI. The LPI-PIXE technique was developed and evaluated for mass determination of most elements having atomic weights between aluminum and lead. Aerosol is size segregated and impacted on coated mylar films which are then bombarded by a focused alpha-particle beam at the Crocker Nuclear Laboratory, University of California, Davis. Nanogram sensitivities are achieved.

A He-Ne laser was used with a 0.25 mm diameter optical fiber to measure the light absorbed by aerosol deposited on coated mylar film. The particle absorption coefficient distribution from 0.05 to 4 μm aerodynamic diameter can now be calculated by using this technique with LPI aerosol deposits. The soot mass distribution can be inferred from these measurements with nanogram sensitivity. This technique is only semiquantitative at the present.

The Twomey non-linear inversion algorithm was evaluated and used to obtain improved mass distributions using calibration data and masses measured on each stage of the LPI. A more accurate determination of the particle extinction coefficient distribution is now possible with the distribution obtained from the LPI and the inversion algorithm.

The experimental techniques used in this research can be applied to other areas of aerosol research. As an example, it may be possible to evaluate different mechanisms of catalyzed SO_2 gas-to-particle conversion through the measurement of the submicron sulfur, iron, manganese, and soot mass distributions. The production of silicon and

iron oxide aerosols of less than 0.1 μm diameter in pulverized coal combustion can now be measured with elemental analysis of LPI samples (Flagan and Taylor, 1980). The soot mass distribution can now be measured for particles greater than 0.05 μm aerodynamic diameter. This could be a useful tool in future diesel aerosol research. Using the LPI with coated mylar as a collection substrate offers additional opportunities for elemental analysis. For example, it may be possible to analyze the samples by instrumental neutron activation to determine the mass distribution of many trace species not accurately determined by PIXE, such as cadmium and arsenic. This could be quite useful for aerosol source resolution and toxicological studies. The prediction and measurement of multicomponent aerosol dynamics is now possible for some systems with the sectional simulation technique of Gelbard and Seinfeld (1980) and the analytical techniques described in this thesis.

5.2 SOME COMMENTS ON AEROSOLS AND VISIBILITY DEGRADATION IN PRISTINE ARID REGIONS

Pristine arid regions such as those found in parts of the southwestern United States are characterized by low aerosol number and mass concentrations, abundant sunlight, and low relative humidity. These factors affect the formation and transport of aerosols and influence the contributions of various chemical species to visibility degradation.

The residence time of visibility-reducing aerosols in arid regions may be relatively long. In Chapters 3 and 4 it was shown that visibility reduction at the two experimental sites was due primarily to

submicron aerosols. The lack of rainfall minimizes aerosol removal by wet deposition (Liljestrand, 1979). Dry deposition is also relatively slow for submicron aerosols in sparsely vegetated arid regions (Davidson and Friedlander, 1978), where the effects of particle sedimentation and impaction on plant elements are suppressed. Due to low particle number concentrations, coagulation is not a major particle growth mechanism in the pristine areas.

The abundant sunlight and low relative humidity have important effects on the formation and growth of sulfate aerosol. Gas-to-particle conversion by heterogeneous droplet phase processes is suppressed relative to gas phase homogeneous reactions. As shown in the sulfur distribution for Trona (Figure 1.1), this may lead to the accumulation of sulfate mass in particle sizes less than 0.26 μm, which are not efficient in scattering visible solar radiation. Since coagulation is relatively slow for particles greater than 0.1 μm, the sulfate aerosol does not grow by this mechanism into larger particles which are more efficient in scattering light. The low relative humidity prevents aerosol growth due to condensation of water on the hygroscopic ammonium sulfate. The aged sulfur distributions measured in China Lake were very similar to that found in Trona.

These results are contrasted with those found in Pasadena, where sulfate usually accumulates in 0.5-1.0 μm diameter particles, shown in Figure 1.2. This may be due to droplet phase conversion, which would favor growth into larger particles (Friedlander, 1978; Gelbard and Seinfeld, 1979a). By virtue of its mass distribution alone the Pasadena sulfate scatters light efficiently. Its ability to pick up

water amplifies the effect. Interestingly enough, the hygroscopic growth of sulfate from this size range has a synergistic effect on its light scattering efficiency. As the sulfate adds water it grows in diameter, and the particle refractive index, m, decreases (Sverdrup, 1977). Examining Figure 2.1 it is seen that as m decreases from 1.54 ($(NH_4)_2SO_4$) to 1.33 (H_2O) the peak efficiency is achieved for larger particles. Thus, a 0.50 μm sulfate particle which grows by addition of water remains at an optimum size for scattering light.

It is apparent from this research that aerosol nitrate is found in very low concentrations in remote arid locations. Virtually all airborne nitrate remains as gaseous nitric acid. The gas phase conversion of NO_2 to HNO_3 in the desert currently has a beneficial effect on visibility. It removes the light-absorbing NO_2 and produces non-absorbing HNO_3 in insufficient concentrations to produce pure aerosol NH_4NO_3. However, it is possible that nitric acid may increase aerosol and soil acidity by its deposition on coarse alkaline aerosol and the ground surface.

In this research I found the effects of soot on light extinction in the desert to be very interesting. It is very efficient on a mass concentration basis in reducing visibility, principally through light absorption. Consistent with theory, the soot particles which were too small to scatter light efficiently nevertheless caused significant visibility degradation by light absorption. Future increases in soot concentration would have disproportionately adverse effects on visibility.

REFERENCES

Allee, P.A., Pueschel, R. F., and Wagner, W. W. (1978) On the Co-Existence of Natural and Man-Made Aerosols in a Rural Environment. Reprinted from Proceedings, 4th Joint Conference on Sensing of Environmental Pollutants, American Chemical Society.

Bergstrom, R. W. (1973). Extinction and Absorption Coefficients of the Atmospheric Aerosol as a Function of Particle Size, Beitr. Phys. Atmos., 46: 223.

Blumenthal, D. L., Richards, L. W., Macias, E. S., Bergstrom, R. W. (1980). Effects of a Coal-Fired Power Plant and Other Sources on Southwestern Visibility. To be presented at the Symposium on Plumes and Visibility: Measurements and Model Components, Grand Canyon, Ariz., Nov. 10-14, 1980.

Cahill, T. A. (1975). "Environmental Analysis of Environmental Samples," in New Uses of Ion Accelerators, J. Ziegler, Ed., 1-75, Plenum Press, NY.

Camp, D. C., Van Lehn, A. L., Loo, B. W. (1978). Intercomparison of Samplers Used in the Determination of Aerosol Composition, EPA 600/7-78-118.

Camp, D. C., Van Lehn, A. L., Rhodes, J. R., and Pradzynski, J. (1975). Intercomparison of Trace Element Determinations in Simulated and Real Air Particulate Samples. X-ray Spectrometry, 4: 123. (CNL PIXE = #15, CNL XRF = #4).

Camp, D. C. (1973). Intercomparison of Trace Element Determinations from Fine Analytical Techniques. A.N.S. Transactions, 17: 106.

Cass, G. R. (1979). On the Relationship between Sulfate Air Quality and Visibility with Examples in Los Angeles. Atmospheric Environment, 13: 1069.

Charlson, R. J., Waggoner, A. P., and Thielke, J. F. (1978). Visibility Protection for Class I Areas: the Technical Basis. Report to Council on Environmental Quality, August, 1978. Available from the National Technical Information Service. PB-288-842.

Cooper, D. W., and Spielman, L. A. (1976). Data Inversion Using Non-linear Programming with Physical Constraints: Aerosol Size Distribution Measurement by Impactors. Atmospheric Environment, 10: 723.

Dalzell, W. H. and Sarofim, A. F. (1969). Optical Constants of Soot and their Applicability to Heat-Flux Calculations. J. Heat Transfer, 91: 100.

Davidson, C. I. and Friedlander, S. K. (1978). A Filtration Model for Aerosol Dry Deposition: Application to Trace Metal Deposition from the Atmosphere. J. Geophysical Research, 83: 2343.

De Luisi, J. J., Furakawa, P. M., Gillette, D. A., Schuster, B. G., Charlson, R. J., Porch, W. M., Fegley, R. W., Herman, B. M., Rabinoff, R. A., Twitty, J. T., and Weinman, J. A. (1976). Results of a Comprehensive Atmospheric Aerosol-Radiation Experiment in the Southwestern United States. Part I: Size Distribution, Extinction Optical Depth and Vertical Profiles of Aerosols Suspended in the Atmosphere. J. Applied Meteorology, 15: 441.

Elder, J. C., Ettinger, H. J., and Nelson, R. Y. (1974). Chamber Studies of Visibility-Reducing Aerosols. Atmospheric Environment, 8: 1035.

Ensor, D. S., Charlson, R. J., Ahlquist, N. C., Whitby, K. T., Husar, R. B., and Liu, B. Y. H. (1972). Multiwavelength Nephelometer Measurements in Los Angeles Smog Aerosol - I. Comparison of Calculated and Measured Light Scattering. J. Colloid Interface Science, 39: 242.

Flagan, R. C. and Taylor, D. D. (1980). Laboratory Studies of Submicron Particles from Coal Combustion. Submitted for presentation at the Eighteenth Symposium (International) on Combustion, University of Waterloo, Ontario, Canada, August, 1980.

Franklin, J. N. (1968). Matrix Theory. Prentice-Hall, Inc., Englewood Cliffs, N. J.

Friedlander, S. K. (1970). The Characterization of Aerosols Distributed with Respect to Size and Chemical Composition. J. Aerosol Science, 1: 295.

Friedlander, S. K. (1971). The Characterization of Aerosols with Respect to Size and Chemical Composition--II. Classification and Design of Aerosol Measuring Devices. J. Aerosol Science, 2: 331.

Friedlander, S. K. (1977). Smoke, Dust and Haze: Fundamentals of Aerosol Behavior. Wiley-Interscience, New York.

Friedlander, S. K. (1978). A Review of the Dynamics of Sulfate Containing Aerosols. Atmospheric Environment, 12: 187.

Fymat, A. L. (1979). Analytical Inversions in Remote Sensing of Particle Size Distributions. 3: Angular and Spectral Scattering in the Rayleigh-Gans-Born Approximation for Particles of Various Geometrical Shapes. J. Applied Optics, 18: 126.

Fymat, A. L. and Mease, K. D. (1978). In Remote Sensing of the Atmosphere: Inversion Methods and Applications, A. L. Fymat and V. E. Zuev, Eds. Elsevier, Amsterdam.

Gelbard, F. and Seinfeld, J. H. (1979a). Exact Solution of the General Dynamic Equation for Aerosol Growth by Condensation. J. Colloid and Interface Science, 68: 173.

Gelbard, F. and Seinfeld, J. H. (1979b). The General Dynamic Equation for Aerosols. J. Colloid and Interface Science, 68: 363.

Gelbard, F. and Seinfeld, J. H. (1980). Simulation of Multicomponent Aerosol Dynamics. Accepted for publication in J. Colloid and Interface Science.

Gibbs, R. J. (1978). Light Scattering from Particles of Different Shapes. J. Geophysical Research, 83: 501.

Grosjean, D. (1977). " Aerosols" in Ozone and Other Photochemical Oxidants, National Research Council, National Academy of Sciences, Washington, D.C.

Grosjean, D. and Friedlander, S. K. (1975). Gas-Particle Distribution Factors for Organic and Other Pollutants in the Los Angeles Atmosphere. J. Air Pollution Control Association, 25: 1038.

Hansen, L. (1979). Personal communication to T. Cahill, University of California, Davis.

Hering, S. V., Flagan, R. C., and Friedlander, S. K. (1978). Design and Evaluation of a New Low-Pressure Impactor. 1. Environmental Science and Technology, 12: 667.

Hering, S. V., Friedlander, S. K., Collins, J. J., and Richards, L. W. (1979). Design and Evaluation of a New Low-Pressure Impactor. 2. Environmental Science and Technology, 13: 184.

Ho, W., Hidy, G. M., and Govan, R. M. (1974). Microwave Measurements of the Liquid Water Content of Atmospheric Aerosols. J. Applied Meteorology, 13(8): 871-879.

Hodkinson, J. R. (1964). Refractive Index and Particle-Extinction Efficiency Factors for Carbon. J. Optical Society of America, 54: 846.

Holland, A. C. and Draper, J. S. (1967). Analytical and Experimental Investigation of Light Scattering from Polydispersions of Mie Particles. J. Applied Optics, 6(5): 511.

Holland, A. C. and Gagne, G. (1970). The Scattering of Polarized Light by Polydisperse Systems of Irregular Particles. J. Applied Optics, 9(5): 1113.

Japar, S. M. and Killinger, D. K. (1979). Photoacoustic and Absorption Spectrum of Airborne Carbon Particulate Using a Tunable Dye Laser. Chemical Physics Letters, 66: 207.

John, W. and Reischl, G. (1978). A Cyclone for Size-Selective Sampling of Ambient Air. AIHL Report No. 187, Air and Industrial Hygiene Laboratory, 2151 Berkeley Way, Berkeley, California 94704.

Kerker, M. (1969). The Scattering of Light and Other Electromagnetic Radiation. Academic Press, New York.

Kittleson, D. B. and Dolan, D. F. (1979). Diesel Exhaust Aerosols. Particle Technology Publication No. 387. University of Minnesota, Minneapolis 55455.

Liljestrand, H. M. (1979). Atmospheric Transport of Acidity in Southern California by Wet and Dry Mechanisms. Ph.D. Thesis, California Institute of Technology, Pasadena, CA 91125.

Lin, C., Baker, M., and Charlson, R. J. (1973). Absorption Coefficient of Atmospheric Aerosol: A Method for Measurement. J. Applied Optics, 12(6): 1356.

Macias, E. S., Radcliff, C. D., Lewis, C. W., and Sawaki, C. R. (1978). Proton-Induced γ-ray Analysis of Atmospheric Aerosols for Carbon, Nitrogen, and Sulfur Composition. Anal. Chem., 50: 1120.

Macias, E. S., Blumenthal, D. L., Anderson, J. A., and Cantrell, B. K. (1979). Characterization of Visibility-Reducing Aerosols in the Southwestern United States: Interim Report of Project VISTTA, MRI 78-IR-1585.

Marple, V. A. and Lui, B. Y. H. (1974). Characteristics of Laminar Jet Impactors. Environmental Science and Technology, 8: 648.

Marple, V. A. and Lui, B. Y. H. (1975). On Fluid Flow and Impaction in Inertial Impactors. J. Colloid and Interface Science, 53: 31.

Mason, B. (1966). Principles of Geochemistry. J. Wiley and Sons, Inc., New York.

Mathews, L. A. and Cronin, H. E. (1980). Size Distributions of Atmospheric Aerosol at China Lake, California. NWC Technical Memorandum TM 4109 (Unclassified), in preparation. Naval Weapons Center, China Lake, CA 93555.

McMurry, P. H. and Friedlander, S. K. (1979). New Particle Formation in the Presence of an Aerosol. Atmospheric Environment, 13: 1635.

Middleton, W. E. K. (1952). Vision Through the Atmosphere. University of Toronto Press, Toronto, Canada.

Mie, G. (1908). Beitrage zur Optik truber Medien, speziell Kolloidaler Metallosungen. Ann. Physik, 25: 377.

Miguel, A. H. and Friedlander, S. K. (1978). Distribution of Benzo[A]Pyrene and Coronene with Respect to Particle Size in Pasadena Aerosols in the Submicron Range. Atmospheric Environment, 12: 2407.

Ouimette, J. R. (1974). Survey and Evaluation of the Environmental Impact of Naval Weapon Center Activities. TM 2426, U.S. Naval Weapons Center. Available from National Technical Information Service.

Patterson, E. M., Gillette, D. A., and Grams, G. W. (1976). The Relationship between Visibility and the Size-Number Distribution of Airborne Soil Particles. J. Applied Meteorology, 15: 470.

Patterson, R. K. and Wagman, J. (1977). Mass and Composition of an Urban Aerosol as a Function of Particle Size for Several Visibility Levels. Atmospheric Environment, 8: 269.

Pierson, W. R. (1978). Particulate Organic Matter and Total Carbon from Vehicles on the Road. Proceedings, Conference on Carbonaceous Particles in the Atmosphere, Berkeley, California, March 20-22, 1978.

Pierson, W. R. and Russell, P. A. (1979). Aerosol Carbon in the Denver Area in November 1973. Atmospheric Environment, 13: 1623.

Pinnick, R. G., Carroll, D. E., and Hofmann, D. J. (1976). Polarized Light Scattered from Monodisperse Randomly Oriented Nonspherical Aerosol Particles: Measurements. J. Applied Optics, 15(2): 384.

Pinnick, R. G., Rosen, J. M., and Hofmann, D. J. (1973). Measured Light-Scattering Properties of Individual Aerosol Particles Compared to Mie Scattering Theory. J. Applied Optics, 12(1): 37.

Richards, L. W. (1979). Ammonia and Sulfate Aerosol Study, Final Report. Prepared for Coordinating Research Council, Inc., by Rockwell International, Environmental Monitoring and Services Center.

Roberts, P. T. and Friedlander, S. K. (1976). Analysis of Sulfur in Deposited Aerosol Particles by Vaporization and Flame Photometric Detection. Atmospheric Environment, 10: 403.

Roessler, D. M. and Faxvog, F. R. (1979). Optoacoustic Measurement of Optical Absorption in Acetylene Smoke. J. Optical Society of America, 69: 1699.

Rosen, H., Hansen, A. D. A., Dod, R. L., and Novakov, T. (1977). Application of the Optical Absorption Technique to the Characterization of the Carbonaceous Component of Ambient and Source Particulate Samples. Report LBL-6844, Lawrence Berkeley Laboratory, Berkeley, California.

Schumacher, P. M. and Spicer, C. W. (1976). Interferences in the Sampling of Particulate Atmospheric Nitrate. Presented at the 172nd ACS Meeting, San Francisco.

Spicer, C. W. (1979). Measurement of Gaseous HNO_3 by Electrochemistry and Chemiluminescence in Current Methods to Measure Atmospheric Nitric Acid and Nitrate Artifacts, R. K. Stevens, Ed. EPA-600/2-79-051, Environmental Protection Agency.

Spicer, C. W. and Schumacher, P. M. (1977). Interferences in Sampling Atmospheric Particulate Nitrate. Atmospheric Environment, 11: 873.

Stelson, A. W., Friedlander, S. K., and Seinfeld, J. H. (1979). A Note on the Equilibrium Relationship between Ammonia and Nitric Acid and Particulate Ammonium Nitrate. Atmospheric Environment, 13: 369.

Sverdrup, G. M. (1977). Parametric Measurement of Submicron Atmospheric Aerosol Size Distributions. Ph.D. Thesis, Particle Technology Laboratory, University of Minnesota, Minneapolis 55455.

Trijonis, J. and Yuan, K. (1978a). Visibility in the Southwest: An Exploration of the Historical Data Base. EPA-600/3-78-039.

Trijonis, J. and Yuan, K. (1978b). Visibility in the Northeast: Long-Term Visibility Trends and Visibility/Pollutant Relationships. EPA-600/3-78-075.

Twomey, S. (1975). Comparison of Constrained Linear Inversion and Interactive Nonlinear Algorithm Applied to the Indirect Estimation of Particle Size Distributions. J. Comp. Phys., 18: 188.

van de Hulst, H. C. (1957). Light Scattering by Small Particles. John Wiley and Sons, Inc., New York.

Waggoner, A. P., Vanderpol, A. J., Charlson, R. J., Larsen, S., Granat, L., and Tragardh, C. (1976). Sulphate-Light Scattering Ratio as an Index of the Role of Sulphur in Tropospheric Optics. Nature, Lond., 261: 120.

Waggoner, A. P. and Charlson, R. J. (1977). Measurements of Aerosol Optical Properties. Proceedings of the Symposium on Denver Air Pollution Study-1973. Russell, P. A., Ed. Volume II , EPA-600/9-77-001.

Weiser, P., Stolzenburg, M., and Baumueller, J. (1977). Aerosol Particles: Remarks on the Optical Properties. J. Applied Optics, 16: 2651.

Weiss, R., Charlson, R. J., Waggoner, A. P., Baker, M. B., Covert, D., Thorsell, D., and Yuen, S. (1976, August). Application of Directly Measured Aerosol Radiative Properties to Climate Models. Presented at the IAMAP/Radiation Commission Meeting, Garmisch Partenkirchen, West Germany.

Weselowski, J. J., John, W., Devor, W., Cahill, T. A., Feeney, P. J., Wolfe, G., and Flocchini, R. (1977). Collection Surfaces of Cascade Impactors, in X-Ray Fluorescence Analysis of Environmental Samples, Ann Arbor Science, Ann Arbor, Michigan.

Whitby, K. T., Liu, B. Y. H., Husar, R. B., and Barsic, N. J. (1972). The Minnesota Aerosol-Analyzing System Used in the Los Angeles Smog Project. J. Colloid and Interface Science, 39: 136.

Whitby, K. T. and Cantrell, B. K. (1979). Electrical Aerosol Analyzer Constants, in Aerosol Measurement, D. A. Lundgren, S. S. Harris, Jr., W. H. Marlow, M. Lippmann, W. E. Clark, M. D. Durham, Eds. University Presses of Florida, Gainsville, Fla.

White, W. H. and Roberts, P. T. (1977). On the Nature and Origins of Visibility-Reducing Aerosols in the Los Angeles Air Basin. Atmospheric Environment, 11: 803.

Wickramasinghe, N. C. (1973). Light Scattering Functions for Small Particles with Applications in Astronomy. John Wiley and Sons, New York.

APPENDIX A

AEROSOL ELEMENTAL MASS DISTRIBUTIONS USING THE LOW PRESSURE IMPACTOR AND ANALYSIS BY PARTICLE INDUCED X-RAY EMISSIONS

A.1 INTRODUCTION

It was shown in Chapter 2 that the contributions of aerosol chemical species to the extinction coefficient can be estimated by numerically integrating their theoretical mass extinction efficiencies with measured mass distributions over the particle size range. The theoretical mass extinction efficiencies for common atmospheric aerosols, shown in Figures 2.1 and 2.2, indicate the importance of the fine ($D < 2$ μm) aerosol in light scattering and absorption.

The low pressure impactor (LPI) is capable of size segregating aerosol for chemical analysis through the "optically active" particle diameter range of 0.1 to 2 μm. Until recently, routine chemical analysis of aerosol size segregated by the LPI was limited to sulfur by the technique of flash volatilization and flame photometric detection (FVFPD).

This appendix describes the use of the LPI with the particle induced X-ray emission (PIXE) technique for elemental analysis. An appropriate LPI aerosol impaction surface was devised for the elemental analysis of aerosol deposits by a focused alpha particle beam at the Crocker Nuclear Laboratory (CNL), University of California, Davis.

Nanogram sensitivities were obtained for most elements having atomic weights between aluminum and lead. The accuracy and precision of the technique were estimated using known standards and field samples. Elemental mass balances and distributions obtained by the LPI-PIXE technique were compared with other analytical techniques.

A.2 EXPERIMENTAL

A.2.1 Sample Collection

In order to evaluate the LPI-PIXE technique ambient aerosol was sampled at Zilnez Mesa, Arizona, from June 27-July 13, 1979, using the sampling arrangement shown in Figure 3.2. The description of the sampling and analysis can be found in Chapter 3. A total of 12 samples were collected, each consisting of a LPI-PIXE field blank, an LPI sample for PIXE analysis, an LPI sample for sulfur analysis by FVFPD, and a Nuclepore filter sample for elemental and ion analysis. These samples were used to evaluate the PIXE focused beam detection limit, field blank values, measurement precision, elemental mass balances, and sulfur mass distributions obtained with the LPI-PIXE technique.

Airborne aerosol sampling sponsored by VISTTA was conducted during the summer of 1979 in the Southwest by Dr. Susanne Hering of the UCLA Air Quality Laboratory in cooperation with the Environmental Protection Agency, Las Vegas. The results of the experiments will be described in a future paper by Dr. Hering. An arrangement similar to Figure 3.2 was used to collect and size segregate fine aerosol for chemical analysis. Sample times for the airborne samples varied from 4

to 6 hours. The results of four of the airborne LPI-PIXE and LPI-FVFPD samples are included in this appendix to compare the aerosol sulfur mass distributions obtained by each technique.

One LPI-PIXE sample was collected on the roof of Guggenheim Laboratory at Caltech from 1127-1437 PST, February 6, 1980, under poor visibility conditions. The mylar substrate was coated with 1.0 µl of 2% vaseline in toluene, resulting in a coating mass density of 90-140 $\mu g/cm^2$. No cyclone was used upstream of the LPI to remove coarse aerosol. This sample was used to test the anti-bounce properties of the vaseline-coated mylar with high aerosol loadings in the LPI.

Ambient aerosol was sampled on the roof of Keck Laboratory at Caltech from February 23-28, 1980. On seven occasions two LPI's with coated stainless steel strips sampled simultaneously to obtain sulfur mass distributions by FVFPD. In one impactor the strips were coated with 90-140 $\mu g/cm^2$ Apiezon L grease, which was twice the coating mass density used in the Zilnez Mesa and the airborne samples. The strips in the other impactor were coated with vaseline. Sample times varied from 6 to 18 hours due to unusually clear dry conditions. No cyclones were used upstream of the LPI's to remove coarse aerosol.

A.2.2 LPI-PIXE Collection Surface

This section provides a general description of the LPI-PIXE collection surface and detailed procedures for preparing the substrate for sampling and analysis.

In each LPI stage the aerosol particles impact on the center of a 3.2 μm-thick coated mylar film (Mylar Type S, 580 μg/cm^2, DuPont Nemours, Inc.). The mylar is fastened to a 25 mm glass disc with a 25 mm circular paper self-adhesive label with a 13 mm center hole. The resulting 13 mm diameter exposed mylar collection surface is much larger than the sample deposits, typically 0.7 to 2.0 mm diameter. In order to eliminate fluttering of the mylar during sampling and possible changes in particle collection efficiency, the mylar is adhered to the glass disc using a thin coating of Apiezon L vacuum grease or vaseline. An exploded view of the LPI mylar collection surface is shown in Figure A.1.

Apiezon L was originally chosen for coating the mylar collection surface to prevent particles from bouncing to the next stage of the LPI. Weselowski et al. (1977) found it to be nonvolatile at a pressure of 1 μm Hg for 3 hours and to have uniformly low blank values for elements measured by PIXE. They found that coatings of 65 μm/cm^2 were adequate to reduce bounce-off of dry coarse and fine ambient aerosols to less than 2% with multi-day impactors operating at 20 lpm and atmospheric pressure. For the Zilnez Mesa and airborne LPI-PIXE samples, a microliter syringe was used to apply 0.50 μl of a 2% by weight solution of Apiezon L in Spectrograde toluene to the center of each collection surface. After evaporation of the toluene, the Apiezon L coating remaining was 4-5 mm in diameter, 44-69 μg/cm^2, and 0.3-0.5 μm thick. It will be shown later in this appendix that this coating density did not eliminate bounceoff of submicron aerosol in the low pressure stages

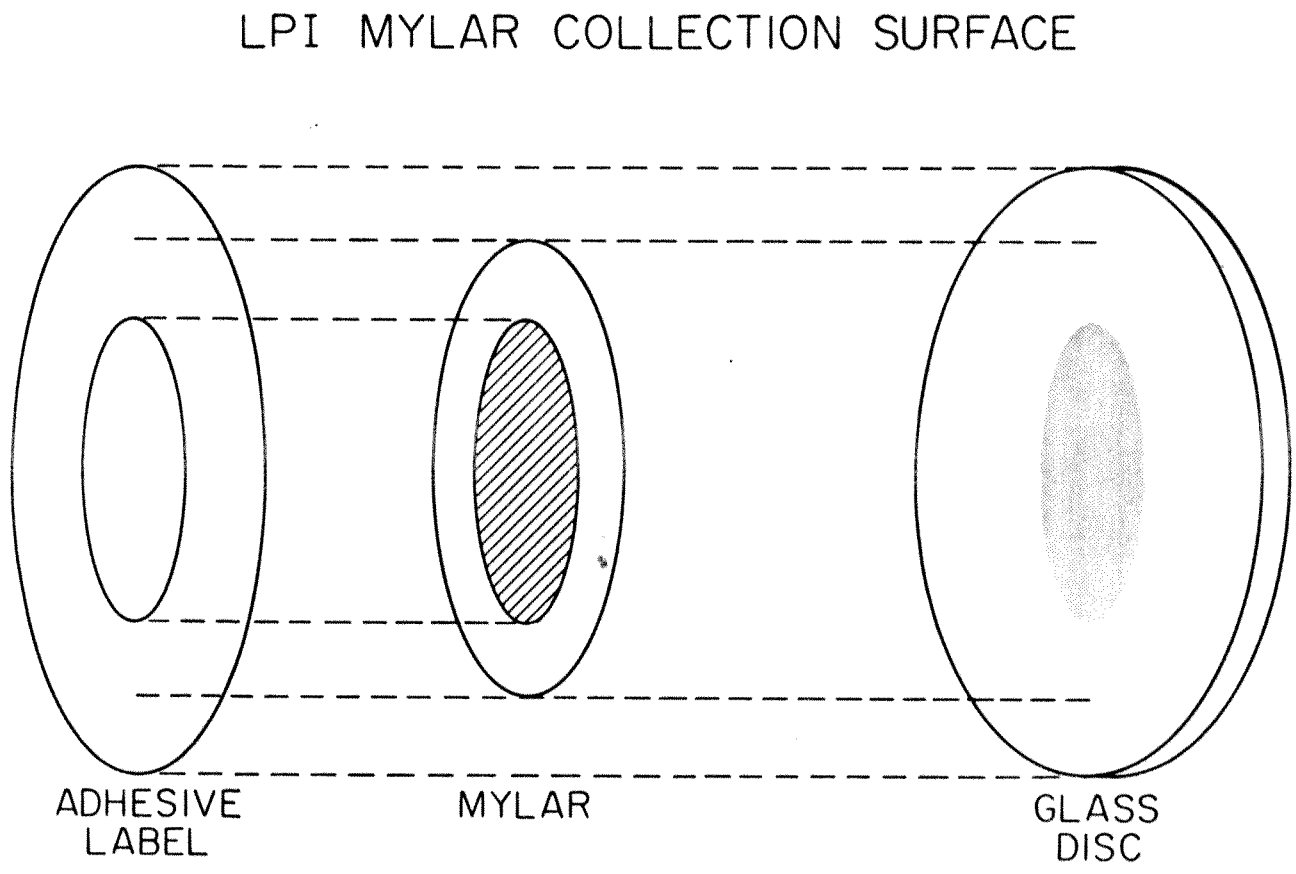

Figure A.1. Mylar collection surface for elemental and light absorption analysis. Mylar is attached to adhesive paper ring whose inner and outer diameters are 13 and 19 mm, respectively. This is fastened to 25 mm glass disc with a 25 mm circular paper self-adhesive label with a 13 mm center hole. A thin coating of Apiezon L vacuum grease on the glass disc acts as an adhesive, preventing the mylar from fluttering. After sample collection the 25 mm label with attached mylar is peeled off the glass disc for analysis.

of the LPI. The recommended mylar coating for the LPI-PIXE samples is currently 1.0 µl of 2% by weight vaseline in toluene, applied 0.50 µl at a time to the center of the impaction surface. It will be shown that this coating prevents particle bounceoff and will produce low elemental blank values.

A.2.2.1 Preparation of LPI-PIXE Collection Surface -

A detailed description of the technique used to prepare the LPI-PIXE collection surface is included in this section. Although the procedure describes how to prepare 8 substrates for one LPI sample, any number can be made in advance if they are stored properly to prevent contamination. It is recommended that one field blank be prepared for each LPI sample to be handled and analyzed exactly as the samples.

Punch out the 13 mm (1/2") diameter centers from eight 19 mm (3/4") and eight 25 mm (1") diameter circular paper self-adhesive labels. Spread mylar (Type S, 580 µg/cm^2, DuPont Nemours, Inc.) on a 3-6 mm thick Teflon sheet and tape the edges of the mylar to the sheet to hold it tight. Remove the backing from the 19 mm outer diameter (OD) self-adhesive paper rings and adhere them to the mylar. Use a 19 mm hand punch to punch out the eight 19 mm OD mylar circles.

Lay the mylar circles on a clear surface with the paper ring side down in a filtered glove box, laminar flow hood, or clean room. Using a Q-tip, clean the bottom mylar surface with toluene. Remove static charge with Po 210 500 µc radioactive decharger. Turn the mylar circle over, exposing the paper ring. Clean eight 25 mm diameter glass discs

with methanol or ethanol. Apply a thin coating of Apiezon L vacuum grease to the 13 mm diameter center of the glass disc. Peel the backing off each 25 mm OD self-adhesive paper ring and adhere it to the top of each 19 mm mylar circle, with the 13 mm hole centered on the exposed mylar surface. This results in a 25 mm OD substrate with a 13 mm mylar center and a 3 mm annular ring of exposed self-adhesive on the backside.

Using a pair of electron microscope (EM) tweezers, place each mylar substrate on a coated glass disc. See Figure A.1 for an exploded view. Press the outside edge of the substrate to the glass disc to adhere it to the disc. Clean the mylar with a Q-tip and toluene. This will also adhere the mylar to the glass disc. Decharge the mylar. Apply 1.0 µl of a 2% by mass solution of vaseline in toluene to the center of the mylar, 0.50 µl at a time. Allow the toluene to evaporate. After properly labeling the disc, load it into the LPI stage.

A.2.2.3 Preparation of LPI-PIXE Sample for Analysis -

After sample collection remove the glass disc from each LPI stage inside a filtered glove box or other clean area. Remove the mylar substrate from the glass disc with EM tweezers. Mount the sample on a properly labeled 35 mm slide with a 13 mm center hole. Use a guide to insure the aerosol deposit is carefully centered on the slide frame. This is critical since the PIXE focused beam is only 3-4 mm diameter. Clean the backside of the mylar with a Q-tip and toluene. Decharge the

mylar. Examine the mounted sample carefully for extraneous lint and other contamination and remove with the EM tweezers.

Mount the slide in a 35-mm slide tray and place in a ziplock bag. Prepare a run sheet (from Crocker Nuclear Laboratory) listing the sample by slide and tray number. Send a copy of the run sheet and the samples to CNL for PIXE analysis. Certified mail with a return receipt is recommended.

A.2.3 Sample Analysis by PIXE Focused Beam

A detailed description of the PIXE analytical system is given by Cahill (1975). Alpha beams from an isochronous cyclotron, possessing energies of 18 MeV, are used to excite X-rays in the aerosol samples, which are mounted at an angle of 45 to the incoming beam. The target slide changer operates under realtime computer control, providing irradiation times of 60-120 seconds. The beam spot is made uniform by use of an aluminum diffusion foil. The X-rays emitted from the sample are detected by a Si(Li) X-ray detector. On-line data collection and reduction codes generate area mass densities for elements between sodium and uranium, with minimum detectable limits ranging from a few nanograms per square centimeter to, when interferences are present, several hundred nanograms per square centimeter.

Internal validation of calibration is routinely performed by analysis of 24 thin standard foils, tests of dead time correction vs. count rate, and routine reanalysis of previously analyzed samples. In addition, three major external interlaboratory comparisons with CNL

PIXE have been made (Camp et al., 1973; Camp et al., 1975; Camp et al., 1978). Based on the results, an absolute accuracy of $\pm$ 10% is achieved.

In order to analyze aerosol deposits no larger than 2 mm in diameter, such as those obtained with the LPI, CNL has developed small area ion beams. A significant increase in sensitivity compared to analysis of filters is achieved using this beam on small deposits. For example, a nominal sensitivity of 10 ng/cm^2 results in a sensitivity of 1 ng for a focused beam of 0.1 cm^2 area. The beam is collimated to a nominal 3 mm diameter and its location is verified on a phosphor. A "burn" is made on Whatman 41 paper mounted on a 35-mm slide frame for determination of beam area and spatial homogeneity.

A.2.3.1 Determination of focused beam area and precision -

Accurate determination of effective beam area by direct measurement of the "burn" on the Whatman 41 paper is rather difficult. The effective area of the beam can also be calculated by placing a known amount of material on a clean substrate and analyzing it. Since the mass is known, the beam area can be found. Twenty-four samples were prepared by scientists at the Energy Related Health Research Laboratory at Davis (Hansen, 1979). These samples contained known amounts of H_2SO_4, $(NH_4)_2SO_4$, K_2SO_4, and hydrated ferrous sulfate; half were coated with plastic to check possible losses in vacuum of sulfur species. The data for these analyses were used to compute the precision of the focused beam. No volatilization of sulfur species was found.

Precisions calculated from these samples varied from ± 12% for hydrated ferrous sulfate to ± 30% for K_2SO_4.

In addition, these samples were used to calculate the effective beam area for X-ray production for the day of the analysis. This was found to be 0.19 ± 0.01 cm^2, which was about 19% higher thna the measured "burn" area of 0.16 cm^2. The "burn" area of the beam used to analyze the Zilnez Mesa field samples was measured to be 0.08 cm^2. Based on the standards, this was corrected to 0.095 cm^2 for determining elemental mass values from area densities.

Accurate determination of the beam area is critical, since the elemental masses on each sample are computed from the product of the elemental mass area densities (ng/m^2) and the beam area. Currently the focused beam area can be measured to within ± 10-20%, resulting in a possible systematic error of that magnitude in the determination of elemental mass.

A.2.3.2 Elemental detection limits and field blank values -

The use of the focused beam results in enhanced sensitivities. Due to the X-ray spectrum produced, the detection limit of one element is influenced by the quantities of other elements present. Lower detection limits of elemental masses are listed in Table A.1 and apply to a clean sample. For some elements they may be up to a factor of three higher for heavily loaded samples.

Table A.1

Detection Limits and Average Blank Values

for CNL PIXE Focused Beam

Element	Lower Detection Limit, ng	Average Vaseline Laboratory Blank Value, ng	Average Apiezon L Field Blank Value, ng
Na	21	*	*
Al	6	7.0 ± 3.3	6 ± 6
Si	4	*	14 ± 8
P	5	*	*
S	4	3.6 ± 0.8	9 ± 4
Cl	4	*	*
K	2	4.1 ± 2.0	*
Ca	1.4	1.4 ± 0.1	2 ± 2
Ti	1.2	*	*
V	1.2	*	*
Cr	1.0	*	*
Mn	0.9	*	*
Fe	0.9	*	0.9 ± 0.9
Ni	0.8	*	*
Cu	0.7	*	*
Zn	1.0	*	1.7 ± 2
Se	1.4	*	*
Br	1.5	2.1 ± 0.4	*
Pb	3.5	*	*

Both laboratory mylar blanks and Zilnez Mesa field blanks were used in the analysis of field samples. The field blanks were first analyzed as samples (lab blanks were used for blank subtraction) to see if any contamination occurred due to handling. An "average" field blank was then used for blank subtraction in subsequent analyses. Major elements on typical impactor field blanks were primarily soil-like particles (Al, Si, Ca, Fe), phosphorus, probably from the mylar backing material, and sulfur from the Apiezon L anti-bounce coatings. The Zilnez Mesa elemental field blank values for a 0.095 cm^2 beam area and a coating of 44-69 $\mu g/cm^2$ Apiezon L vacuum grease are shown in Table A.1.

Three laboratory mylar blanks were coated with 125 $\pm$ 30 $\mu g/cm^2$ vaseline at Caltech and analyzed by PIXE focused beam with a beam area of 0.08 cm^2. The results are shown in Table A.1. Although twice the mass area density of the Apiezon L, the vaseline had a lower sulfur blank. This was verified by FVFPD analysis of Apiezon L applied to stainless steel strips. The higher Apiezon L silicon blank is probably due to contamination in handling and not to the grease itself.

A.2.3.3 Estimate of precision from field samples -

Ten samples were randomly selected from the Zilnez Mesa and airborne samples and reanalyzed at the end of the analysis run in August 1979 with a calculated 0.095 cm^2 beam area. The same set was subsequently reanalyzed in September 1979 with a larger beam area of 0.19 cm^2. For five major elements the ratio of the repeated run value to the original value was calculated for each sample. For each element

the average ratio and its standard deviation was calculated. The standard deviation for each element was used as the precision of the focused beam measurements. The results are shown in Table A.2. Because the samples were collected in very clean air and were not heavily loaded, this test of precision is considered to be a rather stringent one. The field blank precisions for the smaller focused beam were found to be slightly lower than for the laboratory standards and slightly higher than those determined from the 1978 interlaboratory comparison (Camp et al, 1978).

Table A.2

Estimate of CNL PIXE Focused Beam Precision

From Repeated Measurements of Field Samples

Element	Precision, %	
	Beam area 0.095 cm^2	Beam area 0.190 cm^2
Si	17	21
S	8	19
K	16	17
Ca	13	21
Fe	8	29

A.3 RESULTS

A.3.1 Aerosol Sulfur Mass Balance

Total fine aerosol sulfur concentrations were determined from the Zilnez Mesa field samples by three techniques, in addition to the ion-chromatographic determination of sulfate. The Nuclepore filters were analyzed by PIXE for sulfur and by liquid ion chromatography for sulfate. Each of the LPI's provided size resolved sulfur distributions; the total concentrations were found by summing the contributions from each stage. It was assumed that all the fine aerosol sulfur was sulfate. The results of the comparison are discussed in Chapter 3 and shown in Table 3.7. Table 3.8 provided the average ratios and standard deviations of the different determinations of sulfate concentration. Agreement among all methods was good, although the LPI-PIXE sulfate total averaged 2-9% lower than the other techniques and the LPI-FVFPD sulfate was 4-8% high. The LPI-PIXE discrepancy was probably due to error in the determination of the alpha beam area. Sample times for the LPI operated for FVFPD were, in general, not equal to the other techniques. Thus, its comparison with the other techniques is subject to some error.

A.3.2 Mass Balances for Other Species

In a manner similar to that used for sulfur, the total concentrations of other elements can be found by adding the contributions determined by PIXE analysis of each LPI stage. The total was compared with the concentrations of those species determined by PIXE analysis of

the Nuclepore filters. The results for each episode are summarized in Table 3.9. The LPI samples consistently contained small quantities of Al, Zn, and Pb which were below detectable limits by PIXE analysis of Nuclepore filers. With the exception of sulfur, which was found almost exclusively in particles of less than 2 μm aerodynamic diameter, higher elemental mass concentrations were determined by LPI-PIXE than by PIXE analysis of the Nuclepore filters. This is probably due to loss of larger particles from the uncoated Nuclepore filter. The cyclone is operated in such a way that the fine particle airstream flows vertically. Particles are collected on the underside of the Nuclepore filter. Gravitational forces may exceed van der Waals and electrostatic forces for the coarse particles, resulting in their loss by sedimentation. Handling of the filter may also result in loss of larger particles from the filer.

It was found from the LPI-PIXE results that Si, Ca, and Fe were found almost exclusively in particles greater than 1 μm aerodynamic diameter, whereas a substantial fraction of K was often found in the fine mode, particularly during forest fire episodes. When only particles less than 2 μm aerodynamic diameter were considered in the LPI-PIXE results, the agreement with the filter measurement is acceptable. Thus, the coated impaction surfaces of the LPI are more efficient than the Nuclepore filter in collecting the fraction of coarse material which passed through the cyclone.

A.3.3 Comparison of Sulfur Aerosol Mass Distribution: PIXE vs FVFPD

A total of 11 Zilnez Mesa samples and 4 airborne samples were used to compare the aerosol sulfur mass distributions determined by LPI-PIXE and LPI-FVFPD. The airborne samples chosen had higher average sulfur concentrations than the Zilnez Mesa samples. The FVFPD is a somewhat more sensitive technique, with a smaller sulfur blank, 1-2 ng, due to the vaseline coating, and is specific to sulfur. Because of its previous agreement with other measurements of aerosol distributions in sulfur-dominated laboratory and field experiments, FVFPD was used as the standard in this comparison. Sample times for LPI-PIXE varied from less than 4 hours (airborne) to over 47 hours at Zilnez Mesa. Since different sample times were used with each technique, the results of any one episode would not be strictly quantitative. Because of the generally very clean air sampled, a number of the PIXE samples had values within a factor of two of the mean field blank value of 9 ng S. This was almost always true for LPI stages 1 and 2 (D_a > 2 μm). These stages were not used in the comparison, except to note that both techniques agreed in the general lack of any significant sulfur in the coarse particles.

A comparison of the two techniques can be seen in Figure A.2, the composite sulfur distributions obtained by averaging the 15 distributions of each. It is seen that agreement is good for particles greater than 0.50 μm, which are collected near atmospheric pressure in the LPI. However, the distributions diverge for particles collected in the low pressure stages (D_a < 0.50 μm). This is probably due to bounceoff of a

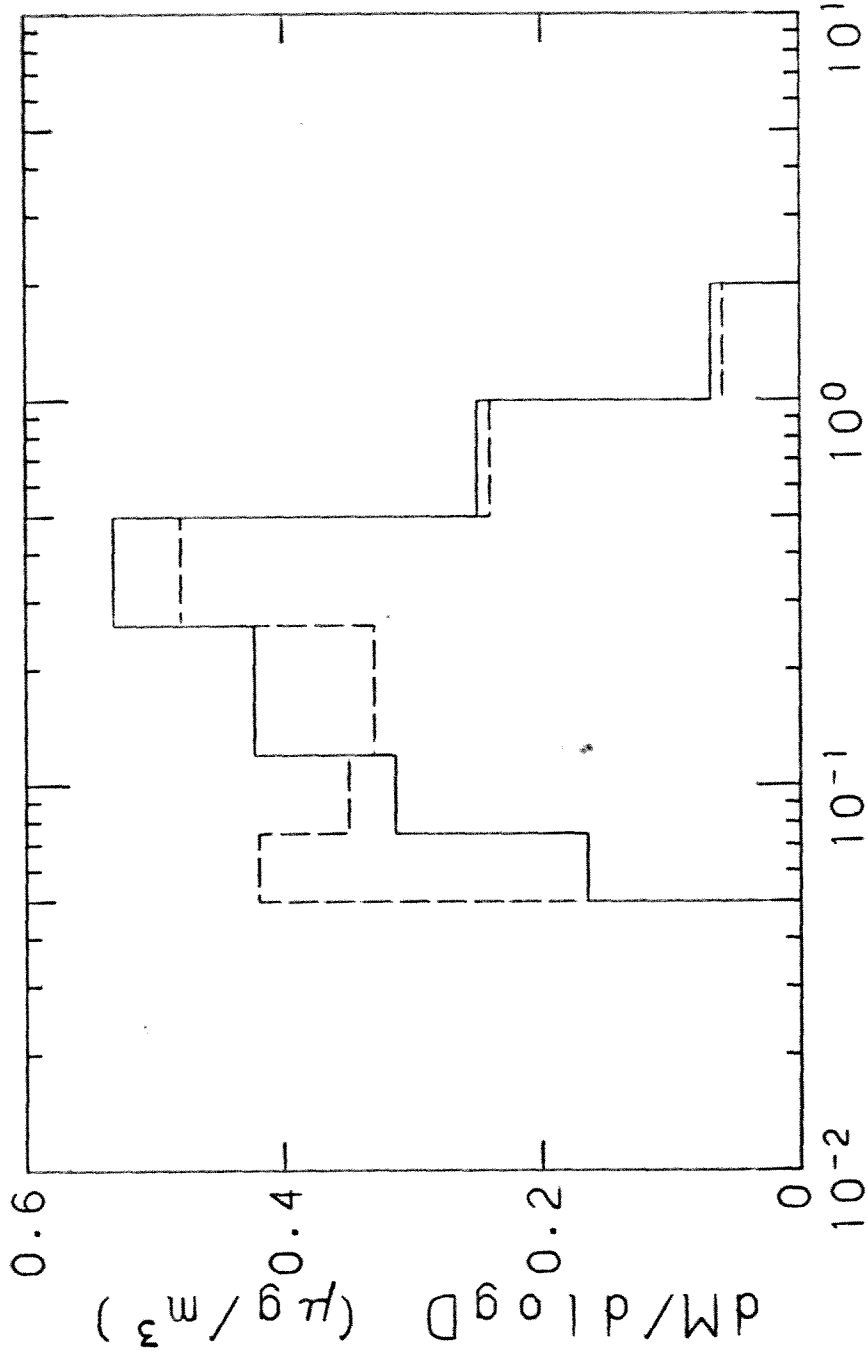

Figure A.2. Aerosol sulfur mass distributions as function of 50% cutoff aerodynamic diameter. Average of 11 ground level samples obtained at Zilnez Mesa, Arizona and 4 airborne samples obtained in Southwest region during June and July, 1979. Aerosol was size segregated with LPI. Results for impaction on vaseline coated stainless steel strips and analysis by FVFPD shown in solid histogram. Results for impaction on Apiezon L coated mylar and analysis by PIXE shown in dashed histogram. Apiezon coating density was 45-69 μg/cm².

fraction of particles from stages 5 and 6 to stages 7 and 8 in the PIXE samples. Excellent agreement was obtained in the overall average sulfur concentrations determined by the two techniques--486 vs. 482 ng S/m^3.

These results indicate that stage 8 was efficient in collecting the particles that bounced from earlier stages but the reasons for this are unclear. The Apiezon L coating of 45-69 $\mu g/cm^2$ did not eliminate bounceoff of the submicron aerosol at the high jet velocities of up to 300 m/sec in the low pressure stages.

The collection efficiency obtained by doubling the Apiezon L coating to 90-140 $\mu g/cm^2$ was compared with vaseline. Each coating was applied to baked stainless steel strips which served as impaction surfaces for the LPI stages. Seven ambient samples using each coating were collected in Pasadena between February 23-28, 1980, under unusually clear, dry conditions and analyzed for sulfur by FVFPD. Sampling times for each coating were identical and were comparable to those of the VISTTA samples, from 6 to 18 hours. No cyclones were used to remove coarse particles upstream of the LPI's. The results of the comparison are seen in Figure A.3. The increased application of Apiezon L resulted in a composite sulfur distribution which agrees well with that obtained with vaseline coating. No significant bounceoff of particles to Stage 8 is evident. Excellent agreement was obtained in the average total sulfur concentrations determined by the two coatings--435 vs 428 ng S/m^3.

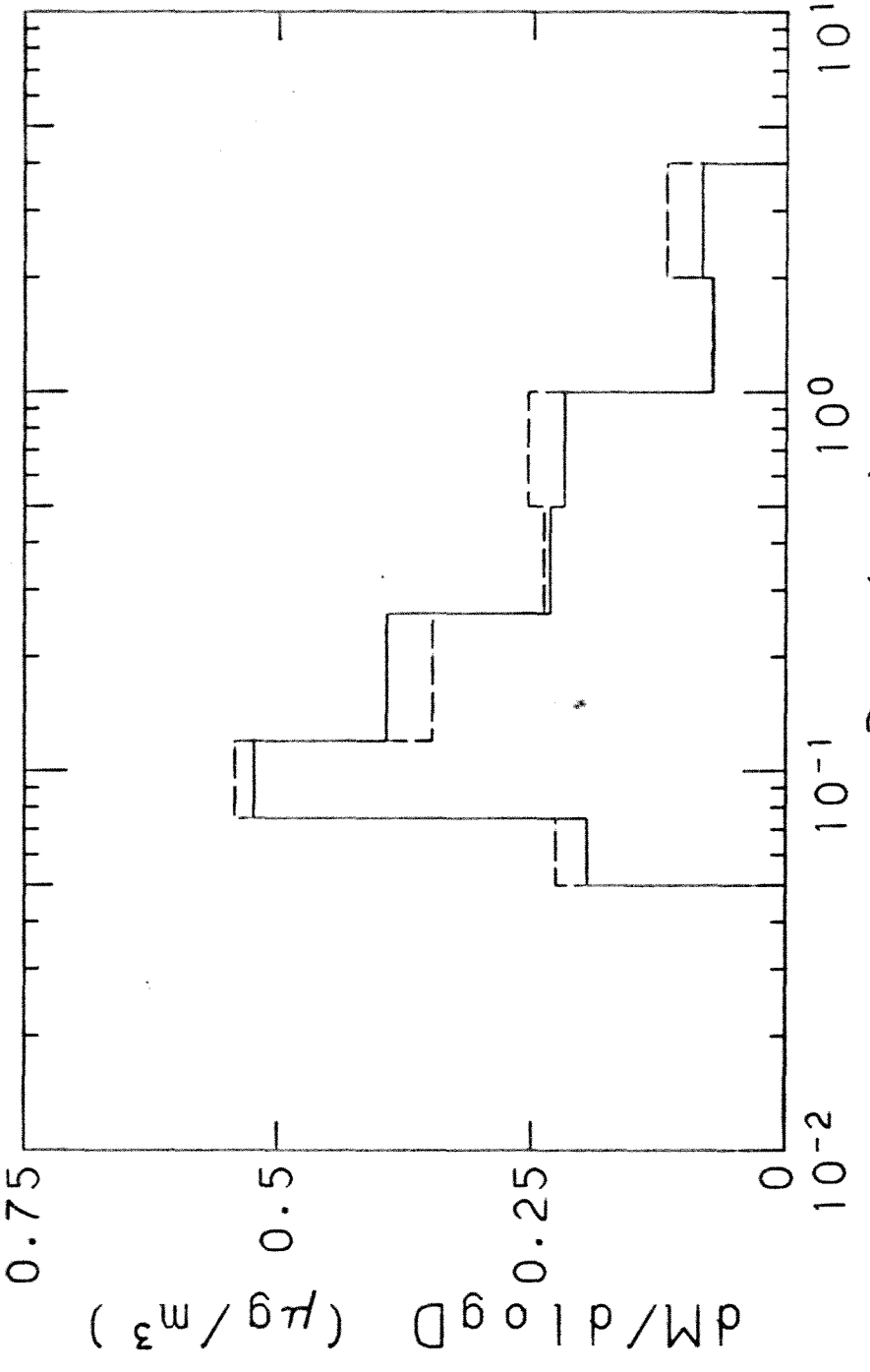

Figure A.3. Aerosol sulfur mass distributions as function of 50% cutoff aerodynamic diameter. Average of 7 samples obtained on roof of Keck Laboratory, Caltech, during February, 1979. Aerosol was size segregated by LPI and analyzed by FVFPD. Results for impaction on vaseline coated stainless steel strips shown in solid histogram. Results for impaction on Apiezon L coated stainless steel strips shown in dashed histogram. Apiezon coating density was 90-140 μg/cm^2.

Thus, bounceoff of submicron dry particles is evident with Apiezon L coatings of 45-69 $\mu g/cm^2$ but is minimized by doubling that amount. Unfortunately the sulfur blank also doubles to about 20 ng, a factor of 5-10 higher than that of vaseline.

A.3.3 Pasadena Elemental Mass Distributions

One LPI-PIXE sample was collected on the roof of Guggenheim Laboratory at Caltech from 1127-1437 PST, February 6, 1970, under poor visibility conditions. The mylar particle impaction surface was coated with vaseline of 90-140 $\mu g/cm^2$ mass area density. No cyclone was used to remove coarse particles upstream of the LPI. This sample was used to test the anti-bounce properties of vaseline-coated mylar with high aerosol loadings in the LPI.

The elemental mass distributions obtained by PIXE analysis of the sample are shown in Figures A.4 and A.5. Total elemental mass concentrations are shown in Table A.3. It is seen that bounceoff of particles to Stage 8 did not occur in the heavily loaded sample when vaseline coating was used.

Figures A.4 and A.5 indicate the diversity in the chemical species in the submicron Pasadena aerosol. The sulfur mass distribution is similar to that which was obtained by LPI-FVFPD from 1430-1515 PST on the same day, shown in Figure B.6. Lead is found in substantial quantities, 3.14 $\mu g/m^3$, and its mass distribution is bimodal. Unlike the remote desert samples, iron is found in the Pasadena submicron aerosol. The submicron distributions of zinc, potassium, and bromine

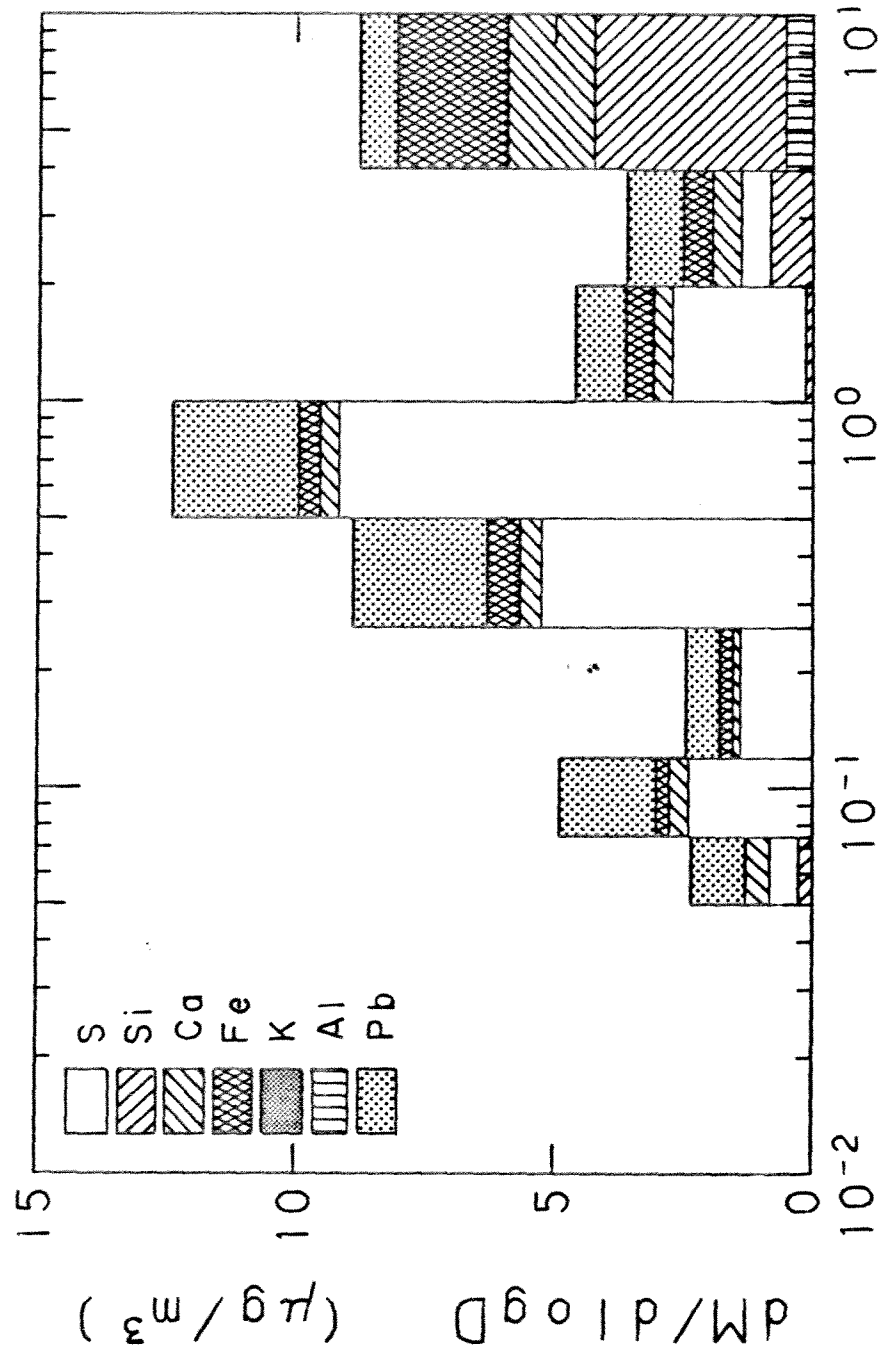

Figure A.4. Mass distributions of major elemental species as function of 50% cutoff aerodynamic diameter. Sample obtained on roof of Guggenheim Laboratory, Caltech, 1127-1431 PST, February 6, 1980. Aerosol was size segregated by LPI onto vaseline coated mylar and analyzed by PIXE. No cyclone preseparator used. Total mass concentration of each species shown in Table A.3.

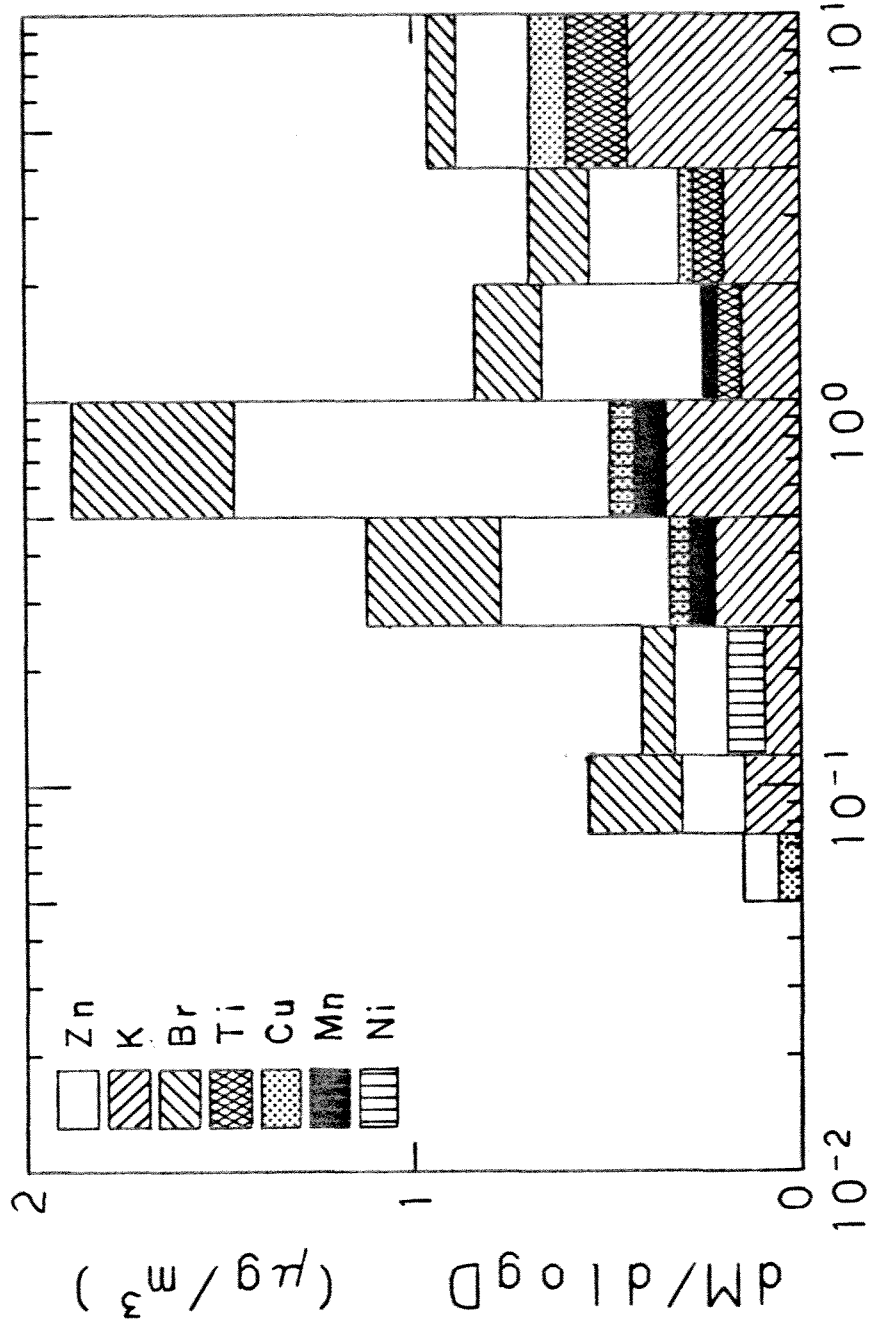

Figure A.5. Mass distributions of minor elemental species as function of 50% cutoff aerodynamic diameter. Sample obtained on roof of Guggenheim Laboratory, Caltech, 1127-1437, PST, February 6, 1980. Aerosol was size segregated by LPI onto vaseline coated mylar and analyzed by PIXE. No cyclone preseparator used. Total mass concentration of each species shown in Table A.3.

Table A.3

Elemental Mass Concentrations Determined by LPI-PIXE, Pasadena, 1127-1437 PST, February 6, 1980

Element	Mass Concentration ug/m^3
Al	0.22
Si	1.40
S	6.28
K	0.53
Ca	1.17
Ti	0.10
V	0.02
Mn	0.06
Fe	1.46
Ni	0.05
Cu	0.10
Zn	0.72
Br	0.43
Pb	3.14

in the Pasadena sample are easily determined with LPI-PIXE. Many measured species accumulated in the 0.5 to 1.0 μm particle diameter range, which is efficient for light scattering.

A.4 SUMMARY AND CONCLUSIONS

The calibrated low pressure impactor and the focused beam PIXE technique have been used together to permit elemental aerosol analysis at the nanogram level from 0.05 to 4 μm aerodynamic diameter. Using prepared standards and field samples the precisions for major species are measured to be 10-20%. Accurate determination of the beam area is necessary and currently limits the accuracy of the technique. Total aerosol sulfur concentrations using the LPI-PIXE technique are in good agreement with three other techniques. Coarse particles are collected with greater efficiency using the LPI than with Nuclepore filters. Using a cyclone preseparator and Apiezon L coatings of 45-69 $\mu g/cm^2$, no bounceoff of coarse particles was found in field samples collected with the LPI.

Aerosol sulfur distributions obtained by LPI-PIXE were compared to those obtained by LPI and analysis by flash volatilization and flame photometric detection (FVFPD), which is specific to sulfur. Some bounceoff of particles less than 0.5 μm diameter to lower LPI stages was measured by PIXE analysis when an Apiezon L mylar coating of 45-69 $\mu g/cm^2$ was used. Doubling the Apiezon L coating to 90-140 $\mu g/cm^2$ was found to minimize the bounceoff in the low pressure stages. Vaseline coating is recommended for future LPI-PIXE samples because of its

better collection efficiency at the high flow rates in the low pressure stages of the LPI, and its low elemental blank values.

It is now possible to calculate the contributions of many chemical species to the extinction coefficient from elemental mass distributions determined by the LPI-PIXE technique.

APPENDIX B

AEROSOL ABSORPTION COEFFICIENT AND SOOT MASS DISTRIBUTIONS USING THE LOW PRESSURE IMPACTOR AND THE INTEGRATING PLATE TECHNIQUE

B.1 INTRODUCTION

In urban areas the absorption of light by suspended particles may contribute substantially to visibility degradation. Simultaneous measurements of the particle absorption coefficient, b_{ap}, and the particle scattering coefficient, b_{sp}, indicate that light absorption by aerosols may contribute from 10% of light extinction in clean background air to 50% of extinction in urban areas such as Denver (Weiss et al.,1976; Waggoner and Charlson, 1977; Charlson et al.,1978).

As discussed in Chapters 3 and 4, b_{sp} can be continuously measured with an integrating nephelometer. No instrument is currently available for routine measurements of b_{ap}. Currently the most common technique for measuring b_{ap} is by the opal glass integrating plate technique of Lin et al. (1973). An opal diffusing glass is used to integrate light scattered by particles collected on the surface of a Nuclepore polycarbonate filter. The reduction in light intensity through the aerosol-coated filter is assumed to be due to light absorption by the particles. The measurement produces a time average b_{ap}. This technique assumes that the optical absorption properties of the aerosol suspended in air are not changed when collected on the filter.

Using optoacoustical techniques under controlled laboratory conditions it is possible to measure b_{ap} due to suspended particles in a sample chamber (Roessler and Faxvog,1979; Japar and Killinger, 1979). Absorption of light by suspended particles generates heat and subsequently produces a pressure rise in the chamber. Modulation of the incident light beam at audio frequencies allows a microphone to monitor the resultant pressure of vibrations as an acoustic signal. For dilute samples the optoacoustic microphone response is directly proportional to the mass concentration of the light absorbing aerosol. The average soot mass absorption efficiencies measured in ambient air with the integrating plate technique agree with those measured from laboratory-generated soot by the optoacoustical technique -- 8-10 m^2/g (Roessler and Faxvog, 1979; Pierson, 1978).

In this thesis research, aerosol is collected on coated mylar films by the low pressure impactor (LPI) for elemental analysis by particle induced X-ray emissions (PIXE). The mylar is transparent and the PIXE analysis is nondestructive. This suggests the possibility of using the integrating plate technique to measure the light absorbed by aerosol deposits from each stage of the LPI. Analysis of all eight LPI aerosol deposits would then provide a particle absorption coefficient distribution as a function of 50% cutoff aerodynamic diameter -- $\Delta b_{ap}/\Delta \log D_{50}$. This would be a direct measurement of the b_{ap} distribution, unlike the b_{sp} distributions which were calculated from the measured aerosol size distributions in Chapters 3 and 4.

If one assumes that all the b_{ap} is due to soot (Pierson and Russell, 1979; Rosen et al., 1977) then the soot mass distributions may be

inferred from the measured b_{ap} distribution by means of Equations 2.6 and 2.11:

$$b_{ap} = \int_0^\infty E_a(m,x,\lambda) f_s(x) dx$$

where $$f_s(x) = dM_{soot}/d\log(D/D_o) \qquad (B.1)$$

and $$x = \log(D/D_o) \quad ; \; D_o = 0.01 \; \mu m$$

E_a is the mass absorption efficiency of soot, shown in Figure 2.2. If one assumes histogram representations of the b_{ap} and soot distributions with respect to particle size, then the following relation will hold for any particle size interval

$$(\Delta b_{api}/\Delta x_i) = \bar{E}_{ai} \, f_{si} \qquad i=1, \ldots, 8 \text{ LPI Stages} \qquad (B.2)$$

$\bar{E}_{ai}$ is the mass absorption efficiency averaged over the particle size interval $[x_i, x_{i+1}]$. In this way the soot mass concentration as a function of particle size can be inferred from the measured Δb_{api}, the known LPI 50% cutoff aerodynamic diameters D_{50i}, and the theoretical mass absorption efficiency averaged over each particle size interval.

This appendix describes and evaluates research in which the opal glass integrating plate technique is used to measure the particle absorption coefficient distribution from aerosol deposits collected with the low pressure impactor. Ambient samples were collected to obtain b_{ap} and inferred soot distributions in remote and urban locations. Balances on b_{ap} and soot concentration were checked by filter measurements.

B.2 EXPERIMENTAL

B.2.1 Sample Collection

Ambient aerosol was sampled with the LPI at two remote arid sites and two urban sites to determine the particle absorption coefficient distribution. A total of 11 samples were analyzed. All LPI samples used mylar collection surfaces coated with 45-69 $\mu g/m^3$ Apiezon L vacuum grease.

Aerosol was sampled at Zilnez Mesa, Arizona, from July 27-July 13, 1979, as described in Chapter 3. Twelve LPI samples were collected. The samples were first analyzed for elemental mass by particle induced X-ray emissions (PIXE) at the Crocker Nuclear Laboratory, University of California, Davis. The samples were then returned to Caltech to measure the particle absorption coefficient, b_{ap}, from the aerosol deposited on each LPI stage. Eight samples were analyzed. Nuclepore and Tissuequartz filter samples were also collected at Zilnez Mesa from which b_{ap} and the soot mass concentrations, respectively, were measured.

One sample was collected at China Lake, California, from 1738-0806 PST April 2-3, 1979. The average measured particle scattering coefficient during the sampling period was $23 \times 10^{-6} m^{-1}$, compared to the 1979 annual average of $25 \times 10^{-6} m^{-1}$ (Chapter 4). The soot mass concentration was determined from a Tissuequartz filter sampling during the same interval as the LPI.

A sample was collected on February 5, 1980 in downtown Los Angeles at the South Coast Air Quality Management District Station #87. Due to the high soot concentration, the sample duration was only 15 minutes, from 0800 to 0815 PST. The site is located near a major freeway and a railroad yard, both sources of soot. Aerosol was also collected on Nuclepore and Tissuequartz filters for determination of b_{ap} and soot

mass concentration.

The last sample was collected on the roof of Guggenheim Laboratory at Caltech from 1415 to 1500 PST on February 6, 1980, under poor visibility conditions. Another LPI was operated during the same interval to obtain the aerosol sulfur mass distribution by flash volatilization and flame photometric detection (FVFPD). No filter samples were collected for determination of b_{ap} or soot mass concentration.

B.2.2. Sample Analysis

The time average particle absorption coefficient was measured from light absorbed by the aerosol deposited on the coated mylar collection sample in each stage of the LPI. The same technique was used for Nuclepore filter samples. The experimental apparatus for making this measurement is shown in Figure B.1. Coherent light at a wavelength of 0.6328 μm is provided by a Spectra-Physics Model 135 5 mW He-Ne laser. The light passes through a 0.25 mm diameter optical fiber (Fiber Optics Development Systems, Santa Barbara, CA) and illuminates the sample. Using the self-adhesive surface, the mylar sample is fastened to a 38 mm diameter opal glass disc. Opal glass is a diffuse radiator. The aerosol deposit faces away from the glass. The distance between the end of the optical fiber and the aerosol deposit is about 0.76 mm (0.030 inch).

Light striking the aerosol deposit can be scattered or absorbed. The forward scattered light is collected by the opal glass and reradiated. The backscattered light is not collected, but Lin et al.(1973) show that its contribution to total scattering is small. Any reduction in light intensity from the sample is therefore due to light absorption. The intensity of the light radiated from the opal glass is measured with

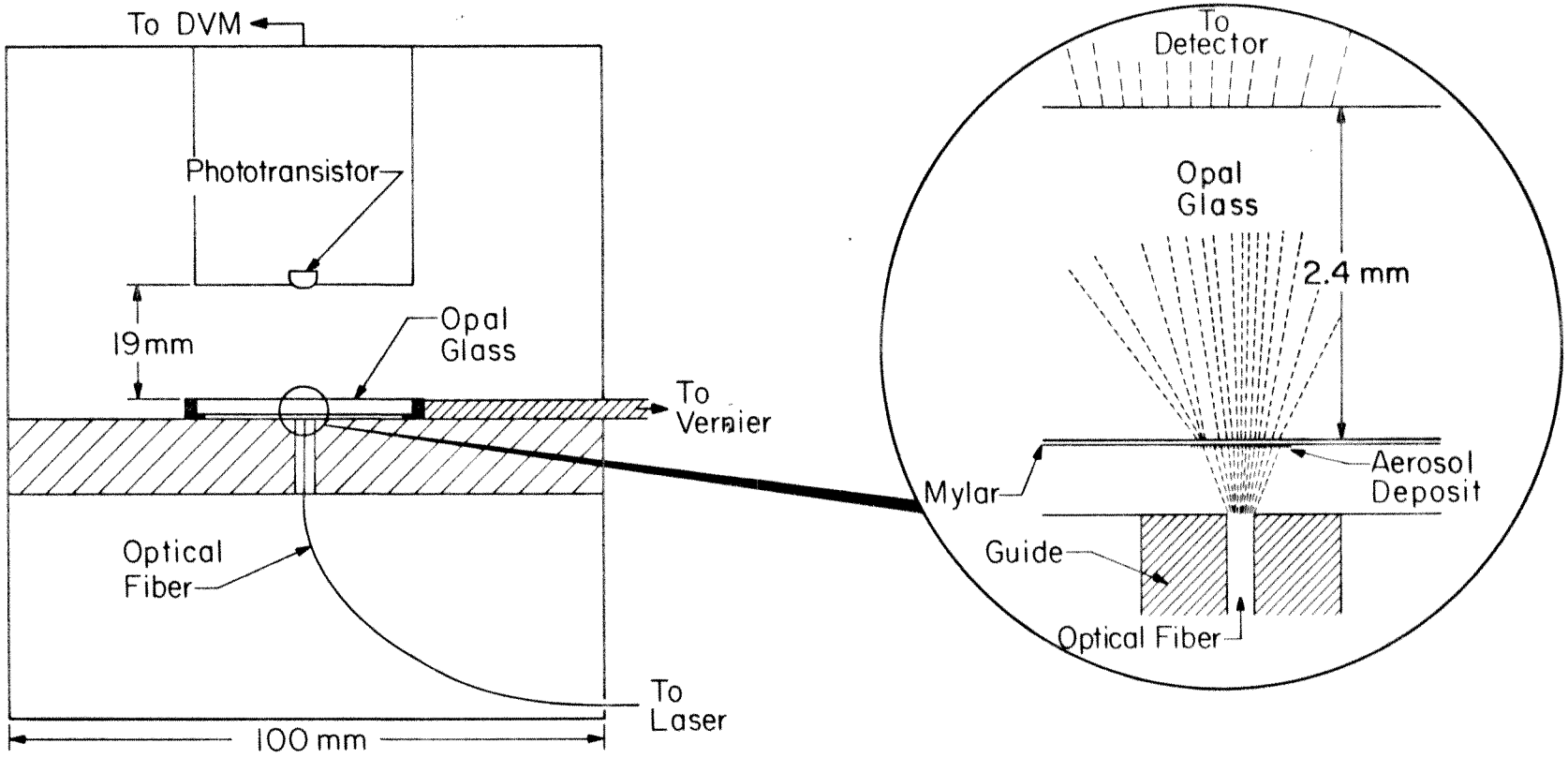

Figure B.1. Apparatus for measuring light absorption by small area aerosol deposits. Aerosol is collected on coated mylar or polycarbonate filter. Coherent light at λ = 0.6328 μm passes through 0.25 mm diameter optical fiber and irradiates aerosol deposit, typically 0.7 to 2.0 mm diameter. Aerosol deposit is moved relative to beam by calibrated vernier. Forward scattered light from aerosol deposit is collected by opal glass and reradiated. Light intensity determined by calibrated phototransistor which provides output voltage to digital voltmeter (DVM). Inside walls of housing painted flat black to minimize reflections.

a Fairchild FPT 120 phototransistor 19 mm from the opal glass. The phototransistor is mounted in a copper housing which contains a 1.4 volt hearing aid battery power supply and a 10 kΩ resistor. The phototransistor collector current is applied across the resistance and measured as a voltage with a digital voltmeter (DVM).

The light intensity variation across the aerosol deposit can be determined by varying the location of the deposit with respect to the light beam. This is accomplished with a microscope vernier attachment which can vary the position of the deposits in the plane perpendicular to the light beam to within ± 0.05 mm.

The phototransistor was calibrated with Kodak No. 96 Wratten gelatin neutral density filters of known opacity which were affixed to the opal glass. The results are shown in Figure B.2.

Because the illuminating end of the optical fiber is about 0.76 mm from the sample deposit, the effective area of the beam at the sample is larger than the optical fiber cross sectional area. The spatial intensity distribution at the opal glass was measured to estimate the effective diameter of the beam. A small strip of opaque black electrical tape was affixed to the opal glass. The strip was moved relative to the beam with the vernier, resulting in a unit step of $I/I_o = 1$ to $I/I_o = 0$. The relative intensity with respect to position in the beam was measured and plotted on a probability scale in Figure B.3. The linear behavior between 0.1 - 1.0 mm indicates that the intensity distribution is approximately Gaussian in this range. The effective width of the beam is estimated from twice the measured standard deviation, which is 0.53 mm. This is smaller than the LPI aerosol deposits, which vary from 0.7 to 2.0 mm diameter.

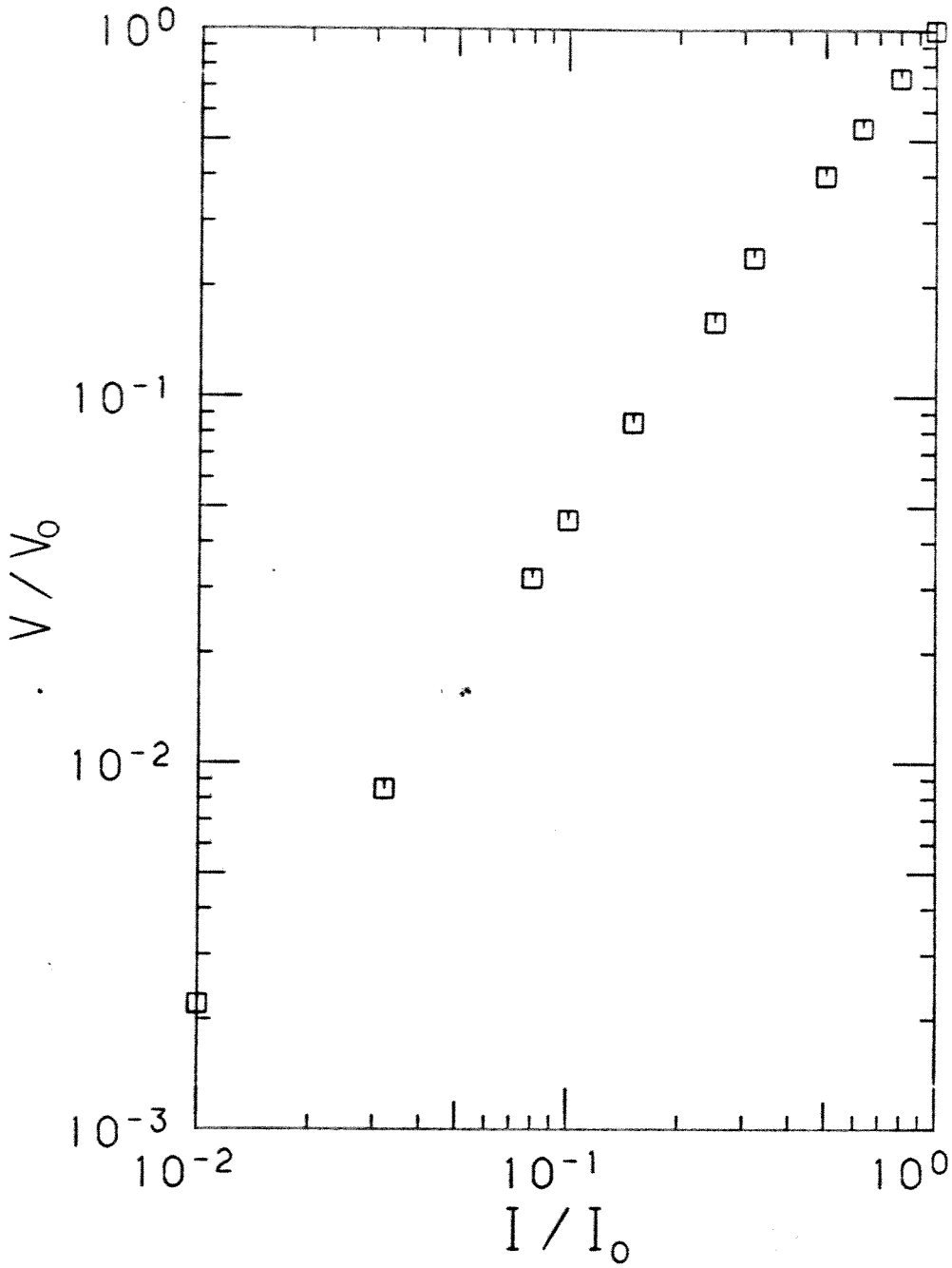

Figure B.2. Voltage-intensity calibration curve for Fairchild FPT 120 phototransistor. Light source was 5 mW He-Ne laser. Light intensity was varied with neutral density filters which were affixed to opal glass between laser and phototransistor.

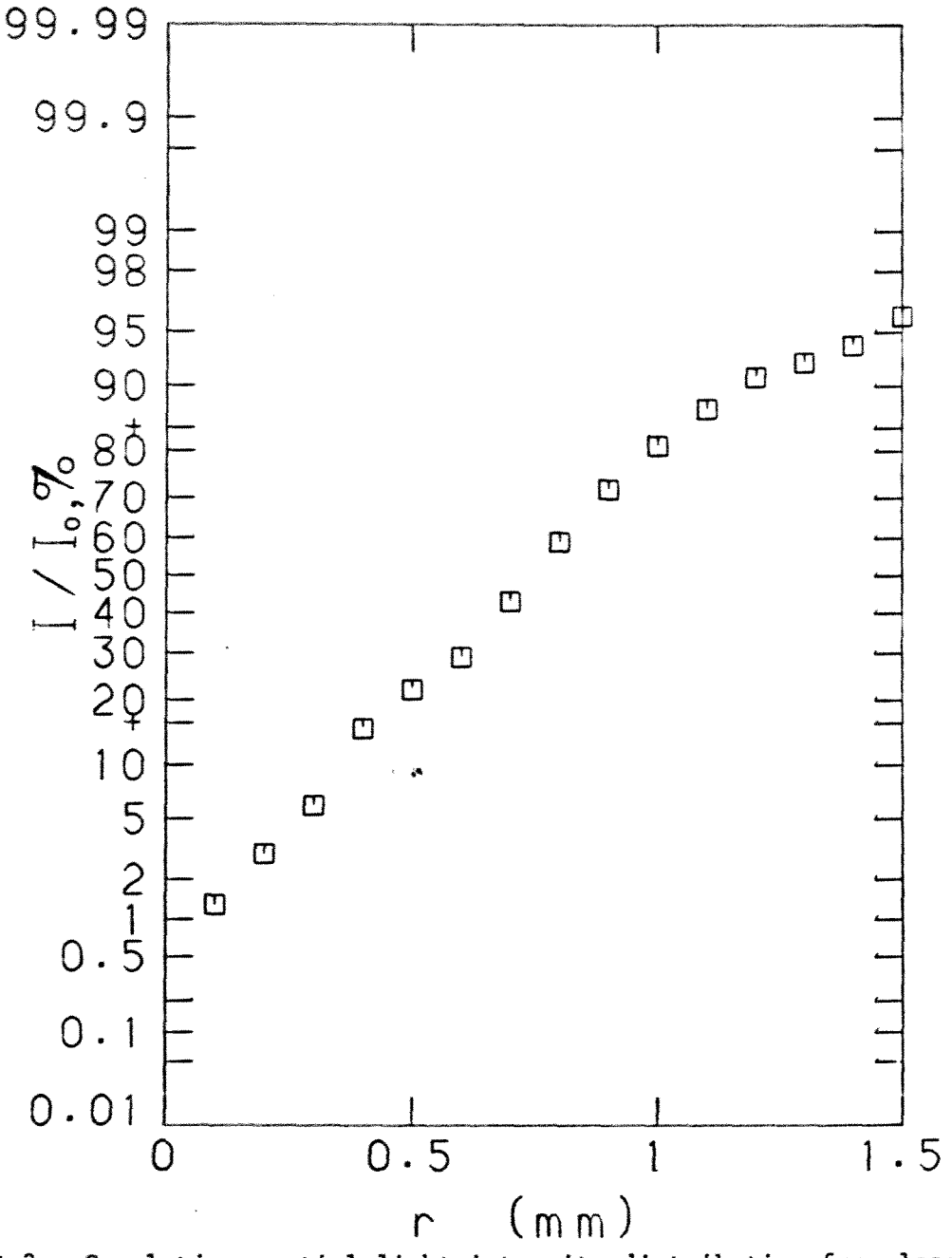

Figure B.3. Cumulative spatial light intensity distribution from laser at opal glass surface, 0.75 mm from end of optical fiber. Strip of black tape affixed to opal glass was moved laterally across beam to vary the intensity detected at phototransistor. The linear intensity plot on the probability scale between 0.1 and 1.0 mm indicates that the spatial intensity distribution is approximately Gaussian in this range. r=0 corresponds to the edge of the beam where light first detected with phototransistor.

B.2.2.1 Lower Detection Limit -

The lower b_{ap} detection limit is determined by the fluctuations in the laser output. After 2 hours of warm-up, the He-Ne laser intensity typically fluctuated at ± 1% of its mean value. Doubling this value results in a detectable $I_o/I = 1.02$. The b_{ap} lower detection limit can be calculated from $b_{ap} = A/S \ln (I_o/I)$, where A is the aerosol deposit area and S is the volume of air sampled (Lin et al., 1973). The b_{ap} lower detection values were calculated for a 1.0 mm diameter aerosol deposit and an LPI flow rate of 1.0 liter per minute. The b_{ap} lower detection limits, which are dependent on sample time, are shown in Table B.1. Necessary sample times would vary from 5-60 minutes in an urban area to 10-40 hours in clean background air.

Table B.1. Particle Absorption Coefficient Lower Detection Limit vs LPI Sample Time

Sample time, hr	b_{ap} Lower detection limit, 10^{-6} m^{-1}
0.01	26.0
0.10	2.6
1.0	0.26
10.0	0.026
100	0.0026

The lower detection limit for the inferred soot mass is determined by the $I_o/I = 1.02$ lower limit. The relationship between the mass of deposited soot for LPI stage i, ΔM_i, the aerosol deposit area, A_i, and the soot mass absorption efficiency, $\overline{E}_i$, is

$$\Delta M_i = (A_i/\overline{E}_i)\ \ell n\ (I_o/I)_i \quad i = 1,\ldots,8$$

Assuming a 1 mm diameter aerosol deposit and a mass absorption efficiency of 8 m^2/g, the lower detectable limit is 2 ng soot.

B.2.2.2 Dynamic Range -

The Beer-Lambert equation which relates the relative intensity over the path length to the extinction coefficient applies only to a dilute suspension. It is therefore estimated that the Beer-Lambert expression will be true to within 10% if

$$.70 \leq (I/I_o) \leq 1$$

Given the lower detection limit of $I_o/I = 1.02$, this results in

$$.36 > [b_{ap}/(A/S)] > .02$$

Thus a dynamic range of about 20 is possible with this technique, both for b_{ap} and inferred soot mass.

B.3 RESULTS

B.3.1 Particle Absorption Coefficient and Soot Mass Distributions

The results for the samples collected at Zilnez Mesa are described in Chapter 3 and summarized in Table 3.5. Although the total particle absorption coefficient varied from sample to sample, the normalized distribution remained rather constant. The distribution, shown in Figure 3.4, was broad with a peak due to particles of 0.26-0.50 μm aerodynamic diameter. The soot mass distribution was inferred from the measured particle absorption distribution using Eq. B.2. The soot distribution averaged over the eight samples collected at Zilnez Mesa is shown in Figure 3.8. The peak in the soot mass distribution occurs in particles between 0.50 -1.0 μm diameter. This is because the theoretical mass absorption efficiency of carbon spheres between 0.5 and 1.0 μm diameter is low, whereas an appreciable amount of absorption was measured in this size range. This resulted in a higher inferred soot concentration at this size.

The results for the Los Angeles and Pasadena urban samples are strikingly different than those obtained at the remote Zilnez Mesa. The particle absorption coefficient distributions measured at these urban sites are shown in Figure B.4. The total b_{ap} measured from the LPI samples was 48 x 10^{-6} m^{-1} and 163 x 10^{-6} m^{-1} for Pasadena and Los Angeles, respectively. These values are about 100 times greater than those measured at Zilnez Mesa. The particle absorption coefficient at the Los Angeles site, near fresh combustion sources, was due almost exclusively to particles of less than 0.2 μm aerodynamic diameter.

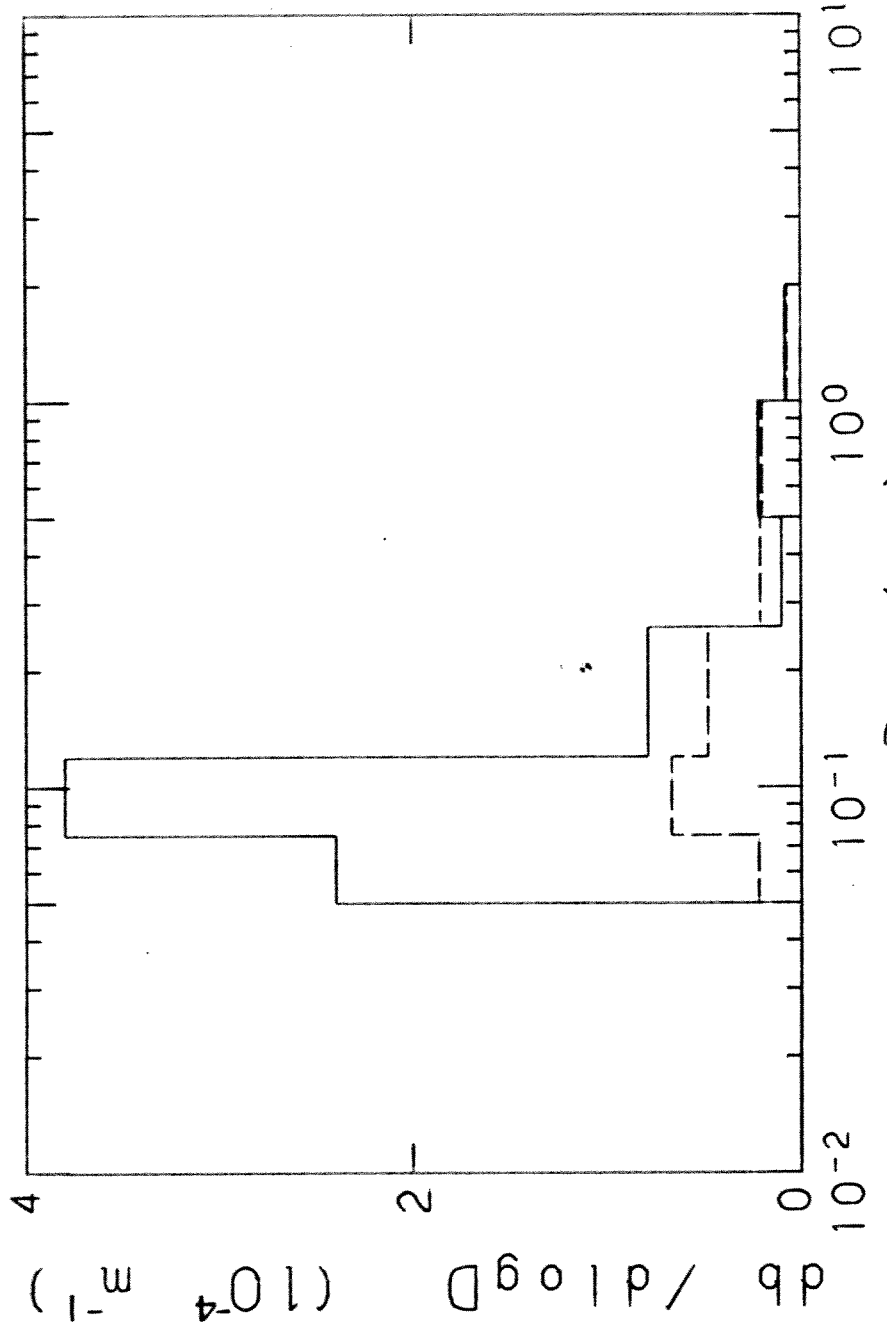

Figure B.4. Particle absorption coefficient distributions. Solid histogram is for sample obtained in downtown Los Angeles, 0800-0815 PST, February 5, 1980. Dashed histogram is for sample obtained on roof of Guggenheim Laboratory, Caltech, 1430-1515 PST, February 6, 1980. Aerosol was size segregated by LPI onto vaseline coated mylar and analyzed by light absorption.

This contrasts with the particle scattering coefficient, b_{sp}, which is dominated by contributions from particles larger than 0.2 μm diameter (Ensor et al., 1972). The Pasadena particle absorption coefficient distribution is somewhat broader than that of Los Angeles. The Pasadena site at Caltech was not located as close to fresh soot sources as the Los Angeles site. Perhaps the Pasadena distribution was a mix of new, smaller diameter soot and older, coagulated soot.

The Los Angeles soot mass distribution was inferred from the measured particle absorption coefficient distribution using values of $m = 1.56 - 0.47i$ and $\rho = 1.0\ g/cm^3$ and is shown in Figure B.5. Summing the contributions from each LPI stage, the total soot mass concentration was $24\ \mu g/m^3$. This compares favorably with a 7-9 AM average value of $20\ \mu g/m^3$ soot which was measured by light reflectance from Tissuequartz filter samples by Washington University. On Figure B.5 the Los Angeles soot distribution is compared with an aerosol volume distribution measured from laboratory diesel engine exhaust (Kittleson and Dolan, 1979). The volume distribution was measured with a Thermo Systems Electrical Aerosol Analyzer. It is seen that the inferred ambient soot distribution obtained near fresh combustion sources is quite similar to that measured from laboratory diesel engine exhaust.

The soot distribution obtained in Los Angeles is quite similar to the distributions of benzo[a]pyrene (BaP) and coronene (COR) measured by Miguel and Friedlander (1978) in Pasadena. They collected ambient aerosol in 1976 and 1977 with the LPI using 25 mm diameter quartz discs coated with vaseline as impaction surfaces. After extraction with benzene,

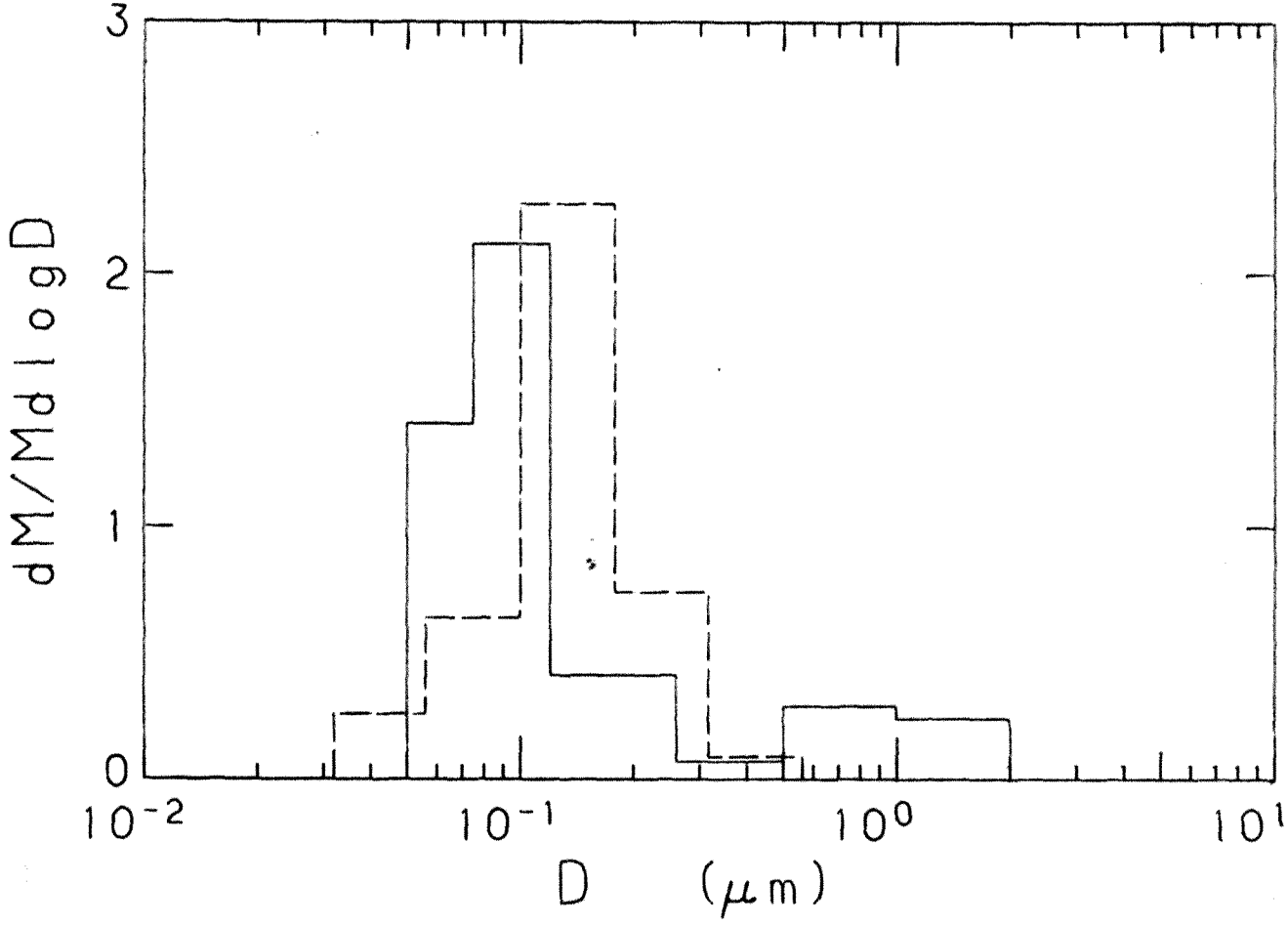

Figure B.5. Comparison of ambient soot mass distribution with that obtained from a laboratory diesel engine. Solid histogram is for sample obtained in downtown Los Angeles, 0800-0815 PST, February 5, 1980. Soot mass distribution inferred from measured particle absorption distribution, Figure B.4. Total inferred soot mass concentration 24 $\mu g/m^3$. Dashed histogram is for aerosol volume distribution from laboratory diesel engine (Kittleson and Dolan, 1979). Aerosol volume distribution measured with electrical aerosol analyser (EAA).

aerosol deposited on each stage of the LPI was analyzed for BaP and COR by thin layer chromatographic and spectrophotofluorometric analysis. They found that the mass distributions for both BaP and COR peaked between 0.075 - 0.12 μm aerodynamic diameter. About 75% of the BaP and 85% of the COR mass was associated with particles of aerodynamic diameter less than 0.26 μm. The similarity between the soot, BaP and COR mass distributions is consistent with the hypothesis that BaP and COR adsorb on the soot at the source, rather than being emitted into the atmosphere and being subsequently scavenged by the ambient aerosol. Indeed, Pierson (1978) and Japar and Killinger (1979) have found that soot particles tend to be very porous and plugged with other hydrocarbons.

As shown in Sections B.2.2.1, soot mass can be inferred with nanogram sensitivity from aerosol deposits obtained with the LPI. This is comparable to the sulfur sensitivity obtained from FVFPD analysis of aerosol collected with vaseline coated stainless steel strips in the LPI. Simultaneous soot and sulfur aerosol distributions may now be obtained for particles greater than 0.05 μm aerodynamic diameter. A sampling time of 0.5 to 1 hour is required for typical urban aerosol. Figure B.6 shows the results of such a measurement, made on the roof of Guggenheim Laboratory, Caltech, February 6, 1980. The sample duration was 45 minutes. The soot mass distribution was inferred from the absorption distribution using values of $m = 1.56 - 0.47i$ and $\rho = 1.0\ g/cm^3$. The total soot and sulfur mass concentrations were 8.9 and 8.1 $\mu g/m^3$, respectively. It is seen in the figure that the mass distribution for each species is broad, but that the maxima in the distributions occur at different particle sizes.

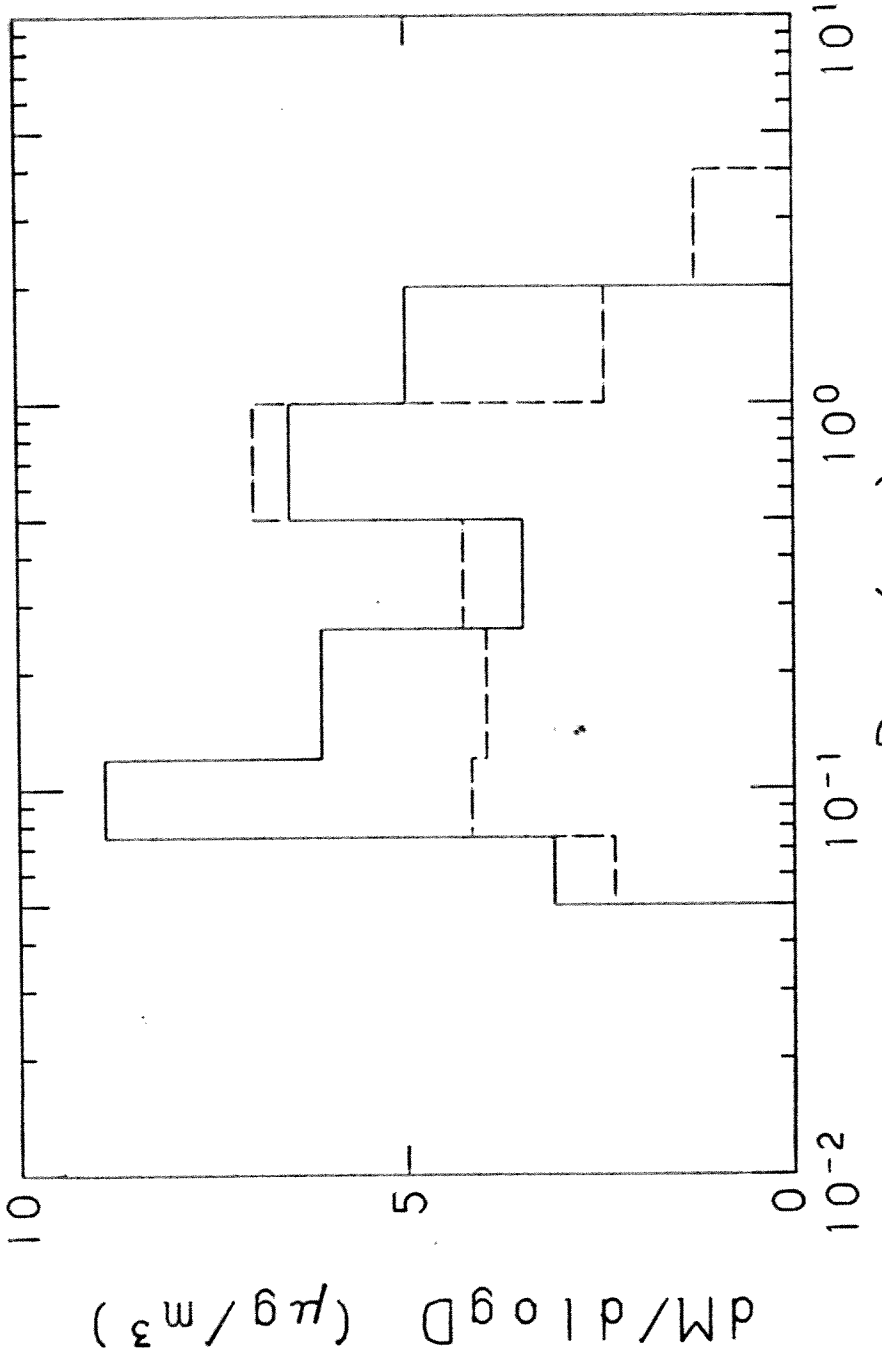

Figure B.6. Comparison of ambient soot and sulfur mass distributions. LPI samples collected on roof of Guggenheim Laboratory, Caltech, 1430-1515 PST, February 6, 1980. Soot distribution, solid histogram, was inferred from measured particle absorption coefficient distribution, Figure B.4. Sulfur distribution, dashed histogram, obtained by FVFPD analysis of aerosol impacted onto vaseline coated stainless steel strips.

B.3.2. Particle Absorption Coefficient and Soot Mass Concentration Balances

By summing the contributions of each stage of the LPI, the total particle absorption coefficient and total soot concentration can be determined for each sample episode. The totals were also determined from filter samples. As indicated earlier, for most samples aerosol was collected on a Nuclepore polycarbonate filter and a Pallflex Tissuequartz filter. The total b_{ap} was measured using the same technique for the Nuclepore filter as for the LPI deposits. By scanning the filters with the vernier, it was found that the aerosol deposit was very uniform across the Nuclepore filter. Total graphitic carbon was determined from the Pallflex filter by Washington University using calibrated optical reflectance.

The results of the b_{ap} and soot balances are shown in Table B.2. It is seen that the total b_{ap} determined from the LPI samples averaged about one-half the b_{ap} determined from the Nuclepore filter samples. However, the total soot concentrations inferred from the LPI samples agreed with those measured from the Pallflex filter samples when a refractive index of 1.96 - 0.66i and particle density of 2.0 g/cm^3 were assumed. When m was assumed to be 1.56 - 0.47i and ρ = 1.0 g/cm^3, then the LPI inferred soot values decreased by a factor of about 2, consistent with the discrepancy in the measurements of the absorption coefficient. It is assumed in this study that the b_{ap} measured from the Nuclepore filter samples is the correct value.

The most probable source of the lower b_{ap} obtained with the LPI samples is the agglomeration and close packing of the particles which results from their impaction on the LPI collection surface. The mass

Table B.2. Particle Absorption Coefficient, b_{ap}, and Soot Concentrations: Comparison of Low Pressure Impactor Results with Filter Measurements

	$b_{ap}, 10^{-6} m^{-1}$		soot, $\mu g/m^3$	
Sample	LPI	Filter	LPI	Filter
China Lake				
4/2/79	0.43	-	0.12	0.12
Zilnez Mesa				
6/27/79	0.68	1.6	0.17	0.2
6/29/79	0.85	2.0	0.21	0.2
7/2/79	0.95	3.3	0.23	0.2
7/3/79	1.30	3.9	0.30	0.3
7/7/79	0.87	1.9	0.20	0.2
7/9/79	0.39	0.4	0.087	0.1
7/10/79	0.48	0.8	0.13	0.1
7/11/79	0.39	0.9	0.085	0.3
Los Angeles				
2/5/80	163	281	41	20
Pasadena				
2/6/80	48	-	12	-

Nuclepore polycarbonate filter used for b_{ap}.

Pallflex Tissuequartz filter used for soot.

LPI soot inferred using $m = 1.96-0.66i$ and $\rho = 2.0\ g/cm^3$.

Lin et al. (1973). Each deposit is illuminated using light of λ = 0.6328 μm passing through a 0.25 mm diameter optical fiber.

It is assumed that carbon soot is responsible for the light absorption by particles. Soot mass distributions were inferred from the absorption measurements assuming spheres of two different refractive indices and densities: 1.96-0.66i, 2 g/cm^3 and 1.56-0.47i, 1 g/cm^3. A sensitivity of about 2 nanograms soot is achieved with this technique.

An average mass absorption efficiency of 8-10 m^2/g was calculated from the b_{ap} and soot mass concentrations measured from filter samples collected at Zilnez Mesa and Los Angeles. This value agrees with measurements by previous investigators of ambient and laboratory soot. The value is consistent with m = 1.56 -0.47i and ρ = 1.0 g/cm^3, as suggested by Dalzell and Sarofim (1969), seen in Figure 2.2. These values are recommended for inferring the soot mass distribution from measurements of b_{ap} with samples collected by the LPI.

It was found that light absorption in Pasadena and Los Angeles was due primarily to particles less than 0.2 μm diameter. The inferred soot distributions were found to be quite similar to those measured from laboratory diesel engine exhaust. Agreement was found between benzo[a]pyrene, coronene, and soot mass distributions taken on different days in the Los Angeles basin.

The particle absorption coefficient measured from LPI samples was considerably lower than that measured from Nuclepore filter samples. Particle agglomeration on the LPI deposits is suspected as the principal cause of the discrepancy. Because of this systematic error, this technique is only semi-quantitative at the present time.

density, in $\mu g/cm^2$, of aerosol deposited on the LPI spots is 10-15 times higher than that on the Nuclepore filter. This could result in reduced absorption efficiency due to the formation of larger particles by agglomeration on the impaction surface. In some cases, the mass density of absorbing particles was sufficiently high to cause transmissions (I/I_o) of less than 50%, out of the Beer-Lambert dilute range. The measurement would underestimate the true contribution of these particles to absorption when suspended. The agglomeration effect would be maximized for particles originally of $D > 0.2$ μm. It is seen in Figure 2.2 that the agglomeration could reduce their mass absorption efficiency. However, for particles less than 0.1 μm, the effect is not so pronounced. Therefore, one should see the least discrepancy in total absorption measured between the LPI and the Nuclepore filter samples when the distribution is dominated by particles of less than 0.1 μm. This is consistent with the Los Angeles and Zilnez Mesa results. The b_{ap} values agree more closely with the Los Angeles sample than with the Zilnez Mesa samples, consistent with the differences in their distributions.

B.4 SUMMARY AND CONCLUSIONS

This appendix described a technique which has been developed to determine the particle absorption coefficient distribution as a function of aerodynamic diameter from 0.05 to 4 μm. The calibrated 8-stage low pressure impactor (LPI) is used to size segregate aerosol on coated mylar films backed by glass discs. The particle absorption coefficient on each stage is measured using the opal glass integrating plate technique of

APPENDIX C

DETERMINATION OF AEROSOL MASS DISTRIBUTIONS USING THE LOW PRESSURE IMPACTOR AND THE TWOMEY NONLINEAR INVERSION ALGORITHM

C.1 INTRODUCTION

In order to estimate the contributions of aerosol chemical species to the extinction coefficient, their distributions with respect to particle size must be known. Figures 2.1 and 2.2 showed that the theoretical mass extinction efficiency of suspended particulates is strongly particle size dependent, exhibiting strong variations between 0.1 and 1.0 μm. For example, a spherical particle of refractive index 1.54 and diameter of 0.4 μm has a mass scattering efficiency at a wavelength of 0.53 μm which is 20 times higher than that of a 0.1 μm diameter sphere of the same refractive index. Most ambient aerosol distributions exhibit large variations throughout the submicron particle size range. Mass median diameters in the submicron range are found to be between 0.2 and 0.5 μm. The calculated particle extinction is a convolution of the mass extinction efficiency and the mass distributions, which are both strongly size dependent in the submicron particle size range.

In this study the species mass distributions are determined from samples collected with the calibrated low pressure impactor (LPI). While the LPI is capable of size segregating particles throughout the submicron range, there is "crosstalk" between stages. The mass distribution data are typically plotted as $\Delta M_i/\Delta \log D_{50i}$, where ΔM_i is the mass collected on stage i, and $\Delta \log D_{50i}$ is the logarithmic particle size interval between the 50% efficiency cutoff diameter for the i^{th} stage and the one preceding it. The use of this distribution may lead to

errors in the calculated extinction coefficient. There is a need for a more accurate mass distribution which is more finely resolved over particle size and which takes account of the calibration data of the LPI.

A variety of inversion techniques are available to obtain size distributions from measured values and calibration data. A review and evaluation of some of the data inversion techniques applied to impactors can be found in Cooper and Spielman (1976). More recent work on general analytical inversions to infer particle size distributions from optical measurements can be found in Fymat and Mease (1978). The technique chosen for use with the LPI is a nonlinear iterative algorithm by Twomey (1975). Its chief advantages are that it assumes no functional form, such as lognormal, for the solution, and that the size resolution in the inverted distribution may be determined by the size resolution in the calibration data instead of the 50% cutpoints.

This appendix discusses the application of the Twomey nonlinear iterative algorithm to invert mass distributions obtained with the LPI. Questions of uniqueness, convergence, sensitivity to calibration data, and other characteristics of the Twomey algorithm are discussed.

C.2 BACKGROUND

The low pressure impactor (LPI) size segregates aerosol into eight stages having 50% cutoff diameters from 0.05 to 4.0 μm aerodynamic diameter. The LPI has been calibrated using monodisperse spheres from 0.01 to 6 μm diameter (Hering et al., 1979; Hering et al.,1978). Because of the large range in diameter it is convenient to introduce the

dimensionless size parameter $x = \log(D/D_o)$. For convenience, D_o is chosen to be 0.01 μm, the lower calibration limit of the LPI. For the LPI the size parameter x would range from about 0 to 3. From the calibration data one obtains the collection efficiency $E_i(x)$ for LPI stage i. $E_i(x)$ represents the efficiency of collection of stage i for particles of size x in the absence of the other stages. $E_i(x)$ varies from 0 to 1. To obtain the performance of stage i while all stages are operating simultaneously, one calculates the fractional collection efficiency, $K_i(x)$, for each stage. $K_i(x)$ may be calculated from the measured $E_i(x)$. It represents the fraction of particles of size x collected by stage i. To calculate $K_i(x)$ one determines the fraction of particles of size x which penetrate the previous stages 1, 2, . . ., i-1, and then multiplies this fraction by the collection efficiency $E_i(x)$. The fraction of particles, $F_{i-1}(x)$, penetrating the previous stages is

$$F_{i-1}(x) = 1 - E_{i-1}(x)\left\{ \cdots \left[1 - E_3(x) \left\{ 1-E_2(x)[1 - E_1(x)] \right\} \right] \cdots \right\}$$

Then $K_i(x) = E_i(x)\ F_{i-1}(x) \qquad i = 2, \ldots, 8$

and $K_1(x) = E_1(x)$.

Since monodisperse particles of only a finite number of sizes were used to calibrate the LPI, $E_i(x)$ and $K_i(x)$ are not known continuously over x. If it is assumed that the efficiencies are a continuous function of the Stokes number then the $E_i(x)$ may be interpolated from measured values of $E_i(x_1)$ and $E_i(x_2)$ for $x_1 < x < x_2$. The work of Marple and Lui(1974,1975)

has shown this assumption to be good. From the measured values of E_i at discrete values of x (Hering et al.,1979; Hering et al.,1978) $K_i(x)$ has been calculated and then interpolated to provide a continuous function. The results are shown in Figure C.1. It is seen that the collection efficiency has a strong dependence on particle size. The steepness in slope and the agreement with theory lead to knowledge of $E_i(x)$ and $K_i(x)$ which are more finely tuned on x than the 50% cutoff size intervals.

If the LPI is 100% efficient in collecting particles of size x, then

$$\sum_{i=1}^{8} K_i(x) = 1$$

When operating with the AIHL cyclone preseparator (John and Reischl, 1978), this is approximately true for aerodynamic diameters ranging from 0.1 to 1.0 μm.

The deposits on each of the LPI stages may be analyzed for elemental mass. Let M_i be the mass of the element of interest measured on stage i. From the known masses, M_i, and the known kernels, $K_i(x)$, one would like to determine the unknown mass distribution $f(x) \equiv dM/dx$. The problem may be stated as follows:

$$M_i = \int_0^\infty K_i(x) f(x) dx \qquad i = 1, \ldots, 8 \qquad (C.1)$$

where $M_i \geq 0$, $0 \leq K_i(x) \leq 1$, and $f(x) \geq 0$.

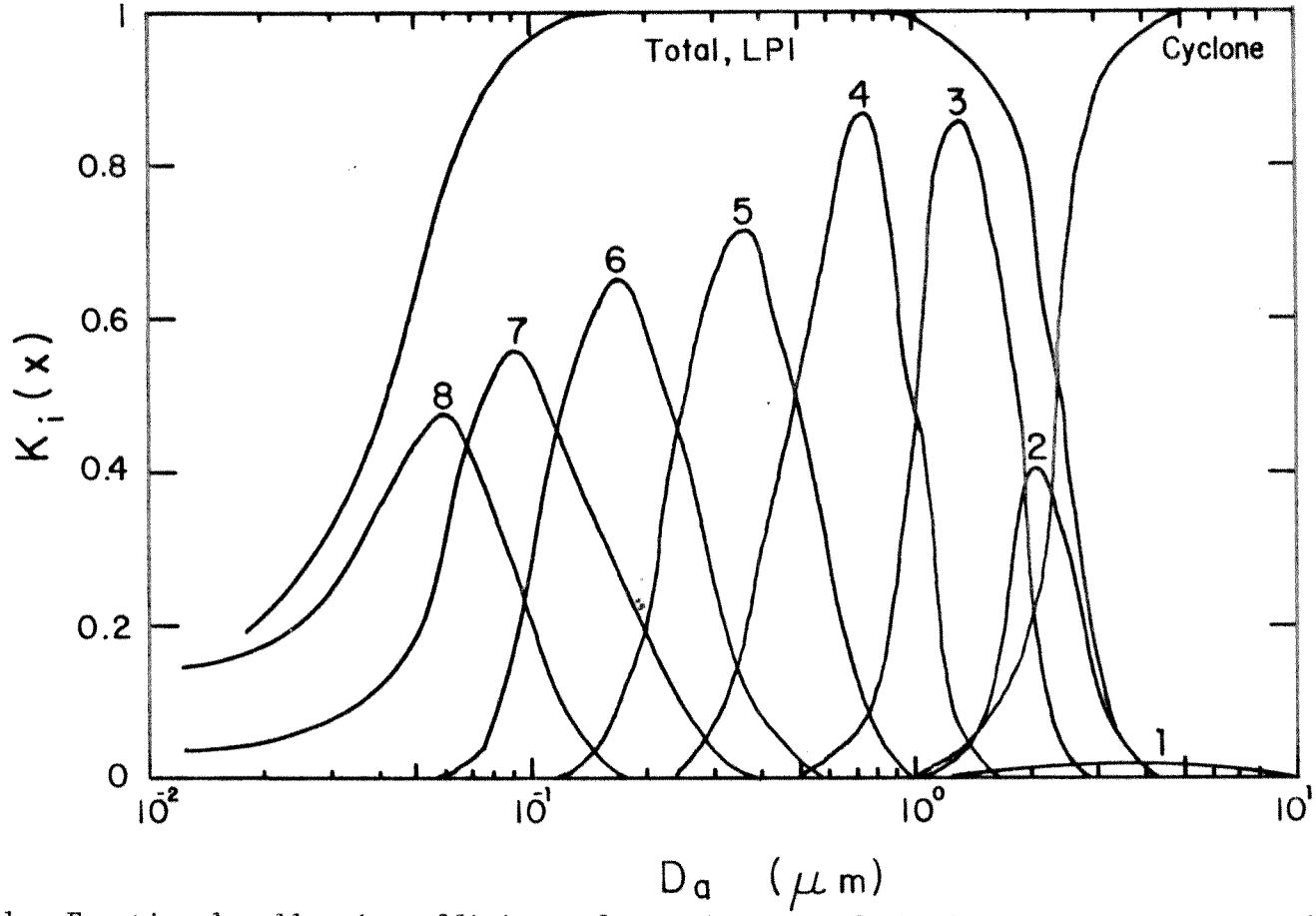

Figure C.1. Fractional collection efficiency for each stage of the low pressure impactor (LPI) when operating downstream of the AIHL cyclone preseparator. $K_i(x)$ represents the fraction of spherical unit specific gravity particles of size x which are collected by stage i. x is the dimensionless particle size: $x=\log(D_a/0.01\ \mu m)$. For example, 22% of the particles of $D_a=0.10\ \mu m$ are collected by stage 6, 54% by stage 7, and 22% by stage 8. 2% of the 0.10 μm particles are not collected by the LPI. $K_i(x)$ was calculated from the measured values of the collection efficiency, $E_i(x)$, at discrete values of x (Hering et al, 1979; Hering et al, 1978). $K_i(x)$ was interpolated between the calculated values. These values apply to the operation of the LPI at 744 mm Hg ambient pressure and 23°C temperature.

In general this is an ill-posed problem for a continuous f(x) because of lack of uniqueness. If we let f*(x) be a solution to Eq. C.1, it is generally possible through the Gram-Schmidt process (Franklin, 1968) to find another solution f**(x) such that

$$f^{**}(x) = f^{*}(x) + \varepsilon f^{+}(x)$$

where f^{+} is orthogonal to each of the kernals $K_i(x)$:

$$\int_0^\infty K_i(x) f^{+}(x)\,dx = 0 \qquad i = 1, \ldots, 8$$

In the limit of $N \to \infty$ the governing equation C.1 takes the form of Fredholm integral equation of the first kind:

$$M(y) = \int_0^\infty K(x,y) f(x)\,dx$$

Even though the information is now much greater by M and K being known continuously on y, this equation can only be solved exactly for a limited number of cases where K(x,y) has a particular form (Fymat, 1979).

If we relax the requirement in Eq. C.1 that f(x) be determined continuously over x and if we are interested only in solutions on a certain interval, say $0<x<3$, then the set of all functions satisfying Eq. C.1 over the interval may fall into quite acceptable limits.

C.3 CASES WHERE UNIQUE SOLUTIONS EXIST

C.3.1 Discrete Distribution

Equation C.1 may be rewritten as a sum of integrals over finite intervals:

$$M_i = \sum_{j=1}^{N} \int_{x_j}^{x_j + \Delta xj} K_i(x) f(x)\, dx = \sum_{j=1}^{N} \overline{(K_i(x) f(x))}_j \; \Delta x_j ; \; i=1,\ldots,8 \quad (C.2)$$

where the overbar denotes the average over the interval $[x_j, x_j+\Delta x_j]$.

Simplifications using this form may result in unique solutions. For example, consider the set of kernels given by

$$K_i = \left\{ \begin{array}{ll} 1 & x_1 \leq x \leq x_{i+1} \\ 0 & x > x_{i+1};\; x < x_i \end{array} \right\} \quad i = 1, \ldots, 8$$

These step functions would result from an ideal impactor which sizes perfectly. Then, from Eq. C.2, we would obtain

$$M_i = \Delta x_i \, \overline{[1 \cdot f(x)]}_i = \Delta x_i \, \overline{f(x)}_i \quad i = 1, \ldots, 8$$

where the $\overline{f(x)}_i$ is the average value over the interval. This results in

$$\overline{f(x)}_i = \frac{M_i}{\Delta x_i} \quad i = 1, \ldots, 8 \quad (C.3)$$

In this case we learn only the average of the mass distribution over the interval -- a histogram. There are obviously an infinite number of functions which have the same average over each interval. This, however, is not critical if we are satisfied only with the average. If we seek the average, it is uniquely determined by Eq. C.3. It is common to plot impactor mass distributions in the form above by assuming the instrument response is ideal. The data are plotted in a histogram as a function of 50% cutoff diameter assuming all particles above D_{50i} are collected by stage i. As Cooper and Spielman (1976) point out, this provides satisfactory results when the instrument resolution is high relative to the variation in the distribution f(x). If f(x) is a broad function the inaccuracy may be quite acceptable. This is generally not the case for most aerosol distributions and impactors.

It is possible to retrieve one other unique distribution from Eq. C.2 if a different assumption is made. If we assume a histogram representation of f(x)

$$f(x) = f_j \quad \text{for } x_j \leq x \leq x_{j+1} \tag{C.4}$$

We then obtain

$$M_i = \sum_{j=1}^{N} \bar{K}_{ij} \, f_j \, \Delta x_j$$

where $\bar{K}_{ij}$ is the average of the kernel function for stage i over the

interval $[x_j, x_{j+1}]$:

$$\bar{K}_{ij} = \frac{1}{x_j} \int_{x_j}^{x_{j+1}} K_{ij}(x)dx$$

If we set N = 8 and choose the x_j cutpoints conveniently, such as 50% efficiency cutoffs, then we have

$$M_i = \sum_{j=1}^{8} [\bar{K}_{ij} \Delta x_j] f_j \quad i = 1, \ldots, 8 \qquad (C.5)$$

This is a system of 8 equations in 8 unknowns, f. This problem is well posed if the matrix $[\bar{K}_{ij} \Delta x_j]$ has an inverse. This technique is probably the simplest way to deal with "crosstalk" between the LPI stages. This approach suffers from the fact that the assumption, Eq. C.4, may not be good if the function varies substantially within each 50% cutoff interval.

C.3.2 Continuous Distribution

It may be possible to obtain a unique solution for f(x) if it can be expressed as a linear combination of the kernels, $K_j(x)$:

$$f(x) = \sum_{j=1}^{8} a_j K_j(x)$$

This would result in the following simplification:

$$M_i = \sum_{j=1}^{8} a_j \phi_{ij} \; ; \; i = 1, \ldots, 8$$

where $\phi_{ij} = (K_i, K_j) = \int_0^\infty K_i(x)K_j(x)dx$

In matrix form this would be written as $\underline{M} = \underline{\phi}A$. Since $\phi_{ij} = \phi_{ji}$, $\underline{\phi}$ is symmetric. If the $K_j(x)$ are linearly independent, then $\underline{\phi}^{-1}$ will exist. If this is the case then the coefficients a_j will be uniquely determined:

$$\underline{A} = \underline{\phi}^{-1}\,\underline{M}$$

f(x) will be positive definite (>0) if ϕ is positive definite, i.e.,

$$\sum_{i=1}^{8}\sum_{j=1}^{8} \phi_{ij}u_iu_j > 0 \quad \text{if } u \neq 0$$

for any function u(x). This will be true if and only if the eigenvalues of $\underline{\phi}$ are positive.

Using the calculated values of $K_i(x)$ for the LPI, the matrix $\underline{\phi}$ was calculated. It was found that the $K_i(x)$ were linearly independent and that the eigenvalues of $\underline{\phi}$ were indeed positive. Thus if the unknown distribution f(x) can be represented by a linear combination of kernal functions, then f(x) can be determined uniquely and it will be positive definite for $M_i > 0$.

If we have a perfect impactor, then K_i would be unit step functions and would be orthonormal:

$$\phi_{ij} = \int_0^\infty K_i(x)K_j(x)dx = \delta_{ij}\Delta x_i$$

This would result in $\underline{\underline{\phi}} = \underline{\underline{\Lambda}}$, where $\underline{\underline{\Lambda}}$ is a diagonal matrix:

$$\underline{\underline{\Lambda}} = \begin{bmatrix} \Delta x_1 & 0 & \cdots & 0 \\ 0 & x_2 & \cdots & 0 \\ \vdots & \vdots & & \\ 0 & 0 & \cdots & \Delta x_8 \end{bmatrix}$$

$\underline{\underline{\Lambda}}^{-1}$ would then be given by

$$\underline{\underline{\Lambda}} = \begin{bmatrix} \Delta x_1^{-1} & 0 & \cdots & 0 \\ 0 & \Delta x_2^{-1} & \cdots & 0 \\ \vdots & \vdots & & \\ 0 & 0 & \cdots & \Delta x_8^{-1} \end{bmatrix}$$

Since $\underline{A} = \underline{\underline{\Lambda}}^{-1} \underline{M}$ then we would have

$$a_i = \frac{M_i}{\Delta x_i} \qquad i=1, \ldots, 8$$

This would result in the following form for f(x):

$$f(x) = \begin{cases} \dfrac{M_1}{\Delta x_2} & x_1 < x < x_2 \\ \dfrac{M_2}{\Delta x_2} & x_2 < x < x_3 \\ \vdots & \vdots \\ \dfrac{M_8}{\Delta x_8} & x_8 < x < 9 \\ 0 & x > x_9,\ x < x_1 \end{cases}$$

Thus, for a perfect impactor the only distribution function that would satisfy the requirement that it be a linear combination of the kernels would be a histogram. In the limit as the number of stages approaches infinity, the step interval would approach zero and the value of f(x) would be determined for each x_i arbitrarily close to x_{i+1}. The distribution would then approach a unique continuous function

$$f(x) = \frac{dM}{dx}$$

C.4 TWOMEY ALGORITHM

In Eq. C.5 the number of tabular points in x was determined by the number of measurements -- 8. An alternative scheme is to drive the divisions in x by the information on K and its rate of change.

The number of divisions in x can then be made independent of the number of measurements. We may then choose small Δx intervals such that the kernel, $K_i(x)$, and the function $f(x)$ are not expected to vary substantially in this interval.

The basis for the Twomey (1975) algorithm is that the unknown function $f(x)$ may be approximated over the interval of interest by a linear combination of kernel functions. The variation in $K_i(x)$ will drive the Δx and the number of tabular points in x,N. This permits the evaluation of the unknown function over intervals smaller than the 50% efficiency size cuts. Assuming a histogram representation for $f(x)$, the problem reduces to

$$M_i = \sum_{j=1}^{N} \overline{K}_{ij} f_j \Delta x_j \qquad i = 1, \ldots, 8 \qquad (C.6)$$

or

$$M_i = \sum_{\ell=1}^{8} \phi_{i\ell} a_\ell \qquad i = 1, \ldots, 8$$

where $\phi_{i\ell} = \sum_{j=1}^{N} \overline{K}_{ij} \overline{K}_{\ell j} \Delta x_j$

with $M_i, f(x_j) \geq 0$

and $0 \leq \overline{K}_{ij} \leq 1$

The a_ℓ are unknown constants.

Instead of solving for a_ℓ directly, Twomey (1975) used a nonlinear iterative algorithm to obtain $f(x_j)$. The value of the function at x_j on the n+1 iteration, $f_{n+1}(x_j)$, is given by

$$\frac{f_{n+1}(x_j)}{f_n(x_j)} = 1 + (r_{in} - 1)\, K_i(x_j) \tag{C.7}$$

where

$$r_{in} = \frac{M_i}{\int K_i(x) f(x)\, dx} \simeq \frac{M_i}{\sum_{j=1}^{N} K_i(x_j) f_n(x_j) \Delta x_j} \tag{C.8}$$

Assuming the histogram representation for f(x), this reduces to

$$\frac{f_{j,n+1}}{f_{j,n}} = 1 + (r_{in} - 1)\, \bar{K}_{ij} \tag{C.9}$$

where

$$r_{in} = \frac{M_i}{\sum_{j=1}^{N} \bar{K}_{ij} f_j \Delta x_j} \tag{C.10}$$

The subscript i corresponds to the impactor stage number, while the subscript n is the iteration number.

As $f_n(x)$ approaches the "correct" solution then r_{in} will approach 1 and $f_{n+1}(x_j)$ will converge to $f_n(x_j)$. An initial distribution $f_0(x_j)$ must be provided. It is usually a "fine tuned" version of the distribution $\Delta M_i/\Delta \log D_{50i}$ obtained from the measured masses M_i and the 50% efficiency cutpoints for each LPI stage.

C.5 CHARACTERISTICS OF THE SOLUTIONS OBTAINED BY THE TWOMEY ALGORITHM

If $f_n(x_j)$ is within the subspace spanned by the kernals $K_i(x_j)$ then $f_{n+1}(x)$ will tend to stay within the subspace for small changes (Twomey, 1975). Since $K_{i\ell}$ is positive definite and $M_i \geq 0$, then $f_n(x)$ will be nonnegative. Since $K_i(x_j) < 1$, $f_{n+1}(x)$ will remain bounded if $f_0(x)$ is bounded.

By the method of the calculus of variations it can be shown that if $f(x)$ can be expressed as a linear combination of the kernals $K_i(x)$ then the optimal solution, $f^*(x)$, is that which minimizes the quadratic deviation from the initial distribution:

$$\int_0^\infty [f^*(x) - f_0(x)]^2 dx = \text{minimum}$$

This is shown in the following derivation. The difference function, $u = f^* - f_0$, can be expressed as a linear combination of the kernals:

$$u(x) = \sum_{i=1}^{8} C_i K_i(x)$$

for $\int_0^\infty u^2 dx = \text{minimum}$, we seek a relationship between $u(x)$ and an arbitrary

function $\psi(x)$ such that

$$\int_0^\infty (u+\varepsilon\psi)^2 dx = \text{minimum}$$

Expanding the integral,

$$\int u^2 dx + \varepsilon^2 \int \psi^2 dx + 2\varepsilon \int u\psi dx = \text{minimum}$$

This will be satisfied if u and ψ are orthogonal:

$$\int_0^\infty u(x)\psi(x)dx = 0$$

Since $u = \sum C_i K_i(x)$, then $\sum_{i=1}^{8} C_i \int K_i \psi dx = 0$

Since not all $C_i = 0$, then ψ and each of the kernels are orthogonal:

$$\int_0^\infty K_i(x)\psi(x)dx = 0 \quad i = 1, \ldots, 8$$

For our inversion problem we require that

$$M_i = \int K_i(x)\, f^*(x)dx \quad i = 1, \ldots, 8 \qquad (C.11)$$

We then seek a $\psi(x)$ such that

$$M_i = \int K_i(x)[f^*(x) + \varepsilon\psi(x)]dx \quad i = 1, \ldots, 8$$

Letting

$$M_i' = M_i - \int K_i f_0(x)dx$$

then

$$M_i' = \int K_i(x)u(x)dx + \varepsilon\int K_i(x)\psi(x)dx$$

This will be satisfied if $K_i(x)$ and $\psi(x)$ are orthogonal, as required earlier for minimization of quadratic deviation. Thus, the function $f^*(x)$ which satisfies the mass relationship, Eq. C.11, also insures that its quadratic deviation from the original function $f_0(x)$ is minimized.

C.6 TEST OF THE TWOMEY ALGORITHM

A number of tests were performed on the Twomey algorithm to determine its effectiveness in inverting the LPI data. The tests were concerned with questions of uniqueness, convergence, sensitivity to calibration data, and sensitivity to initial guess distributions.

In these tests the discrete form of the conservation equation was used:

$$M_i = \sum_{j=1}^{N} \bar{K}_{ij} f_j \Delta x_j \quad i = 1, \ldots, 8$$

Consistent in the variation in the calibration data, a logarithmic diameter interval $\Delta x_j = 0.0625$ was used, resulting in 16 data points per decade. Upper and lower bounds on the particle size domain were chosen to be 6.0 and 0.01 μm respectively. The number of intervals, N, was equal to 45. The initial distribution, f_{j0}, was generated from the $\Delta M_i / \Delta \log D_{50i}$ data. A fraction of the mass measured on each of the LPI stages was assigned to each interval and then a running average was calculated. The initial distribution, f_{j0}, was thus simply a "fine tuned" version of the data. The algorithm generated a new $f_{j,n}$ from $f_{j,n-1}$ using equations C.9 and C.10. The $f_{j,n}$ was then used to calculate the mass, M_i^n, that would be collected on each LPI stage resulting from $f_{j,n}$:

$$M_i^n = \sum_{j=1}^{N} \bar{K}_{ij} f_{j,n} \Delta x_j \quad i = 1, \ldots, 8.$$

If the calculated M_i^n were within an acceptable error of the measured M_i for all i, then the $f_{j,n}$ was considered to be the "correct" value,

C.6.1 Uniqueness

There is no mathematical assurance that the inverted distribution obtained from the Twomey algorithm will be unique over the particle size domain of interest. To test for uniqueness, bimodal lognormal input distributions were generated of the, i.e.,

$$f(\ln D_j) = \frac{A}{\sqrt{2\pi}\ \ln \sigma_1} \exp\left[-\frac{1}{2}\left(\frac{\ln D_j - \ln D_1}{\ln \sigma_1}\right)^2\right]$$

$$+ \frac{1-A}{\sqrt{2\pi}\ \ln \sigma_2} \exp\left[-\frac{1}{2}\left(\frac{\ln D_j - \ln D_2}{\ln \sigma_2}\right)^2\right]$$

The function was normalized so that $\int_{-\infty}^{\infty} f(\ell nD)d\ell nD = 1$.

The parameters A, D_1, D_2, σ_1, and σ_2 were varied over reasonable ranges. Masses on each stage of the LPI were then simulated from $f(\ell nD_j)$ using the calibration data $K_i(x_j)$ and the relation

$$M_i = \sum_{j=1}^{N} K_i (x_j) f(x_j) \Delta x_j$$

These simulated masses were then used as input to the Twomey algorithm. The inverted distribution from the algorithm was then compared with the input bimodal lognormal distribution.

It was found that the Twomey algorithm faithfully retrieved the correct distribution from 0.05 to 2.0 μm when the cyclone separator data were included. The useful range extended up to 4 μm with the absence of the cyclone. These limits correspond to the 50% efficiency cutoff diameters on the first and last stages of the impactor. The inversion algorithm was capable of resolving narrow distributions have a geometric standard deviation, σ, of 1.1. The algorithm did not generally produce inverted distributions which were more or less narrow than the input distribution. Some typical results are shown in Figures C.2a-C.2f.

Twomey (1975) noted that the computation time for the algorithm was considerably longer than for the linear inversion techniques. In this work this characteristic was noticed in cases where the allowed error between the calculated M_i^n and the measured M_i was very small. For a 0.1% error, up to 1000 iterations were sometimes necessary, requiring substantial computation time on a PDP-11/60 computer.

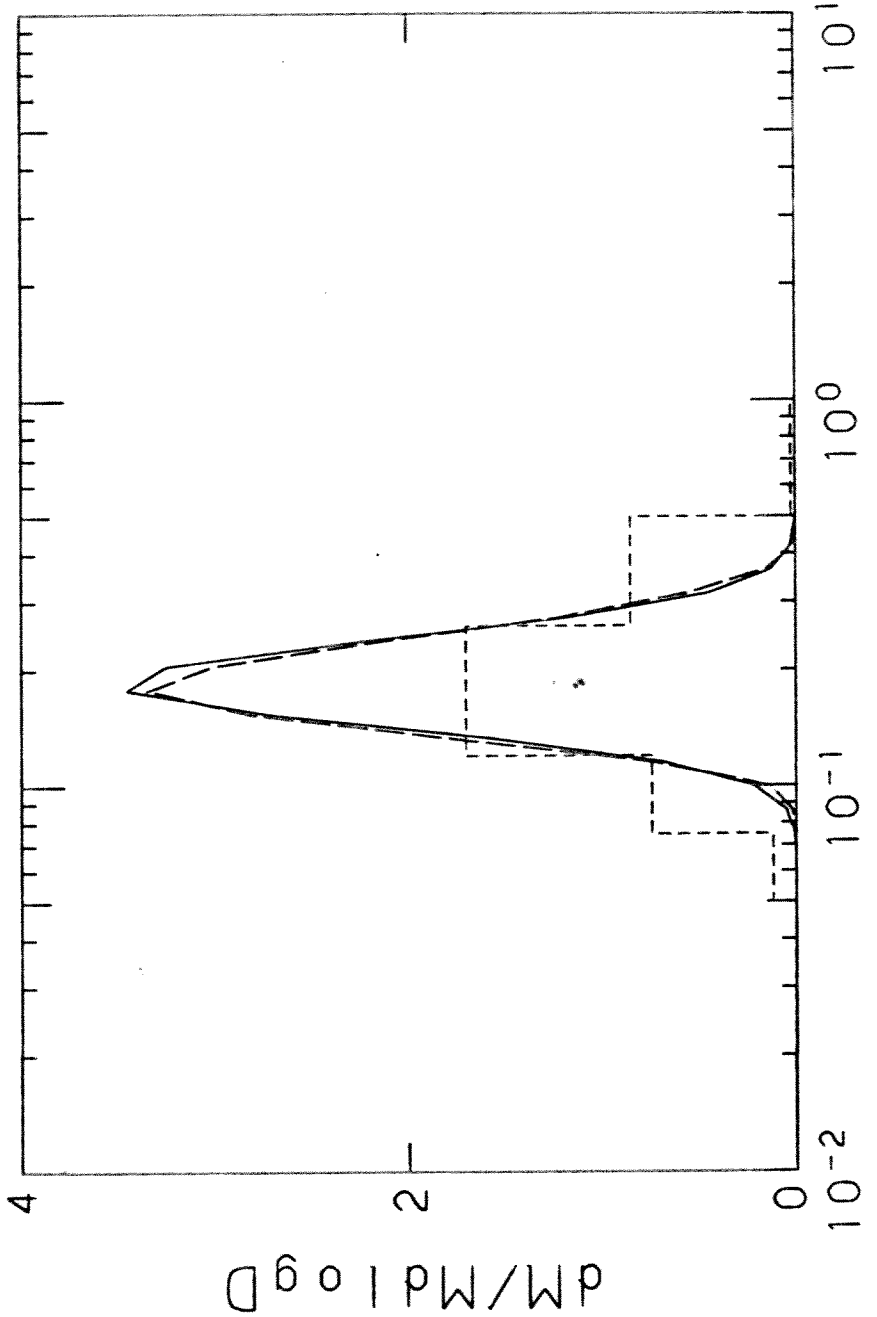

Figure C.2a. Test of Twomey inversion algorithm. Solid curve is input lognormal distribution and long dash curve is inverted distribution after 200 iterations. Short dash curve is computed distribution of unit specific gravity aerosol mass collected by low pressure impactor with respect to 50% aerodynamic cutoff diameter. Input parameters: 0.20 µm geometric mean diameter; 1.3 geometric standard deviation.

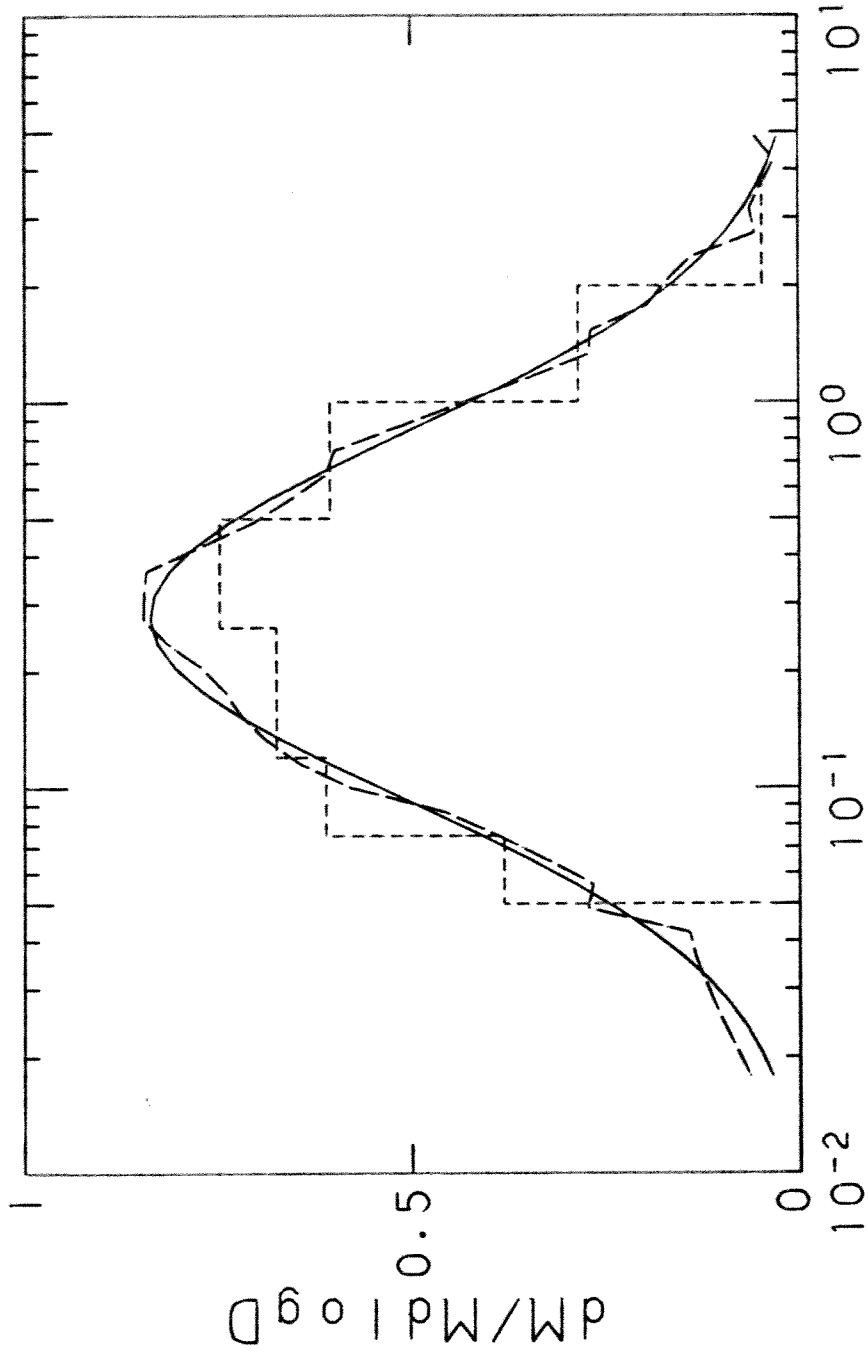

Figure C.2b. Test of Twomey inversion algorithm. Solid curve is input lognormal distribution and long dash curve is inverted distribution after 200 iterations. Short dash curve is computed distribution of unit specific gravity aerosol mass collected by low pressure impactor with respect to 50% aerodynamic cutoff diameter. Input parameters: 0.30 μm geometric mean diameter; 3.0 geometric standard deviation.

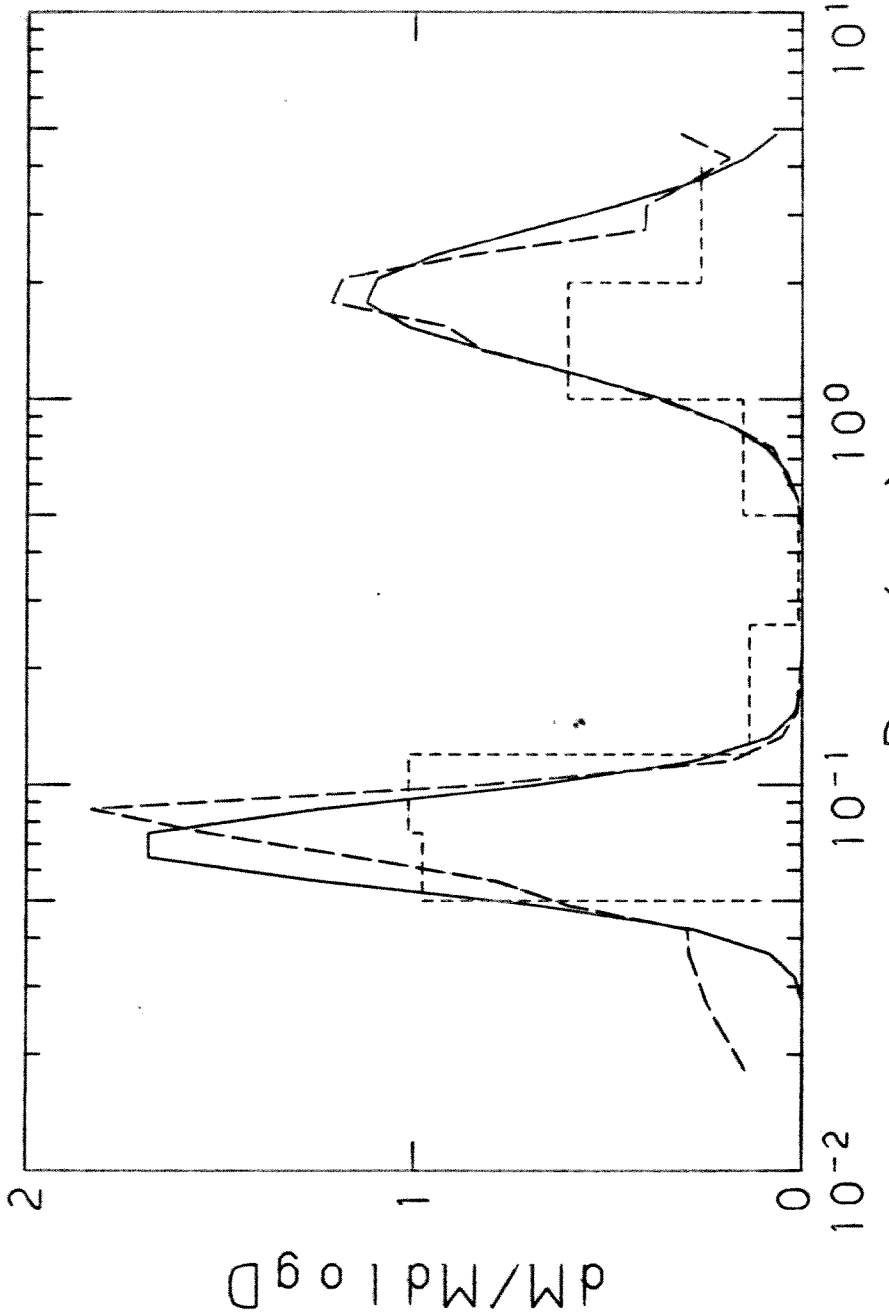

Figure C.2c. Test of Twomey inversion algorithm. Solid curve is input bimodal lognormal distribution and long dash curve is inverted distribution after 200 iterations. Short dash curve is computed distribution of unit specific gravity aerosol mass collected by low pressure impactor with respect to 50% aerodynamic cutoff diameter. Input parameters: 0.75 μm and 2.0 μm geometric mean diameters; 1.3 and 1.5 geometric standard deviations, respectively.

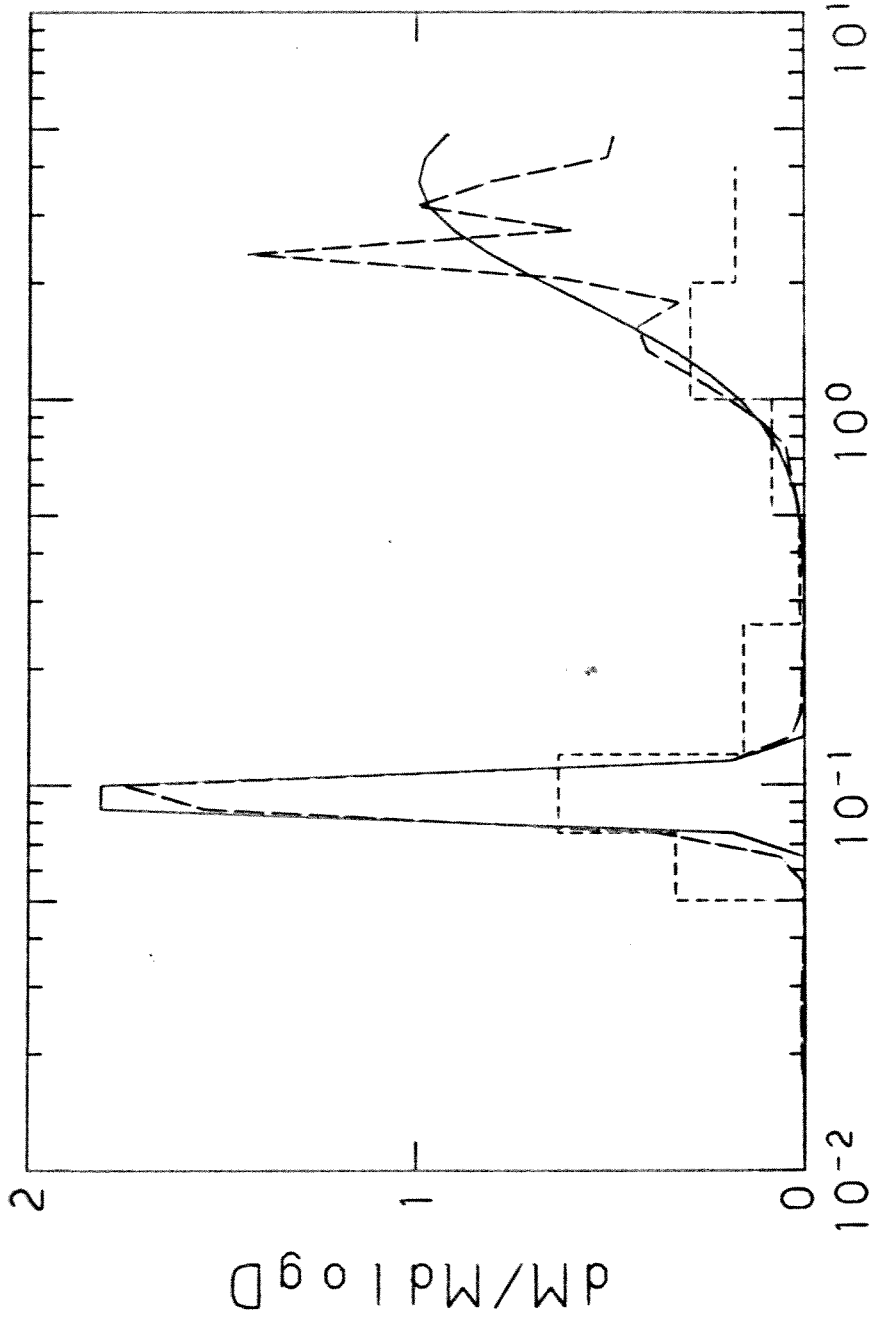

Figure C.2d. Test of Twomey inversion algorithm. Solid curve is input bimodal lognormal distribution and long dash curve is inverted distribution after 200 iterations. Short dash curve is computed distribution of unit specific gravity aerosol mass collected by low pressure impactor with respect to 50% aerodynamic cutoff diameter. Input parameters: 0.1 and 0.4 μm geometric mean diameters; 1.1 and 2.0 geometric standard deviations, respectively.

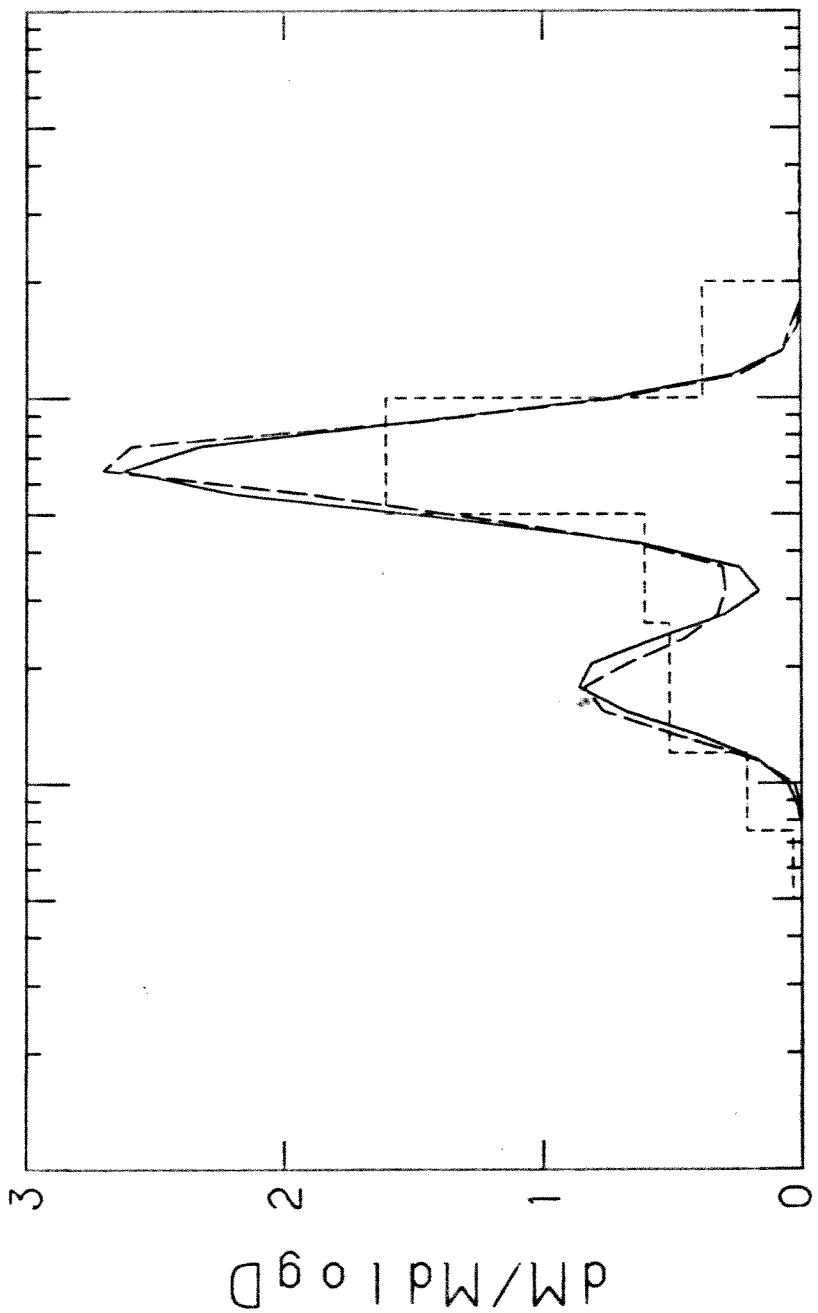

Figure C.2e. Test of Twomey inversion algorithm. Solid curve is input bimodal lognormal distribution and long dash curve is inverted distribution after 200 iterations. Short dash curve is computed distribution of unit specific gravity aerosol mass collected by low pressure impactor with respect to 50% aerodynamic cutoff diameter. Input parameters: 0.2 and 0.7 μm geometric mean diameters; 1.3 and 1.3 geometric standard deviations, respectively.

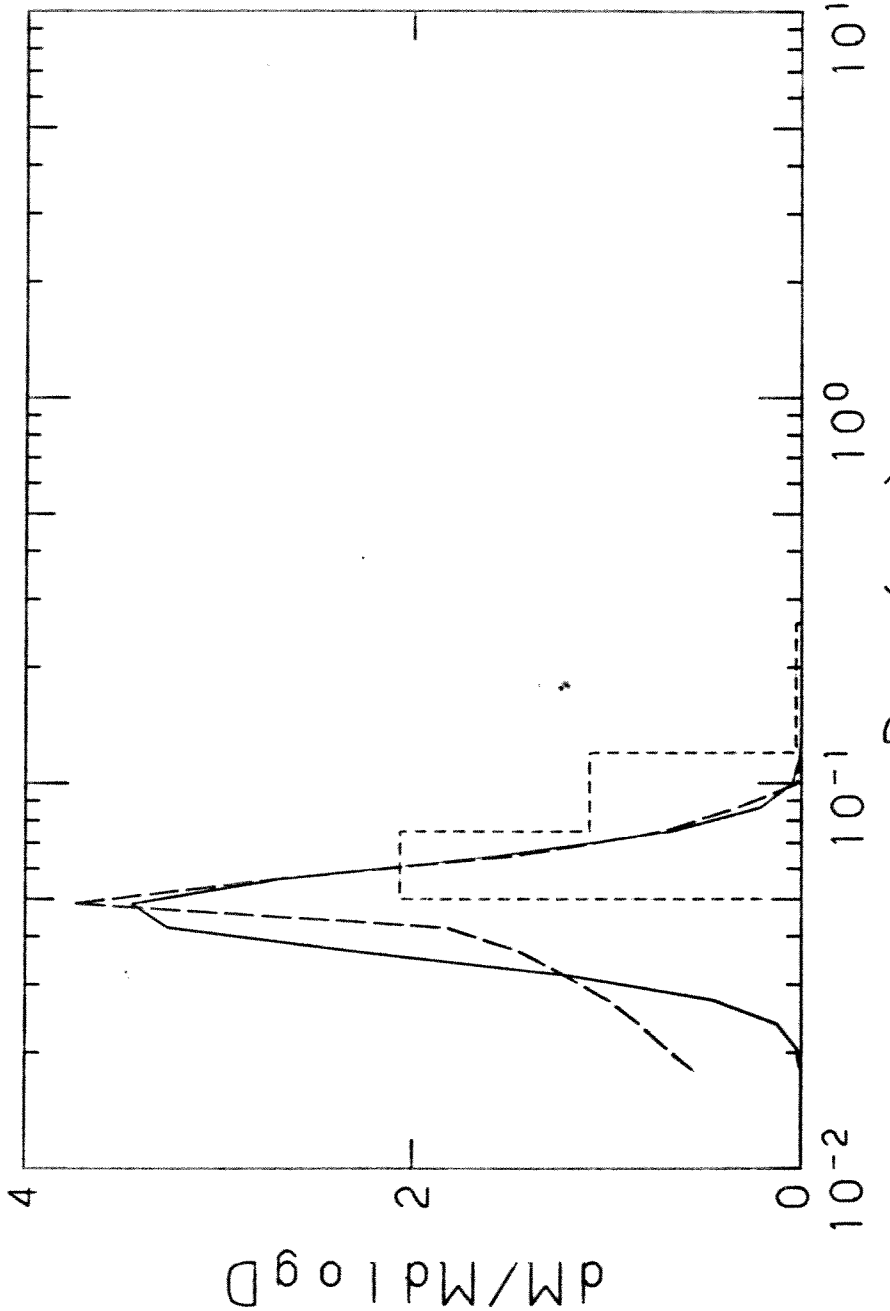

Figure C.2f. Test of Twomey inversion algorithm. Solid curve is input lognormal distribution and long dash curve is inverted distribution after 200 iterations. Short dash curve is computed distribution of unit specific gravity aerosol mass collected by low pressure impactor with respect to 50% aerodynamic cutoff diameter. Input parameters: 0.05 μm geometric mean diameter; 1.3 geometric standard deviation.

When a more realistic error is used, consistent with actual measurement error, the computation time drops radically. The error of measurement for elements analyzed by flash volatilization and flame photometric detection and by particle induced X-ray emissions is about 2 nanograms. When this $\pm$ 2 ng error is prescribed the algorithm usually inverts successfully in 4 to 40 iterations.

C.6.2 Sensitivity to Initial Distribution, $f_o(x)$

The Twomey inversion algorithm is most successful in inverting distributions where the function f(x) can be expressed as a linear combination of the kernel functions $K_i(x)$. As shown before if this linear combination criterion is satisfied, the optimum function $f^*(x)$ is that which minimizes the quadratic deviation between it and the initial distribution $f_o(x)$. This would indicate the possibility that the final inverted distribution may be dependent upon the choice of the initial distribution. This hypothesis was tested by generating bimodal input test functions as before and using a uniform constant $f_o(x) = C$, instead of a smooth version of $\Delta M_i/\Delta \log_{50i}$. It was found that for a large variety of distributions there was no appreciable difference between the inverted distributions obtained from the two different initial distributions.

C.6.3 Sensitivity to Calibration Data

The calibration data are not known with perfect accuracy. The measurements made with the monodisperse aerosols were subject to error. The interpolation between calibration points by means of a smooth function was also subject to error. In order to test the sensitivity of the inverted distribution to variation in the calibration data, the collection efficiencies, $E_i(x)$, were randomly varied. The mean and standard deviation in the inverted mass distribution was then calculated. The standard deviation was then taken to be the error in the inverted distribution for the chosen error in the calibration data.

The collection efficiencies $E_i(x)$ were randomly varied using the following form:

$$E_i'(x_j) = \delta_{1i} + (1+\delta_{2i})E_i(x_j) \quad i=1, \ldots,8 \qquad (C.12)$$

δ_{1i} and δ_{2i} were normally distributed random variables between -1 and +1. These had the effect of changing the slope and "intercept" of the collection efficiency curve for each stage of the LPI, corresponding to errors in measured particle size and collection efficiency, respectively, in calibration. The new kernels, $K_i'(x_j)$ were then calculated using these $E_i'(x_j)$. The standard deviations of δ_{1i} and δ_{2i} were varied from $\pm$ 0.1% (.001) to $\pm$ 20% (0.20).

It was found that no instabilities resulted in the inverted distributions; they preserved their shape and peak. However, the variation in the inverted distributions was found to be quite sensitive to variation in the collection efficiency $E_i'(x)$. Typical results are plotted in Figures C.3a-C.3e. The accuracy in the calibration data are probably no better than $\pm 10\%$ corresponding to $\delta_{1i} = \delta_{2i} \tilde{=} 0.05$. For these values the resultant error in the inverted distribution is approximately $\pm 30\%$ for typical distributions.

C.7 SUMMARY AND CONCLUSIONS

The Twomey nonlinear inversion algorithm was evaluated for inverting mass distributions obtained with the low pressure impactor (LPI). Simulations on a PDP-11/60 computer indicated that the algorithm successfully retrieved test distributions from 0.05 to 4.0 μm, corresponding to upper and lower 50% efficiency cutoff diameters of the LPI. The computation time required for convergence was strongly dependent on the error criteria prescribed. For errors representative of current mass determination techniques, the convergence was typically achieved in seconds. For typical distributions the final inverted distribution was not sensitive to the initial guess distribution. The inverted distribution was found to be quite sensitive to errors in the calibration data. A 10% error in calibration may result in approximately 30% error in the inverted distribution.

The inversion program developed for this research provides a histogram distribution of 16 values per decade in equal logarithmic intervals

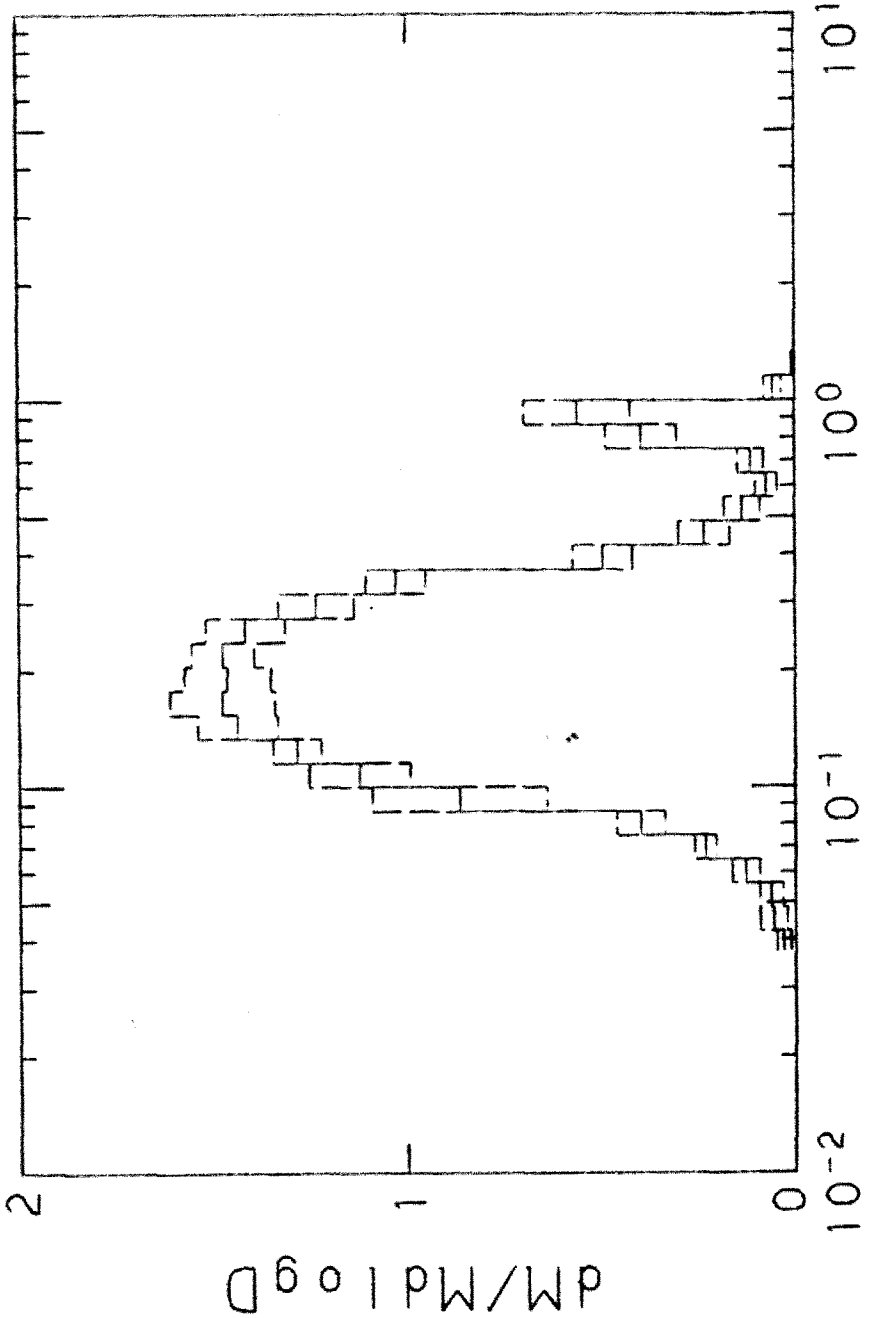

Figure C.3a. Sensitivity of inverted mass distribution to uncertainty in LPI calibration data. Sept. 5-7, 1979, China Lake sulfur distribution, Figure 4.5c, was used as test distribution. The collection efficiency of each stage of the LPI was randomly varied about the measured value (Hering et al, 1979; Hering et al, 1978) using Equation C.12. Inverted distributions were determined for each of the randomly varied collection efficiencies. The solid histogram is the average of 100 inverted distributions, while the dashed histograms above and below the average are the standard deviations. Standard deviations in δ_1 and δ_2 were 0.01 and 0.01, respectively.

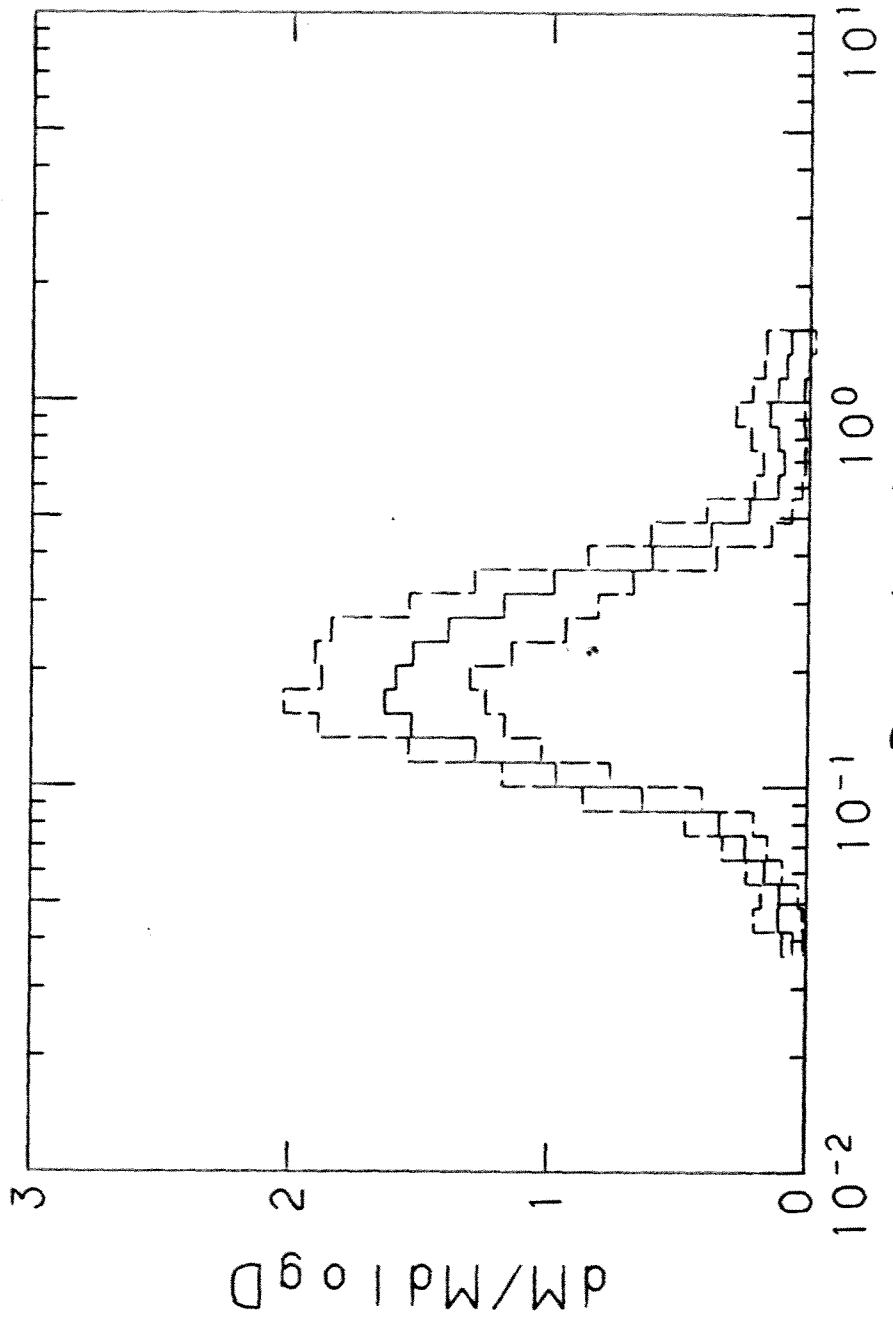

Figure C.3b. Sensitivity of inverted mass distribution to uncertainty in LPI calibration data. Sept. 5-7, 1979, China Lake sulfur distribution, Figure 4.5c, was used as test distribution. The collection efficiency of each stage of the LPI was randomly varied about the measured value (Hering et al, 1979; Hering et al, 1978) using Equation C.12. Inverted distributions were determined for each of the randomly varied collection efficiencies. The solid histogram is the average of 100 inverted distributions, while the dashed histograms above and below the average are the standard deviations. Standard deviations in δ_1 and δ_2 were 0.05 and 0.05, respectively.

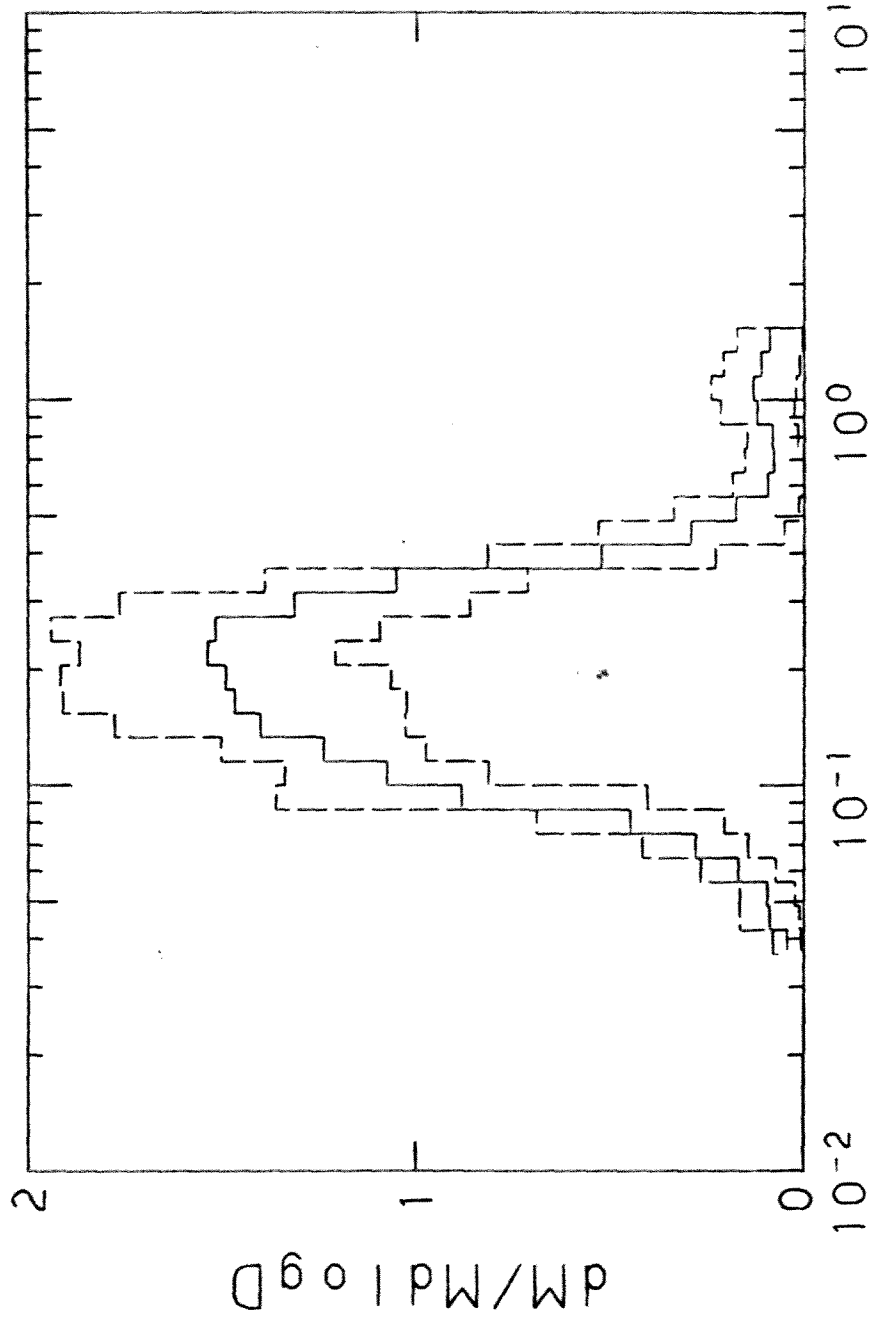

Figure C.3c. Sensitivity of inverted mass distribution to uncertainty in LPI calibration data. Sept. 5-7, 1979, China Lake sulfur distribution, Figure 4.5c, was used as test distribution. The collection efficiency of each stage of the LPI was randomly varied about the measured value (Hering et al, 1979; Hering et al, 1978) using Equation C.12. Inverted distributions were determined for each of the randomly varied collection efficiencies. The solid histogram is the average of 100 inverted distributions, while the dashed histograms above and below the average are the standard deviations. Standard deviations in δ_1 and δ_2 were 0.05 and 0.001, respectively.

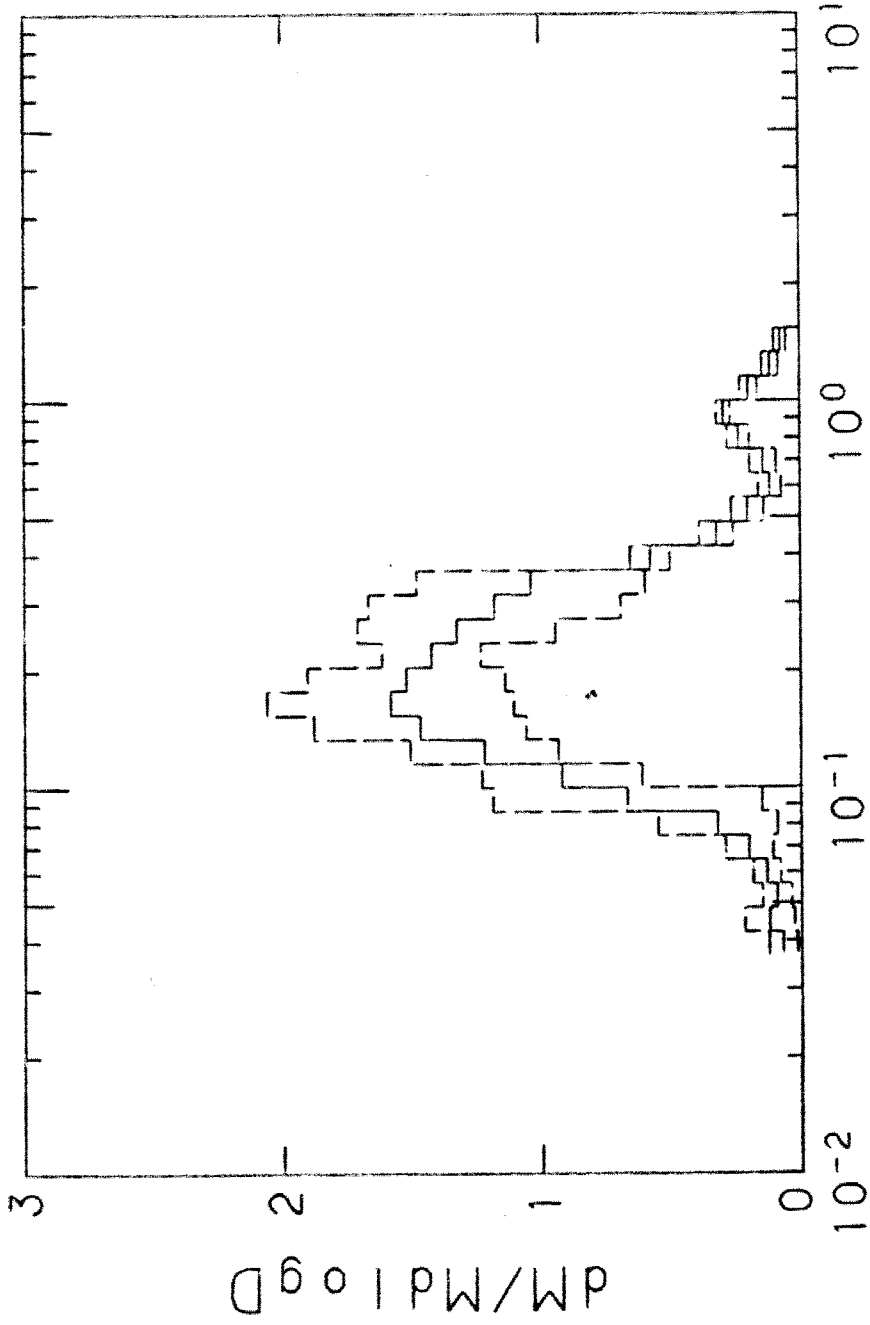

Figure C.3d. Sensitivity of inverted mass distribution to uncertainty in LPI calibration data. Sept. 5-7, 1979, China Lake sulfur distribution, Figure 4.5c, was used as test distribution. The collection efficiency of each stage of the LPI was randomly varied about the measured value (Hering et al, 1979; Hering et al, 1978) using Equation C.12. Inverted distributions were determined for each of the randomly varied collection efficiencies. The solid histogram is the average of 100 inverted distributions, while the dashed histograms above and below the average are the standard deviations. Standard deviations in δ_1 and δ_2 were 0.001 and 0.10, respectively.

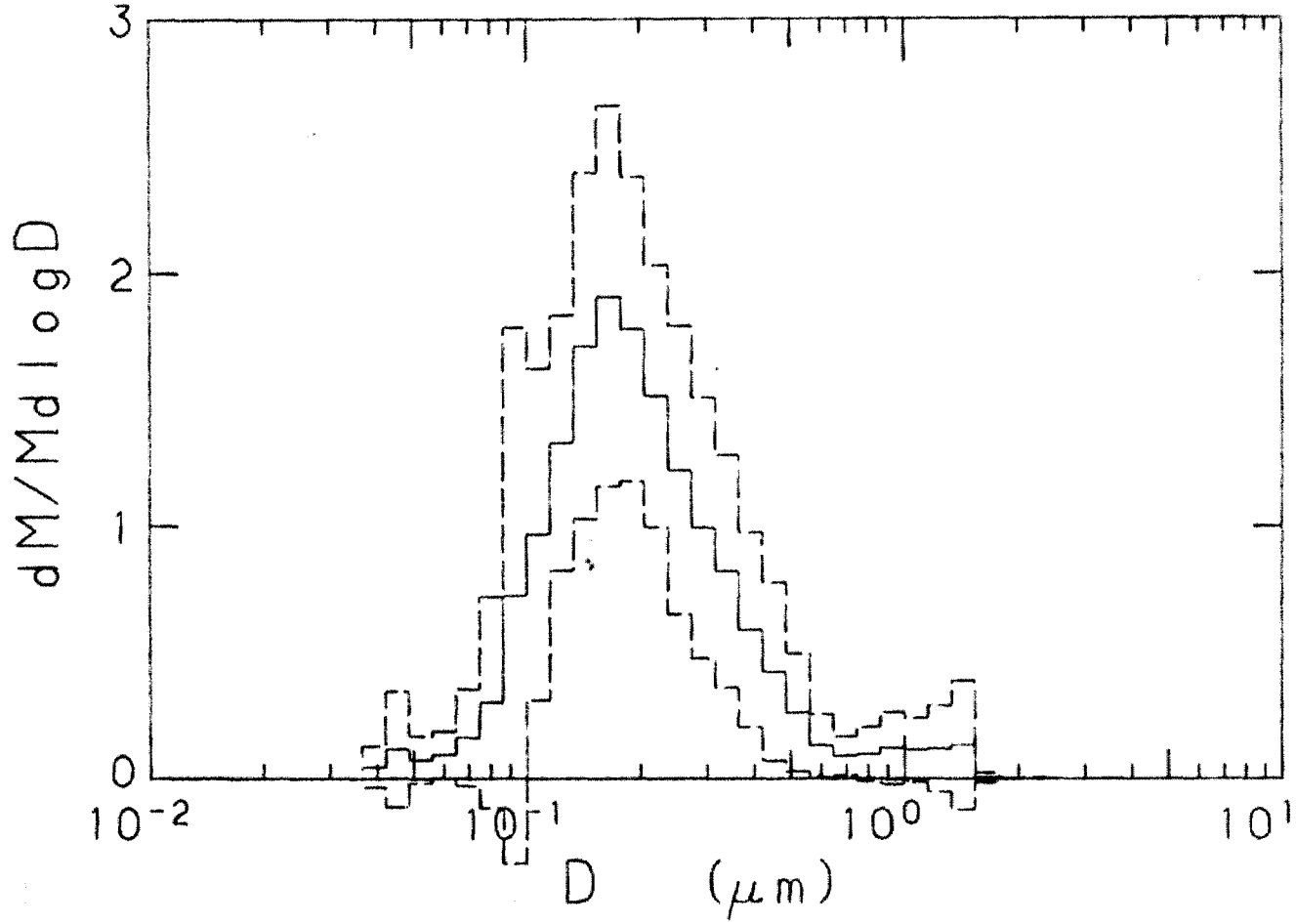

Figure C.3e. Sensitivity of inverted mass distribution to uncertainty in LPI calibration data. Sept. 5-7, 1979, China Lake sulfur distribution, Figure 4.5c, was used as test distribution. The collection efficiency of each stage of the LPI was randomly varied about the measured value (Hering et al, 1979; Hering et al, 1978) using Equation C.12. Inverted distributions were determined for each of the randomly varied collection efficiencies. The solid histogram is the average of 100 inverted distributions, while the dashed histograms above and below the average are the standard deviations. Standard deviations in δ_1 and δ_2 were 0.10 and 0.10, respectively.

from 0.01 to 6.0 μm. Values of the inverted distribution outside the range of 0.05 to 4.0 μm may be subject to substantial error. A more accurate determination of the particle extinction coefficient distribution is now possible with the inverted distribution obtained from the LPI and the Twomey algorithm.

APPENDIX D. EXPERIMENTAL DATA

Low Pressure Impactor Data

Location	Start Date	Start Time	T	Code	M	EM1	EM2	EM3	EM4	EM5	EM6	EM7	EM8
CHINA LAKE	090579	0000 PST	16.7	5	999	0	0	36	82	266	375	152	45
CHINA LAKE	102078	0000 PST	16.7	5	999	0	0	46	533	603	373	102	48
CHINA LAKE	070278	0000 PST	16.7	5	999	0	0	31	79	197	294	128	38
CHINA LAKE	090779	0823 PST	16.7	13	999	8	29	23	8	0	0	0	0
CHINA LAKE	090779	0823 PST	16.7	8	999	15	26	21	0	0	0	0	0
CHINA LAKE	090779	0823 PST	16.7	7	999	0	18	15	0	7	0	0	0
CHINA LAKE	090779	0823 PST	16.7	5	999	7	12	77	76	129	147	87	128
CHINA LAKE	090779	0823 PST	16.7	4	999	66	162	132	9	0	0	0	0
ZILNEZ MESA	JUN-JU	L 79 AVE	16.7	8	49	15	31	19	10	1	1	1	3
ZILNEZ MESA	JUN-JU	L 79 AVE	16.7	7	71	7	11	9	11	22	13	5	4
ZILNEZ MESA	JUN-JU	L 79 AVE	16.7	20	369	0	11	17	63	121	101	44	17
ZILNEZ MESA	JUN-JU	L 79 AVE	16.7	5	369	0	5	9	53	89	67	35	32
ZILNEZ MESA	JUN-JU	L 79 AVE	16.7	4	167	50	115	73	11	1	3	5	6
ZILNEZ MESA	JUN-JU	L 79 AVE	16.7	3	0	7	40	20	4	6	0	1	1
ZILNEZ MESA	JUN-JU	L 79 AVE	16.7	13	20	10	21	15	4	1	0	0	0
ZILNEZ MESA	062779	1920 MST	23.1	3	0	39	29	18	8	62	0	0	0
ZILNEZ MESA	062779	1920 MST	23.1	4	443	87	96	39	0	0	22	12	8
ZILNEZ MESA	062779	1920 MST	23.1	5	369	0	5	13	55	50	78	46	27
ZILNEZ MESA	062779	1920 MST	23.1	7	48	49	9	5	10	12	13	7	4
ZILNEZ MESA	062779	1920 MST	23.1	8	45	45	24	0	0	0	0	11	0
ZILNEZ MESA	062779	1920 MST	23.1	13	16	9	19	11	2	4	50	2	0
ZILNEZ MESA	062879	1947 MST	17.2	3	0	0	32	43	0	0	0	0	0
ZILNEZ MESA	062879	1947 MST	17.2	4	229	20	77	88	0	0	32	65	45
ZILNEZ MESA	062879	1947 MST	17.2	5	763	0	18	22	96	164	95	52	35
ZILNEZ MESA	062879	1947 MST	17.2	7	76	0	5	12	6	12	3	12	0
ZILNEZ MESA	062879	1947 MST	17.2	8	52	4	20	19	3	4	16	0	13
ZILNEZ MESA	062879	1947 MST	17.2	13	0	0	13	12	2	4	0	0	0
ZILNEZ MESA	062979	1402 MST	23.1	3	0	0	0	43	3	0	0	5	0
ZILNEZ MESA	062979	1402 MST	23.1	4	232	14	231	185	21	0	7	0	0
ZILNEZ MESA	062979	1402 MST	23.1	5	949	0	9	25	258	363	229	103	86
ZILNEZ MESA	062979	1402 MST	23.1	7	94	1	21	23	23	23	16	8	8
ZILNEZ MESA	062979	1402 MST	23.1	8	62	7	41	41	8	0	0	0	0
ZILNEZ MESA	062979	1402 MST	23.1	13	57	8	39	40	6	3	1	0	0
ZILNEZ MESA	062979	1402 MST	23.1	20	949	5	15	19	227	589	326	186	101
ZILNEZ MESA	070279	1326 MST	20.9	3	44	15	29	32	2	5	0	4	3
ZILNEZ MESA	070279	1326 MST	20.9	4	214	13	239	98	32	0	0	20	0
ZILNEZ MESA	070279	1326 MST	20.9	5	589	0	6	15	84	135	117	57	32
ZILNEZ MESA	070279	1326 MST	20.9	7	105	6	21	12	17	29	22	10	6
ZILNEZ MESA	070279	1326 MST	20.9	8	67	9	57	23	8	0	0	0	0
ZILNEZ MESA	070279	1326 MST	20.9	13	27	5	42	23	5	1	0	1	0
ZILNEZ MESA	070279	1326 MST	20.9	20	589	0	7	26	178	255	291	89	24
ZILNEZ MESA	070379	1154 MST	45.8	3	0	11	152	76	5	6	4	6	8
ZILNEZ MESA	070379	1154 MST	45.8	4	344	71	598	259	19	0	0	3	0
ZILNEZ MESA	070379	1154 MST	45.8	5	306	0	13	32	116	292	185	90	32
ZILNEZ MESA	070379	1154 MST	45.8	7	191	10	71	41	64	184	99	28	11
ZILNEZ MESA	070379	1154 MST	45.8	8	86	46	175	76	42	0	0	0	0
ZILNEZ MESA	070379	1154 MST	45.8	13	30	12	109	66	13	5	1	1	0
ZILNEZ MESA	070379	1154 MST	45.8	20	306	0	155	125	261	358	355	165	86

Low Pressure Impactor Data (continued)

Location		Start Date	Start Time		T	Code	M	EM1	EM2	EM3	EM4	EM5	EM6	EM7	EM8
ZILNEZ	MESA	070579	1400	MST	22.5	3	0	22	25	21	9	11	0	0	0
ZILNEZ	MESA	070579	1400	MST	22.5	4	154	273	41	72	4	0	29	25	62
ZILNEZ	MESA	070579	1400	MST	22.5	5	300	2	3	16	28	76	50	28	77
ZILNEZ	MESA	070579	1400	MST	22.5	7	54	13	6	6	4	10	10	0	8
ZILNEZ	MESA	070579	1400	MST	22.5	8	29	10	13	15	6	4	0	13	19
ZILNEZ	MESA	070579	1400	MST	22.5	13	0	11	9	12	0	1	0	0	0
ZILNEZ	MESA	070579	1400	MST	22.5	20	300	0	14	56	38	118	69	45	9
ZILNEZ	MESA	070679	1346	MST	22.7	3	0	13	19	33	6	0	0	0	0
ZILNEZ	MESA	070679	1346	MST	22.7	4	136	17	62	88	8	0	25	40	46
ZILNEZ	MESA	070679	1346	MST	22.7	5	123	0	1	12	34	52	53	34	27
ZILNEZ	MESA	070679	1346	MST	22.7	7	87	4	6	12	12	31	22	14	16
ZILNEZ	MESA	070679	1346	MST	22.7	8	45	9	21	34	56	0	0	0	0
ZILNEZ	MESA	070679	1346	MST	22.7	13	0	1	20	14	3	0	0	0	0
ZILNEZ	MESA	070679	1346	MST	22.7	20	123	0	5	4	57	74	40	11	4
ZILNEZ	MESA	070779	1326	MST	22.9	3	0	0	51	31	14	4	0	0	0
ZILNEZ	MESA	070779	1326	MST	22.9	4	139	111	136	111	14	0	0	0	0
ZILNEZ	MESA	070779	1326	MST	22.9	5	150	0	2	14	57	94	52	35	17
ZILNEZ	MESA	070779	1326	MST	22.9	7	86	14	11	18	29	60	19	13	7
ZILNEZ	MESA	070779	1326	MST	22.9	8	66	9	21	34	56	0	0	0	0
ZILNEZ	MESA	070779	1326	MST	22.9	13	16	1	20	14	3	0	0	0	0
ZILNEZ	MESA	070779	1326	MST	22.9	20	150	0	10	4	25	47	61	28	5
ZILNEZ	MESA	070879	1402	MST	22.8	3	0	0	27	26	12	9	0	0	0
ZILNEZ	MESA	070879	1402	MST	22.8	4	93	201	91	106	7	7	51	41	38
ZILNEZ	MESA	070879	1402	MST	22.8	5	263	0	8	21	53	85	75	62	33
ZILNEZ	MESA	070879	1402	MST	22.8	7	56	10	9	8	12	15	12	13	0
ZILNEZ	MESA	070879	1402	MST	22.8	8	43	15	19	17	6	4	0	0	12
ZILNEZ	MESA	070879	1402	MST	22.8	13	16	4	12	11	3	0	0	0	0
ZILNEZ	MESA	070879	1402	MST	22.8	20	263	0	1	3	52	105	88	37	11
ZILNEZ	MESA	070979	1311	MST	24.1	3	0	20	66	20	0	0	0	0	0
ZILNEZ	MESA	070979	1311	MST	24.1	4	103	85	123	72	0	0	0	0	0
ZILNEZ	MESA	070979	1311	MST	24.1	5	233	3	5	9	34	68	72	73	50
ZILNEZ	MESA	070979	1311	MST	24.1	7	17	7	6	7	7	8	4	3	4
ZILNEZ	MESA	070979	1311	MST	24.1	8	35	70	27	18	5	2	0	3	0
ZILNEZ	MESA	070979	1311	MST	24.1	13	11	9	22	16	3	0	0	2	0
ZILNEZ	MESA	070979	1311	MST	24.1	20	233	0	5	5	17	26	81	39	9
ZILNEZ	MESA	071079	1458	MST	24.2	3	0	12	69	22	7	9	0	5	0
ZILNEZ	MESA	071079	1458	MST	24.2	4	78	8	128	50	21	0	0	0	0
ZILNEZ	MESA	071079	1458	MST	24.2	5	150	0	6	7	31	61	85	29	54
ZILNEZ	MESA	071079	1458	MST	24.2	7	0	3	12	6	7	13	10	3	4
ZILNEZ	MESA	071079	1458	MST	24.2	8	25	8	38	17	4	0	0	0	3
ZILNEZ	MESA	071079	1458	MST	24.2	13	11	1	23	14	5	0	0	0	0
ZILNEZ	MESA	071079	1458	MST	24.2	20	150	0	0	25	32	67	81	19	4
ZILNEZ	MESA	071179	1700	MST	41.7	3	0	0	250	45	12	0	0	0	10
ZILNEZ	MESA	071179	1700	MST	41.7	4	142	25	324	186	87	3	0	0	23
ZILNEZ	MESA	071179	1700	MST	41.7	5	200	0	7	13	54	150	168	79	95
ZILNEZ	MESA	071179	1700	MST	41.7	7	22	12	26	18	17	14	7	2	3
ZILNEZ	MESA	071179	1700	MST	41.7	8	38	21	101	57	23	3	2	0	1
ZILNEZ	MESA	071179	1700	MST	41.7	13	19	10	61	41	20	3	0	0	0

T: sample time in hours

Code: 3 = Al; 4 = Si; 5 = S by PIXE; 7 = K; 8 = Ca; 13 = Fe; 20 = S by FVFPD

M: elemental mass concentration by filter, in ng/m^3

EMi: blank corrected elemental mass collected on stage i of LPI, in ng

999: data missing

China Lake Filter Data

Filter #	Start Date	Start Time (PST)	T	Volume	$\bar{b}_{sp}$	$\bar{b}_{ap}$	M_T	C_T	Soot	$SO_4^=$	NO_3^-	NH_4^+	Al	Si	S	K	Ca	Fe	Pb
104	227	830	72.2	91.9	10.0	99.9	4940	520	110	820	70	330	42	92	317	16	18	23	36
112	307	930	47.5	59.8	10.0	99.9	5650	490	120	810	65	270	61	172	320	43	26	38	37
118	313	1055	22.3	27.1	35.0	99.9	10500	710	240	2000	110	730	0	85	811	20	0	17	42
128	314	1030	21.8	27.5	38.0	99.9	10200	3710	400	3740	270	1400	0	95	1160	0	0	41	45
133	321	830	24.0	29.6	25.0	99.9	8420	1490	210	1710	390	640	0	85	842	32	12	21	34
103	322	910	23.2	29.0	30.0	99.9	9580	3240	270	3250	370	1030	0	76	980	0	7	10	39
136	329	854	24.4	30.7	10.0	99.9	6230	1230	150	1160	110	420	0	77	532	15	0	17	2
202	402	1738	14.5	17.6	22.0	99.9	5390	420	120	1020	160	260	0	284	459	48	74	79	20
204	403	853	30.3	36.3	1.3	3.5	6470	1170	210	1180	310	280	108	352	504	80	107	109	39
213	404	1530	24.0	28.7	9.3	3.8	5400	1320	200	670	130	250	63	250	353	61	64	66	35
205	405	1544	17.0	20.4	23.0	6.7	9710	2690	390	1470	270	580	70	177	624	53	83	69	68
214	411	1600	17.0	15.8	15.0	2.2	7910	5370	650	1210	180	370	112	122	628	69	24	45	60
209	426	940	27.5	23.9	9.6	0.5	3180	1830	60	970	90	330	52	229	486	37	44	49	13
210	430	1500	16.7	14.8	23.0	2.1	5610	1830	180	1950	23	610	130	389	997	69	101	99	30
211	501	750	24.2	20.3	12.0	2.5	5620	999	999	910	50	320	69	258	450	51	67	65	35
317	515	1400	18.8	16.4	28.0	5.1	11800	1570	140	2010	110	660	124	834	951	229	206	178	29
303	516	900	25.3	23.4	30.0	6.4	12300	1530	160	2710	310	880	109	480	984	175	174	157	51
302	521	900	22.5	15.8	46.0	99.9	21100	2860	200	4710	140	1660	35	505	2088	129	129	141	87
304	522	743	25.5	14.6	45.0	6.0	20100	2520	220	4790	50	1860	52	382	2084	123	118	144	63
309	604	820	29.0	24.4	22.0	3.2	9360	1040	110	640	60	450	39	342	440	112	94	115	35
310	605	1330	18.9	15.9	39.0	7.2	16000	1990	210	2720	290	780	209	628	1016	250	144	169	62
313	607	745	30.0	25.7	17.0	99.9	7170	470	50	540	70	90	233	610	257	114	122	150	9
316	615	1055	22.9	19.3	27.0	5.1	12200	1390	140	1070	630	470	171	493	573	293	108	119	24
402	620	745	25.0	27.4	39.0	6.2	15700	1550	170	2930	1030	1040	88	329	1066	467	145	87	56
408	626	735	24.1	26.7	32.0	5.5	11700	1130	130	1930	240	800	15	160	709	173	64	88	48
406	627	750	23.6	25.1	35.0	4.9	12400	1180	150	2590	360	960	59	241	889	201	77	85	39
401	628	735	27.3	25.8	43.0	99.9	14300	1400	160	3140	500	1050	115	389	1187	308	123	127	48
318	702	700	24.6	22.9	33.0	5.2	9450	1180	140	2210	180	720	16	262	817	98	85	76	39
314	705	710	24.0	21.2	28.0	4.5	11700	1280	150	2130	120	820	75	266	1021	202	38	68	65
400	709	948	21.7	20.5	14.0	2.8	7620	550	90	1550	0	500	999	222	539	69	63	59	61
320	710	740	23.3	22.4	22.0	4.9	10700	1010	160	1580	50	650	57	412	462	220	93	116	45
312	711	710	24.5	18.4	24.0	6.6	12100	1930	200	1970	80	780	125	421	1079	190	94	110	54

99.9: data missing

Chine Lake Filter Data (continued)

Filter #	Start Date	Start Time(PST)	T	Volume	$\bar{b}_{sp}$	$\bar{b}_{ap}$	M_T	C_T	Soot	$SO_4^=$	NO_3^-	NH_4^+	Al	Si	S	K	Ca	Fe	Pb
421	731	2000	11.0	9.9	35.0	6.0	13000	1070	200	1690	0	680	0	389	868	86	15	72	42
436	803	1000	6.0	5.4	39.0	7.6	16700	1632	1007	3990	190	1160	0	492	1229	167	27	18	72
437	806	900	6.0	5.2	26.0	2.0	14200	1150	100	1780	0	670	0	383	969	241	27	76	75
700	806	1900	11.0	8.8	47.0	9.0	23900	2450	290	3100	210	1090	0	1411	1305	372	296	309	124
701	807	900	6.0	5.3	25.0	5.1	14900	571	571	2740	130	738	0	85	822	109	27	47	76
702	807	1900	11.0	9.7	45.0	6.9	18100	1853	900	3540	310	1080	0	538	1021	254	42	75	168
704	808	1900	11.0	9.6	51.0	7.6	18200	1308	797	3150	700	1040	0	645	1129	257	91	124	124
706	809	1900	11.0	9.6	51.0	8.1	18700	2172	859	3830	320	1290	0	312	985	121	81	81	102
712	815	2000	11.0	9.6	47.0	8.6	17600	6781	966	3340	150	1190	0	548	1693	232	15	62	43
714	816	2000	11.0	11.1	8.7	2.2	5900	712	318	750	50	218	0	556	378	86	13	28	37
715	817	900	7.0	6.8	11.0	2.2	8400	195	195	1190	90	295	0	330	567	102	19	40	54
718	821	1000	6.0	5.9	8.5	2.5	10000	1083	285	1000	0	227	0	245	554	34	24	49	67
719	821	2000	11.0	9.6	29.0	6.7	15100	813	734	3430	190	1200	0	306	1279	22	27	53	42
816	905	1000	6.0	5.9	17.0	2.5	12500	2500	560	1680	50	535	0	99	923	44	31	22	96
817	905	2110	7.8	7.3	49.0	8.8	19700	5600	1100	4240	440	1430	0	663	1766	188	80	70	58
818	906	1210	6.4	8.6	24.0	5.9	11500	2100	620	1920	310	582	0	356	662	81	16	93	102
819	906	2329	10.3	13.5	37.0	7.9	11800	3100	890	2370	190	797	0	587	766	128	57	113	74
820	907	1100	7.0	9.6	34.0	7.6	9800	2500	910	3650	120	1170	0	921	1539	187	120	120	40
827	1110	0	24.0	21.2	24.0	4.7	5800	2500	587	1530	170	528	0	278	494	47	7	70	74
848	1118	0	24.0	21.2	8.1	1.6	4500	569	167	609	70	161	0	304	221	41	39	36	18
840	1119	945	23.5	21.7	9.0	0.9	4600	191	71	264	30	20	0	343	133	60	66	42	18
844	1120	930	23.5	20.4	24.0	5.1	6000	1182	670	504	180	20	0	591	133	123	122	82	68
849	1211	0	24.0	20.9	24.0	3.9	8400	1149	443	1110	230	56	0	1037	171	161	183	155	24
847	1212	1000	22.3	19.4	18.0	8.2	7000	1702	739	166	30	22	0	865	65	119	81	127	123
845	1215	600	22.0	19.1	13.0	5.5	5800	1196	510	316	130	75	0	591	161	130	69	81	70
838	1217	900	18.0	15.4	15.0	7.2	7900	1681	791	418	210	87	0	597	227	157	95	76	73
843	1220	900	23.8	21.2	12.0	3.5	5400	966	369	888	140	290	0	325	381	56	47	30	21
836	1221	900	24.0	20.9	4.6	3.6	6000	775	548	471	80	124	0	330	78	74	57	64	508
835	1228	1100	23.0	20.0	15.0	8.8	8400	2440	1047	718	170	196	0	532	206	142	71	97	223

T: sample time, hours

Volume: air volume sampled by Nuclepore filter, m^3

$\bar{b}_{sp}$, $\bar{b}_{ap}$: average b_{sp}, b_{ap} during sampling interval, in $10^{-6} m^{-1}$

All mass concentrations are in ng/m^3